The Physical Role of Transverse Deep Zones in Improving Constructed Treatment Wetland Performance

by

Anne F. Lightbody

B.S./M.S. Biology
Yale University, 1999

M.S. Civil and Environmental Engineering
Massachusetts Institute of Technology, 2004

Submitted to the Department of Civil and Environmental Engineering
in partial fulfillment of the requirements for the degree of

Doctor of Philosophy in the Field of Environmental Engineering

at the

MASSACHUSETTS INSTITUTE OF TECHNOLOGY

September 2007

Signature of Author .....
Department of Civil and Environmental Engineering
August 3, 2007

Certified by .....
Heidi M. Nepf
Professor of Civil and Environmental Engineering
Thesis Supervisor

Accepted by .....
Daniele Veneziano
Chairman, Departmental Committee for Graduate Students

The Physical Role of Transverse Deep Zones in Improving Constructed Treatment Wetland Performance

by

Anne F. Lightbody

Submitted to the Department of Civil and Environmental Engineering
on August 3, 2007, in partial fulfillment of the
requirements for the degree of
Doctor of Philosophy in the Field of Environmental Engineering

Abstract

Velocity heterogeneity is often present in wetland systems and results in some influent water remaining in the wetland for less than the expected residence time. This phenomenon, known as short-circuiting, alters the distribution of the chemical and biological transformations that occur within the wetland and decreases performance in constructed treatment wetlands. In this thesis, field observations, experiments in a laboratory physical model, and mathematical modeling are used to explore the ability of transverse deep zones to mitigate the negative effect of short-circuiting on constructed wetland performance.

Field observations were used to quantify short-circuiting in a 360-acre constructed treatment wetland in Augusta, Georgia. In each of the three marsh sections examined, between three and six narrow flowpaths were found that together carried 20–70% of the flow at a velocity at least ten times faster than the rest of the marsh.

One known method for offsetting the deleterious effect of short-circuiting flowpaths is to include several transverse deep zones within each wetland cell. To study the physical mechanisms behind this proposed strategy, laser-induced fluorescence (LIF) was used within a laboratory scale model of a short-circuiting wetland with a transverse deep zone. Water exiting a fast flowpath formed a jet that initially entrained co-flowing fluid and spread laterally but then, due to the drag present within the system, reached a final width that depended on the width of the upstream flowpath.

Finally, the understanding of flow patterns gained by the field and laboratory experiments were combined into an analytical streamtube model. Modeled results revealed that a transverse deep zone can offset the adverse impact of short-circuiting flowpaths through two separate mechanisms. When lateral mixing is present within the deep zone, it dilutes the water that has traveled through the fast flowpath. In addition, deep zones likely reduce the probability that fast flowpaths will align throughout the entire wetland, which increases the probability that all water will receive some treatment even when no lateral mixing is present within the deep zones. These results indicate that deep zones may improve performance when properly sized and located within a constructed treatment wetland.

Thesis Supervisor: Heidi M. Nepf
Title: Professor of Civil and Environmental Engineering

Acknowledgments

Thanks to Heidi Nepf for her patience, her creativity, her passion for fluid mechanics, and her willingness to take on a reformed biologist. I would not have come this far in this field without her support and encouragement. Her ability to bring out the best in each student at all levels is truly inspirational.

Jim Bays provided the engineering motivation for this work, along with continual reality checks, new approaches, and enthusiasm.

I would also like to thank the other members of my thesis committee, Eric Adams and Ole Madsen, for their time and many helpful comments.

Yukie Tanino, Aaron Chow, Brian White, Marco Ghisalberti, Molly Palmer, Enda Murphy, Kevin Zhang, and the other Parsons Environmental Fluid Mechanics students provided invaluable insights and perspective.

This work would not have been possible within the assistance of MIT undergraduates Maggie Avener, Lindsey Sheehan, Amanda Sorenson, Kat Vader, Mary Harding, and Jamie Fleischfresser; Dr. Gene Eidson, Oscar Flite, and other staff at the Southeastern Natural Sciences Academy; and Mark Andrews at Operations Management International, Inc.

I will always be grateful to NKL and JCL for their unending support and enthusiasm; LCL, for telling me to go to graduate school in the first place; and the rest of

my family for their continued love and support.

Thanks to dln, AD, EL, DSH, SIC, SEC, RLD, BD, MCS, SC, ERF, KFM, MK, CCB, all of my many teammates, the residents of Random Hall, MITOC, and everyone else who has helped keep me sane over the last five years.

Finally, I am grateful for the funding agencies that allowed me the freedom to work on a project of my own devising: the National Defense Science and Engineering Graduate Fellowship Program, the Switzer Foundation, the Martin Family Foundation, and the National Science Foundation. Any opinions, findings, or recommendations expressed in this material are mine alone and do not necessarily reflect the views of the National Science Foundation.

Contents

List of Figures

List of Tables

List of Symbols

a	Volumetric frontal area of vegetation or other distributed elements
A	Wetland surface area
A_{cell}	Wetland cell surface area
A_{dz}	Deep zone surface area
A_m	Cross-sectional area of the main flow path
A_s	Cross-sectional area of the storage zone
b_C	Half-width of the jet concentration curve
$b_{c,o}$	Initial half-width of the jet concentration curve
b_f	Fast flowpath width
Σb_f	Total width of parallel fast flowpaths
b_I	Half-width of the fluorescein intensity curve
b_m	Lateral position of jet centerline
b_u	Half-width of jet velocity curve
$b_{u,o}$	Initial half-width of jet velocity curve
b_δ	Lateral distance between two fast flowpaths
b_j	Half-width of the full jet
B	Wetland width
B_f	Wetland width associated with a single fast flowpath
$\hat{B}$	Jet width length scale
c	Instantaneous concentration
$\bar{c}$	Concentration averaged over turbulent fluctuations
c'	Concentration deviation from temporal average
$\bar{c}''$	Spatial deviation of time-averaged concentration

$\langle\bar{c}\rangle$	Concentration averaged over depth and turbulent fluctuations
$\langle\bar{c}\rangle_a$	Concentration averaged over turbulent fluctuations and the cross-section
$c*$	Background concentration
c_e	Wetland exit concentration
$c_{e,f}$	Concentration at the end of a fast flowpath
$c_{e,f1}$	Concentration at the end of a fast flowpath within the first marsh section
$c_{e,f2}$	Concentration at the end of a fast flowpath within the second marsh section
$c_{e,dz}$	Concentration at the end of a deep zone
$c_{e,j}$	Concentration at the end of the jet portion of the deep zone
$c_{e,k}$	Concentration at the end of the non-jet portion of the deep zone
$c_{e,s}$	Concentration at the end of a slow flow zone
$c_{e,s1}$	Concentration at the end of a slow flow zone within the first marsh section
$c_{e,s2}$	Concentration at the end of a slow flow zone within the second marsh section
$c_{e,s2,a}$	Concentration at the end of a slow flow zone within the second marsh section that passed through the fast flowpath in first marsh section
$c_{e,s2,b}$	Concentration at the end of a slow flowpath within the second marsh section that did not pass through the fast flowpath in first marsh section
c_m	Jet midline concentration
c_o	Entrance concentration
$c_{o,j}$	Concentration entering the jet
$c_{o,k}$	Concentration entering the non-jet portion of the deep zone
$c_{release}$	Release concentration
c_s	Concentration of slow-flow zone
C_a	Surface drag coefficient

C_d	Stem drag coefficient
C_f	Bed drag coefficient
C_w	Wall drag coefficient
C_z	Chezy resistance factor
d	Stem diameter
Da	Damkohler number
D_m	Molecular diffusivity
D_z	Vertical diffusivity
f_u	Self-similar function for lateral velocity distribution
f_C	Self-similar function for lateral concentration distribution
f_o	Darcy-Weisbach friction coefficient
Fr	Froude number
$F_{d,x}$	Drag force in the longitudinal direction
$F_{d,y}$	Drag force in the lateral direction
$F_{d,z}$	Drag force in the vertical direction
$\langle F_{d,x} \rangle$	Depth-averaged drag force in the x-direction
$\langle F_{d,y} \rangle$	Depth-averaged drag force in the y-direction
g	Gravitational constant
h	Water depth
$\langle h \rangle_a$	Spatially averaged wetland depth
h_{dz}	Deep zone depth
h_m	Marsh water depth
$\bar{I}$	Time-averaged dye intensity
I_m	Maximum dye intensity
I_C	Integral of jet concentration distribution
I_{CC}	Integral of jet concentration distribution squared
I_u	Integral of jet velocity distribution
I_{uu}	Integral of jet velocity distribution squared
$j_{release}$	Mass flux of dye release
$j_{dz,exit}$	Mass flux exiting deep zone

J	Jet mass flux
J_o	Initial jet mass flux
k_a	Areal removal rate
k_{dz}	Areal removal rate in the deep zone
k_f	Areal removal rate in fast flowpaths
k_s	Areal removal rate in slow flow zones
k_v	Volumetric removal rate
K_x	Longitudinal dispersion coefficient
K_y	Lateral dispersion coefficient
L	Wetland length
ΔL	Length of a portion of a wetland
L_{dye}	Distance traveled by dye
L_{dz}	Length of a deep zone
$L_{dz,min}$	Minimum length of a deep zone that fully dissipates momentum and can be constructed
L_m	Length of marsh section
L_{m1}	Length of first marsh section
L_{m2}	Length of second marsh section
L_{m3}	Length of third marsh section
L_{slope}	Length of deep zone entrance slope
m	Jet momentum flux
m_o	Fast flowpath momentum flux
Σm_f	Momentum flux within all fast flowpaths
$M_{release}$	Mass released
n	Number of measurements
n_{cell}	Number of cells
n_{dz}	Number of deep zones
$n_{dz,opt}$	Optimal number of deep zones
n_f	Number of fast flowpaths
n_M	Manning's coefficient

n_v	Stem density
N	Number of equivalent tanks in series (TIS)
N_{dz}	Number of equivalent TIS for deep zone
N_f	Number of equivalent TIS for fast flowpath
N_m	Number of equivalent TIS for a marsh area
N_s	Number of equivalent TIS for slow flow zone
O	Order of magnitude
p	Exponent associated with the evolution of jet midline velocity
P	Pressure
$\bar{P}$	Pressure averaged over turbulent fluctuations
P'	Deviation from time-averaged pressure
P_∞	Pressure far outside of a jet
Pe	Peclet number
q_j	Jet volumetric flow rate
q_k	Flow rate not in the jet
q_{kb}	Flow rate that passed through a fast flowpath in the first marsh section but not in the second
q_f	Volumetric flow rate of a single fast flowpath
Σq_f	Volumetric flow rate of all fast flowpaths
q_s	Flow rate through slow zones
q_{sb}	Flow rate in slow zone portion of second marsh that did not pass through upstream flowpath
Q	Wetland volumetric flow rate
Q_f	Volumetric flow rate of a region of wetland with a single flowpath
r^2	Correlation coefficient
r	Exponent associated with evolution of jet width
$\dot{r}$	Volumetric reaction rate
$\langle \dot{r} \rangle$	Depth-averaged reaction rate
$\dot{r}_b$	Bed reaction rate
$\dot{r}_s$	Surface reaction rate

R	Hydraulic radius
Re	Reynolds number
Re_d	Stem Reynolds number
Re_h	Depth Reynolds number
Re_j	Jet Reynolds number
$Re_{j,o}$	Initial jet Reynolds number
Re_m	Marsh Reynolds number
S	Shallowness parameter
S_E	Energy slope
t	Time
t_{dye}	Dye travel time
t_{pf}	Plug flow time of transit
$\hat{T}$	Time scale
T_{det}	Effective detention time
T_{dz}	Average residence time within deep zone
$T_{dz,min}$	Minimum residence time within deep zone
T_f	Transport time within fast flowpaths
T_{f1}	Transport time in a fast flowpath within first marsh section
T_{f2}	Transport time in a fast flowpath within second marsh section
T_m	Average transport time within marsh
T_{m1}	Average transport time within first marsh section
T_{m2}	Average transport time within second marsh section
T_{peak}	Time of peak
T_s	Transport time within a slow flow zone
T_{s2}	Transport time in a slow flow zone within the second marsh section
u	Instantaneous longitudinal velocity
$\bar{u}$	Longitudinal velocity averaged over turbulent fluctuations
u'	Deviation from time-averaged longitudinal velocity
$\langle\bar{u}\rangle$	Longitudinal velocity averaged over turbulent fluctuations and over depth

$\bar{u}''$	Deviation from the depth-averaged longitudinal velocity
u^*	Friction velocity
u_c	Co-flow velocity
u_{dye}	Dye transport velocity
u_m	Jet midline velocity
$u_{m,o}$	Jet initial midline velocity
u_{peak}	Peak velocity within a fast flowpath
u_{pf}	Plug flow velocity
$u_{pf,m}$	Marsh plug flow velocity
$\hat{U}$	Characteristic velocity scale
U_{10}	Wind velocity ten meters above the ground
U_f	Transport velocity of a fast flowpath
U_m	Average marsh flow velocity
U_s	Transport velocity of slow flow zone
v	Instantaneous transverse velocity
$\bar{v}$	Transverse velocity averaged over turbulent fluctuations
v'	Deviation from time-averaged transverse velocity
$\langle\bar{v}\rangle$	Transverse velocity averaged over turbulent fluctuations and over depth
$\bar{v}''$	Deviation from the depth-averaged transverse velocity
v_e	Entrainment velocity
V	Wetland volume
V_{dz}	Deep zone volume
V_o	Voltage
w	Instantaneous vertical velocity
$\bar{w}$	Vertical velocity averaged over turbulent fluctuations
w'	Deviation from time-averaged vertical velocity
$\langle\bar{w}\rangle$	Vertical velocity averaged over turbulent fluctuations and over depth
$\bar{w}''$	Deviation from the depth-averaged transverse velocity
$\bar{w}_b$	Time-averaged vertical velocity at the bed
w_p	Settling velocity

$\bar{w}_s$	Time-averaged vertical velocity at the surface
x	Longitudinal coordinate
$\hat{x}$	Distance to end of jet development region
x_{ub}	Longitudinal position of jet velocity width virtual origin
x_{cb}	Longitudinal position of jet concentration virtual origin
x_{diss}	Distance of complete jet dissipation
x_{weak}	Distance to jet decaying from strong jet to weak jet
x_u	Longitudinal position of jet velocity virtual origin
x_{Cu}	Longitudinal position of jet concentration virtual origin
$\hat{X}$	Longitudinal length scale
y	Lateral coordinate
y_1	Lateral location of fast flowpath in first marsh zone
y_2	Lateral location of fast flowpath in second marsh zone
y_3	Lateral location of fast flowpath in third marsh zone
y_4	Lateral location of fast flowpath in fourth marsh zone
$\hat{Y}$	Lateral length scale
z	Vertical distance below the surface
α_e	Entrainment coefficient
β_C	Constant of jet concentration half-width growth
β_m	Constant of jet midline migration
β_u	Constant of jet half-width growth
β'_u	Constant of jet half-width growth as a function of water depth
γ_C	Constant of jet maximum concentration decay
γ_u	Constant of jet velocity decay
Γ	Gamma function
δ	Non-dimensional lateral distance between fast flowpaths
δ_D	Dirac delta function
ϵ_s	Lateral exchange
η_u	Nondimensional lateral coordinate for velocity
η_C	Nondimensional lateral coordinate for velocity

θ	Deep zone entrance slope
κ	Scale factor between fast-flow path peak and average velocities
λ	Lateral mixing coefficient
ν	Kinematic viscosity
ν_t	Turbulent eddy viscosity
ξ_u	Lateral Gaussian velocity distribution coefficient
ξ_C	Lateral Gaussian concentration distribution coefficient
ρ_a	Air density
ρ_{dye}	Dye density
ρ_w	Water density
σ	Standard deviation
σ_t^2	Temporal variance
τ	Nominal wetland residence time
τ_b	Bottom shear stress
$\tau_{b,x}$	Longitudinal bottom shear stress
$\tau_{b,y}$	Lateral bottom shear stress
τ_s	Surface shear stress
$\tau_{s,x}$	Longitudinal surface shear stress
$\tau_{s,y}$	Lateral surface shear stress
ϕ	Vegetation volume fraction
ψ	Fraction of fast flow that passes into fast flowpath in next marsh section
ψ'	Fraction of fast flow that passes into fast flowpath in later marsh sections
ω_z	Vertical vorticity
$\omega_{z,o}$	Initial vertical vorticity

List of Abbreviations

1-D	one-dimensional
2-D	two-dimensional
3-D	three-dimensional
ADV	acoustic Doppler velocimetry
BOD_5	5-day biological oxygen demand
C	Celsius
CCD	charge-coupled device
CTD	Conductivity, Temperature, and Depth
DND	Damkohler number distribution
HLR	hydraulic loading rate
HRT	hydraulic residence time
LDV	laser Doppler velocimetry
LIF	laser-induced fluorescence
NOAA	National Oceanic and Atmospheric Administration
RGB	red, green, and blue
RTD	residence time distribution

TIS	tanks in series
TSS	total suspended solids
USDA	United States Department of Agriculture
USGS	United States Geological Survey
WWTP	Wastewater Treatment Plant

Chapter 1

Introduction

1.1 Brief introduction to constructed treatment wetlands

Even though they comprise less than 2% of the earth's surface and store less than 0.001% of the earth's water (Thurman 1997, pp. 79-80; Mitsch and Gosselink 2000, pp. 35-37), wetlands play an important role in the earth's water cycle. Often likened to nature's kidneys, wetlands remove nutrients, metals, pathogens, chemicals, and sediments traveling through them. In addition, they provide habitat to species ranging from dragonflies to mink to rare species of birds. They can provide water storage during times of peak flows. They slow flow and allow infiltration to occur. Salt marshes and mangroves reduce shoreline erosion during storms. Understanding and predicting how water and dissolved and suspended matter travel through wetlands are crucial to understanding the ability of wetlands to play each of these vital roles.

One of the most important and useful roles of wetlands is that of water purification: removing sediment and contaminants from polluted waters. Contaminants that enter a wetland, either natural or constructed, are removed through a combination of chemical, biological, and physical mechanisms, which act to consume, break down, bury, or volatize contaminants. A natural wetland is an intricate, complicated assemblage of hydrology, soils, and ecology. Although they cannot and often do not

attempt to replicate the full complicated structure of natural wetlands, constructed wetlands are increasingly used to harness wetlands' natural ability for water quality improvement in wastewater and storm water applications.

In addition to providing pollutant removal, treatment wetlands provide many ancillary benefits to the community. With good design, constructed wetlands can become scenic locations to which neighbors and visitors alike come to enjoy walking, hiking, jogging, biking, nature art and photography, and wildlife observation. They can be the focus of science education activities in such disciplines as entomology, zoology, water chemistry, microbiology, and botany (Reitberger et al., 2000). Within North America alone, over 1,400 species of wildlife have been found in treatment wetlands, including 824 species of aquatic invertebrates, 78 species of fish, 21 species of amphibians, 31 species of reptiles, 22 species of mammals, and 412 species of birds (Knight et al., 2000*a*). Wetlands are well known for providing productive habitat for both resident and migratory avian species, which makes them popular with bird-watchers (Reitberger et al., 2000). Treatment wetlands may be able to provide habitat for endangered and threatened bird species, especially useful in areas where their habitat is threatened (Connor and Luczak, 2002). Potential commercial uses include hunting, fishing, trapping, plant harvesting, and aquaculture (Knight et al., 2000*a*). One of the only fears about wetlands is that they may be able to provide wet locations where mosquitoes can breed. Long-term planning, including the introduction of predators, can inhibit mosquito breeding, and at this stage there is little risk of constructed wetlands creating a risk of mosquito-transmitted disease (Dale et al., 2002; Walton, 2002). In fact, constructed wetlands are so desirable that homeowners are willing to pay an average premium of $10,000 for a view of a well-designed wetland (Schueler, 2000).

There are numerous types of constructed wetlands, with free-surface wetlands (also known as surface flow systems) the most analogous to natural open water wetlands. This thesis explores the pollutant removal abilities of free-surface constructed treatment wetlands with emergent macrophytes that have permanent standing water over the soil surface (Fig. 1-1). This thesis focuses on wetlands that treat steady

flows, rather than storm water or tidal inputs.

1.2 Constructed treatment wetland costs

Economics drive the decision to construct a free-surface treatment wetland. Although ancillary benefits may be important, the decision depends ultimately on the cost to build and operate a wetland designed to provide a certain level of treatment. Direct comparison with conventional treatment plants shows that in some locations treatment wetlands can provide as good treatment as conventional plants can for a fraction of the cost. For example, a detailed case study by Hey et al. (2005) in greater Chicago found that using wetlands instead of advanced treatment processes to remove excess nutrient and phosphorus from wastewater results in an annual savings of 51–63%.

Table 1.1 provides information on costs reported in the literature for surface-flow treatment wetlands. Capital costs associated with wetland construction are 2–14 $\$/m^2$. Construction costs differ substantially between wetlands, since they depend on many site-specific factors, including wetland area, existing site use, hydrology, climate, influent water quality, and effluent standards. For example, land costs alone can differ by as much as 2000% in rural areas within different portions of the U.S. (U. S. Department of Agriculture, 2006); siting a wetland in an urban area would of course increase costs substantially.

One of the most important benefits of choosing a wetland over a water treatment plant is that operations and maintenance costs for wetlands are typically much lower than for conventional treatment. Typical annual maintenance activities include mowing and inlet and outlet inspection and cleaning. Up to three times over the life of a wetland, the forebay may need to be dredged and vegetation to be replanted. These activities are only periodic, however, and operators require little training. Annual cost savings can be large. For example, Brodie et al. (1989) report that switching from a traditional wastewater treatment method for acid mine drainage (sediment pond with sodium hydroxide addition) to a constructed wetland decreased annual

maintenance costs from $28,5000 to $3,700. As a result, constructed wetlands can represent substantial cost-savings over their life cycle.

1.3 Dimensions of free-surface constructed treatment wetlands

Surface-flow wetlands within North America vary in size from 0.0004–1406 ha, with 75% smaller than 10 ha (U. S. Environmental Protection Agency, 2000). Wetland lengths in the field can vary from $L = O(100\text{ m})$–$O(10\text{ km})$, and wetland widths from $B = O(10\text{ m})$–$O(10\text{ km})$. A bottom slope (hydraulic gradient) of 0.01–0.5% is recommended for surface-flow wetlands, depending on the wetland length and flow resistance (U. S. Environmental Protection Agency, 2000; Mitsch and Jorgensen, 2004, p. 246). The wetland volume $V = A\langle h\rangle_a$, where A is the wetland area and $\langle h\rangle_a$ is the water depth averaged over the wetland surface area. Many constructed wetlands contain pockets of deeper open water of depth h_{dz} interspersed with vegetated marsh areas of average depth h_m. When the depth of the wetland is variable, it may be difficult to measure the average depth $\langle h\rangle_a$ and therefore determine accurately the wetland volume (Keller and Bays, 2002).

Water depths in shallow marsh regions are restricted by practical considerations: an average water depth $h_m \leq 15$ cm may not allow water to flood completely a mature marsh that contains some plant detritus, and water depths greater than $h_m = 30$–45 cm may inhibit plant health and growth (Knight et al., 2000*b*; Thullen et al., 2005). Macrophyte species within these freshwater systems typically include hydrophilic species such as *Typha latfolia* (cattail), *Phragmites australis*, *Juncus* spp. (rushes), *Scirpus* spp. (bulrushes), *Eleocharis* (spikerushes), and *Sagittaria* spp. (arrowheads) (cf. Kadlec and Knight, 1996). Different species are able to tolerate different flooding regimes and may uptake different amounts of contaminants (Tanner, 1996; Giovannini and da Motta Marques, 1999; Bragato et al., 2006). The dense vegetation within marsh areas shelters the water surface from the wind, which hinders

the exchange of oxygen and other gases (Brix, 1994).

Deep zones within wetlands, which may also be called ditches or ponds, provide many important functions, including an increase in habitat diversity for species ranging from invertebrates to birds, a quiescent area that promotes sedimentation and passive aeration, interior locations for operational water quality sampling, a suitable habitat for mosquito predators, and a deep-water refuge for fish and other wildlife in dry weather (Knight et al., 2000*b*; Reitberger et al., 2000; Sartoris et al., 2000*b*; Bays and Knight, 2002; Thullen et al., 2002, 2005). To suppress emergent vegetation, deep zones must be deeper than $h_{dz} \approx 1.25$ m (U. S. Environmental Protection Agency, 2000); as a result, water depth h often varies over wetland length. The depth ratio between shallow and deep zones is approximately $h_{dz}/h_m = 0.4$. Depending on the cohesiveness of wetland bottom sediment, the slope between the marsh and deep zone areas is typically between 3:1 and 10:1; steeper slopes will tend to erode or slump over time (Frossard et al., 1996; Knight et al., 2000*b*). A small flat area at least 2-m wide at the bottom of the deep zone is often required during construction, creating a minimum deep zone length in a full-scale wetland of approximately $L_{dz,min} = 15$ m (J. S. Bays, pers. comm.). Wetlands can be graded to a constant elevation with as low as ± 3 cm variation, although grading within the range of ± 15 cm is more typical (Knight et al., 2000*b*).

The volumetric flow rate Q through a constructed wetland often depends on the size of the wetland. Constructed wetlands are typically designed to receive a hydraulic loading rate HLR $= Q/A =$ 1–5 cm/d (Kadlec and Knight, 1996, p. 583). The nominal hydraulic residence time (HRT) of a wetland is:

$$\tau = \frac{V}{Q} = \frac{\langle h \rangle_a}{\text{HLR}} \tag{1.1}$$

Note that, if two wetlands have the same mean depth and the same HLR, then they will also have the same HRT τ, independent of their area. To ensure sufficient contaminant removal, constructed treatments wetlands typically have HRTs of $\tau =$ 7–14 d (Kadlec and Knight, 1996, p. 583). Note that the HRT is a theoretical quantity;

in many wetlands, the presence of dead zones occluded from the main flowpath results in an effective system residence time T_{det} that is less than τ.

The vegetation within the marsh regions can be characterized by the stem density n_v (units of 1/length^2), average diameter d (units of length), and volumetric frontal area a (units of 1/length); the non-dimensional volume fraction of vegetation will be represented by $\phi \approx ad$. In freshwater wetlands, the vegetation volume fraction is typically in the range $\phi = 0.01$–0.15 (e.g., Jadhav and Buchberger, 1995). Let $U_m = Q/[Bh_m(1-\phi)]$ represent the average shallow-zone fluid velocity and thus the average velocity entering the deep zones. Flow around individual stems is controlled by the stem Reynolds number, $Re_d = U_m d/\nu$, where ν is the kinematic viscosity of water.

Vegetation is often patchy within constructed wetlands. Parr (1990) found that only 35% of constructed wetlands ever achieved macrophyte growth in 90% or more of the area designed to become marsh. Despite being planted and seeded, a small constructed wetland in Finland remained sparse for at least two years after initial construction (Koskiaho, 2003). On the other hand, a small constructed wetland in Fort Deposit, Alabama, had complete vegetative cover one year after construction (Bays and Knight, 2002).

1.4 Pollutant removal within free-surface wetlands

The ability of both constructed and natural wetlands to remove contaminants is well documented (Tilley and Brown, 1998). For example, wetlands have been able to remove over 80% of nitrogen and over 90% of total phosphorus, total suspended solids (TSS), 5-day biological oxygen demand (BOD_5), heavy metals, and pathogens (Sundaravadivel and Vigneswaran, 2001; Kadlec, 2003*b*). Some wetlands have exhibited a decrease in removal of some contaminants (e.g., fecal coliforms) over time, though ammonium removals remained 96–98% for over 20 years in Wildwood, Florida (Kadlec, 1979), and phosphorus removal rates rebounded to initial levels after maintenance in the Orlando Easterly Wetland (Wang et al., 2006). In fact, some free-

water-surface wetlands have remained effective for over 80 years (Kadlec et al., 2000).

Many wetland processes can be approximated as first order, following the equation:

$$\frac{\partial \bar{c}}{\partial t} = \frac{k_a}{h}(\bar{c} - c*) \tag{1.2}$$

where $\bar{c}$ is the concentration of a contaminant of interest averaged over turbulent fluctuations, t is time within the wetland, k_a represents an areal removal rate with units of length per time, and $c*$ is a background concentration. For some contaminants, the removal process itself is a first-order reaction. For example, TSS concentration decreases due to particle settling, which in a fully mixed system is linearly related to the average concentration within the water column:

$$\frac{\partial \langle \bar{c} \rangle_a}{\partial t} = \frac{w_p}{h}(\langle \bar{c} \rangle_a - c*) \tag{1.3}$$

where $\langle \bar{c} \rangle_a$ is the concentration of TSS averaged over the wetland cross-section and w_p is the average settling velocity. Ammonification, which is the conversion of organic nitrogen to ammonia, is a first-order process mediated by bacteria (Kadlec and Knight, 1996, pp. 380-383). Other contaminants, such as BOD_5 and inorganic nitrogen, are removed via a complicated combination of multiple pathways, but the overall process can be approximated as first order (Kadlec and Knight, 1996). Data suggest that for some contaminants the areal removal rate k_a rather than the volumetric removal rate k_v (units of 1/time) is constant over a depth range of 0.2–1.0 m (Kadlec, 1997), perhaps because removal occurs through processes mediated by sunlight or by contact with the bed. For such processes, the amount of contaminant per unit bed area $\langle \bar{c} \rangle_a \langle h \rangle_a$ declines following a first-order relationship. In a region of a wetland with constant depth the two quantities can be easily interchanged $k_a = \langle h \rangle_a k_v$. The Damkohler number $Da = k_v \tau = k_a/\mathrm{HLR}$ provides a comparison between a wetland's contaminant removal rate and flow rate. If $Da \gg 1$, water remains in the wetland long enough to have its concentration reduced to near background levels. On the other hand, if $Da \ll 1$, the wetland is undersized, and water exits the wetland before it has experienced much removal.

Removal rates within surface-flow wetlands vary depending upon the contaminant of interest (Table 1.2). For example, for phosphorus, the areal removal rates are in the range 2–24 m/yr for a constructed emergent marshes with hydraulic loading rates ranging from HLR $= Q/A = 0.4$–20 cm/d (Kadlec and Knight, 1996, p. 466); these values translate to a Damkohler number $Da = k_a/\text{HLR} = 0.1$–7, with an average range of 1–3. Other studies have shown $Da \approx 5$ for nitrogen, and $Da > 20$ for total suspended sediments. In addition, depending on the contaminant of interest, the removal rate may depend on the water temperature, dissolved oxygen, pH, organic carbon availability, season, and wetland age (Spieles and Mitsch, 2000). Note that these removal rates are average values reported from whole-wetland studies, which average over local biogeochemical processes, which can have rates that differ from this mean based on such heterogeneous parameters as the local flow speeds and level of oxygen (Eriksson, 2001). Detailed measurements of local removal rates under realistic flow conditions are rarely available, however.

Although constructed wetlands have the potential to improve water quality significantly, there is a large range in the removal rates observed. Some wetlands even increase the concentration of pollutants such as nitrogen and fecal coliforms (Kadlec, 2003*b*). The hydraulics of constructed wetlands, including water depths, flow velocities, HRTs, and residence time distributions (RTDs), affect internal processes and are crucial to predicting contaminant removal within the wetland. Designing a constructed wetland to achieve a specified performance goal requires the accurate prediction, and ideally optimization, of flow patterns through the wetland.

1.5 Short-circuiting in constructed wetlands

For nearly all removal processes, removal is maximized with plug-flow circulation, which results when water moving through the wetland experiences no longitudinal dispersion and all water reaches the exit at exactly the nominal HRT, τ. This idealized situation is rarely observed, however, and during slug tracer releases the peak concentration often reaches the outlet well before τ (Kadlec, 1994; Werner and Kadlec,

2000; Persson et al., 1999). This phenomenon is called short-circuiting. For example, in an 81-ha wetland in Florida, 32% of the flow exits the wetland in only 0.3τ (Keller and Bays, 2002). There is not a clear-cut definition of short-circuiting, although Thackston et al. (1987) suggested that a flow pattern should be classified as short-circuiting if significant fractions of dye reach the exit before $(0.3–0.4)\tau$.

The most obvious form of fast flowpath occurs where a portion of the wetland lies below the average marsh elevation. An extreme example is a tidal creek system, in which flow is dominated by transport within incised creek channel networks that are clearly visible in aerial photographs (Arega and Sanders, 2004). Most natural wetlands include a channelized streamflow component (Mitsch and Gosselink, 2000, p. 122). In many natural wetlands, macrophytes fringe a central, deeper open channel, with a large fraction of the flow carried by that channel (Cooper, 1994). Stern et al. (2001) observed that a central channel carried more than 50% of the flow in a natural wetland in Westchester, New York. Blahnik and Day (2000) noted that a tracer front moved rapidly through a forested wetland following deeper channelized areas with less dense vegetation. Constructed wetlands may also have deeper channels that create preferential flowpaths. For example, within the Everglades Nutrient Removal Project and the Orlando Easterly Wetlands in Florida, abandoned agricultural ditches and borrow canals oriented parallel to flow create dramatic short-circuiting (Guardo and Tomasello, 1995). Detailed aerial photographs and internal concentration measurements of the Everglades system showed that 1.2-m-deep ditches oriented parallel to flow constituted only 8% of the surface area of the cell but allowed 44–46% of the dye move at 3.3–4.1 cm/s; 54–56% of the flow traveled at approximately 1.1 cm/s through shallower vegetated zones (Dierberg et al., 2005). In a slug release in the Des Plaines Experimental Wetland EW3, the combination of shallow fringing areas with dense macrophytes and a central deeper open-water area with some floating aquatic vegetation and algae led to a peak outlet concentration at the outlet after only 3 d, when the nominal retention time was 10.5 d (Kadlec, 1994). The central ponded area in the Monash University Research Wetland in Australia allows incoming water to travel directly to the outlet (Somes et al., 1999). In a 700-ha wetland in Houghton

Lake, Michigan, deer paths resulted in depressions parallel to water flow, and within a 1.25-ha wetland in Hillsdale, Michigan Hillsdale, Michigan, muskrats were observed to create and use deep-water pathways through marsh areas; both types of paths created preferential flowpaths and short-circuiting (Kadlec, 1987; Kadlec et al., 2007).

However, not all fast flowpaths are marked by a different elevation (Dal Cin and Persson, 2000), and those that are not are more subtle and therefore more difficult to identify. For example, soil oxygen availability, microtopography, and vegetation clonal reproduction can interact to create patches of different types of vegetation (Marani et al., 2006), and changes in vegetation type and density can lead to differential travel times (Stern et al., 2001; Wörman and Kronnäs, 2005). Large interspersed patches of submerged aquatic vegetation and emergent cattail stands likely contributed to the observed velocity heterogeneity in the Everglades Nutrient Removal Project (Nungesser and Chimney, 2006). Martinez and Wise (2003*b*) found that nearly all of the 17 cells within a 520-ha constructed wetland in Florida exhibited sharp concentration peaks at the outlet within a third of the HRT. Internal measurements within a 60 m^2 wetland in North Carolina revealed a spatial variation of 400% in measured maximum concentrations (Rash and Liehr, 1999). DePaoli (1999) performed numerical simulations to show that random distributions of vegetation patches can create short-circuiting through the wetland; this effect is similar to percolation through heterogeneous porous media (e.g., Isichenko, 1992). Thullen et al. (2002) found that bulrush vegetative propagation created a patchy spatial distribution with dense (up to $n_v = 992$ stems/m^2) patches interspersed to areas with no bulrush stems.

Over time, vegetation heterogeneity can develop into discernable flowpaths. For example, Bays and Knight (2002) observed small channelized flowpaths in a portion of a ten-year-old 6-ha constructed wetland in Fort Deposit, Alabama. Kjellin et al. (2007) report that sparse vegetation contributed to short-circuiting in a treatment wetland in Ekeby, Sweden. Tracer releases in three small (50-m^2) wetlands that had initially been graded flat and planted with a uniform *Typha* cover revealed completely different flow patterns, an effect attributed to a heterogeneous pattern of litter accu-

mulation and plant density (Romero et al., 2000). In the Prado Wetlands in Riverside County, California, Lin et al. (2003) observed two major peaks in the outlet concentration record, which they attribute to two main flow paths through the wetland. It is likely that some amount of short-circuiting is always present in vegetated systems (Kadlec and Knight, 1996, p. 238).

The presence of short-circuiting alters the distribution of the chemical and biological transformations that occur within the wetland (Harvey et al., 2005). By creating deviations from plug flow, the velocity heterogeneity in a wetland can lead to reduced water quality improvements. For example, internal phosphorus concentrations measurements showed higher phosphorus removal rates in shallow vegetated regions than within the deeper canals that created short-circuiting within the Everglades Nutrient Removal Project (Dierberg et al., 2005). Low nutrient removal rates in a portion of a constructed wetland in east London in the United Kingdom were attributed to damage to the reed beds by grazing animals, which allowed water to flow directly from one sampling station to the next (Carapeto and Purchase, 2002). Keefe et al. (2004) observed in the Tres Rios wetlands that in a channelized cell reactive tracer losses were only one fifth of those in an unchannelized cell. Wörman and Kronnäs (2005) used a numerical model of the 35-ha Alhagen wetland system in Nynäshamn, Sweden, to show that increasing the correlation length of heterogeneity of the vegetation density changes the wetland's RTD, which reduces the removal achieved by the system. Through its marsh regions, a manmade oxbow wetland developed a central channel that had different levels of suspended sediments (higher turbidity) than the marsh regions on either side (Fink and Mitsch, 2007). Kadlec and Knight (1996, pp. 246-247) present a numerical simulation of a short-circuiting wetland that shows that, even if the wetland removal rate and background concentration are known accurately, the existence of different flow velocities will decrease performance 30% below the plug-flow expectation. The presence of short-circuiting must therefore be taken into account when considering treatment wetland performance. Even though some amount of short-circuiting is present in nearly all wetland systems, to date methods are not available to confidently mitigate for its presence.

1.6 Models of constructed wetlands

Because it is impossible to build full-scale wetlands to test every design parameter, it is necessary to use models that reflect important aspects of the flow while allowing the comparison of different design configurations. In particular, understanding and accounting for short-circuiting are vital for constructing accurate and useful models of wetland systems (Bolster and Saiers, 2002). The following types of models are currently used for wetland design (Fig. 1-2), although not all are appropriate for use in a situation with non-ideal flow patterns.

1.6.1 Prototype wetlands

Mesocosm and pilot-scale wetlands are often constructed to determine site-specific removal rates and background concentrations. The influent is typically the same source water, and the flow rate through the wetland is scaled to provide the same area-specific loading. Full-scale wetland design can then be finalized by incorporating observations of the performance of the pilot-scale wetland (Maine et al., 2006). For example, Gearheart et al. (1989) reported that 375-m^2 pilot cells were able to predict the BOD_5 removal ability of full-scale wetlands later constructed on the same site. However, when short-circuiting is present, the average removal rates obtained from detailed observations of a small system are not identical to those of a full-scale system built at the same site because flow patterns are likely different in the full-scale model. These detailed studies of rate constants must therefore be coupled with a hydraulic model of the full-scale system.

1.6.2 Physical models

Physical models have been used to explore the effect of drag due to vegetation within a canopy of either natural vegetation (Shi et al., 1996; Järvelä, 2002; Lee et al., 2004) or vegetation mimics such as vertical rods (Hodges et al., 1997; Nepf, 1999). In addition, physical models using a uniform distribution of dowels, brush bristles, and silicone tubes have been constructed to explore the sediment deposition and bed

erosion (Okabe et al., 1997; Jin and Römkens, 2001; Jordanova and James, 2003). These models do not account, however, for the presence of short-circuiting or the presence of different depths.

Arzabe (2000) and Lightbody et al. (2007) have used physical models to examine flow patterns within a wetland with heterogeneous velocities. Arzabe (2000) constructed a 20:1 scale physical model of the Tres Rios wetlands in Phoenix, Arizona, that comprised a shallow marsh region with randomly distributed circular cylinders followed by a transverse deep zone. The flow leaving the vegetated area consisted of alternating bands of positive and negative vorticity that scaled on the length scale of heterogeneity within the marsh array. While traveling across the subsequent deep zone, these regions of high vorticity became weaker and eventually disappeared, losing 60% of their initial vorticity over a distance of 6–33 cm (Arzabe, 2000). In addition, when the Reynolds number $Re = \frac{Q}{B\nu(1-\phi)}\frac{h_{dz}}{h_m} > 800$, vertical recirculation was created in the deep zones.

There are two limitations associated with using this model to understand flow within a short-circuiting wetland. First, Arzabe (2000) studied stem-generated velocity heterogeneity. Over an entire wetland, stem-scale velocity heterogeneity will average to enhance lateral transport and mixing (Nepf et al., 1997), unlike persistent short-circuiting that affects flow even at the wetland scale. Velocity perturbations downstream of a fast flowpath will have a larger magnitude and size and therefore may be more difficult to dissipate. Unlike in a wetland with heterogeneous flowpaths, no slow-moving water (co-flow) was present. Second, Arzabe (2000) did not include drag within the modeled deep zone. It will be shown below (Chap. 2) that drag is a crucial element of flow within constructed wetlands.

Lightbody et al. (2007) constructed a 15:1 model of the treatment wetlands associated with the J. B. Messerly Wastewater Treatment Plant (WWTP) in Augusta, Georgia. A fast flowpath was represented by a gap left between brushes in the modeled marsh area; therefore, the length scale associated with the short-circuiting flowpath, b_f, was greater than the length scale of heterogeneity within the vegetated marsh, d. The lower resistance associated with the gap within the marsh area created

a fast flowpath through the marsh region with a velocity ratio $U_f/U_s = 7$–45 higher than that of the slowly flowing marsh regions. The presence of a short-circuiting flowpath created lateral recirculation and enhanced the development of vertical recirculation within a downstream deep zone, an observation that was doubtless affected by the lack of drag within the deep zone.

1.6.3 Numerical models

Numerical models of constructed wetlands attempt to solve the governing differential equations (Appendix A) at discrete locations within the flow (cf. Kadlec and Knight, 1996, pp.260–266). Most formulations are two-dimensional depth-averaged models. As presented in Sec. A.2, under steady-state conditions when precipitation balances evapotranspiration plus infiltration, or net precipitation is negligible, the governing equations for a wetland with variable bottom topography are:

$$\frac{\partial[h\langle\bar{u}\rangle]}{\partial x} + \frac{\partial[h\langle\bar{v}\rangle]}{\partial y} = 0 \tag{1.4}$$

$$\langle\bar{u}\rangle\frac{\partial[h\langle\bar{u}\rangle]}{\partial x} + \langle\bar{v}\rangle\frac{\partial[h\langle\bar{u}\rangle]}{\partial y} = -gh\frac{\partial h}{\partial x} - \left(\nu_{t,xx}\frac{\partial^2[h\langle\bar{u}\rangle]}{\partial x^2} + \nu_{t,xy}\frac{\partial^2[h\langle\bar{u}\rangle]}{\partial y^2}\right) - \frac{1}{\rho_w}\langle F_{d,x}\rangle \tag{1.5}$$

$$\langle\bar{u}\rangle\frac{\partial[h\langle\bar{v}\rangle]}{\partial x} + \langle\bar{v}\rangle\frac{\partial[h\langle\bar{v}\rangle]}{\partial y} = -\left(\nu_{t,yx}\frac{\partial^2[h\langle\bar{v}\rangle]}{\partial x^2} + \nu_{t,yy}\frac{\partial^2[h\langle\bar{v}\rangle]}{\partial y^2}\right) - \frac{1}{\rho_w}\langle F_{d,y}\rangle$$

$$\langle\bar{u}\rangle\frac{\partial[h\langle\bar{c}\rangle]}{\partial x} + \langle\bar{v}\rangle\frac{\partial[h\langle\bar{c}\rangle]}{\partial y} = K_x\frac{\partial^2[h\langle\bar{c}\rangle]}{\partial x^2} + K_y\frac{\partial^2[h\langle\bar{c}\rangle]}{\partial y^2} \pm k_v h\left(\langle\bar{c}\rangle - c*\right) \tag{1.6}$$

where x is the longitudinal coordinate, y is the lateral coordinate, $\langle\bar{u}\rangle$ is the time-averaged and depth-averaged longitudinal velocity averaged over depth, $\langle\bar{v}\rangle$ is the time-averaged and depth-averaged lateral velocity, g is the gravitational acceleration constant, ρ_w is the water density, ν_t is eddy viscosity, $\langle F_{d,x}\rangle$ and $\langle F_{d,y}\rangle$ are the total drag forces, $\langle\bar{c}\rangle$ is the time-averaged and depth-averaged concentration, K_x and K_y are dispersion coefficients, and the rate of contaminant gain or loss within the fluid volume is assumed to be first order. The overbar indicates quantities that have been averaged over turbulent fluctuations, and angle brackets indicate depth-averaged

quantities. It is assumed that transport due to variations over depth is much greater than transport due to temporal correlations. These continuous equations are discretized and solved using numerical techniques. To characterize drag, many models use a Chèzy or Manning's roughness coefficient, which assumes fully rough-turbulent flow through open water over a flat bed (Sec. A.2). Although this situation does not reflect flow through dense vegetation, the equations have successfully been extended as empirical relationships, in which the roughness coefficients are considered to be the effective hydraulic roughness (D'Alpaos et al., 2006). For example, Jenkins and Greenway (2005) used a finite-element numerical model that combines a quadratic stem drag with a bed drag to produce an equivalent Manning's roughness. In addition, lateral dispersion and eddy viscosity will be modified within a marsh region (Nepf, 1999).

Drag, dispersion, and eddy viscosity are assumed to be spatially uniform within most models of marsh regions (e.g., Hammer and Kadlec, 1986; Jadhav and Buchberger, 1995; Bolster and Saiers, 2002; Conn and Fiedler, 2003; Jenkins and Greenway, 2005). However, models can be made that represent more precisely the natural heterogeneity in vegetation present in wetland vegetated areas by assigning different parameter choices to different elements within the model (DePaoli, 1999; John et al., 2001). Previous work has shown that numerical models are capable of successfully mimicking flow in a wetland with varying topography and vegetation density (Feng and Molz, 1997; Koskiaho, 2003). A two-dimensional depth-averaged model successfully modeled measured velocities within a wetland in Victoria, Australia (Somes et al., 1999). Within a 20-km by 45-km flow domain, Swain et al. (2004) used a horizontally varying Manning's coefficient that reflected surveys of vegetation species distribution and detailed measurements of flow resistance of different vegetation species; due to the large scale of the model, individual grid cells were 305 m on a side. In fact, within models of large wetlands, grid cells are often at least 30 meters on a side so cannot capture smaller-scale variability, even though vegetation patches and fast flowpaths can have smaller scales of heterogeneity (Thompson et al., 2004). When present, smaller scale features such as channel networks must therefore be modeled explicitly (e.g., Guardo

and Tomasello, 1995; Li et al., 2003; Swain et al., 2004; Thompson et al., 2004).

DePaoli (1999) used a two-dimensional vertically integrated model to explore flow in a wetland with interior velocity heterogeneity. When 20% of the wetland elements were randomly assigned to be very sparse vegetation, flow in the regions with sparse vegetation was found to be as much as seven times greater than in regions with dense vegetation. The mean velocity over the entire marsh increased, and as a result the HRT decreased by 19% over the case of continuous vegetation. When the 20% sparseness was concentrated in connected flowpaths, the HRT decreased even more, and the hydraulic efficiency sharply declined, confirming the importance and deleterious effect of short-circuiting.

Although numerical techniques can accurately predict flow through heterogeneous wetland systems, they require detailed data about the specific wetland basin under consideration, including geometry, bottom topography, inlet and outlet structure locations, and vegetation distributions, and they also require calibration to field measurements. Furthermore, they need large investments of human and computer resources to set up, calibrate, and run. As a result, they are suitable to detailed explorations of conditions within a particular region of interest, such as the Everglades National Park (Swain et al., 2004). Frequently, however, too large an investment is required to generalize results beyond a specific configuration and input conditions. Other numerical techniques, including multiple regression analysis and artificial neural networks, have successfully been used to model flows through wetlands, but they also require enormous training datasets, which are unavailable prior to construction (Tomenko et al., 2007). Therefore, although numerical methods are a valuable tool when finalizing a specific wetland design, they are unwieldy when used to compare many possible design elements.

1.6.4 Plug flow reactors

The simplest analytic approach to modeling flow through a constructed treatment wetland is to assume plug flow (e.g., $\frac{\partial \langle \bar{c} \rangle}{\partial y} = 0$ and $K_x = 0$ in Eq. 1.4). If plug flow is coupled with an assumed first-order removal process (Eq. 1.2), the rate of change in

contaminant concentration at any longitudinal position x will be:

$$\frac{\mathrm{d}\langle\bar{c}\rangle_a}{\mathrm{d}x} = -\frac{k_a A}{hQ}(\langle\bar{c}\rangle_a - c*) \tag{1.7}$$

where the concentration $\langle\bar{c}\rangle_a(x)$ is the local average concentration, k_a is the total areal removal rate (which may result from several biogeochemical processes), A is the wetland surface area, Q is the flow rate through the wetland, and $c*$ is the background concentration. Note that k_a and $c*$ are lumped parameters, which may result from the combination of many different removal mechanisms. Because k_a results from biological processes, it is not surprisingly a function of temperature and can be predicted using the Arhennius equation (e.g., Reed et al., 1995, p. 224). Eq. 1.7 can be integrated to give the concentration at any longitudinal location within the wetland:

$$\langle\bar{c}\rangle_a(x) = (c_o - c*)\exp\left(-\frac{k_a}{h}\tau\frac{x}{L}\right) + c* \tag{1.8}$$

where c_o is the inlet concentration, $\tau = V/Q$ the total wetland HRT, and L the total wetland length. Currently, designers of constructed wetlands typically estimate wetland performance based on size alone, using a first-order removal rate that is constant regardless of wetland shape, bathymetry, and vegetation characteristics (e.g., Kadlec and Knight, 1996; Economopoulou and Tsihrintzis, 2004; Tarutis et al., 1999). Field studies have shown that in some cases Eq. 1.8 fits observed spatial patterns of concentration measurements (Tanner et al., 1995; Walker, 1995; Kadlec et al., 1997; Reilly et al., 2000; Wong et al., 2000, 2006). However, when wetlands exhibit large amounts of short-circuiting, such as during the winter in cold climates, plug-flow models cannot predict removal and a more detailed understanding of wetland flow patterns and chemistry is required (Goulet et al., 2001). In any event, despite its prevalence as a model assumption, perfect plug flow is never obtained because some velocity heterogeneity is always present, which results in dispersion (Wörman and Kronnäs, 2005). Therefore, in nearly all wetlands, plug flow is not an appropriate model of flow (Kadlec et al., 1993). Moreover, assuming plug flow under conditions of short-circuiting can result in large overpredictions of the wetland removal and hence

undersizing of a designed wetland (Kadlec and Knight 1996, p. 256; Economopoulou and Tsihrintzis 2004).

1.6.5 Residence time distributions and the tanks-in-series model

Plug flow cannot describe the velocity heterogeneity present within wetlands, so more complicated models become necessary. The RTD is the probability density function for residence time; it describes the amount of time various fractions of water spend in the wetland (Fig. 1-3). An empirical method for determining the amount of time that various parcels of fluid remain in the wetland is to measure the RTD using a slug tracer release, which under steady conditions will produce:

$$\mathrm{RTD}(t) = \frac{\langle \bar{c} \rangle_a(t)}{\int_0^\infty \langle \bar{c} \rangle_a(t)\ \mathrm{d}t} \tag{1.9}$$

The effective residence time T_{det} is simply the first moment of the RTD:

$$T_{det} = \int_0^\infty t\mathrm{RTD}(t)\ \mathrm{d}t \tag{1.10}$$

If plug flow conditions exist, all the flow exits at the wetland HRT τ:

$$\mathrm{RTD}(t) = \delta_D(t - \tau) \tag{1.11}$$

where δ_D represents the Dirac delta function. At the other extreme, when mixing is so strong that the concentration within the wetland is at all times uniform, the wetland can be represented by a continuously stirred tank reactor, and the RTD is given by:

$$\mathrm{RTD}(t) = \frac{1}{\tau}\exp(t/\tau) \tag{1.12}$$

Most wetlands have a RTD intermediate between Eq. 1.11 and Eq. 1.12. In addition, regions of dense vegetation or stagnant water can reduce the effective flow volume of the wetland, which leads to hydraulic efficiency $T_{det}/\tau < 1$. Short-circuiting does not

directly cause low hydraulic efficiency, but both contribute to non-ideal wetland flow patterns (Persson et al., 1999).

When the removal rate is constant throughout the wetland, a simple convolution between the RTD and the removal process provides the outlet concentration (Danckwerts, 1953). For a first-order removal process, the outlet concentration c_e from a given RTD is given by:

$$c_e = c_o \int_0^\infty \mathrm{RTD}(t) \exp(-\frac{k_a}{h} t)\ \mathrm{d}t \tag{1.13}$$

The discretized form of this equation has been found to predict the outlet concentration from real wetlands (Alvord and Kadlec, 1996). For plug flow conditions with a background concentration, Eq. 1.13 reduces simply to Eq. 1.8. For a continuously stirred reactor, the outlet concentration is given by:

$$c_e = \frac{c_o - c*}{1 + k_a \tau / h} + c* \tag{1.14}$$

In many wetlands, the RTD appears similar to one that would be produced by a number N of fully mixed tanks in series (TIS) (Kadlec and Knight, 1996; Chen et al., 1999; Persson et al., 1999; Kadlec, 2000). The RTD for a TIS model of a wetland with an HRT τ is given by the gamma probability density function (Carleton, 2002):

$$\mathrm{RTD}(t) = \frac{(\tau/N)^{-N}\, t^{N-1} \exp\left(-tN/\tau\right)}{\Gamma(N)} \tag{1.15}$$

where $\Gamma(N) = \int_0^\infty t^{N-1} \exp(-t)\ \mathrm{d}t$ is the gamma function. This formulation is equivalent to a plug-flow reactor with dispersion, which would be quantified by the Peclet number Pe; the Peclet number can be converted to an equivalent number of TIS as $\frac{1}{N} = \frac{2}{Pe} - \frac{2}{Pe^2}[1 - \exp(-Pe)]$ (Kadlec and Knight, 1996, p. 254). Note that this equation allows non-integer values of N, which is appropriate for a numerical abstraction, but when N is an integer it takes the simpler form $\Gamma(N) = (N-1)!$. Plug flow is observed as $N \to \infty$; a continuously stirred tank reactor is observed when $N = 1$. RTDs from tracer tests of a wide variety of wetlands suggest that for most systems

$N = 2$ to 8 (Kadlec and Knight, 1996). Linking a train of stirred reactors in series, each with inlet and outlet concentrations, produces the following expression for the wetland outlet concentration (Kadlec and Knight, 1996, p. 251):

$$c_e = \frac{c_o - c*}{(1 + Da/N)^N} + c* \tag{1.16}$$

An alternative formulation is to model the flow as plug flow with dispersion, which also results in analytic solutions (e.g., Kadlec and Knight, 1996).

Although TIS models account for longitudinal dispersion within a wetland, these models are one-dimensional (1-D) and assume a single flowpath between the entrance and the exit. This assumption does not capture the heterogeneous flow velocities present in a short-circuiting wetland, and measurements of internal concentrations reveal that the TIS model is not adequate to model flow as it travels through a real wetland (Kadlec, 1994). Kadlec (2000) presented a hypothetical model wetland of uniform depth and with five parallel, non-interacting plug-flow flowpaths, each characterized by a distinct flow rate and removal rate. The simulated cross-sectionally-averaged concentration $\langle \bar{c} \rangle_a(y)$ declined exponentially along the wetland, apparently following Eq. 1.2, yet the fit k_a and $c*$ were completely different from the various k_a and single $c*$ values input to the system and, moreover, were dependent on the flow rate through the wetland. From these results, Kadlec (2000) concludes that a 1-D model, even with dispersion or a flow-dependent removal rate, cannot accurately represent a wetland in which multiple flowpaths coexist in parallel. In general, models that account for a non-ideal RTD will fail to predict the effluent concentration when removal rates are spatially heterogeneous within the wetland (Danckwerts, 1953).

1.6.6 Storage zone model

A different approach to accounting for velocity heterogeneity is to model vegetation as dead zones that have no mean velocity but exchange fluid with the actively flowing region. Transient storage models have been successfully used to model exchange between rivers and the hyporheic zone (e.g., Runkel, 1998). Kadlec (1994) found that

three fully mixed side storage zones and a central main-flow section closely matched the tracer response curve within one of the cells within the Des Plaines Experimental Wetland. Werner and Kadlec (2000) extended this model by introducing dispersion in the central plug flow region and considering an infinite number of fully mixed side storage zones; they found that this model could represent 49 former tracer studies of constructed wetlands. In a detailed study of the Orlando Easterly Wetland, Martinez and Wise (2003*a*) found that a 1-D model with dead zones fit the data for individual cells. Keefe et al. (2004) were able to use a storage zone model to replicate observed tracer test RTDs within the Tres Rios wetlands.

In a transient storage approach, the equation for the main flowpath, simulated by plug flow plus dispersion and exchange with the storage zone, is:

$$\frac{\partial \langle \bar{c} \rangle_a}{\partial t} = -\frac{Q}{A_m}\frac{\partial \langle \bar{c} \rangle_a}{\partial x} + \frac{1}{A_m}\frac{\partial}{\partial x}\left(A_m K_x \frac{\partial \langle \bar{c} \rangle_a}{\partial x} \right) + \epsilon_s (c_s - \langle \bar{c} \rangle_a) \tag{1.17}$$

where A_m is the cross-sectional area of the main flowpath, ϵ_s is the storage zone exchange coefficient, and c_s is the storage zone solute concentration. The coupled equation for the concentration within a fully mixed stationary storage zone is:

$$\frac{\mathrm{d}c_s}{\mathrm{d}t} = -\epsilon_s \frac{A_m}{A_s}(c_s - \langle \bar{c} \rangle_a) \tag{1.18}$$

where A_s is the cross-sectional area of the storage zone. This modeling approach assumes much faster exchange between the main flow compartment and side storage zones than advection (or flushing) within the storage zones (cf. Nepf et al., 2007). Although this simplification was appropriate in the small EW3, which contains fringing vegetation around a central deep area and had a modeled exchange flow rate as great as the wetland flow rate (Kadlec, 1994), it would not be appropriate in a wider wetland in which the lateral exchange timescale $\hat{Y}^{\,2}/K_y$ is much greater than the longitudinal advection timescale L/u_{pf}, where u_{pf} is the plug-flow velocity through the wetland. For example, Keefe et al. (2004) noted that the best-fit value for lateral exchange within a storage zone model of the Tres Rios constructed wetlands is several orders of magnitude less than typical vales for rivers. Even though the model para-

meters can be tweaked to fit the RTD in those situations, the fitting parameters are empirical and not reflect actual wetland processes, making it difficult to extrapolate parameters to different systems or different flows within the same system (Hart et al., 1999).

1.6.7 Stream tube models

To explicitly account for the existence of velocity heterogeneity within a wetland, Kadlec and Knight (1996, p. 245) proposed that a wetland can be modeled as consisting of parallel non-interacting flow paths, which can be called streamtubes. Dispersion is not present within any streamtube, but the heterogeneous velocities among different flowpaths mimic dispersion through differential advection. The RTD of a streamtube system consists of a set of distinct peaks, representing the arrival of different plugs at the wetland exit (Kadlec, 2000), and the outlet concentration is given by the convolution of the concentration associated with each peak and the RTD (Wörman and Kronnäs, 2005). If the removal rate differs among different streamtubes, then $k_v = k_v(t)$, and the wetland is more conveniently described by a Damkohler number distribution (DND):

$$\mathrm{DND}(k_v t) = \frac{\langle \bar{c} \rangle_a (k_v t)}{\int_0^\infty \langle \bar{c} \rangle_a (k_v t)\ \mathrm{d}(k_v t)} \tag{1.19}$$

Note that $\mathrm{RTD}(t) = \mathrm{DND}(k_v t)\frac{\mathrm{d}Da}{\mathrm{d}t}$. The concentration averaged over the flow cross-section $\langle \bar{c} \rangle (y)$ within such a system is given by the convolution of Eq. 1.8 with the DND given in Eq. 1.19 (Carleton, 2002):

$$\frac{\langle \bar{c} \rangle_a - c*}{c_o - c*} = \int_0^\infty \mathrm{DND}(k_v t) \exp\left(-k_v t \frac{x}{L}\right)\ \mathrm{d}(k_v t) \tag{1.20}$$

Carleton (2002) noted that even though a gamma distribution may describe both $\mathrm{RTD}(t)$ and $\mathrm{DND}(k_v t)$ well, if different values of N are associated with the two distributions, then k_v is spatially variable and an analytic solution linking $\mathrm{RTD}(t)$ and $\mathrm{DND}(k_v t)$ is not possible. As passage time within the wetland increases, the stream tube analogy breaks down, and wetland longitudinal dispersion becomes Fickian (Car-

leton and Montas, 2007).

A stream tube model is a simple and tractable method for modeling flow through a wetland, and it explicitly captures the presence of short-circuiting. It is appropriate for a wetland system when lateral mixing is much slower than longitudinal transport. It is, however, an abstraction of flow through the wetland and, like all models, is only useful to the extent that its assumptions are justified and its predictions match field measurements (Pilkey and Pilkey-Jarvis, 2007).

1.7 Constructed wetland design features that can mitigate for short-circuiting

Wetland design incorporates many site-specific features, including the initial topography, inlet flow rates, soils, hydrology, influent contaminant concentrations, and acceptable discharge standards (Whittle and Philcox, 1996; Conn and Fiedler, 2003). Reducing hydraulic short-circuiting is one of the most important goals for constructed wetland design (Whittle and Philcox, 1996). Dierberg et al. (2005) pointed out that the time to consider and optimize hydraulic performance is during wetland construction, before the wetlands are flooded and plants have become established. However, rigorous scientific support for many wetland design guidelines is still lacking. Even so, several previous studies have suggested wetland performance depends on several design elements, including wetland size, wetland shape, the number of cells, inlet and outlet structures, the presence of transverse berms, and the presence of transverse deep zones (Persson and Wittgren, 2003).

1.7.1 Wetland size

Wetland size is one of the most important parameters in increasing treatment wetland performance. Increasing wetland size increases the Damkohler number and reduces the areal loading rate, which for a wide range of contaminants results in a lower outlet concentration (Kadlec and Knight, 1996). For example, Tilley and Brown

(1998) reported that a constructed wetland removed 8% of total phosphorus with an HRT of 3.3 hours but removed 82% with an HRT of 20 hours. In an experimental overland flow test bed of constant width, Doody et al. (2006) found that phosphorus removal was directly proportional to test bed length, under both steady and non-steady flow conditions. Even when short-circuiting is present, if the wetland is large enough even fast-moving water will remain long enough for a significant fraction of contaminants to be removed.

However, since land, construction, and planting costs are all proportional to wetland area (Table 1.1), there is a large economic incentive to make wetlands and treatment ponds as small as possible. In addition, in areas with high rates of evapotranspiration, increasing the size of a wetland will increase evaporative wetland losses, which will reduce the amount of treated water produced (Gerke et al., 2001).

1.7.2 Wetland shape

Most constructed treatment wetlands are rectangular, to maximize the wetland treatment area (on a rectangular land parcel) and minimize the construction costs that would be generated by a more sinuous shape (Whittle and Philcox, 1996). The most important features in determining wetland shape are therefore the aspect ratio of the rectangular footprint and the presence of internal berms.

Short-circuiting within any type of basin is reduced when the basin is long and narrow, so when its length to width ratio $L/B \gg 1$ (Thackston et al., 1987). For example, Whittle and Philcox (1996) suggested that the length to width ratio should be at least 5:1 and optimally at least 20:1. When vegetation is not distributed uniformly and preferential flowpaths are present, a higher length:width ratio still decreases short-circuiting. For example, Jenkins and Greenway (2005) reported that increasing the length:width ratio from 1.4 to 17.5 increases the hydraulic efficiency T_{det}/τ for a wetland with fringing vegetation from 0.21 to 0.74. However, Reed et al. (1995, p. 203) noted that very high aspect ratios (above 10:1) dramatically increase the head drop within the wetland, which can perversely increase the tendency to develop short-circuiting flow paths. In addition, a high aspect ratio increases the re-

quired berm length per wetland area, and berm construction costs represent a sizeable fraction of wetland costs (Knight, 1987).

Persson et al. (1999) used a two-dimensional vertically integrated hydrodynamic model to simulate slug releases in thirteen small hypothetical ponds, each 1.5 m deep. The hydraulic efficiency (defined by the authors as T_{peak}/τ, where T_{peak} is the time between a slug release and when the peak concentration is measured at the wetland outlet) was calculated for each pond under steady flow condition. Three ponds were found to have good hydraulic efficiency, including a pond with a length:width aspect ratio of 10:1 and a 2:1 rectangle with baffles that created a long serpentine flow path.

Other researchers have also documented how a long flowpath can be created by the placement of internal berms to create a serpentine flow path. For example, even though it reduced the volume of the wetland, adding baffles to a 12-ha Finnish wetland with a 1:1 ratio significantly increased the hydraulic efficiency (decreased the short-circuiting) within it (Koskiaho, 2003). Numerical simulations indicate that adding baffles results in an increase in hydraulic detention time and a reduction in short-circuiting, as long as the baffles are high enough that they are not overtopped during periods of high water (Matthews et al., 1997; Conn and Fiedler, 2003). Similar effects have been found in both field and numerical experiments in open waste stabilization ponds. In a study of the addition of two interior baffles to a lagoon in Ginebria, Columbia, Bracho et al. (2006) found that the baffles increased performance efficiency from 22-45% to 74-97%. Moreover, the baffles reduced short-circuiting of tracer through the wetland, delaying the time of peak tracer measurement at the outlet. Abbas et al. (2006) used a finite element numerical model to show that adding four baffles to a waste stabilization pond increased BOD_5 removal efficiencies from 16% to 82% for a pond with a length:width ratio of 1:1, and from 22% to 96% for a pond with a length:width ratio of 4:1.

Although increasing the aspect ratio of a wetland can improve performance, it will also increase costs. Hammer and Knight (1994) note that a wetland with an aspect ratio other than 1:1 will have proportionally more edge area and will therefore result in greater berm construction costs. The addition of internal berms will also add to

the cost of the wetland.

1.7.3 Multiple cells in series

Another method for improving wetland flow patterns is to divide large wetland cells into multiple smaller cells. Well-designed constructed wetlands have multiple parallel flow trains, which allow treatment to continue even when a portion of the wetland is taken off line for maintenance (Kadlec and Knight, 1996). In addition, removal increases when each train consists of multiple cells in series. For example, in a pilot wetland in Arcata, California, cells with a 10:1 aspect ratio divided by baffles into eight sequential compartments had an 86% removal of BOD_5, compared to 71% for a cell split into only two compartments and 78% for one split into four (Gearheart et al., 1989). Numerical simulations show that dividing a wetland into multiple TIS provides periodic lateral mixing, which increases removal within a wetland Kadlec (2000).

Creating multiple cells in series can, however, be expensive. Each cell division requires the construction of an additional berm and the inclusion of more inlet and outlet structures. In addition, the creation of interior berms increases the hydraulic resistance of the wetland; for example, Gearheart et al. (1989) reports that each cell berm created a head drop of 2.5 cm. Because pump costs depend on the required head, increasing the resistance within the system will increase pump capital costs and ongoing energy requirements.

1.7.4 Inlet and outlet structures

Due to the slow flows within wetland systems, the momentum created by inlets can have a large effect on flow distribution within marsh areas (Somes et al., 1999). Numerical simulations of flow in a 10-ha, 4-m-deep, unstratified reservoir in the United Kingdom indicated that changing a single off-center inlet to a transverse manifold with spaced outlets that distributed flow transversely across the upstream edge increased the hydraulic efficiency of the wetland. Similarly, a numerical simulation of

flow through a 2:1 basin showed that increasing the number of inlets from one to three increased the predicted nitrogen removal within a constructed wetland by 14%; conversely, when only a single inlet and outlet are present, moving both to the same lateral bank decreased removal by 56% (Persson and Wittgren, 2003). Other methods of increasing hydraulic performance include more numerous inflow and outflow structures to distribute flow laterally (Dierberg et al., 2005). The importance of inlet structures decreases as the aspect ratio of the wetland increases; in numerical simulations, Koskiaho (2003) found that flow patterns within a wetland with aspect ratio greater than 4:1 were unaffected by the number and position of the inlet structures.

Although inlet and outlet structures can be used to promote the spreading of flow across a wetland, they are expensive. Depending on wetland flow, each additional structure costs between $1,000 and $1,000,000, so the decision to include multiple structures cannot be taken lightly, especially in a large wetland system (U. S. Environmental Protection Agency, 2000; Hey et al., 2005).

1.7.5 Transverse berms and bands of vegetation

To maximize removal rates, it is beneficial to create a system with hydraulics as close to plug flow as possible. A numerical simulation of flow through a small wetland pond predicts that adding a shallow berm makes a wetland exhibit flow patterns more similar to plug flow (i.e., increases the equivalent number of TIS) and increases its predicted nitrogen removal by 18% (Persson and Wittgren, 2003); adding additional transverse berms increases the equivalent number of TIS even more (Persson et al., 1998). A numerical simulation of possible modifications to an existing wetland constructed along an old creek bed showed that adding periodic transverse benches would produce flow patterns closest to plug flow (Somes et al., 1998). However, adding additional roughness to constructed wetlands will reduce wetland volume and HRT. Poorly located islands can also perversely increase short-circuiting by funneling flow between them, as was observed in the Magle Wetland Park in Hässleholm, Sweden (Persson, 2005). In addition, over time shallow vegetation and porous berms can become saturated with silt and cease to be effective (O'Brien, 1976).

1.7.6 Deep zones

The addition of transverse deep zones has been postulated as a mechanism for improving performance in short-circuiting wetlands. Deep zones may also represent a significant cost savings because they may replace an increase in aspect ratio, internal berm construction, or inlet and outlet structures. Deep zones are usually planted with a lower density of macrophyte species, so planting costs will be reduced. Moreover, in a wetland that would otherwise require fill for external berm construction, deep zones can serve as a borrow pit.

Several studies, primarily at the pilot scale, have shown that transverse deep zones can improve contaminant removal compared to the performance of cells without deep zones. For example, in a comparison of two 0.1-ha research cells at the Hemet/San Jacinto Wetland Research Facility in California, the cell with an interior deep zone removed more than twice as much nitrogen as a cell with continuous vegetation (Thullen et al., 2002, see Table 1.3). Knight et al. (1994) reported that at the Champion Paper Mill in Pensacola, Florida, cells with transverse deep zones were able to produce a lower outlet concentration of several contaminants, compared to cells without deep zones in the same wetland system. Eger (1994) reported that 0.02-ha free water surface wetlands with six internal transverse trenches were able to remove 86% of nickel from acid mine drainage, compared to only 40% for wetlands with peat berms that created a serpentine flow. Andersen et al. (2003) explained that deep zones within the Eastern Municipal Water District Multipurpose Demonstration Wetland at the Hemet/San Jacinto Regional Water Reclamation Facility in California were deepened and extended in part to increase ammonia nitrogen removal. On the other hand, Kadlec (2005*a*) found no difference in dispersion or either ammonia or nitrate removal ability among twelve tiny (0.12-ha) research wetland cells in the Tres Rios wetlands in Phoenix, Arizona, that each had between zero and three 3.6-m-long internal deep zones.

In many wetlands, removal rates are lower within deep areas than within active marsh areas (Kadlec, 2005*b*), and in this situation there is a tradeoff associated with

adding more or larger deep zones. The optimal size or area of a deep zone is not known with certainty. For example, Schueler (1992) suggested that 15% of the area of a shallow marsh system should be allocated to deep water. Hammer and Knight (1994) suggested that the deep zone area should be 10–20% of the wetland and should be spaced intermittently along the wetland. In a comparison of forty-six wetlands with no deep zones, fifty-eight wetlands with some open water, and seventy-two ponds, Kadlec (2005*b*) presented data that show that the average removal rate is highest for wetlands with between 5 and 35% open water, which may or may not be deeper than the surrounding marsh areas. Bathymetric data are available for a smaller number of studies. Table. 1.3 presents dimensions and contaminant removal abilities of thirteen surface-flow constructed wetlands that have deep zones of varying sizes. In general, wetlands with deep zones perform at least as well if not better than companion cells that lack deep zones.

1.8 Effects of deep zones on contaminant removal within free-surface wetlands

The data cited above suggest that properly sized and located deep zones may be able to improve the performance of larger constructed treatment wetlands. The mechanisms for how deep zones improve wetland performance, however, are still not well understood. One effect could be a direct promotion of contaminant removal. Deep zones provide additional space for the storage of settled particulate matter and associated contaminants (Kadlec and Knight, 1996, pp. 336-337). Deep zones can permit the establishment of periphyton colonies, which can actively contribute to denitrification and phosphorus removal (McCormick et al., 2006; Sirivedhin and Gray, 2006). Thullen et al. (2002) suggested that interspersing dense vegetation with open water may increase light penetration, and therefore high levels of dissolved oxygen and photolysis. On the other hand, some studies have postulated that deep zones create anaerobic conditions that improve contaminant removal, in particular denitrification

(U. S. Environmental Protection Agency, 2000).

One important effect of deep zones is to increase the volume of the wetland, which increases its HRT τ and may increase observed removal efficiency (Wong et al., 1999). The data for the Champion wetland in Table 1.3 can be used to estimate the effect of deep zone volume increase. Assuming plug flow, adopting a simple first-order removal model with a constant rate constant for each contaminant, and using volume data for each cell to calculate cell-specific HRTs suggest that the volume increase explains only 35% of the observed nitrate removal and 50% of the observed TSS removal. Other researchers have noted that the presence of deep zones reduces the wetland-averaged volumetric removal rate (Kadlec, 2005*a*). Because volume addition can predict only approximately half of the observed increase in removal, deep zones are likely to have some other effect in addition to increasing wetland volume.

Others have suggested that the primary effect of deep zones is on flow pattern. For example, in their study of the Champion wetlands, Knight et al. (1994) found that cells with deep zones had a hydraulic efficiency T_{det}/τ that was higher and closer to 1 than in those cells without deep zones. One important feature of wetland deep zones may be their ability to generate lateral mixing. In a marsh region within a wetland, flow is dominated by drag due to vegetation, and the resulting flow is unidirectional, though not necessarily all at the same speed if short-circuiting flowpaths are present (Andradóttir and Nepf, 2000). If a portion of the marsh is replaced by an unvegetated deep zone, then lateral mixing is possible in that region. Tracer studies imply that deep zones that stretch laterally across the wetland may redistribute flow laterally, forming more uniform flow conditions, even if the water has short-circuited the region just upstream of the deep zone (Kadlec and Knight, 1996). The interaction of short-circuiting flowpaths and deep zones may be able to create vertical and lateral recirculation, which may create that transverse flow (Lightbody et al., 2007). For example, vertical recirculation separated the flow regions upstream and downstream of the deep zone, so the number of observed tanks in series was equal to or greater than the number of deep zones (Fox et al., 2002). The periodic generation of lateral mixing would have the effect of compartmentalizing a wetland into discrete

units, increasing the equivalent number of TIS (Kadlec, 2000). Alternatively, others have suggested that the most important effect of deep zones is to dissipate velocity heterogeneity contributed by jets resulting from flow through a low resistance area (Fox et al., 2002).

However, the mechanism by which deep zones redistribute flow laterally is not well understood. Deep zones stretching transversely across an entire wetland are frequently used with the expectation that they decrease short-circuiting (cf. Knight and Iverson, 1990; Kadlec and Knight, 1996; Simi and Mitchell, 1999). It has previously been suggested that deep zones tend to "remix channeled flows" to increase plug flow characteristics (Gerke et al., 2001). For example, several sources suggest constructing alternating deep and shallow zones perpendicular to the flowpath so that the wetland cross-section has uniform hydraulic resistance, which reduces the potential for short-circuiting (Whittle and Philcox, 1996; Thullen et al., 2005). On the other hand, in a numerical study, DePaoli (1999) found that transverse open-water zones produced lateral circulation but did not redistribute flow across the wetland when short-circuiting flowpaths are present, although this effect may be a result of the coarse finite difference grid or the low roughness within the model. Wind may play a role in lateral mixing. Vegetation can shield the water body from wind effects leading to short-circuiting and mixing (Wong et al., 2000); the absence of vegetation within the deep zones would create a local area for transverse mixing.

Although deep zones are frequently included in constructed wetland designs under the presumption that they improve flow patterns through wetlands, their exact contribution to flow patterns under typical flow conditions is still poorly understood. Little documentation of the efficacy of deep zones exists in the literature; further, the optimal number, size, and shape of deep zones are still unknown. In fact, it is possible that, because deep zones allow lateral momentum transport, they are able to link previously unconnected sparse areas, increasing the short-circuiting present in the wetland (cf. DePaoli, 1999).

1.9 Present approach

It has been proposed that the presence of deep zones increases performance by compensating for the effect of short-circuiting within the marsh region. Previous work has suggested that lateral mixing may be an important factor in the ability of deep zones to improve performance. However, it is still not known how much lateral mixing is present under realistic conditions. In addition, the effect of lateral mixing in deep zones on transport through the entire wetland system is not well understood. In this study, these two important questions are explored to create design guidelines for the inclusion of deep zones within constructed wetlands.

First, a field study of a large constructed wetland in Augusta, Georgia, was performed to obtain detailed measurements of the distribution, dimensions, and flow through fast flowpaths. Within the Augusta wetland, lateral mixing is low within the vegetated regions, creating narrow, distinct fast flowpaths surrounded by slow flow. Moreover, when this fast-flowing water enters the deep zones, it may create some initial entrainment but then rapidly decays to background velocity levels; observations suggest that wind is primarily responsible for lateral mixing.

Next, based on these observations, a laboratory scale model was constructed of a fast flowpath entering a deep zone, which allowed the study of the effect of the deep zone length and the presence of a downstream fast flowpath on jet-induced spreading within the deep zone.

Finally, the understanding of flow patterns gained by the field and laboratory experiments is used to create a conceptual mathematical model that examines the effect of wetland short-circuiting on performance. Note that here only deep zones oriented transverse to the flow direction are considered; deep channels that run parallel to the flow direction will create short-circuiting by conveying flow directly to the outlet (e.g., Dierberg et al., 2005).

The numerical model shows that deep zones can improve wetland performance through two separate mechanisms. When lateral mixing is present within the deep zone, it dilutes the water that has traveled through the fast flowpath and reduces the

fraction of water that short-circuits the entire wetland length. In addition, by dissipating the high velocity associated with the fast flowpaths, it is likely that deep zones reduce the probability that fast flowpaths will align throughout the entire wetland. Therefore, even when no lateral mixing is present within the deep zones, there is a much greater probability that all water will receive some treatment, again increasing performance. There are several important factors that affect the impact of transverse deep zones. In particular, the wetland must be large relative to the removal rate; if $Da < 1$, then, by removing productive removal area, deep zones will always result in reduced performance. However, deep zones may improve performance when properly sized and located within a constructed treatment wetland.

Table 1.1: Surface-flow wetland costs. Sources are listed in the table. Table is continued on the following page.

Source	Wetland	Location	Area (ha)	Land $/m^2	Annual operations and maintenance Personnel $/m^2/yr	Sampling $/m^2/yr	Materials $/m^2/yr	Total $/m^2/yr
Brodie et al. (1989)	TVA Flat Rock	Jackson County, AL	0.3	-	-	-	-	1.2
Hammer et al. (1993)	Sand Mountain	DeKalb County, AL	0.6	-	-	-	-	-
Frossard et al. (1996)	model assumptions		9	0.2	-	-	-	14.2
Kadlec and Knight (1996)	model assumptions		-	-	-	-	-	0.1
Kadlec et al. (2000)	Incline Village	Nevada	175	-	-	-	-	0.05
Korkusuz and Yurteri (2000)	Mogan-Eymir	Turkey	3–22	1.9	-	-	-	-
Linde and Alsbro (2000)	Ekeby	Eskilstuna, Sweden	30	0.5	-	-	-	-
Reitberger et al. (2000)	DuPont	Victoria, TX	53	-	-	-	-	-
Ates and Ozesmi (2002)	Eskikaraagac	Turkey	0.3	3.3	-	-	-	-
Hey et al. (2005)	model assumptions		607	0.5	0.003	0.001	0.001	0.005

Table 1.1, cont.

Source	Capital and construction costs							
	Earthwork		Clearing	Levees	Structures	Vegetation	Planning, design	Total
	$/m^2	$/m^3	$/m^2	$/m	$/m^2	$/m^2	$/m^2	$/m^2
Brodie et al. (1989)	1.7	-	-	-	-	-	1.7	13.7
Hammer et al. (1993)	0.9	-	-	-	-	1.2	-	2.2
Frossard et al. (1996)	-	2.7	0.5	-	-	-	-	-
Kadlec and Knight (1996)	0.5	-	-	-	-	-	-	-
Kadlec et al. (2000)	1.2	-	-	-	0.5	0.0	-	2.4
Korkusuz and Yurteri (2000)	1.7	-	-	-	-	-	-	-
Linde and Alsbro (2000)	3.0	-	-	-	-	0.2	1.0	5.4
Reitberger et al. (2000)	3.0	-	-	-	2.0	0.4	-	5.7
Ates and Ozesmi (2002)	4.0	-	-	-	-	-	-	-
Hey et al. (2005)	0.1	-	-	310–492	$10,000 each	-	-	5.8

Table 1.2: Average first-order areal removal rates and Damkohler numbers for surface flow wetlands, based on the results of the North American Treatment Wetland Database. Damkohler numbers calculated using the average hydraulic loading rate (HLR) value of 1–5 cm/d. Data from Kadlec and Knight (1996, p. 583-584).

Contaminant	Areal removal rate, k_a	Damkohler number, Da
Total suspended sediment (TSS)	1000 m/yr	55–275
Total phosphorus	12 m/yr	1–3
Biological oxygen demand (BOD_5)	34 m/y	2–9
Organic nitrogen	17 m/yr	1–5
Ammonium	18 m/yr	1–5
Nitrate	35 m/yr	2–10
Total nitrogen	22 m/yr	1–6
Fecal coliforms	75 m/yr	4–20

Table 1.3: Locations, dimensions, and pollutant removal capabilities of previously studied surface-flow wetlands with internal deep zones. Sources are listed in the table. Table is continued on following pages.

Wetland	Cells	Location	Source
Minot	-	Minot, ND	Hammer and Knight (1994), Hammer and Burckhard (2000)
Messerly	Cells 6, 7, 8, & 12 Cells 1 & 5	Augusta, GA Augusta, GA	Eidson et al. (2005)
West Jackson County	-	MS	CH2M Hill (1993), Hammer and Knight (1994)
Hemet/San Jacinto	1994-1998 after 1999 research cells	San Jacinto, CA San Jacinto, CA Hemet, CA San Jacinto, CA San Jacinto, CA	Chendorain et al. (1998), Sartoris et al. (2000*b*), Sartoris et al. (2000*a*), Thullen et al. (2002) Andersen et al. (2003)
Kingman	n	Kingman, AZ	Pinney et al. (2000), Gerke et al. (2001)
Fort Deposit	n	Fort Deposit, AL	Knight and Iverson (1990), Bays and Knight (2002)
Tres Rios	H1 H2 R4, R6, R12 R7, R8, R10 R5, R9, R11 R1, R2, R3	Phoenix, AZ Phoenix, AZ Phoenix, AZ Phoenix, AZ Phoenix, AZ Phoenix, AZ	City of Phoenix (2001), Keefe et al. (2004), Kadlec (2005*a*)
Saginaw	n	Saginaw, MI	Kadlec (2003*a*)
BP Oil	n	Bulwer Island, Australia	Simi and Mitchell (1999), Simi (2000)
Champion	Cell A Cell B Cell C Cell D Cell E Cell F	Pensacola, FL Pensacola, FL Pensacola, FL Pensacola, FL Pensacola, FL Pensacola, FL	Knight et al. (1994)
North Carolina A&T	-	Greensboro, NC	Reddy et al. (2001), Stone et al. (2004)
Ag. College	-	Bible Hill, Nova Scotia	Smith et al. (2006)
Henley Brook	experimental ponds	Perth, Australia	Lund et al. (2001)

Table 1.3, cont.

Wetland	Wetland area, A (ha)	Number of cells, n_{cell}	Parallel/ Series	Cell L/B	h_m (m)	Total Q (m^3/d)	Total τ (d)
Minot	51	4	P	4	0.15–0.3	1896–28761	0.41–0.81
Messerly	49	4	P	4	0.2–0.25	33690	5.4
	24	2	P	4	0.2–0.25	16845	11.5
West Jackson County	23	7	P/S	3	0.1–0.3	6550–6663	5.6–5.7
Hemet/San Jacinto	9.9	1	-	8	0.46	4848–5102	22–23
	9.9	1	-	8	0.5	8089	23.07549505
	0.77	8	P	5	0.46	653.8	13
	0.11	1	-	4.5	0.46	76.8	5–9
	0.11	1	-	4.5	0.46	76.8	5–9
Kingman	9	3	-	14	0.2	3300–4500	5–10
Fort Deposit	6	2	P	4.6	0–0.6	227–795	15–20
Tres Rios	1.34	1	-	3.8	0.15–0.46	1229–2817	2.4–5.5
	1.28	1	-	3.8	0.15–0.46	1177–2697	2.4–5.5
	0.12	3	P	2	0.3	66–90	7.1–10.3
	0.12	3	P	2	0.3	66–90	8.2–11.8
	0.12	3	P	2	0.3	66–90	9.2–13
	0.12	3	P	2	0.3	66–90	6.1–8.7
Saginaw	0.74	2	P	1.8	0.37	110	25
BP Oil	0.72	2	P	4.3	0.2–0.4	1590	1.8
Champion	0.4	1	-	2.5	0.2	40–480	4–48
	0.4	1	-	2.5	0.2	40–480	3–33
	0.2	1	-	5	0.2	20–120	10–57
	0.2	1	-	5	0.2	20–120	6–158
	0.1	1	-	10	0.2	10–240	3–67
	0.1	1	-	10	0.2	10–240	1–34
North Carolina A&T	0.04	6	P	4	0.15	6–12	11–21
Ag. College	0.02	2	P	4	0.15	0.3	45–52
Henley Brook	0.01	3	P	3	0.2–0.5	45–135	0.33–1

Table 1.3, cont.

Wetland	Total N_{dz}	Internal N_{dz}	h_{dz} (m)	L_{dz} (m)	Slope	Internal A_{dz}/A_{cell}	Total A_{dz}/A_{cell}
Minot	2	2	0.6	221	3:1–6:1	59 %	59 %
Messerly	3	2	1.4	209	-	20 %	30 %
	1	1	1.4	418	-	60 %	60 %
West Jackson County	2	1–3	-	?	-	5 %	5 %
Hemet/San Jacinto	10	7–9	1.8	12	-	47 %	50 %
	8–9	6–7	1.8	30	-	47 %	50 %
	2	1	1.8	21	2:1–4:1	37 %	50 %
	1	1	1.68	17.4	2:1–4:1	27 %	25 %
	0	0	-	-	-	0 %	0 %
Kingman	3	2	1	25	-	7 %	13 %
Fort Deposit	3	3	1.5	6	-	3 %	3 %
Tres Rios	7	5	1.375	12	-	24 %	25 %
	5	3	1.375	20	-	24 %	25 %
	3	1	1	3.6	2:1	8 %	20 %
	4	2	1	3.6	2:1	16 %	28 %
	5	3	1	3.6	2:1	25 %	35 %
	2	0	1	3.6	2:1	0 %	13 %
Saginaw	3	1	-	6	-	5 %	14 %
BP Oil	5	3	1	10	-	25 %	31 %
Champion	1	0	1.2	10	0	0 %	5 %
	3	2	1.2	10	0	21 %	25 %
	1	0	1.2	17.5	0	0 %	5 %
	3	2	1.2	17.5	0	37 %	35 %
	1	0	1.2	25	0	0 %	5 %
	3	2	1.2	25	0	53 %	55 %
North Carolina A&T	1	1	0.75	20	-	50 %	50 %
Ag. College	2	1	1	3	-	18 %	16 %
Henley Brook	1	1	1	5	5:1	33 %	33 %

Table 1.3, cont.

Wetland	Total nitrogen (mg N/L)	Ammonia nitrogen (mg NH_3-N/L)	Nitrite (mg NO_2-N/L)	Nitrate (mg NO_3-N/L)	Inorganic nitrogen (mg N/L)	Organic nitrogen (mg N/L)	Total Kjeldahl Nitrogen (mg TKN-N/L)
Minot	0	68	0	0	0	0	0
Messerly	0	69	0	0	0	-41	16
	0	49	0	0	0	-63	-5
West Jackson County	0	73	0	0	0	0	0
Hemet/San Jacinto	36	24	96	29	0	64	0
	28	35	51	-17	0	-3	0
	40	47	74	-61	46	9	0
	63	58	73	14	57	-22	0
	30	6	87	35	18	-6	0
Kingman	66	0	0	0	0	0	0
Fort Deposit	0	90	0	0	0	0	0
Tres Rios	58	72	97	64	0	0	53
	59	75	37	64	0	0	53
	46	50	0	68	0	0	0
	52	59	0	65	0	0	0
	54	59	0	65	0	0	0
	54	43	0	59	0	1	0
Saginaw	0	67	0	0	0	0	0
BP Oil	0	10	0	0	0	0	7
Champion	61	79	0	85	0	51	58
	73	91	0	88	0	63	71
	56	64	0	78	0	53	54
	70	47	0	96	0	56	54
	49	41	0	85	0	49	45
	48	40	0	87	0	45	44
North Carolina A&T	35	43	0	0	0	0	44
Ag. College	0	97	0	0	0	0	0
Henley Brook	0	0	0	0	0	0	0

Table 1.3, cont.

Wetland	Total Phosphorus (mg P/L)	Ortho-phosphate (mg P/L)	BOD_5 (mg/L)	acsTSS (mg/L)	Total coliforms (CFU/100 mL)	Volatile organic compounds (mg/L)
Minot	48	0	60	83	92	0
Messerly	19	20	40	-38	0	0
	22	22	5	-267	0	0
West Jackson County	0	0	80	74	0	0
Hemet/San Jacinto	5	0	0	0	0	0
	8	0	0	0	0	0
	-23	0	55	-3	99	0
	-35	0	-20	20	98	0
	-23	0	0	50	93	0
Kingman	0	28	87	93	0	0
Fort Deposit	0	0	88	91	0	0
Tres Rios	0	0	25	33	0	63–83
	0	0	30	46	0	0
	0	0	0	0	0	0
	0	0	0	0	0	0
	0	0	0	0	0	0
	0	0	0	0	0	0
Saginaw	0	0	0	0	0	0
BP Oil	2	4	6	15	0	0
Champion	62	0	52	83	0	0
	71	0	67	88	0	0
	44	0	48	80	0	0
	20	0	50	88	0	0
	40	0	38	78	0	0
	39	0	38	77	0	0
North Carolina A&T	27	48	48	67	0	0
Ag. College	93	0	99	96	0	0
Henley Brook	3	7	0	0	7	0

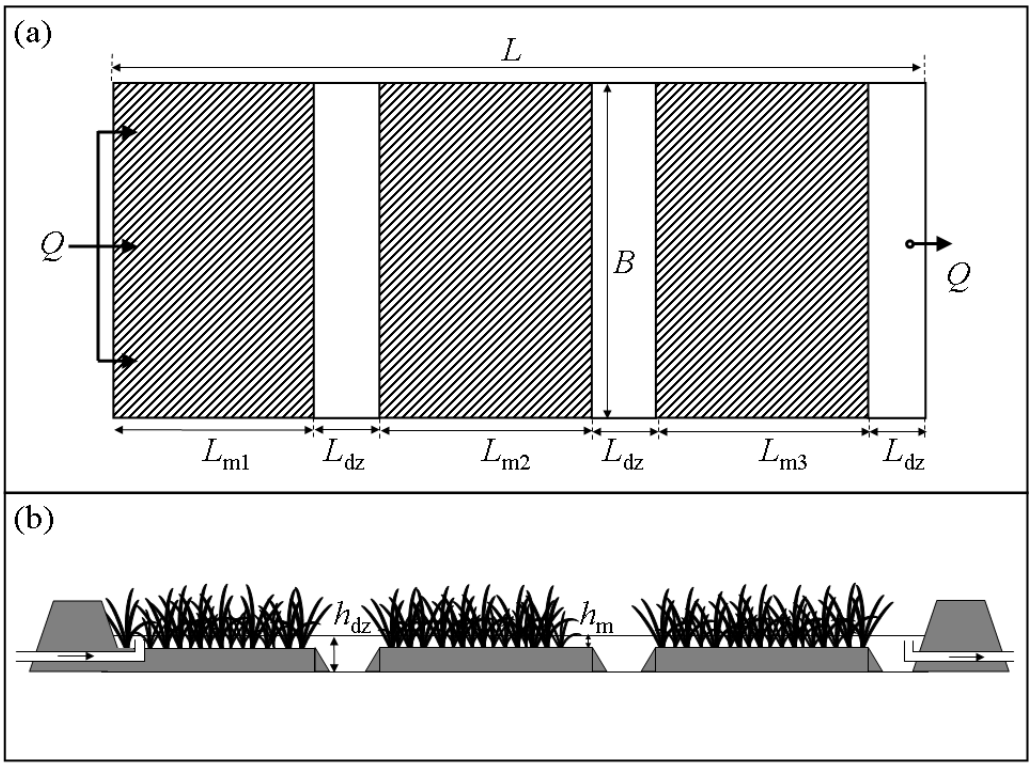

Figure 1-1: Definition sketch of a free-surface constructed treatment wetland with deep zones that stretch transversely across the entire wetland width. (a) Top view, showing three inlet structures, two internal deep zones, one outlet deep zone, and one outlet structure. Hatching indicates regions with emergent macrophytes. (b) Side view showing the marsh depth h_m and deep zone depth h_{dz}.

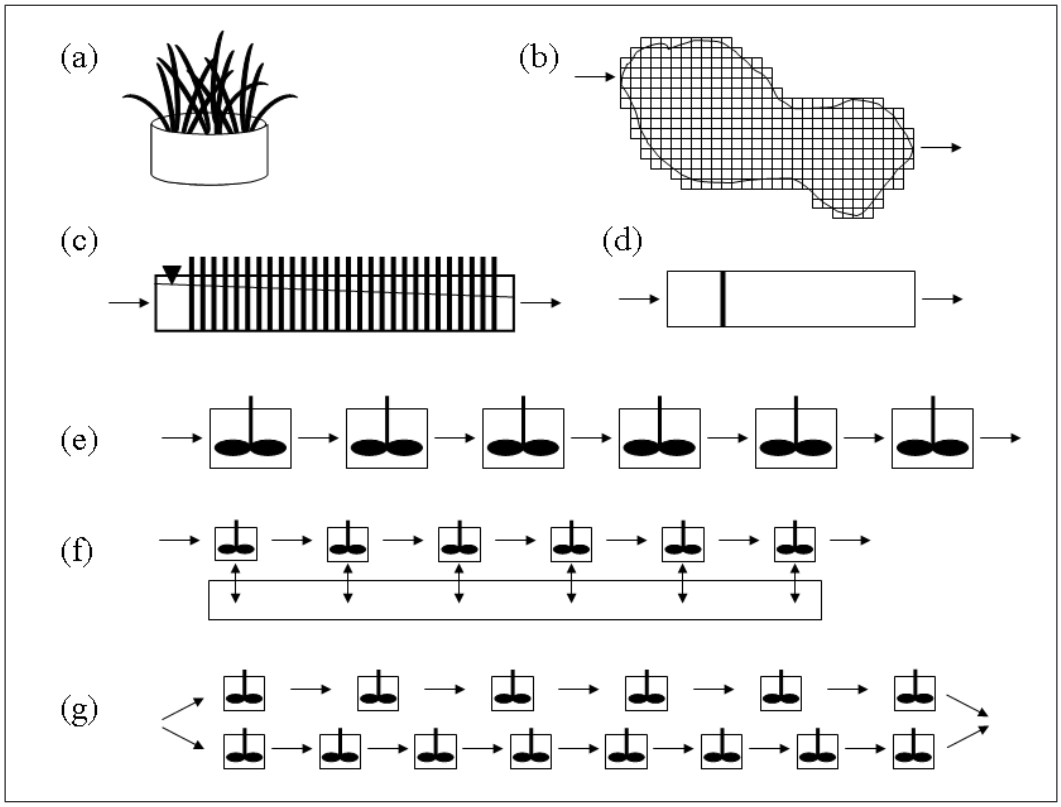

Figure 1-2: Sketches of models used for constructed treatment wetland design. (a) Bench-scale prototype (bucket) models. (b) Two-dimensional finite-element or finite-difference hydrodynamic models. (c) Plug flow reactor, showing one plug traveling through the system. (d) Tanks-in-series model, showing six continuously stirred tank reactors in series. (e) Transient storage zone model, in which each simulated tank along the main flowpath exchanges fluid with a well-mixed storage zone. (f) Stream tube model, showing two flowpaths each represented by a different number of tanks in series.

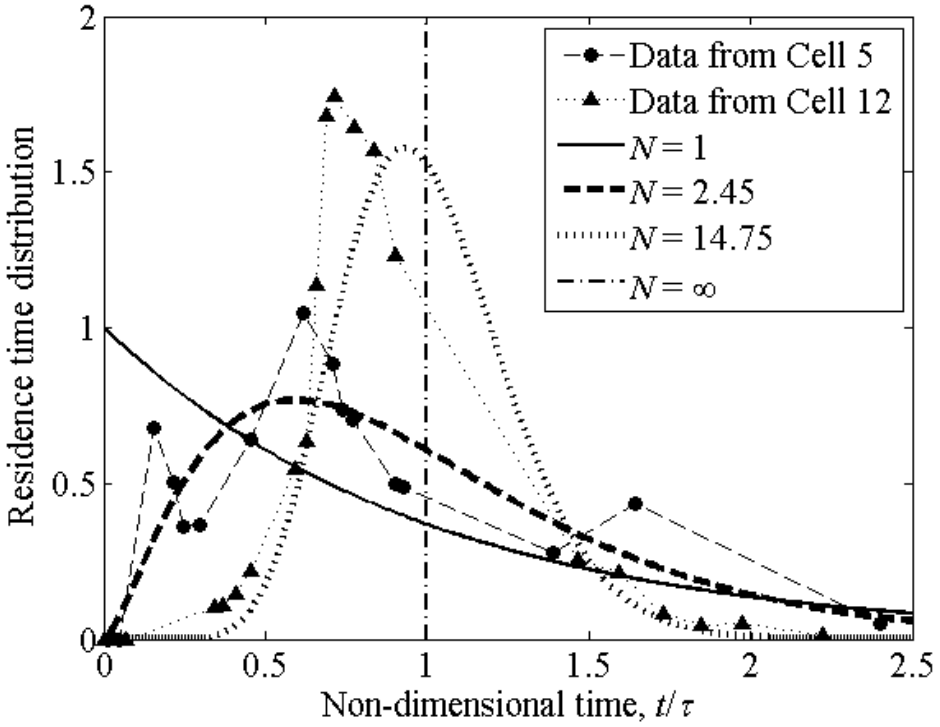

Figure 1-3: Sample residence time distributions (RTDs) within constructed treatment wetland sections. RTD data from a tracer study performed by Eidson et al. (2005) in Cells 5 and 7 of the Augusta wetland in September and October 2005. The Cell 5 data show a peak at $t/\tau \approx 0.2$, indicating the presence of short-circuiting. The curve with an equivalent number of tanks in series of $N = 2.45$ is the best fit between the data from Cell 5 and the family of gamma probability density functions given by Eq. 1.15; the curve with $N = 14.75$ corresponds to the data from Cell 7. The curve with $N = \infty$ would be produced if plug flow were present.

Chapter 2

Observations of short-circuiting flowpaths within a free-surface wetland in Augusta, Georgia, USA

This chapter uses detailed field measurements to characterize both the velocity heterogeneity within the marsh platform as well as the interaction of fast flowpaths with deep open-water zones. To date, the contribution of short-circuiting to overall flow through a wetland has only been inferred from wetland-scale tracer studies. Here, flow measurements are made at the scale of individual fast flowpaths within a 360-acre constructed treatment wetland in Augusta, Georgia, to directly quantify the size, distribution, and flow speed of the fast flowpaths through marsh areas. In addition, the water traveling within fast flowpaths is tracked as it enters an open-water region. Secondary goals of this study are to quantify both the amount of lateral mixing present within a deep zone receiving short-circuiting flow and the temperature differences between vegetated and open-water zones. This work has been submitted for publication to Limnology and Oceanography (Lightbody et al., Submitted).

2.1 Site description

Field observations were performed during July 2006 within the 360-acre constructed treatment wetlands associated with the J. B. Messerly Wastewater Treatment Plant (WWTP) in Augusta, Georgia (33.38°N, 81.95°W, Fig. 2-1). The wetlands were built between 1997 and 2002 to provide additional nitrogen removal from treatment plant effluent before it is discharged to the Savannah River. Observations were carried out within three of the twelve wetland cells. During the construction of each of these cells, grading was used to remove natural microtopography, and the remaining bottom topography was configured into an alternating pattern of marshes and ditches (Fig. 2-2). Construction of Cell 12 was completed in 2000; construction of Cells 6 and 7 was finished in 2002. In all three of these cells, plugs of *Zizaniopsis miliacea*, *Typha* sp., and *Scirpus* sp. were planted uniformly on 3 ft. centers in marsh regions (Eidson and Flite, 2005). Aerial observations confirmed that the vegetation had successfully colonized the entire marsh surface and that the dominant remaining species was *Z. miliacea*.

During July 2006, the marsh regions of the cells had an average water depth of $h_m \approx 48$ cm, although bottom wrack occluded much of the flow area and limited active water flow to within 15–30 cm of the water surface. The ditches, or deep zones, extended an additional 90 ± 5 cm ($n = 18$), for a water depth in the deep zone of $h_{dz} = 130 \pm 7$ cm ($n = 18$). Each cell has a total length of $L \approx 550$ m and a total width B between 207 ± 3 m and 254 ± 3 m (Fig. 2-2). Within each cell, there are three transverse deep zones (counting the final deep collection area), each with a length $L_{dz} \approx 45$ m. Each deep zone has an entrance slope of $\theta = 12$–$17°$ (range of six measurements in each cell), which is equivalent to a slope between 3.5:1 and 4.8:1 The volume of water in each wetland cell is $V \approx 68,000$ m^3. The primary vegetation in the marsh region, *Z. miliacea*, typically has a stem diameter of $d \approx 3$ cm (Fox and Haller, 2000) and would be expected to have a stem density of $n_v \approx 100$ 1/m^2 (Campagna and da Motta Marques, 2001), so solid volume fraction $\phi \approx 0.1$.

Steady flow conditions were present within the Messerly wetlands during July

2006. Flow exiting the WWTP entered a settling pond and then a distribution canal, from which weirs controlled the flow rate into each of the twelve individual cells. According to WWTP records, the flow rate entering the wetland system was 1170 ± 20 L/s and was approximately constant over the course of the study (Fig. 2-3a). Neither entrance nor exit weirs into the individual cells were adjusted over the duration of the study. Data from a previous study within this wetland imply that under steady flow conditions the flow rate entering each cell, Q, is 1/12 of the total wetland discharge with an uncertainty of $\pm 30\%$ (Flite et al., 2006). The same study suggests that infiltration and evapotranspiration within this wetland are negligible compared to the average discharge Q, so the flow rate entering and leaving each of the wetland cells depends primarily on the plant flow rate (Flite et al., 2006). The United States Geological Survey (USGS) gaging station (station number 02196999) at the Savannah River Lock and Dam, located 1 km away, recorded a total of only 2.5 cm of rainfall between 1 July and 28 July (Fig. 2-3b). The flow rate entering and exiting each cell was therefore assumed constant at $Q = 100 \pm 30$ L/s, for an hydraulic loading rate HLR $= Q/BL \approx 4$ cm/d.

The nominal hydraulic residence time (HRT) $\tau = V/Q \approx 8$ d within each cell. Based on the total flow rate, the mean, or plug-flow, velocity in the cell is $u_{pf} = Q/[Bh(1-\phi)]$, where h is the local water depth; $u_{pf} = 0.1$ cm/s in marsh areas. If plug-flow conditions are present, the time for water to travel a length ΔL will be:

$$t_{pf} = \Delta L / u_{pf} = \frac{\Delta L \; B \; h(1-\phi)}{Q} \tag{2.1}$$

Wind was recorded at the National Oceanic and Atmospheric Administration (NOAA) weather station at the Augusta airport (KAGS), less than 2 km away. The wind had a strong diurnal pattern of intensity (Fig. 2-6a) and also varied direction over the course of the study (Fig. 2-6b). Air temperature was recorded at the same station (Fig. 2-3c).

2.2 Methods

Tracer studies were used to determine the degree of short-circuiting within one vegetated marsh section of three different cells. The sampling areas within Cells 6 and 7 were the vegetation just upstream of the first deep zone; the sampling area in Cell 12 was the vegetation just upstream of the second deep zone. Dye was released across the entire cell twice at each site: Cell 6 beginning at 10:52 h on 12 July and 09:27 h on 21 July, Cell 7 at 09:47 h on 19 July and 08:38 h on 24 July, and Cell 12 at 09:23 h on 18 July and 09:54 h on 26 July. Each study consisted of the release of a known volume between 100–1000 mL of Intracid Rhodamine WT (Crompton and Knowles 20% liquid solution, density $\rho_{dye} = 1.1$ g/L) in a line across the cell upstream of a region of dense vegetation of width $L_{dye} = 34$–37 m. Dye was injected using a field pump, which was towed across the cell at 0.3–0.4 m/s, pumping Rhodamine WT at a constant rate of 200 mL/min into the wetland. To rapidly dilute the dye and reduce density effects, the dye was immediately stirred into an approximately 1-m-wide swath of surrounding swamp water. Over a week or more, Rhodamine WT is not conservative and will adsorb to sediments and plant matter, which will result in an underestimation of travel times during a full-scale study in a wetland (Cooper, 1994; Lin et al., 2003; Keefe et al., 2004). However, it has been used successfully in short-term studies of less than 6 days (e.g., Stern et al., 2001; Lin et al., 2003). Each of the studies reported here was less than 96 hr long.

The appearance of the dye downstream of the vegetation was detected by towing an in-situ fluorometer (Seapoint Sensors, Exeter, New Hampshire) connected to a Conductivity, Temperature, and Depth (CTD) probe (Ocean Sensors, San Diego, California) within the deep zone along the downstream edge of the vegetation. The fluorometer sampled at 8 Hz, and its voltage output was calibrated using known concentrations of the Rhodamine stock solution diluted in fresh water (Fig. 2-4). Sampling continued up to 79 hr after each release. The depth of the fluorometer was varied on different lateral traverses, which each took approximately 15 minutes. To accurately record boat position, stakes were placed at 8- to 60-m increments along

the width of the deep zones, and records were kept of the time the boat passed each. Linear interpolation was then used to determine boat position between stakes. A handheld GPS unit (eTrex Venture, Garmin, Olathe, Kansas, ±5 m accuracy) was used to spot check the stake and boat positions.

Fast flowpaths were assumed to exist upstream of the points at which dye was first observed within the deep zone. In particular, a fast flowpath was defined as contributing more dye than the lateral average during the first $t_{pf}/2$ after release. For each tracer study, the concentration recorded before $t_{pf}/2$ after release was interpolated using a triangle-based cubic fitting algorithm to a 1-min by 0.25-m grid and integrated over time to find the average concentration, $\langle\bar{c}\rangle(y)$, during this time interval, where y indicates lateral distance across the cell; x indicates longitudinal distance. In addition, at each lateral position where dye was observed between 0 and $t_{pf}/2$, the arrival time of the peak concentration, t_{dye}, was used to estimate the average transit time of tracer through the fast flowpaths, $u_{dye} = L_{dye}/t_{dye}$. To estimate the uncertainty in these calculations, several point releases were performed with the fluorometer fixed directly at the outlet of an identified flowpath. These continuous point records were then resampled at 20-minute intervals, which was the average interval between successive traverses, and used to calculate values of $\langle\bar{c}\rangle$ and t_{dye}. The reported uncertainties associated with the $\langle\bar{c}\rangle$ and t_{dye} values are the sum in quadrature of the difference between the continuous point measurements, the resampled point measurements, and the traverse measurements.

In the areas identified as fast flowpaths, detailed observations of flow speed were then undertaken using small-scale releases of a non-fluorescent tracer (food coloring), surface floaters, and a two-dimensional (2-D) sideways-looking acoustic Doppler velocimetry (ADV) probe (Flowtracker, SonTek/YSI, Inc., San Diego, California). The Flowtracker acquired 1-min-long point measurements of the water velocity exiting the densely vegetated regions. Preliminary analysis confirmed that 1 minute was long enough for the measurement to reach a stable mean value; only mean flow was resolved or will be discussed. Factory specifications state that the Flowtracker is capable of measuring between 0.1 cm/s and 500 cm/s with an accuracy of 1%, although

it was not possible to attain repeatable measurements for a time-averaged velocity $\bar{u} < 0.5$ cm/s. The ADV probe was fixed to a staff gage resting on the marsh bed. Before each measurement, wrack and vegetation were removed from the 10-cm-wide area between the probe arms and the sampling volume. The ADV measurements were focused around the fast flowpaths identified by the tracer study.

A ruler was used to measure the depth h_m and the width b_f of each fast-flow region. The lateral flowpath boundaries were assumed to exist at the nearest cutgrass clump on either side of the main flowpath, which, as shown by detailed flow measurements in several fast flowpaths, coincided with the location where the flow velocity decreased below the detection limit. Σb_f represents the total width of fast flowpaths within a cell.

Velocity records were used to estimate flow rates through the fast flowpaths as follows. The velocity distribution in each fast flowpath was normalized by the peak velocity, the flowpath width, and the full flowpath depth. The normalized data from all fast flowpaths were then pooled to create a composite velocity distribution (Fig. 2-5). The composite profile was integrated over depth and width to define the scale factor κ between the average velocity U_f and the peak velocity u_{peak} within a fast flowpath, such that $U_f = \kappa u_{peak}$. The error associated with the scale factor was estimated as the standard deviation of sub-group scale factors estimated for fifty random subsamples of 25 measurements each. The flow rate for each fast flowpath was then calculated as $q_f = U_f h_m b_f = \kappa u_{peak} h_m b_f$, where b_f is the width of that flowpath. The total flow rate, Σq_f, through the n_f fast flowpaths within a given cell was estimated by summing the individual flow rate measurements from across an entire cell. Within each cell, the fraction of flow carried within fast flowpaths is given by $\Sigma q_f / Q$. From continuity, the depth-averaged velocity within the slow-flow zones is then given by:

$$U_s = \frac{Q - \Sigma q_f}{h_m (B - \Sigma b_f)(1 - \phi)} \tag{2.2}$$

where h_m includes the region of wrack near the bed.

To characterize transport within the open-water deep zones, the fluorometer was

also used to make periodic lateral transects at eight staked longitudinal positions within the deep zone downstream of the studied marsh region. Dye concentration was measured for up to 79 hr after a dye release within each cell: 09:27 h on 21 July in Cell 6, 08:38 h on 24 July in Cell 7, and 09:54 h on 26 July in Cell 12. Before analysis, synoptic results were averaged over depth and interpolated to a 1-m x 1-m grid. The data resolution was not high enough to identify the 1% or even 10% contour, so the longitudinal extent of the evolving tracer clouds was defined as the location where the concentration equaled 30% of the maximum concentration observed at that time. Because tracer reached the downstream edge of the deep zone before it mixed laterally, it was possible to distinguish the evolving plumes from flowpaths in different halves of the deep zone, and the extension of the dye front was calculated separately for each lateral half of the deep zone. The speed of the tracer cloud was calculated as the rate of change in the longitudinal position of the tracer front.

Temperature loggers (HOBO temperature logger, Onset Computer Co., Bourne, Massachusetts) were deployed during each dye release. At least three loggers were placed on a thermister chain in the middle of the deeper open-water area, two loggers were placed at mid-depth within dense vegetation 5 m upstream of the deep zone, and one logger was placed within an identified fast flowpath 5 m upstream of the deep zone. When multiple loggers were deployed simultaneously in similar sites, temperature data were averaged and the difference in measurements was used to estimate uncertainty. To create a composite daily temperature cycle for each position, the nightly minimum temperature was subtracted, and results were conditionally averaged over the 24 days of deployment.

2.3 Results and discussion

2.3.1 Flow and transport through vegetated regions

In each of the three cells examined, tracer studies revealed the presence of multiple fast flowpaths distributed across the width of the cell. As an example, Fig. 2-7 shows

the concentration transects measured at the downstream end of a band of dense cutgrass of length $L_{dye} = 38 \pm 5$ m. Distance across the cell is plotted on the y-axis; the x-axis is time. Color denotes measured concentration. Because of boat turning, it was not possible to sample within 4 m of each side bank. If plug flow existed within the vegetation, the peak concentration would be observed at $t_{pf} = 11 \pm 4$ hr (Eq. 2.1), where the major source of uncertainty is from the cell flow rate Q. Fig. 2-7 shows dye exiting the vegetation at several distinct lateral positions at as early a time as $t = 29$ min, indicating the presence of fast flowpaths near $y = 8$ m, 45 m, 105 m, 145 m, and 185 m.

Fig. 2-8 shows the time-averaged concentration profile recorded up to $t_{pf}/2$ after release within all three studied cells. Similar results (not shown) were obtained for a repeat dye release within each of these cells. Between the peaks, dye concentrations were typically below the detection limit of the fluorometer. The dye studies in Fig. 2-8 were used as a guide in identifying fast flowpaths, the lateral positions of which are indicated by letters. In instances where two fast flowpaths were closer than 2 m apart, the sum of the two was considered to be one flowpath. Within each of the three cells, between three and six distinct flowpaths transported more dye than the average. Due to time constraints, fast flowpaths F, G, and L were characterized by only the tracer study; the average of other fast flowpaths was used in calculating total values for each cell. Flowpath C was located too close to the bank to identify using the boat-mounted fluorometer but was identified on foot when performing velocity measurements.

More detailed tracer studies were conducted at flowpath A. Two types of measurements were taken. First, the fluorometer was fixed in one horizontal location, and the concentration at different depths was recorded (Fig. 2-9a). The peak concentration was recorded at $z = 11$ cm below the surface, and concentrations above background were observed down to 6 cm above the bed ($z = 46$ cm). Fig. 2-9b compares observations between a fluorometer fixed at the flowpath exit and a fluorometer making lateral traverses while mounted on a boat. The vertical axis shows the recorded concentration, normalized by the concentration just after injection. The horizontal axis

shows the time since the release occurred a distance $L_{dye} = 37 \pm 5$ m upstream. Note that the peak arrival times from the fixed and traverse measurements are similar, suggesting that the transit time calculated from the lateral traverses is comparable to what would have been observed using multiple stationary recording fluorometers. In addition, the five curves represent five different releases on three different days, yet they produced similar concentration responses, confirming the repeatability of these measurements and the steadiness of the flow pattern. Finally, even though $t_{pf} = 11 \pm 4$ hr, the center of mass of recovered dye occurred only 34 ± 2 min ($n = 5$) after release, verifying that this is a region of elevated velocity, with flow thirteen times faster than the mean flow, and also that $t_{pf}/2$ is sufficiently long to identify the center of mass. The equivalent number of tanks in series (TIS) for the five curves shown in Fig. 2-9b are, respectively, $N = 6.4$, $N = 12.1$, $N = 7.1$, $N = 4.9$, and $N = 6.5$.

ADV measurements revealed that these fast flowpaths had a maximum velocity up to $u_{peak} = 7.8$ cm/s (Table 2.1). The sample velocity transect shown in Fig. 2-10a, taken at the depth of peak velocity, illustrates that the velocity measured exiting the fast flowpaths was much higher than that measured in the slow-flow zones on either side. Because the ADV instrument was unreliable below 0.5 cm/s, it can only be concluded that the velocity exiting the vegetation is less than 0.5 cm/s; from Eq. 2.2, the velocity depth-averaged U_s should be less than $u_{pf} \approx 0.1$ cm/s. Similarly, water velocities measured by Brueske and Barrett (1994) more than 20 m from the inlet of a small constructed wetland were approximately 3.6 cm/s within sparse submerged vegetation and 0.3 cm/s within dense cattails.

The parameters describing each fast flowpath are presented in Table 2.1. The average fast flowpath width was $b_f = 2.5 \pm 0.5$ m and the average total water depth in the marsh regions was $h_m = 0.48 \pm 0.02$ m. The actively flowing water depth was smaller, since there was a deep layer of wrack near the bed. The total fast-flowpath width was $\Sigma b_f = 3 \pm 1$ m, 11 ± 1 m, and 21 ± 1 m in Cells 6, 7, and 12, respectively (Table 2.2). The widths of these cells were, respectively, $B = 213 \pm 3$ m, 207 ± 3 m, and 254 ± 3 m, so the fraction of area occupied by fast flowpaths was, respectively,

$\Sigma b_f/B = 0.016 \pm 0.004$, 0.05 ± 0.01, and 0.08 ± 0.01 in Cells 6, 7, and 12. Note that these numbers reflect what was observed. It is possible that other flowpaths were present but not identified. These numbers therefore provide a lower bound on the fraction of short-circuiting water within these wetland cells.

Detailed measurements of the velocity profile were carried out within several fast flowpaths. In all velocity distributions, the velocity peak was near the middle of the flowpath and within the upper third of the water column. There was at least one measurement within that zone within each fast flowpath. The vertical velocity profile is not logarithmic, and in fact a substantial region near the bed had no flow due to accumulated dead vegetation (e.g., the lower 13 cm of the water column in Fig. 2-10a). The horizontal velocity profile also deviates from that within a banked channel because the edges of the fast flowpaths were porous, consisting of clumps of vegetation that contributed roughness. A composite velocity profile constructed from 96 velocity measurements within fifteen fast flowpaths indicated that the average velocity U_f over the flow cross-section was $32 \pm 7\%$ of the peak measured velocity: $U_f = (0.32 \pm 0.07)u_{peak}$. Among the several fast flowpaths, the average velocity U_f varied between 0.3 and 2.7 cm/s. Note that the average velocities observed at the fast flowpath exit U_f are the same order of magnitude as and roughly proportional to the velocities inferred from the mean travel time of tracer through the vegetation u_{dye} in Table 2.1), showing the two methods are consistent and suggesting that the fast flowpaths are coherent through the vegetated marsh region. Similarly, previous work found that a fast-moving stream has limited exchange with surrounding dense vegetation (Su and Li, 2002).

The average velocity U_f for each identified fast flowpath and its measured dimensions were combined to produce the flow rate q_f within that flowpath (Table 2.1). For Cells 6, 7, and 12, the total volume of fast flow $\Sigma q_f = 18 \pm 2$ L/s, 45 ± 5 L/s, and 64 ± 13 L/s, respectively (Table 2.2). When compared with the average flow through the cells ($Q = 100 \pm 30$ L/s), these data indicate that the fraction of flow traveling within fast flowpaths was $\Sigma q_f/Q = 0.2$–0.7. The ratios between the fast-flow velocity and the mean velocity are $U_f/u_{pf} = 8$–12 and the ratios between the fast and slow

velocities in each cell are $U_f/U_s = 14$–20. These results suggest that at least 20% of the flow has a residence time that is less than 1/8 ($\approx 13\%$) of the nominal residence time. Also note that the amount of short-circuiting flow was greatest in Cell 12, which started operation two years prior to the other two cells, suggesting that the problem of short-circuiting can worsen over time.

Similar ratios can be estimated for other wetlands. For example, in a tracer study at a 77-hectare wetland in central Florida, the peak tracer concentration at the outlet was observed after 0.4 d, while the nominal HRT was 19 d (Keller and Bays, 2002), suggesting that the peak concentration traveled through a short-circuiting flowpath for which $U_f/u_{pf} \approx (19\text{ d})/(0.4\text{ d}) = 48$. Tracer test data from four cells in the Orlando Easterly wetland suggest that $U_f/U_s = 2$–22 and the ratio of fast-flowpath flow rate to total flow rate $\Sigma q_f/Q \approx 0.5$ (Martinez and Wise, 2003*b*).

The (perhaps unavoidable) development of fast flowpaths should be considered when planning any large tracer study. Traditionally, tracer studies are planned based on the nominal HRT; for example, Frossard et al. (1996) recommends a first sample at 0.1 τ. However, the presence of short-circuiting means that a large fraction of dye will emerge well before the nominal HRT, and using the nominal HRT in planning calculations can result in undersampling the peak (Keller and Bays, 2002). Similarly, in groundwater studies, short-circuiting can allow tracer to rapidly pass beyond the end of an array of sampling wells, necessitating the installation of additional wells downgradient in the middle of a study (e.g., Broholm et al., 2001). Note also that, because a wetland is not laterally homogeneous, it is not valid to assume that multiple outlets within a wetland will have the same residence time distribution (RTD) (e.g., Keller and Bays, 2002), because outlets directly downstream of a fast flowpath can have a very different RTD from outlets in regions without fast flowpaths.

2.3.2 Transport through unvegetated deep zones

After the water flowed out of the marsh region, it entered a transverse deep zone (see Fig. 2-2). Fig. 2-11a shows the spatial distribution of dye at various times after a release within the upstream marsh in Cell 6. The color scale indicates the

average concentration over depth. The plug-flow time of transit, t_{pf}, was 11 ± 4 hr through the marsh and an additional 32 ± 11 hr through the deep zone. However, the dye concentration at the downstream edge of the deep zone reached 30% of the maximum concentration within the deep zone only 10.7 hr after first entering the deep zone, which was less than 40% of the expected plug-flow transit time. Fig. 2-11b,c show the results for similar releases in Cells 7 and 12. The tracer again reached the downstream edge quickly, by 6.8 hr and 5.3 hr after release, which was 6.2 hr and 4.7 hr after entering the deep zone, respectively, again indicating non-uniform flow conditions within the deep zone.

At $t_{pf}/2$ after release, by definition, all of the tracer within the deep zone had traveled through the marsh area in less than the plug-flow time of transit. The total mass of dye within the deep zone at this point in time, Σm_f, was 20%, 30%,and 42% of what had been released $M_{release}$ within Cells 6, 7, and 12, respectively. These values are an estimate of the fraction of tracer mass that traveled through fast flowpaths. Note the good agreement between $\Sigma q_f/Q$ and $\Sigma m_f/M_{release}$, both of which are measures of the fraction of flow carried by fast flowpaths. Because it was expected that dye began to leave the deep zones before the dye that had traveled through the slow-flow zones entered, it is not surprising that 100% of the released dye was not observed simultaneously within the deep zone. The mass flux exiting the deep zone, $j_{dz,exit}$, can be estimated from the concentration at the downstream edge, $j_{dz,exit} = \langle\bar{c}\rangle(x = L_{dz})Q$. Fig. 2-12 also shows the integral of this mass flux, which is the cumulative mass that has left the deep zone. The curves are expected to asymptote at $M_{release}$ if the tracer is conservative.

The advance of the tracer front across the deep zone can be used to estimate the speed of the fast-flow water within the deep zone. Fig. 2-13 shows the speed of the dye front for the three releases shown in Fig. 2-11. The speed of the tracer front decayed to background within 5–10 m of the beginning of the deep zone, after which the tracer traveled across the deep zone at a speed at the same order of magnitude as the expected plug-flow velocity u_{pf}. The thick layer of periphyton near the bed of the deep zone may have contributed to this rapid decay of fast-flow momentum. Similarly,

Brueske and Barrett (1994) reported that water velocities decayed to background levels within 20 m of the inlet to an open water region in a small constructed wetland. These results suggest that these wetlands were not represented by previous physical models of deep zones within constructed wetlands that did not include enhanced roughness (Sec. 1.6.2).

The tracer also spread laterally as it moved through the deep zone. In Cell 6 (Fig. 2-11a), tracer that had entered the deep zone by 0.6 hr after release had spread across the width of the deep zone by 10.7 hr. In Cell 7 (Fig. 2-11b), tracer that had entered by 1.6 hr and had spread across the entire width of the deep zone by 26 hr; in Cell 12 (Fig. 2-11c), tracer that had entered by 1.1 hr and had spread across the whole width by 10.1 hr. In these three cases the dye spread across the width of the deep zone on the order of $\hat{T} \approx 10$ hr. Because dye entered from multiple fast flowpaths, the lateral length-scale over which the dye mixed as the distance between fast flowpaths, $\hat{Y} \approx$ 50–100 m. This leads to an estimated dispersivity of $K_y \approx \hat{Y}^2/\hat{T} \approx$ 0.07–0.3 m^2/s, or a nondimensional dispersion coefficient of $K_y/u_{pf}\hat{Y} =$ 1–3. Previous work on dispersion in open water suggests that at scales of 50–100 m the horizontal dispersion coefficient falls in the range $K_y =$ 0.02–0.05 m^2/s for a patch that is much smaller than the basin (Lawrence et al., 1995). This range is slightly less than the dispersivity observed here.

Two factors may contribute to the observed dispersion of tracer: jet entrainment and wind. First, the introduction of fast-flowing water through a confined area can create lateral mixing through shear instabilities. The amount of jet entrainment and hence mixing depends on the excess momentum within the fast-flowing region (e.g., Abramovich, 1963). However, the rapid decay of the excess velocity and hence momentum (see Fig. 2-13) likely limits the contribution of jet-induced mixing to within 10 m of the upstream edge of the deep zone. Therefore, in this system, it is likely that wind contributed most to the observed mixing. The wind speed during all releases was 2.1 ± 0.2 m/s(cf. Fig. 2-6). This speed is sufficient to impact transport within an unvegetated area, since surface water speed is approximately 2% of the wind speed at 10 m above the surface (Wetzel, 1975, p. 97), so a 2 m/s wind would

be expected to advect dye 50 m in less than 1 hr.

Perhaps most importantly, the deep zone is small enough that the wind can relatively quickly establish basin-scale circulation. For a wind speed 10 m above the earth surface of $U_{10} = 2.1$ m/s, the timescale for development of wind-induced surface circulation across the width of the deep zone would be $\hat{Y}/0.02U_{10} \approx$ 1–2 hr (George, 1981). When turbulence is caused by wind shear and the shear velocity $u^* = \sqrt{\frac{\rho_a}{\rho_w} C_a} U_{10} \approx \frac{1}{1000} U_{10}$ (Fischer et al., 1979, pp. 161-162), where ρ_a is the air density, ρ_w is the water density, and C_a is the drag coefficient, then the timescale for the development of fully-developed circulation over depth is $h_{dz}/u^* \approx 11$ min. The sum of these processes is shorter than the observed diurnal wind cycle (Fig. 2-6) and also less than the observed timescale of longitudinal dye transport across the deep zone ($\approx$ 6 hr, cf. Fig. 2-11). Therefore, basin-scale circulation will be present and will contribute to mixing.

The amount of lateral spreading of the fast-flowing water depended both on the strength and orientation of the local wind. In the first six hours after the release in Cell 6 on 21 July, the wind was 2.9 ± 0.7 m/s oriented parallel to the main flow direction. In the release in Cell 7 on 24 July, the wind was 1.3 ± 0.4 m/s again parallel to the main flow direction, though in the opposite direction to the flow. In the release in Cell 12 on 26 July, the 3.9 ± 0.6 m/s wind was oriented perpendicular to the main flow direction so directed along the width of the deep zone, blowing from $y = 250$ m toward $y = 0$ m. Fig. 2-14 shows the average dye concentrations at different depths between 4.1 and 5.6 hr after release for the three dye releases presented in Fig. 2-11. When the wind was oriented parallel to the direction of flow, there was mixing over depth but little mixing between water transported within different fast flowpaths (Fig. 2-14a and 2-14b). However, wind directed perpendicular to flow enhanced lateral spreading of the dye in a depth-averaged sense (Fig. 2-14c). In addition, in this release, the wind created distinct patterns of dye concentration over depth. At 5.3 hr after release, tracer was observed primarily near the surface ($z = 10$ cm) at the downwind edge of the deep zone (near $y = 0$ m) and at depth ($z = 79$ cm) at the upwind edge (near $y = 250$ m). These observations suggest that the wind had created a basin-

scale circulation within the deep zone, advecting surface water from west to east, and creating a return current near the bottom of the deep zone from east to west. It is clear from these cases that, depending on its orientation relative to the long axis of the deep zone, mild wind has the potential to redirect flow. Predictions of the effect of a deep zone on chemical fate within a wetland should therefore consider both windy and non-windy conditions. For example, the central pond in a southern California constructed wetland providing tertiary treatment for reclaimed water was designed with full exposure to prevailing winds to maximize mixing (Sartoris et al., 2000*b*). Note, however, that wind directed transversely across a wide wetland cell can result in excessive setup that overtops the surrounding berm (Eidson et al., 2005).

2.3.3 Comparison of temperature within vegetated and unvegetated regions

Temperature loggers were deployed throughout the study period. First, consider the loggers located within the open-water deep zones (Fig. 2-15). These loggers show both dynamic fluctuations in response to meteorological changes and a typical diurnal signal, with a daily minimum in the early morning and a daily maximum in the late afternoon. In general, the air temperature follows a similar cycle, but the temperature fluctuations within the water are not as extreme as they are in the air (cf. Fig. 2-3c). The composite temperature record shows that, at the surface of the open water, temperatures increased an average of 3°Celsius (C) above the nightly minimum (Fig. 2-16). This thermal variation was damped near the bed; at $z = 60$ cm, temperatures increased to only 0.5°C above the daily minimum. The vertical variation in diurnal heating created thermal stratification within the open water during daylight hours. For example, on 10 July, there was a 7°C difference between the temperatures 10 cm below the surface and 60 cm below the surface (Fig. 2-15). Similarly, at a 60-cm-deep site within the Florida Everglades under calm weather conditions,, the water column reached a maximum stratification in mid-afternoon of approximately 3°C (Schaffranek and Jenter, 2001). Mats of duckweed (*Lemnaceae*) were present

within the open areas and at times were located above the thermister chains, but all measurements were taken at least 10 cm below these mats. Dale and Gillespie (1976) report that the temperature 2 cm below a duckweed mat can be up to 11°C higher than the temperature within adjacent open water at the same depth. However, at a depth of $z = 10$ cm and below there is little difference between an open water column and a duckweed cover (Dale and Gillespie, 1976).

Now consider the temperatures measured within the open water of the deep zones and the temperatures measured within the marsh. Temperature fluctuations were reduced within the densely vegetated areas, which at their peak remained an average of 2°C cooler than the surface of the open areas. Fast flowpaths within the vegetated areas were 0.9°C warmer than the slow-flow areas, and in some cases their temperature approached that of the surface of the open-water zones (cf. 27 July in Fig. 2-15). The higher temperature in the fast flowpaths is likely caused by advection from the warm temperatures within an upstream open-water area. If the water within the fast flowpaths short-circuited the entire marsh region at the same velocity as observed at the exit, then it would have left an upstream open-water deep zone approximately 2–4 hr before it entered the deep zone; on the other hand, the water traveling through the slow-flow zone would have spent about 30 hr in dense vegetation. Because the timescale for diurnal cooling is approximately 12 hr, only the water traveling through the fast flowpath would be expected to retain the upstream temperature signature.

Also note that the peak temperatures within both the dense vegetation and the deep portions of the open water occurred later in the day than they did at the surface of the open water. As shown in Fig. 2-16, the maximum temperature at the surface of the deep zone occurred at 16:30 h, the maximum temperature 30 cm below the deep zone surface and within the fast flowpaths occurred at 18:00 h, and the maximum temperature within the vegetation occurred at 20:00 h. The lag in temperature maxima with depth has elsewhere been attributed to vertical heat transfer from surface to deep waters (Dale and Gillespie, 1976).

These observations of spatial and temporal variation in temperature records are consistent with observations elsewhere. For example, Kadlec (2006) reports that the

water temperature fluctuates diurnally by 6°C within the Hayfield cell in the Tres Rios wetlands, with a daily minimum at 08:00 h and a daily peak at 18:00 h. In a southern California treatment wetland, water temperatures within a band of mixed *Schoenoplectus acutus* and *S. californicus* were up to 2.5°C lower than those within a nearby 12-m-wide open-water band (Sartoris et al., 2000*b*). In the large Stormwater Treatment Areas near the Florida Everglades, temperature variability was reduced in stands of *Typha domingensis* Pers. and *T. latifolia* L. sp. stands when compared to open water (Chimney et al., 2006). During the growing season, the floating water hyacinth *Eichhornia crassipes* damps temperature fluctuations compared to both the air and to a nearby submerged canopy of *Ceratophyllum* (Ultsch, 1973).

The horizontal temperature differences that were observed in the Augusta wetland are sufficient to create density-driven exchange flows. For the values observed in the Augusta wetland, the method presented by Tanino et al. (2005) predicts exchange currents between the vegetation and deep zones with a speed up to 0.9 cm/s and a direction that reverses twice during each 24-hr period. This flow speed is an order of magnitude larger than the water velocity through the densely vegetated marsh ($U_s <$ 0.1 cm/s) and could result in the exchange of 8 L/s between a vegetated region and an adjacent deep zone. It may also contribute flux in the reverse direction from the mean hydraulic gradient, which would enhance dispersion. However, the estimated thermal exchange is less than 10% of the pumped flow rate through this wetland (100 L/s), so it probably does not play an important role here. Convective vegetated exchange flows may be important in a natural wetland that lacks an imposed flow. Oldham and Sturman (2001) observed nightly exchange currents with a velocity of 0.05–0.2 cm/s in a constructed wetland mesocosm in Western Australia that had *Schoenoplectus validus* growing in the shallow regions. Within a small midwestern lake, a temperature difference of 2°C between a shallow vegetated area and a deeper open-water area was observed to drive horizontal exchange flow of 0.0003 m^2/hr between the two areas, which constituted a large fraction of overall flux between the two regions (James and Barko, 1991).

The difference in temperature between the vegetated and unvegetated portions

of the wetland may also be important for other reasons. First, if temperature varies both temporally and spatially throughout the wetland, a single measurement at one location is not representative of the entire wetland. Second, removal rates for contaminants such as nitrate are proportional to the local temperature (Bachand and Horne, 2006), so predictions of removal based on the open-water temperature may overestimate removal within the vegetated portions of a wetland. Finally, the different temperatures within the dense vegetation and the fast flowpaths suggest that fast flowpaths could be identified using thermal remote sensing techniques. During the late afternoon and evening the surface of the deep zone ($z = 10$ cm) is up to 1.2°C warmer than the fast flowpath, which is up to 0.6°C difference warmer than 30-cm below the surface of the deep zone (Fig. 2-16). Mid-afternoon temperature transects of the water entering the deep zone suggest that locations where fast flowpaths were previously identified in fact have a warmer temperature than water 30 cm below the surface of the deep zone (Fig. 2-17). More detailed work is necessary to determine whether it is possible to use temperature as a natural tracer. Until such a method has been developed, identifying and characterizing specific fast flowpaths will continue to require intense, focused effort.

2.4 Conclusion

This study presented a detailed investigation of short-circuiting within marsh regions of uniform depth in a large constructed wetland. Discrete fast flowpaths were observed in every section of dense vegetation, which had been planted with uniform vegetation five years previously. Because natural wetlands are even more likely to exhibit heterogeneous patches of vegetation and channelized flowpaths, these results suggest that short-circuiting may be present in wetlands of all types.

Fast flowpaths that together accounted for 20–70% of the flow through these cells. The flowpaths constituted 2–8% of the width of each marsh area and contained flow traveling 14–20 times as fast as through dense vegetation. This degree of velocity variation confirms that plug flow is a poor approximation to flow through wetlands.

Moreover, this heterogeneity complicates the modeling of biogeochemical processes within wetlands and limits the ability to infer full-scale wetland function based on small-scale test wetlands, because the pattern of short-circuiting may be different.

Although short-circuiting complicates the representation of flow in free-surface wetlands, this study suggests that two velocities may be sufficient to describe water movement through a wetland. In the Augusta wetland, there was not a continuous variation in flow velocities; rather, the distribution was binary. The fast flowpaths had a velocity $U_f = 1.0 \pm 0.2$ cm/s, and the slow flow had a velocity $U_s = 0.06 \pm 0.03$ cm/s. Similarly, Keller and Bays (2002) found that the residence time distribution for a short-circuiting 81-ha wetland in Florida could be fit by assuming that the wetland consisted of only two flowpaths of distinct flow speeds. Therefore, a numerical model of wetland flow need not consider an infinite number of stream tubes (e.g., Carleton, 2002) but may simply consist of a fast and a slow velocity. Further work is necessary to quantify the small-scale patterns of flow within wetlands of all types.

Table 2.1: Dimensions and velocity measurements for each fast flowpath identified in Fig. 2-8. The columns provide the following information: the lateral position of the flowpath, y; the width of the flowpath, b_f; the water depth within the marsh, h_m; the travel speed of the center of mass of dye emerging from the flowpath, u_{dye}; the peak measured velocity within the flowpath, u_{peak}; the cross-sectional-average velocity within the flowpath, U_f; and the average flow rate within the flowpath, q_f. Dashes indicate locations where direct measurements were not taken.

Flowpath	Cell	y (m)	b_f (m)	h_m (m)	u_{dye} (cm/s)	u_{peak} (cm/s)	U_f (cm/s)	q_f (L/s)
A	6	5 ± 3	0.7 ± 0.1	0.28 ± 0.01	1.6 ± 0.5	7.8 ± 0.1	2.7 ± 0.2	5 ± 1
B	6	186 ± 3	1.1 ± 0.1	0.44 ± 0.01	1.9 ± 0.6	3.2 ± 0.2	1.1 ± 0.2	6 ± 1
C	6	207 ± 3	1.6 ± 0.1	0.45 ± 0.01	-	2.9 ± 0.3	1 ± 0.2	7 ± 2
D	7	9 ± 3	2.4 ± 0.1	0.45 ± 0.01	0.7 ± 0.2	2.5 ± 0.2	0.9 ± 0.2	10 ± 2
E	7	49 ± 3	1.4 ± 0.1	0.43 ± 0.01	0.9 ± 0.2	4.4 ± 0.5	1.5 ± 0.2	9 ± 2
F	7	105 ± 3	2.4 ± 0.1	0.48 ± 0.01	1.0 ± 0.3	-	-	-
G	7	145 ± 3	2.4 ± 0.1	0.48 ± 0.01	0.5 ± 0.1	-	-	-
H	7	180 ± 3	1.3 ± 0.1	0.44 ± 0.01	0.5 ± 0.1	0.8 ± 0	0.3 ± 0.2	2 ± 1
I	7	186 ± 3	0.9 ± 0.1	0.42 ± 0.01	0.5 ± 0.1	2.3 ± 0.7	0.8 ± 0.4	3 ± 1
J	12	20 ± 3	3.8 ± 0.1	0.57 ± 0.01	0.5 ± 0.1	0.8 ± 0.1	0.3 ± 0.2	6 ± 5
K	12	37 ± 3	8.2 ± 0.1	0.53 ± 0.01	0.4 ± 0.1	1 ± 0.1	0.3 ± 0.2	15 ± 10
L	12	75 ± 3	2.4 ± 0.1	0.48 ± 0.01	0.3 ± 0.1	-	-	-
M	12	221 ± 3	2.7 ± 0.1	0.53 ± 0.01	0.6 ± 0.2	1.4 ± 0.1	0.5 ± 0.2	7 ± 3
N	12	234 ± 3	1.2 ± 0.1	0.6 ± 0.01	0.6 ± 0.2	3 ± 0.1	1.0 ± 0.2	7 ± 2
O	12	246 ± 3	3.2 ± 0.1	0.6 ± 0.01	0.7 ± 0.2	2.8 ± 0.1	1.0 ± 0.2	18 ± 4

Table 2.2: Average short-circuiting parameter values for each studied cell. Mass values are shown for the second release in each cell (e.g., results in Fig. 2-11).

Parameter	Units	Cell 6	Cell 7	Cell 12
Cell width, B	m	213 ± 3	207 ± 3	254 ± 3
Cell flow rate, Q	L/s	100 ± 30	100 ± 30	100 ± 30
Dye travel length, L_{dye}	m	37 ± 5	38 ± 5	34 ± 5
Plug-flow velocity, u_{pf}	cm/s	0.1 ± 0.03	0.1 ± 0.03	0.08 ± 0.02
Plug-flow transit time, t_{pf}	hr	11 ± 4	11 ± 4	12 ± 4
Number of fast flowpaths, n_f	-	3	6	6
Total fast flowpath width, Σb_f	m	3 ± 1	11 ± 1	21 ± 1
Total flowpath flow rate, Σq_f	L/s	18 ± 2	45 ± 5	64 ± 13
Average fast velocity, U_f	cm/s	1.1 ± 0.1	0.9 ± 0.1	0.6 ± 0.1
Average slow velocity, U_s	cm/s	0.09 ± 0.03	0.06 ± 0.03	0.03 ± 0.02
Mass released, $M_{release}$	g	910 ± 10	870 ± 10	1110 ± 10
Mass recovered by $t_{pf}/2$, Σm_f	g	180 ± 80	260 ± 100	470 ± 70
$\Sigma b_f/B$	-	0.016 ± 0.004	0.05 ± 0.01	0.08 ± 0.01
$\Sigma q_f/Q$	-	0.2 ± 0.2	0.5 ± 0.2	0.7 ± 0.2
U_f/U_s	-	14 ± 3	15 ± 3	20 ± 3
U_f/u_{pf}	-	12 ± 3	9 ± 3	8 ± 3
$\Sigma m_f/M_{release}$	-	0.20 ± 0.09	0.30 ± 0.12	0.42± 0.06

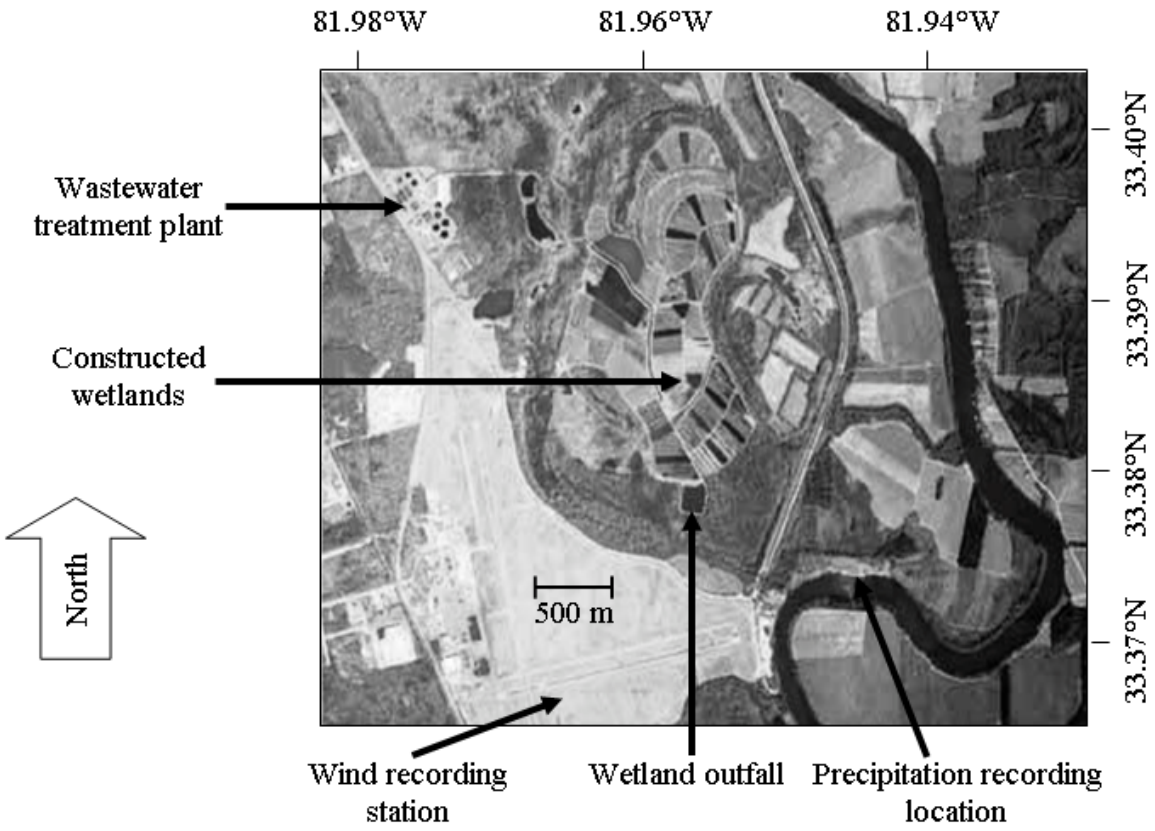

Figure 2-1: Aerial photograph of the Messerly constructed treatment wetland, including the WWTP that discharges into the wetland and the wetland outfall to a stream that discharges into the Savannah River. The locations of the USGS precipitation and NOAA wind and air temperature measurement stations are also shown. The thick arrow indicates the direction of true north. Infrared image taken 04 March 2006 by the USDA.

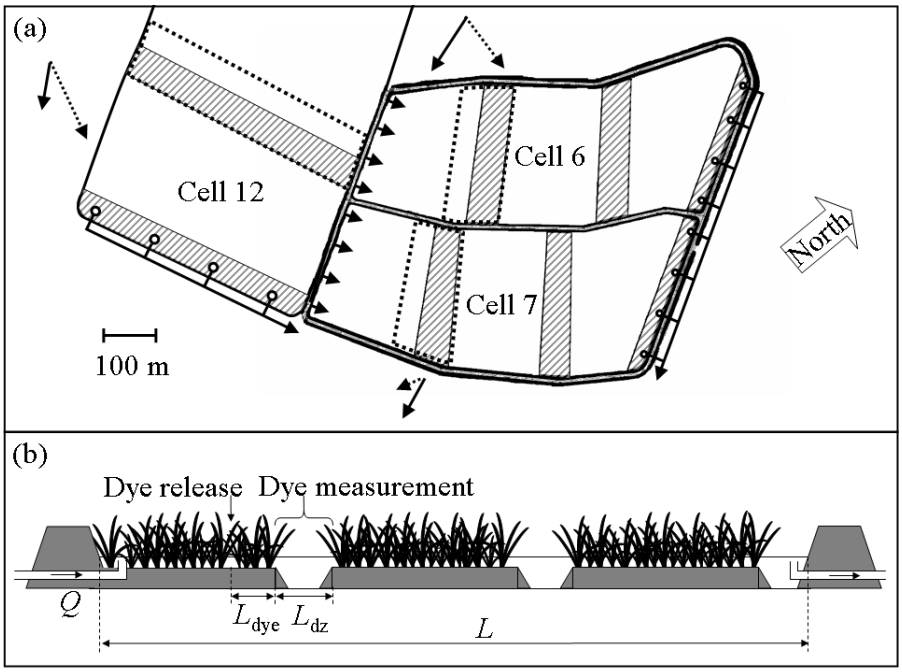

Figure 2-2: Studied cells within the Messerly wetland. (a) Plan view of the three studied cells. Deep zones are marked by hatching. Thick dotted lines surround the regions where dye studies were performed. The thin solid arrows indicate the average speed and direction of the wind over the full duration of the deep zone dye release experiments shown in Fig. 2-11; the thin dashed arrows indicate the average speed and direction of the wind during the first six hours after those releases. (b) Schematic side view of a longitudinal cross-section through one of the cells, highlighting the bathymetry of the deep zones and the location of dye injection and measurement.

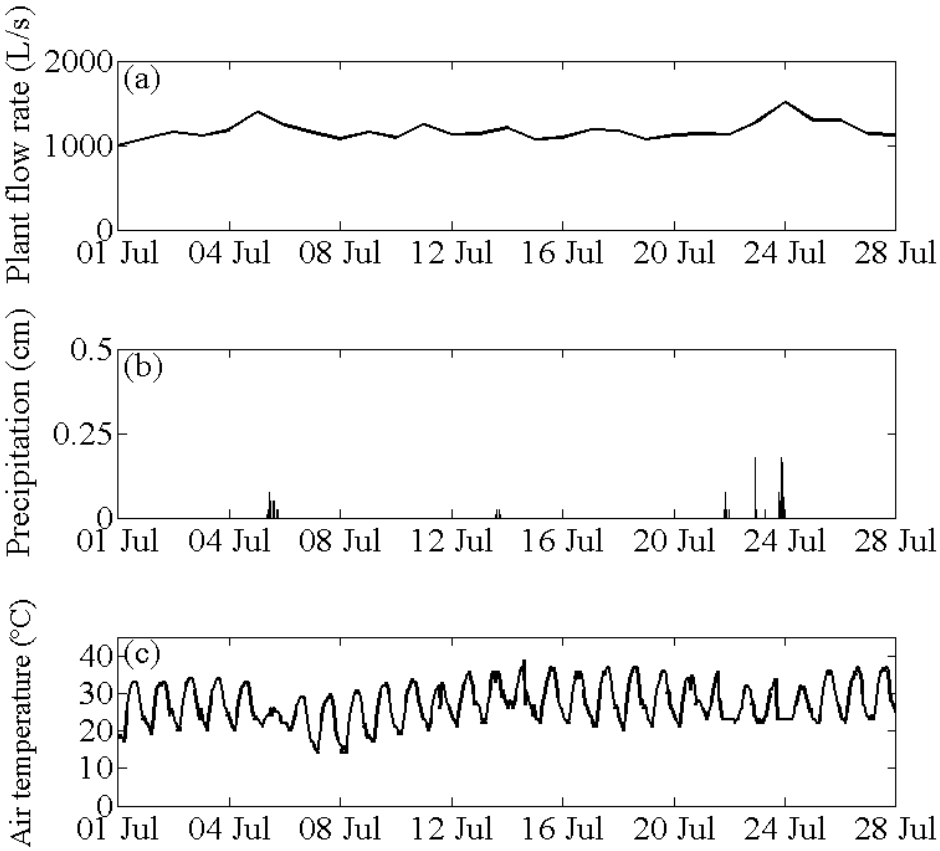

Figure 2-3: Time series of plant discharge flow rate, precipitation, and air temperature. (a) Plant flow rate discharging into the distribution pond upstream of all twelve wetland cells. (b) Precipitation recorded in 15-minute intervals at nearby USGS gaging station. In total, 0.53 cm of rain fell on July 6, 0.05 cm on July 14, 0.25 cm on July 22, 0.30 cm on July 23, and 1.35 cm on July 24. (c) Air temperature recorded at nearby NOAA station.

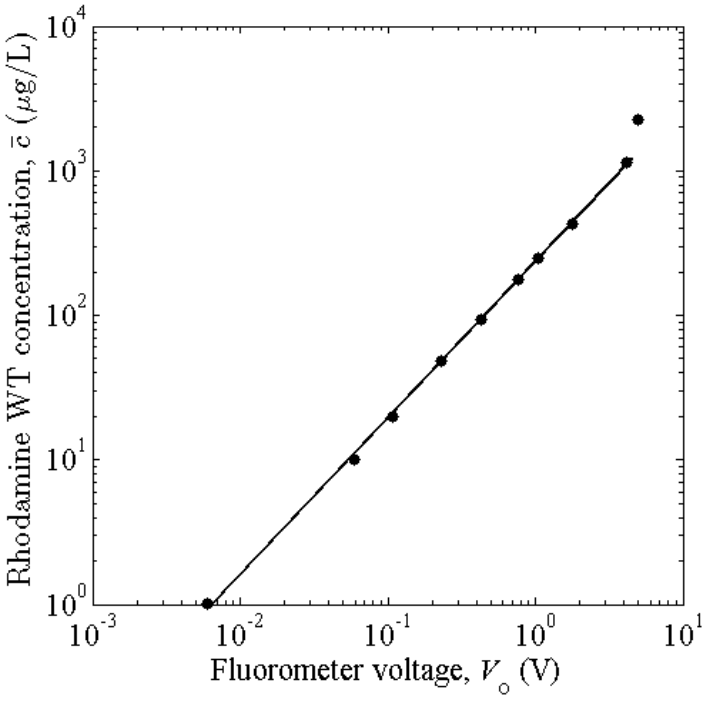

Figure 2-4: Rhodamine WT calibration curve. Comparison between Seapoint Sensors flow-through fluorometer voltage output and the concentration of Intracid Rhodamine WT. The equation of the least-squares line between output voltage $V_o < 4.55$ and time-average concentration is $\log_{10}(\bar{c}) = 1.08 \log_{10}(V_o) + 2.37$.

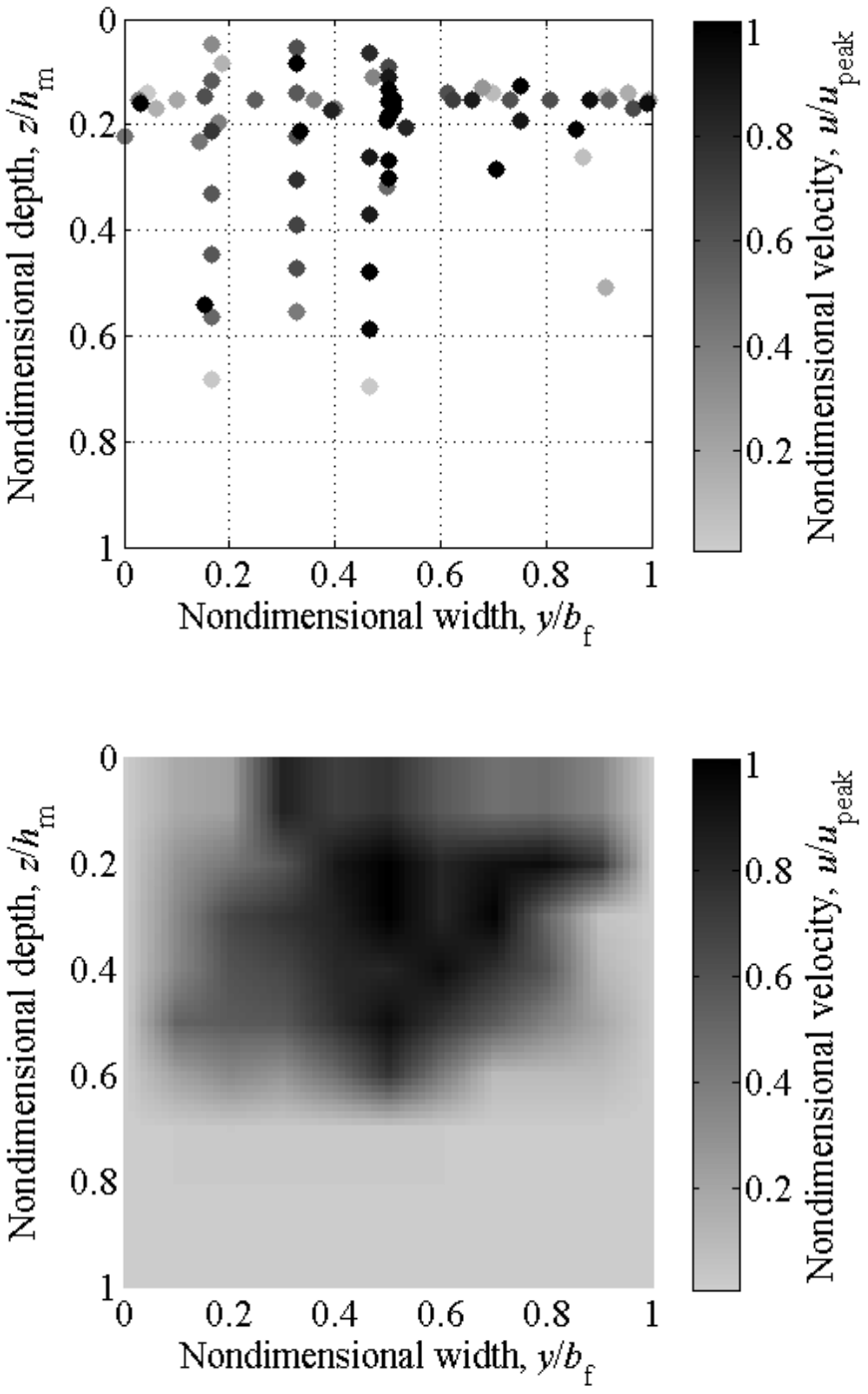

Figure 2-5: Composite velocity profile within fast flowpaths. (a) Velocity measurements within fast flowpaths normalized by the peak velocity, the flowpath width, and the full flowpath depth. (b) Interpolated composite velocity distribution.

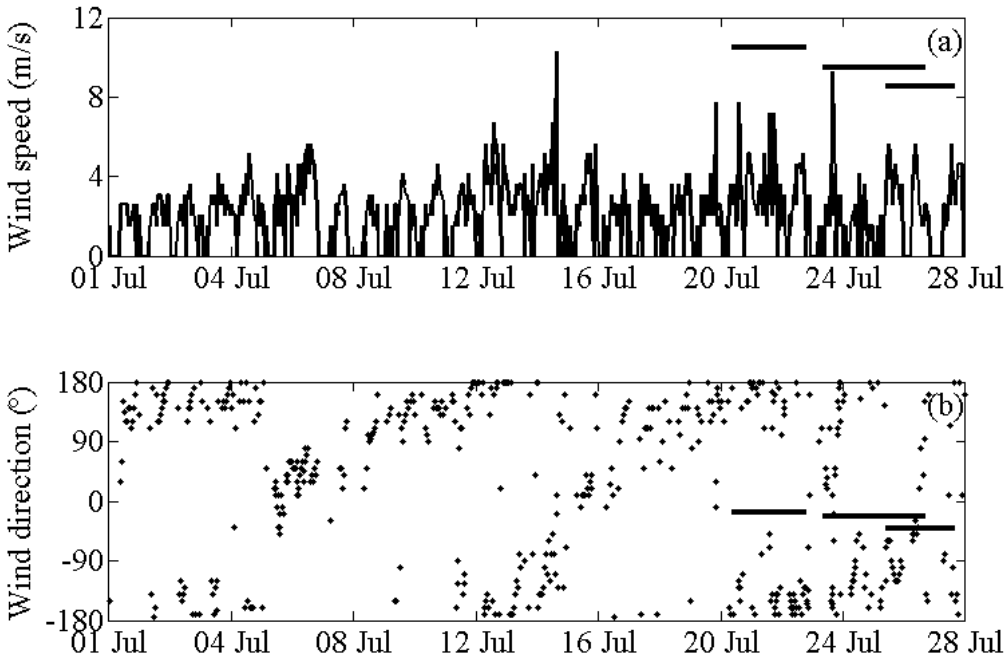

Figure 2-6: Time series of wind speed and direction. (a) Wind speed recorded at nearby NOAA station. Horizontal bars indicate the duration of the deep zone tracer experiments shown in Fig. 2-11. (b) Direction from which wind is blowing in degrees from true north recorded at nearby NOAA station. Horizontal bars indicate the average wind direction over the duration of the deep zone tracer experiments.

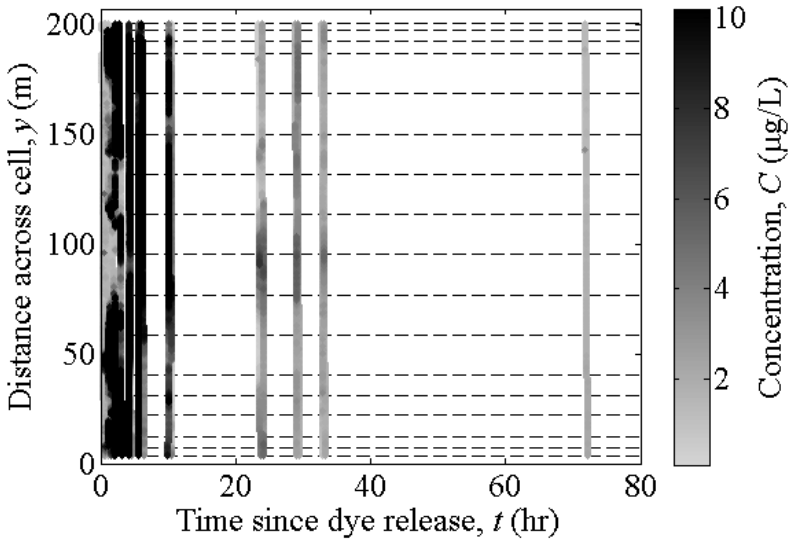

Figure 2-7: Breakthrough curve of dye exiting a 38-m-long swath of continuously vegetated marsh in Cell 7. Each point measurement is colored to represent measured Rhodamine WT concentration. Horizontal dashed lines mark the position of reference stakes on the bank. The release was on 19 July and the expected time to exit is $t_{pf} = 11 \pm 4$ hr.

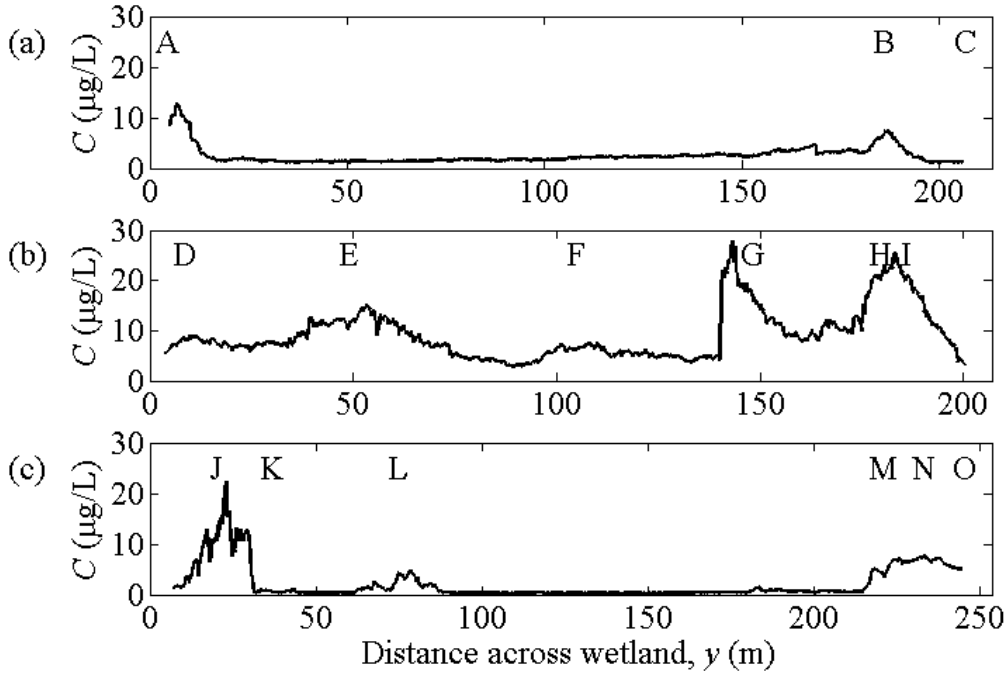

Figure 2-8: Concentration measured exiting a 34- to 38-m-long swath of continuously vegetated marsh in three wetland cells: (a) Cell 6 on 12 July, (b) Cell 7 on 19 July, and (c) Cell 12 on 18 July. The plotted concentration is the average recorded at each lateral position before $t_{pf}/2$. Each concentration peak is marked with a letter and described in more detail in Table 2.1. Flowpath C was located too close to the bank to identify using the boat-mounted fluorometer but was identified on foot when performing velocity measurements.

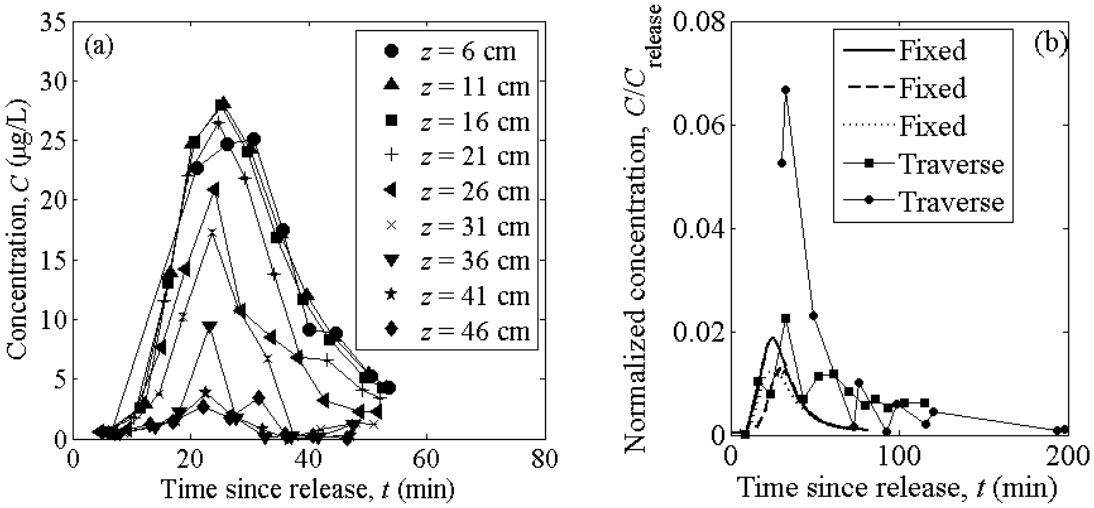

Figure 2-9: Records of concentration exiting a fast flowpath (Path A in Table 2.1). (a) Detailed measurements of dye concentration at different depths a few meters downstream of the flowpath mouth, where the local water depth was 52 cm and z indicates depth below surface. (b) Records of concentration exiting from Path A, normalized by the mixed concentration just after release. In the "fixed" observations, the recording fluorometer was placed at a stationary location in the middle of Path A and dye was injected at a single location directly upstream. In the "traverse" observations, the fluorometer was located on a boat that was traversing the wetland and dye was injected across the width of the cell. The expected plug flow time of transit is $t_{pf} = 630 \pm 210$ min.

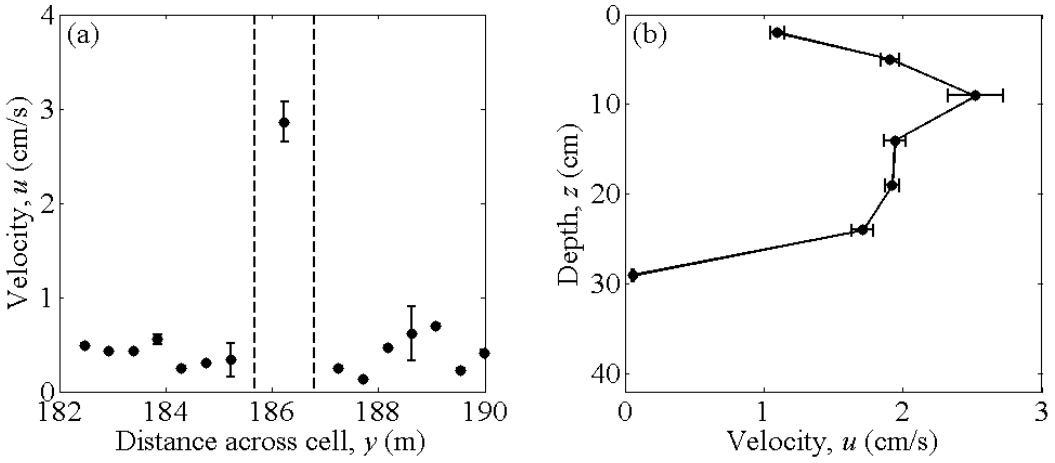

Figure 2-10: Sample point measurements of water velocities exiting dense vegetation. (a) Transect across the mouth of a fast flowpath (Path B). Vertical dashed lines indicate the edges of the flowpath, which had a width $b_f = 1.1$ m. From continuity, the expected slow-flow zone velocity was $U_s \approx 0.1$ cm/s. Vertical bars indicate the standard error of the mean velocity at each lateral position. (b) Vertical transect at the midline of a fast flowpath (Path I). The marsh water depth was $h_m = 42$ cm. Horizontal bars indicate the standard error of the mean velocity at each vertical position.

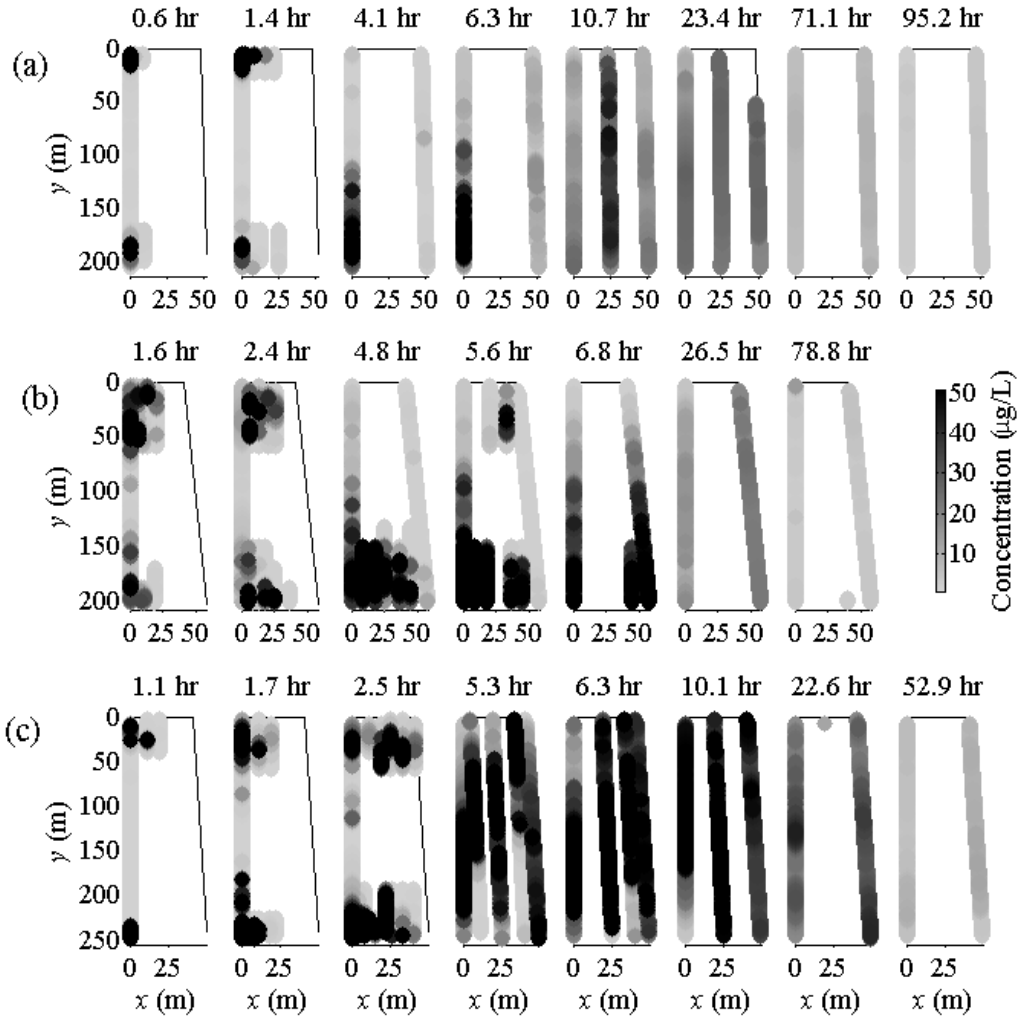

Figure 2-11: Depth-averaged dye concentrations at various times after release within an open-water deep zone in (a) Cell 6, (b) Cell 7, and (c) Cell 12.

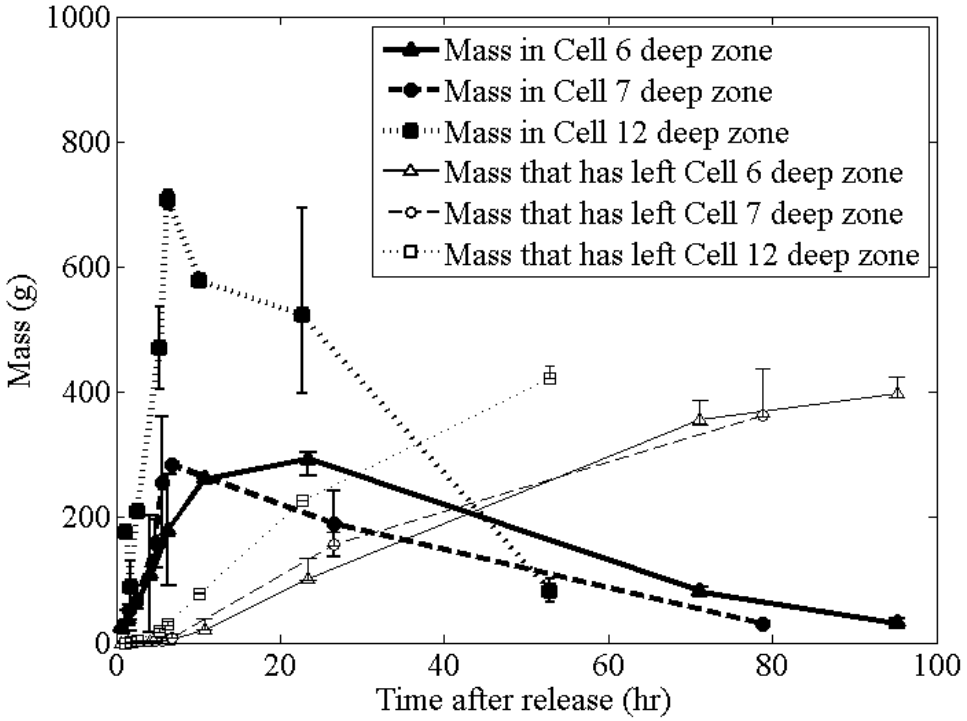

Figure 2-12: Estimates of mass within the deep zone for the three studies shown in Fig. 2-11. Estimates of the deep zone mass are obtained by interpolating the concentration measurements shown in Fig. 2-14 to completely fill the deep zone. Estimates of the mass leaving the deep zone are obtained from the average concentration observed at the downstream edge of the deep zone. Vertical bars indicate uncertainty based on different methods of data interpolation.

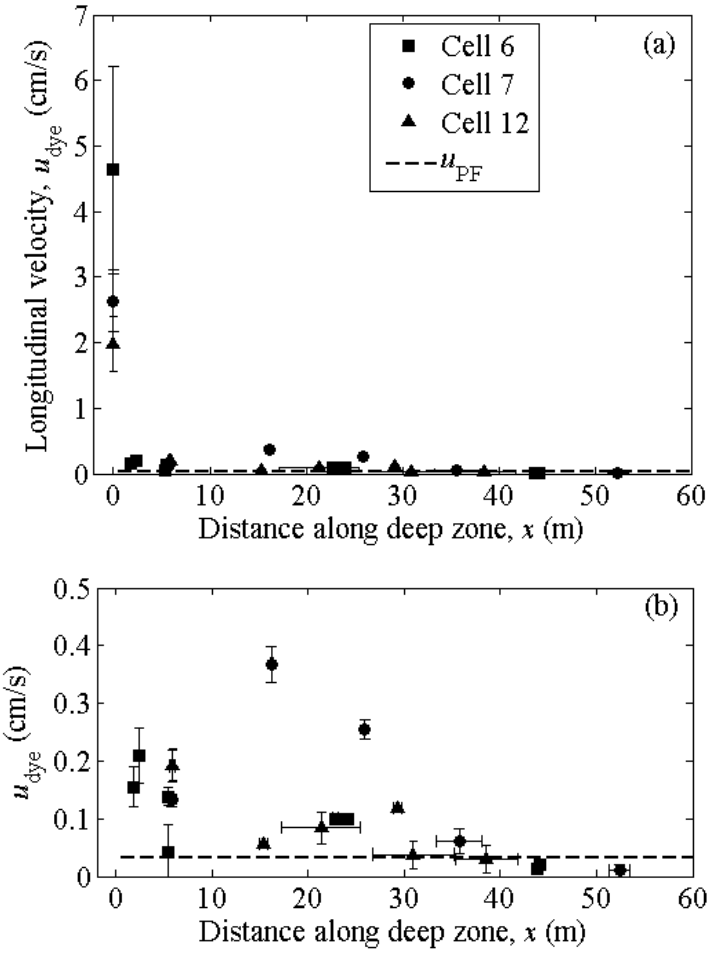

Figure 2-13: Estimated velocity of the front of the tracer cloud as a function of distance into the deep zone for the tracer releases shown in Fig. 2-11. Horizontal and vertical bars indicate the uncertainty associated with each measurement. (a) The velocity reported at a longitudinal position $x = 0$ is the average peak velocity measured exiting from fast flowpaths (Table 2.1). (b) Close up of the dye transport velocity measured within the deep zone.

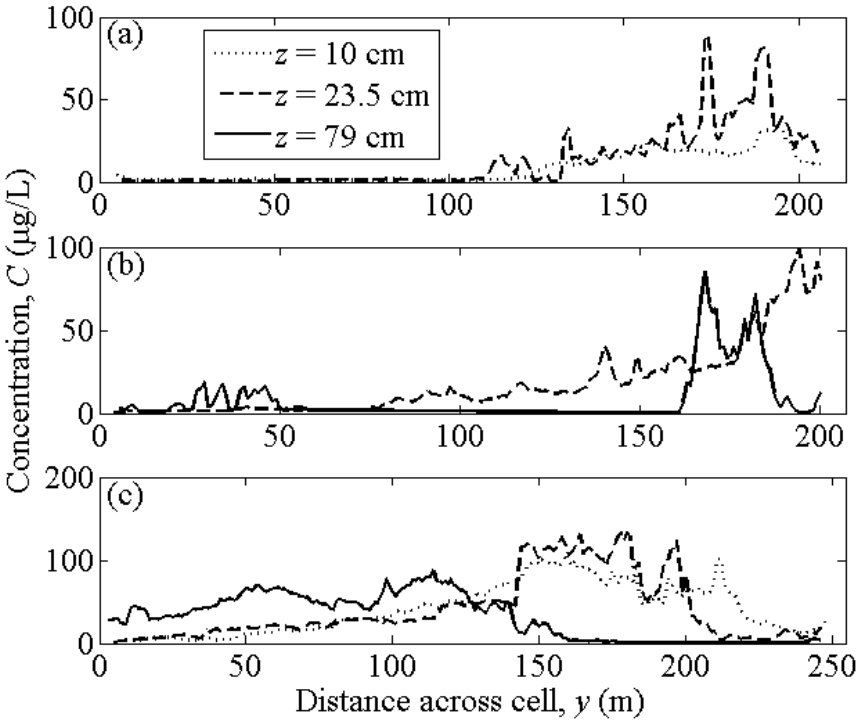

Figure 2-14: Dye concentrations at different depths for the three dye releases shown in Fig. 2-11: (a) Cell 6 6.3 hr after tracer release with the wind parallel to flow, (b) Cell 7 5.6 hr after release with the wind parallel to flow, and (c) Cell 12 5.3 hr after release with the wind perpendicular to flow.

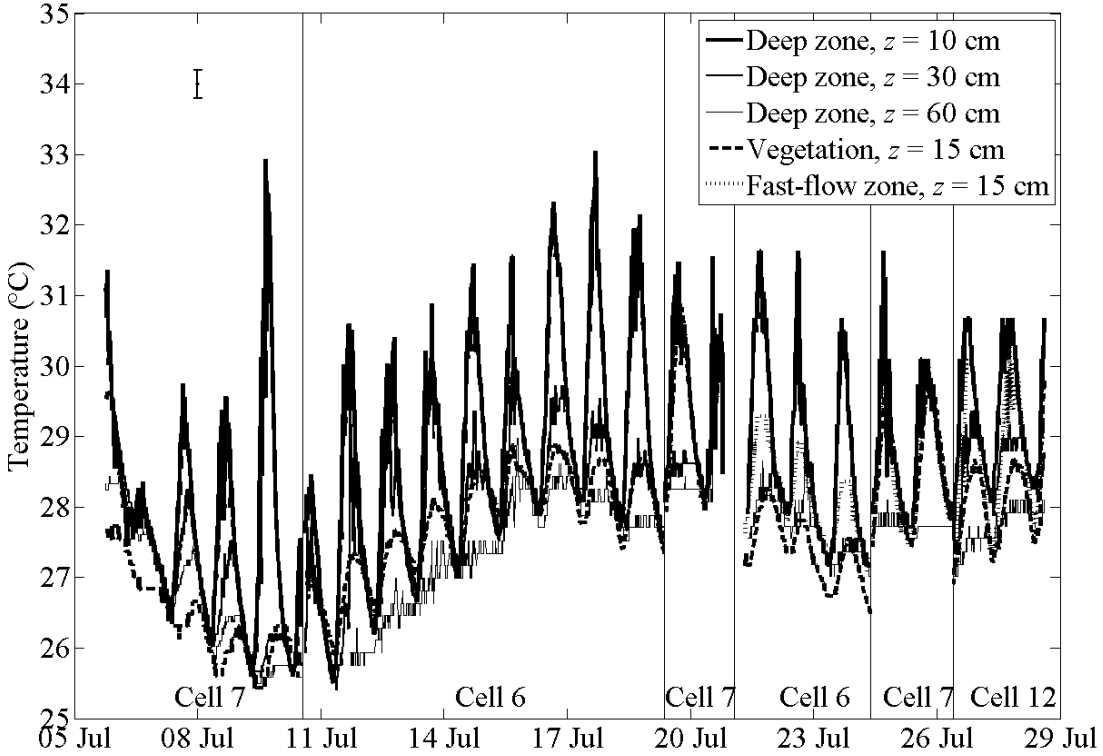

Figure 2-15: Temperature recorded by submerged loggers. Vertical lines separate deployments in different wetland cells. Within each cell, loggers were placed in up to five different locations: three different depths within the open deep zone, between 10- and 20-cm deep within a densely vegetated region, and 15-cm deep within a fast flowpath. The vertical line in the upper left portion of the plot indicates the average expected uncertainty for all lines.

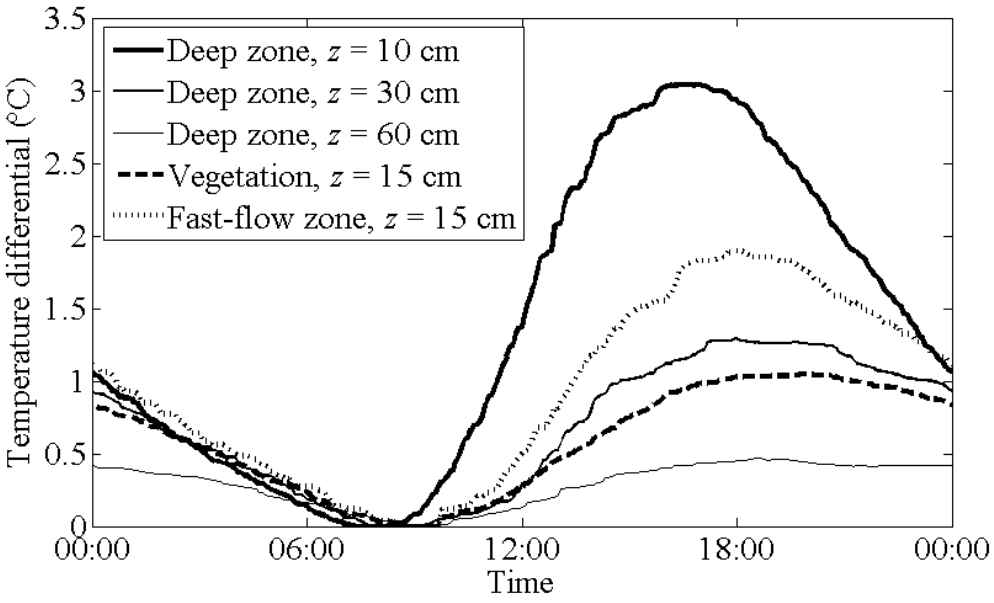

Figure 2-16: Composite temperature record from temperature logger data shown in Fig. 2-15. Results are plotted as deviations from the nightly minimum temperature.

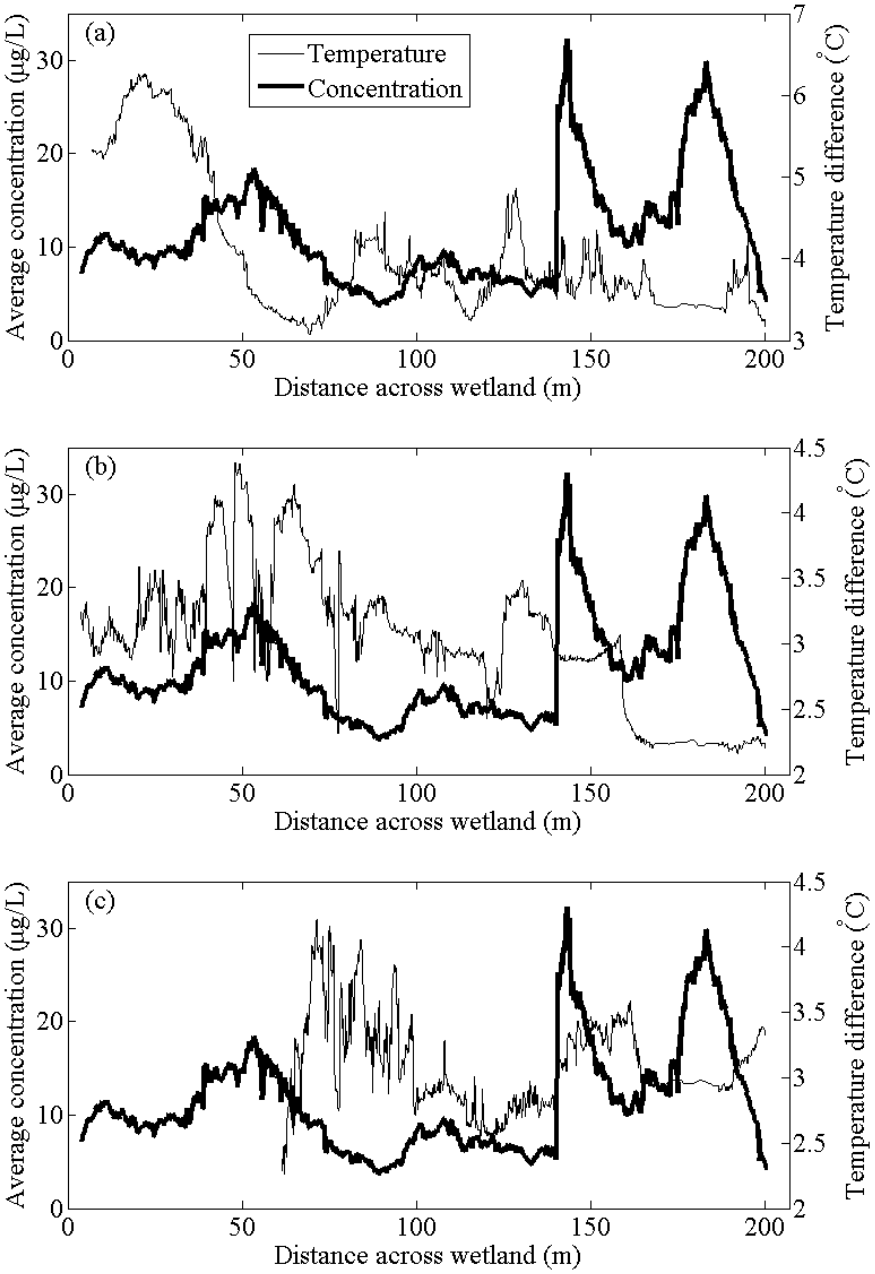

Figure 2-17: Comparison between lateral locations that contribute short-circuiting flow and water temperature entering the deep zone. The thick line shows the average dye concentration measured exiting a 38-m-long swath of vegetation before $t_{pf}/2$ in Cell 7 on 19 July (Fig 2-8b). The thin lines show the difference between 30-cm-deep CTD measurements of temperature taken during boat transects at the downstream edge of the vegetation and a simultaneous stationary logger measurement at the same depth (z = 30 cm line in Fig. 2-15) at (a) 2:30 pm, (b) 3:30 pm, and 5:00 pm on 24 July.

Chapter 3

Laboratory physical modeling of flow within a deep zone in a wetland downstream of a fast flowpath

This chapter describes a laboratory investigation of flow patterns created by a short-circuiting flowpath of narrow width entering an unvegetated deep zone within a wetland. The fast flowpath creates a jet entering the deep zone, which, as expected from previous studies of shallow jet behavior, entrains co-flowing fluid. Due to the inclusion of drag within the deep zone, however, the excess momentum within the jet rapidly decays to background (plug-flow) levels. Downstream of the point of excess momentum dissipation, jet entrainment and lateral spreading cease within the quiescent laboratory flume. The presence of a fast flowpath through the downstream marsh region does not affect the rate of jet spreading or the decay of centerline velocity.

3.1 Overview of turbulent jets and the integral jet equations

Consider a single fast flowpath with velocity U_f and concentration c_o continuously exiting from a marsh region where water on either side is traveling at speed U_s with concentration $c_{e,s} = 0$ (no background concentration; Fig. 3-1). The width of the fast flowpath is b_f and its flow rate is q_f. The total domain has width B_f, which is the region of fluid within the deep zone that is closer to this flowpath than any other flowpath. For a narrow wetland containing a single fast flowpath, $B_f = B$, where B is the total wetland width; in a wide wetland, in which n_f parallel fast flowpaths are present and are evenly spaced, the wetland region associated with each flowpath $B_f = B/n_f$. The marsh section has plug flow velocity $u_{pf,m} = Q_f/B_f h_m(1-\phi)$, where Q_f is the flow rate through this marsh section, h_m the marsh water depth, and ϕ the volume fraction of vegetation within the marsh. The velocity of the co-flow beside the jet is denoted by u_c, which is initially equal to the slow-zone flow velocity $U_s = (u_{pf,m}B_f - U_f b_f)/(B_f - b_f)$.

The fast flow has initial momentum greater than that of the surrounding, slow-moving fluid and forms a jet. When the jet Reynolds number $Re_j = \frac{U_f b_f}{\nu} > 2000$, where ν is the fluid kinematic viscosity, the flow is turbulent (Lee and Chu, 2003, p. 21). The turbulent eddies that develop at the edge of the jet entrain co-flowing fluid with less momentum into the jet, resulting in a decrease in jet velocity over distance. Simultaneously, the volume flux q_j within the jet increases due to the entrainment, which results in the dilution of the jet water. Note that large turbulent eddies are primarily responsible for entrainment, while smaller-scale eddies mix the fluid within the jet, so entrainment is a necessary precursor to but not sufficient for complete mixing (Giger et al., 1991). Far downstream, once the jet momentum is completely dissipated, all fluid has the same velocity $u_{pf} = Q_f/B_f h(1-\phi)$, where h is the local water depth and ϕ is the local volume fraction of flow obstructions, assuming that vertical recirculation is not present so the flow fills the depth.

The origin of the coordinate system is located at the center of the jet when it first

encounters the deep zone. Let x represent the longitudinal direction downstream of where the jet first enters the deep zone. Let y represent the transverse distance from the jet centerline in an unconfined system or, in this study, the transverse distance from the flume wall. Finally, let z represent the vertical distance below the surface. The centerline of the jet, located at $b_m(x)$, is the lateral location of the maximum time-averaged and depth-averaged velocity, called the centerline velocity $u_m(x)$; its initial value is $u_{m,o}$. The jet half-width $b_u(x)$ is defined as the distance between the jet centerline and the lateral location where the depth-averaged longitudinal velocity $\langle\bar{u}\rangle(x, y) = \frac{1}{2}u_m(x)$, where the overbar indicates an average over turbulent fluctuations and angled brackets indicate a depth-averaged quantity. The initial jet half-width is $b_{u,o}$. In an unconfined system, the initial jet half-width is half of the flowpath width ($b_{u,o} \approx \frac{1}{2}b_f$); in a system discharging along a wall, the initial width is approximately the flowpath width ($b_{u,o} \approx b_f$).

It is here assumed that there are no fluid density differences within the wetland (i.e., water density ρ_w is constant). In a fresh-water wetland, differential density results from temperature differences, which may be present during certain times of the day (Sec. 2.3.3); this condition will be considered in Chap. 5. It is also assumed that the scale of flow is small enough that Coriolis effects are negligible, that no wind is present, that all tracers are conservative, and that depth varies in the longitudinal direction only.

As explained in App. A (Sec. A.3), it is convenient to consider the evolution of jet volumetric flux q_j, jet excess momentum flux m, and jet mass flux J by integrating the Reynolds-averaged governing equations within the jet region over depth and width (i.e., across the y and z coordinates). The equations are integrated over the full water depth $h = h(x)$ and across the full jet width from $y = 0$ (the flume wall or the centerline symmetry plane) to a location outside the jet, denoted by b_j, where $\langle\bar{u}\rangle = u_c$ and the jet concentration $\langle\bar{c}\rangle = c_{e,s} = 0$. Note that this process averages over instantaneous temporal and spatial fluctuations, which can be significant during the initial region of jet development (List and Dugan, 1994). Following previous experimental work, turbulent fluctuations are assumed to be negligible (Lee and Chu,

2003; Gaskin et al., 2004). The entrainment hypothesis hold that the entrainment velocity $v_e = \frac{1}{h}\frac{\mathrm{d}q_j}{\mathrm{d}x}$ at the edge of the jet is proportional to the jet characteristic velocity, here taken to be the centerline excess velocity (Morton et al., 1956). Under this assumption:

$$v_e = \alpha_e(u_m - u_c) \tag{3.1}$$

where α_e is the entrainment coefficient, which has been assumed constant when drag is absent. Therefore, the jet is expected to entrain fluid as long as its velocity is elevated over that of the background co-flow velocity.

The integral quantities of a jet are the volumetric flow rate q_j:

$$q_j = \int_0^{b_j} h\langle\bar{u}\rangle \, \mathrm{d}y \tag{3.2}$$

the excess momentum flux:

$$m = \int_0^{b_j} \rho_w h\langle\bar{u}\rangle(\langle\bar{u}\rangle - u_c) \, \mathrm{d}y \tag{3.3}$$

and the mass flux:

$$J = \int_0^{b_j} h\langle\bar{c}\rangle\langle\bar{u}\rangle \, \mathrm{d}y \tag{3.4}$$

where $\langle\bar{c}\rangle$ is the time-averaged and depth-averaged concentration. Following Lee and Chu (2003, pp. 186-187), the integral forms of the equations that describe the development of jet velocity in the presence of co-flow are the continuity equation:

$$\frac{\mathrm{d}q_j}{\mathrm{d}x} = \frac{\mathrm{d}}{\mathrm{d}x}\int_0^{b_j} h\langle\bar{u}\rangle \, \mathrm{d}y = \alpha_e h(u_m - u_c) \tag{3.5}$$

and the depth-averaged x-momentum equation:

$$\frac{\mathrm{d}m}{\mathrm{d}x} = \frac{\mathrm{d}}{\mathrm{d}x}\int_0^{b_j} \rho_w h\langle\bar{u}\rangle(\langle\bar{u}\rangle - u_c) \, \mathrm{d}y = -\langle F_{d,x}\rangle \tag{3.6}$$

where $\langle F_{d,x}\rangle$ is the spatially and temporally averaged longitudinal drag; the negative sign indicates that it acts to decrease jet momentum. The initial excess momentum

flux m_o is an important physical quantity controlling the behavior of a plane jet that effectively replaces individual values of b_f and U_f. That is, for a given value of m_o, the same normalized velocity profile within the jet will be obtained for different combinations of b_f and U_f (Rajaratnam, 1976). Finally, the expression for conservation of scalar mass is:

$$\frac{\mathrm{d}J}{\mathrm{d}x} = \frac{\mathrm{d}}{\mathrm{d}x}\int_0^{b_j} h\langle\bar{c}\rangle\langle\bar{u}\rangle \; \mathrm{d}y = 0 \tag{3.7}$$

which indicates that jet mass flux J is conserved.

3.2 Expectations for jet development

A turbulent jet issuing into a quiescent fluid creates a laminar shear layer at its edge. The shear layer contains an inflection point, which makes the layer unstable, and vortices are rapidly (by $x \approx b_f$) initiated that create mixing between the jet fluid and the ambient fluid (List, 1982). After the mixing has started, but before some small distance $\hat{x}$ from the entrance, the mixing has not penetrated fully to the center of the jet, leaving a potential core at the center with velocity U_f. At a length $\hat{x}$ from the entrance the shear layers on each edge of the jet have grown inward enough to erase the potential core, and the jet has reached a fully developed state. For $x > \hat{x}$, the centerline velocity u_m begins to decrease with distance downstream, and the jet is called fully developed. In general, $\hat{x} \leq 5b_f$ (Rajaratnam, 1976), so for $x \gg 5b_f$ this region constitutes only a small portion of the jet and can be neglected.

An important feature of the fully developed region of many jets is that they have self-similar velocity profiles in the absence of co-flow. Self-similarity means that, at any longitudinal position $x > \hat{x}$, the transverse velocity profile $\langle\bar{u}\rangle(x, y)$ normalized by the centerline velocity $u_m(x)$ has a constant shape when plotted against the transverse coordinate y normalized by the jet half-width b_u. In other words, if $\eta_u = y/b_u$, then $\langle\bar{u}\rangle/u_m$ is only a function of η_u:

$$\frac{\langle\bar{u}\rangle}{u_m} = f_u(\eta_u) = f_u\left(\frac{y}{b_u}\right) \tag{3.8}$$

Under conditions of self-similarity, the shape of the jet at any point downstream can be fully described by the length scale $b_u(x)$, the velocity scale $u_m(x)$, and the shape $f_u(x)$. Similarity also implies a constant normalized turbulence intensity distribution for $x > \hat{x}$ (Rajaratnam, 1976). Observations confirm that the approach to self-similarity is independent of the initial velocity distribution at the inlet (Kundu and Cohen, 2002, p. 351). Although the final stages of jet dilution are accomplished by small-scale eddies that create turbulent diffusion, jet entrainment is dominated by mixing by the large, dominant eddies that scale with the width of the jet (Lee and Chu, 2003). Therefore, non-dimensional jet spreading is independent of the size of the jet.

Within the fully developed region of a jet without co-flow, it is expected that concentration profiles will also exhibit self-similarity. The nondimensional concentration is assumed to adopt a nondimensional curve when normalized by the concentration half-width b_C, which is the location where $\langle\bar{c}\rangle$ equals half its centerline value c_m. The transverse coordinate is nondimensionalized as $\eta_C = y/b_C$, and the self-similar concentration distribution function f_C can be written as:

$$\frac{\langle\bar{c}\rangle}{c_m} = f_C(\eta_C) = f_C\left(\frac{y}{b_C}\right) \tag{3.9}$$

where f_C is expected to be constant with distance downstream.

3.2.1 Plane jet over a flat bed in the absence of co-flow and drag

Previous work has shown how jet parameters change with distance downstream within the fully developed region of a planar jet over a flat bed [i.e., $h \neq h(x)$] in the absence of drag; this type of jet is called a free jet. The expression for the velocity profile (Eq. 3.8) can be substituted into the excess volume flux equation (Eq. 3.5):

$$\frac{\mathrm{d}q_j}{\mathrm{d}x} = \frac{\mathrm{d}}{\mathrm{d}x}\left(u_m b_u h \int_0^{b_j} f_u(\eta_u)\ \mathrm{d}\eta_u\right) = \alpha_e h(u_m - u_c) \tag{3.10}$$

and the excess momentum flux equation (Eq. 3.6):

$$\frac{\mathrm{d}m}{\mathrm{d}x} = \frac{\mathrm{d}}{\mathrm{d}x}\left[\rho_w \int_0^{b_j} h u_m (u_m - u_c) b_u \; f_u^2(\eta_u) \; \mathrm{d}\eta_u\right] = 0 \tag{3.11}$$

Within the self-similar region of jet development ($x \gg \hat{x}$), the integrals of the velocity distribution $I_u = \int_0^{b_j} f_u(\eta_u) \; \mathrm{d}\eta_u$ and $I_{uu} = \int_0^{b_j} f_u^2(\eta_u) \; \mathrm{d}\eta_u$ depend on the self-similar velocity distribution only and not x, and the parameters b_u and u_m are functions of x only. Therefore,

$$\frac{\frac{\mathrm{d}}{\mathrm{d}x}(u_m b_u)}{(u_m - u_c)} = \frac{\alpha_e}{\int_0^{b_j} f_u(\eta_u) \; \mathrm{d}\eta_u} \tag{3.12}$$

$$\frac{\mathrm{d}}{\mathrm{d}x}\left[u_m (u_m - u_c) b_u\right] = 0 \tag{3.13}$$

Eq. 3.12 and Eq. 3.13 can be solved assuming simple forms for the velocity $u_m(x)$ and the jet width $b_u(x)$:

$$u_m \propto x^p \tag{3.14}$$

$$b_u \propto x^r \tag{3.15}$$

and substituting them into Eq. 3.12 noting that, because the right-hand side of the equation is constant with x, the left-hand side must be as well. That is, if h is constant and $u_c = 0$, then for $x \gg \hat{x}$:

$$\frac{\frac{\mathrm{d}}{\mathrm{d}x}(u_m b_u)}{u_m} \propto \frac{\frac{\mathrm{d}}{\mathrm{d}x}(x^p x^r)}{x^p} = x^{p+r-1} x^{-p} \propto x^0 \tag{3.16}$$

Thus, $p = 1$ and b_u increases linearly with x. In fact, this latter condition is a direct result of the entrainment hypothesis and is a sufficient criterion for a similarity solution to exist (Stolzenbach and Harleman, 1971). Substituting Eqs. 3.14 and 3.15 into Eq. 3.11, it is clear that $r + 2p = 0$, so the exponent $p = -1/2$. In fact, the condition for self-preservation in a free planar jet is $u_m \propto x^{-1/2}$ (Bradbury, 1965). Finally, substituting Eqs. 3.8 and 3.9 into Eq. 3.7 yields an expression for the mass

flux of a dissolved scalar:

$$\frac{\mathrm{d}J}{\mathrm{d}x} = \frac{\mathrm{d}}{\mathrm{d}x}\left[u_m b_u c_m b_C h \int_0^\infty f_C\left(\frac{y}{b_C}\right)\ f_u\left(\frac{y}{b_u}\right)\ \mathrm{d}y\right] = 0 \tag{3.17}$$

so:

$$\frac{\mathrm{d}}{\mathrm{d}x}(u_m b_u c_m b_C h) = 0 \tag{3.18}$$

Experiments have shown that b_C grows linearly with x just like b_u does, and also that c_m and u_m decay in proportion to $x^{-1/2}$ (Hinze, 1975).

The full equations, including fitting coefficients, take the form:

$$\frac{b_u}{b_{u,o}} = \beta_u\left(\frac{x}{b_{u,o}} - \frac{x_{ub}}{b_{u,o}}\right) \tag{3.19}$$

$$\left(\frac{U_f}{u_m}\right)^2 = \gamma_u\left(\frac{x}{b_{u,o}} - \frac{x_u}{b_{u,o}}\right) \tag{3.20}$$

$$\frac{b_C}{b_{u,o}} = \beta_C\left(\frac{x}{b_{u,o}} - \frac{x_{cb}}{b_{u,o}}\right) \tag{3.21}$$

$$\left(\frac{c_o}{c_m}\right)^2 = \gamma_C\left(\frac{x}{b_{u,o}} - \frac{x_{Cu}}{b_{u,o}}\right) \tag{3.22}$$

where the scaling velocity $U_f = q_f/h_m b_f$ and the virtual origins $x_{ub} = b_{u,o}/\beta_u$ and $x_{cb} = b_{u,o}/\gamma_C$ are located at $x < 0$, thereby allowing the jet to have a nonzero width at $x = 0$. In general, $x_u \ll \hat{x}$ so can be neglected within the fully developed region of the jet (Fischer et al., 1979, p. 328). The coefficient $\beta_u = b_u/x$ is the rate of spreading in jet velocity half-width b_u, the coefficient $\beta_C = b_C/x$ is the rate of spreading in jet concentration half-width, the coefficient γ_u is the rate of velocity decay (cf. Figure 3-1), and the coefficient γ_C is the rate of decay in maximum measured concentration. In general, a scalar within the jet spreads faster than its velocity signature so $b_C(x) > b_u(x)$ at any position x, which implies that the turbulent Schmidt number is less than one.

To provide a complete prediction of the jet velocity and concentration distribution, it is necessary to determine $\hat{x}$, f_u (η_u), β_u, γ_u, γ_C, β_C, x_u, x_{ub}, x_{Cu}, and x_{cb} plus the initial values U_f and b_f. These constants can be obtained experimentally, and the

results allow the calculation of the volumetric, momentum, and mass flux for a self-similar jet. Experimental results have shown that, if the initial jet Reynolds number $Re_{j,o} = U_f b_f/\nu > 10^4$, the coefficients of proportionality are not a function of $Re_{j,o}$ (Rajaratnam, 1976, p. 248ff).

Detailed experiments have been performed to characterize the spreading and dissipation within planar jets in the absence of drag. For example, Bradbury (1965) used Pitot and static tubes and laser Doppler velocimetry (LDV) to take detailed measurements of pressure and velocity distributions of the flow field in a plane jet discharging into a small co-flow; the study was performed in air. Bashir and Uberoi (1975) examined the velocity and temperature distribution within a two-dimensional heated air jet; temperature differences were too small to affect fluid density.

In the flow development region of a planar jet ($x < \hat{x}$), it can be shown from comparison with free plane shear layers that $\frac{q_j}{q_f} = 1 + 0.035\frac{x}{b_{u,o}}$ and that the entrainment velocity $v_e = 0.035U_f$ (Rajaratnam, 1976). By the end of the flow development region, $q_j = 1.4q_f$ (Albertson et al., 1950).

Within the fully developed region of a planar jet, the non-dimensional velocity shape function $f_u(\eta_u)$ can be described using the Tollmien series solution, which is based on Prandtl's mixing length hypothesis, or a Goertler-type solution based on Prandtl's eddy-viscosity model (Rajaratnam, 1976). Rajaratnam (1976) compares these two solutions to experimental results for a circular jet and finds that they both agree reasonably well with experimental data. To first approximation, it is also possible to represent the velocity distribution with a Gaussian curve (List, 1982), which is known as the Reichart solution:

$$\frac{\langle \bar{u} \rangle}{u_m} = \exp(-\xi_u \eta_u^2) \tag{3.23}$$

where ξ_u is a constant that, from theoretical considerations, equals $-\ln(0.5) = 0.693$ (Chu and Baines, 1989). When $\xi_u = 0.693$, the integrals of $f_u(\eta_u)$ are constant and evaluate to $I_u = \int_{-\infty}^{\infty} f_u^2(\eta_u)\, \mathrm{d}\eta_u = 2.15$ and $I_{uu} = \int_{-\infty}^{\infty} f_u^2(\eta_u)\, \mathrm{d}\eta_u = 1.49$ (Giger et al., 1991). Free planar jet studies also show that the concentration profile follows

a Gaussian distribution (Hinze, 1975, pp. 531ff.):

$$\frac{\langle \bar{c} \rangle}{c_m} = \exp(-\xi_C \eta_C^2) \tag{3.24}$$

Although instantaneous concentration profiles within a turbulent jet reflect the presence of turbulent eddies, when time-averaged, the instantaneous concentration profiles collapse to a regular smooth Gaussian profile in the cross-section (Chu et al., 1999).

Rajaratnam (1976) reviewed several previous experimental studies of free planar jets to find that $\gamma_u = 3.1$–3.7 and $\beta_u = 0.097$–$0.114 \approx 0.1$. A literature review by Giger et al. (1991) found that the average value for the jet spreading coefficient $\beta_u = 0.106$. Jirka (2006) suggests that $\beta_u = 0.14$ and $\gamma_u = 3.36$. With these values for γ_u, the centerline excess velocity decays to 5% of its initial value approximately $x_{diss} = 100 b_f$ downstream (Rajaratnam, 1984; Jirka, 2004). Jirka (1994) reports that $\beta_C = 0.135$. Within a free jet, one set of empirical results suggests that $\alpha_e = 0.053$ (Rajaratnam, 1976); a review of multiple studies suggests that $\alpha_e = 0.057$ (Giger et al., 1991). Experimental values for these constants can be evaluated to determine whether momentum has been conserved far downstream of the jet entrance. For example, a review of twenty seven studies showed no net momentum loss (Giger et al., 1991). Scalars typically mix more rapidly than turbulence within a plane jet. For example, Jirka (1994) recommends a value of $\beta_C = 0.135$, which is higher than the typical value for velocity spreading β_u. Table 3.1 presents the constants obtained from these studies and other previous laboratory experiments of jet evolution.

3.2.2 Plane jet with co-flow over a flat bed in the absence of drag

Experimental observations confirm that the profiles within the fully developed region of a strong jet in weak co-flow [$(u_m - u_c)/u_c \gg 1$] can be approximated as self-similar: when the excess velocity $\langle \bar{u} \rangle - u_c$ is normalized by the centerline excess velocity $u_m - u_c$, it is a function only of dimensionless lateral distance $\eta_u = y/b_u$ (Hinze 1975, pp. 521–525; Rajaratnam 1976, p. 63). In addition, similarity analysis on the equations of

motion shows that it is expected that $(u_m - u_c) \propto x^{-1/2}$ and $b_u \propto x$ (Rajaratnam, 1976, pp. 67-68). The constants associated with jet shape and entrainment differ somewhat from a jet without co-flow (Table 3.1).

Within the fully developed region of a strong jet, over the range $(u_m - u_c)/u_c > 0.2$, to first order the shape of the jet can be described by a Gaussian curve with $\xi_u = 0.6749$ (Bradbury, 1965). An alternative equation is $(\langle \bar{u} \rangle - u_c)/(u_m - u_c) = (1 - \eta_u^{1.5})^2$ (Abramovich, 1963, p. 180). Within a jet within weak co-flow, the centerline jet velocity decays with $\gamma_u = 0.54$ (Rajaratnam, 1976, p. 71), which is slightly higher than the average for jets without co-flow. Experimental results for a jet within constant depth show that for $U_f/U_s \leq 15$ the observed jet half-width $b_u(x)$ is less than the value obtained in a plane free jet, indicating that $\beta_u < 0.1$, which is its value for a turbulent plane jet without co-flow (Rajaratnam, 1976, p. 73). For example, for $U_f/U_s = 6.25$, $\beta_u \approx 0.075$ (Bradbury, 1965).

The length of the flow development region in a compound jet $\hat{x}$ increases as the velocity difference between the jet and the co-flow decreases. For example, a compound plane jet with $U_s = 0.5U_f$ will have a flow development length of $40b_f$, as compared to $12b_f$ for a simple plane jet (Rajaratnam, 1976).

As it travels downstream, an initially strong jet will lose momentum and decay to become a weak jet in strong co-flow [e.g., $(u_m - u_c)/u_c \ll 1$] after a distance $x_{weak} = [\rho_w h_m b_{u,o} I_{uu} u_{m,o}(u_{m,o} - u_c)]^{1/2}/U_s$ (Gaskin and Wood, 2001). Once the excess velocity within the jet dissipates to closer to the background velocity, then different spreading relationships apply (Davidson and Wang, 2002). In particular, $(u_m - u_c) \propto x^{-1/2}$ and $b_u \propto x^{-1/2}$ (Rajaratnam, 1976, pp. 67-69). Self-similarity is not possible when strong co-flow is present (Hinze, 1975, pp. 521-525).

3.2.3 Plane jet over a flat bed in co-flow discharging next to a wall

A jet discharging along a solid surface can entrain fluid from one fewer direction. In a wetland, this situation would occur if a fast flowpath were located adjacent to a

side bank; in this study, a wall jet is produced because the fast flowpath is located next to the flume wall. When this situation occurs, an additional momentum sink is introduced, which affects the lateral velocity distribution of the jet. Assuming a quadratic drag law, the drag due to this momentum sink can be written:

$$\langle F_{d,x} \rangle = \rho_w C_w u_m (u_m - u_c) \tag{3.25}$$

where C_w is a drag coefficient that acts at the wall. If the wall is smooth (the wall stress is "small"), then the wall shear stress does not significantly decrease momentum flux (Rajaratnam, 1976). However, the presence of a solid surface limits the size of the eddies normal to the wall, which may reduce the transverse spreading within a wall jet.

Consider a plane jet of thickness b_f and initial uniform velocity U_f in co-flow of velocity u_c discharging adjacent to, and parallel to, a solid surface. In the fully developed flow region, the velocity profile $\langle \bar{u} \rangle(y)$ is self-similar: within the boundary layer near the wall, the profile increases from zero at the wall to a maximum u_m at $y = b_m$. Outside of the boundary layer, the velocity decreases to the co-flow velocity u_c at large y (Rajaratnam, 1976). Experiments have shown that the appropriate length scale for the boundary layer is b_m and that for the outer layer is $b_u - b_m$, and the appropriate velocity scales are u_m and $u_m - u_c$, respectively. When nondimensionalized using these scales, experimental results collapse within the fully developed region of the jet (Rajaratnam, 1976, p. 247). Kruka and Eskinazi (1964) found that the similarity curve for a wall jet entering a fluid for which $U_f = 10U_s$:

$$\frac{\langle \bar{u} \rangle}{u_m} = \operatorname{sech}^2(\eta_u - 0.14) \tag{3.26}$$

whereas Rajaratnam (1976, p. 217, citing Verhoff, 1963) suggests:

$$\frac{\langle \bar{u} \rangle}{u_m} = 1.48 \eta_u^{1/7} \left[1 - \operatorname{erf}(0.68 \eta_u)\right] \tag{3.27}$$

The concentration profile within the outer flow is expected to be similar to that of

the velocity profile. Within the inner region near the wall, a conservative tracer will experience a no-flux boundary condition, so the gradient in the average concentration $\frac{\mathrm{d}\langle\bar{c}\rangle}{\mathrm{d}y} = 0$ at the wall.

As for a free jet in co-flow, there are two different types of jet behavior: for strong jets ($(u_m - u_c)/u_c \gg 1$), $(u_m - u_c) \propto x^{-1/2}$ and $b_u \propto x$, but for weak jets ($(u_m - u_c)/u_c \ll 1$), $(u_m - u_c) \propto x^{-1/2}$ and $b_u \propto x^{1/2}$ (Rajaratnam, 1976, p. 248). Experiments have shown that the position of the maximum velocity b_m increases linearly with the coefficient $\beta_m = \frac{\mathrm{d}b_m}{\mathrm{d}x} = 0.011$ for $x < 400b_f$ (Kruka and Eskinazi, 1964). The velocity half-width b_u (measured between the maximum velocity and the location in the outer flow where the velocity equals half the maximum velocity) also increases linearly, with $\beta_u = 0.06$ (Kruka and Eskinazi, 1964) or $\beta_u = 0.068$ (Rajaratnam, 1976), so the wall jet grows only two thirds as fast as a planar free jet. Experimental results also indicate that $\gamma_u = 0.53$ and $\alpha_e = 0.35$ (Rajaratnam, 1976). For $10^4 < Re_{j,o} < 10^5$, the length of the flow development region is between $6.1b_f$ and $6.7b_f$ (Rajaratnam, 1976).

3.2.4 Plane jet over a flat bed in the presence of drag

Within a shallow system, bed drag, like drag due to side walls, will decrease the excess momentum within a planar jet. Assuming a quadratic drag law, the drag force due to bed drag can be written (Jirka, 1994):

$$\langle F_{d,x}\rangle = \rho_w C_f \int_0^{b_j} \langle\bar{u}\rangle \left(\langle\bar{u}\rangle - u_c\right)\ \mathrm{d}y \tag{3.28}$$

where C_f is a drag coefficient that acts at the bed. Even though C_f is a weak function of local velocity and local relative roughness, for turbulent jets it can be approximated as constant (Fang and Stefan, 2000). Several previous studies have examined the effect of bed drag on the velocity distribution and entrainment of planar jets.

Lee et al. (1977) and Lee and Jirka (1980) observed the development of a multiport diffuser apparatus of length $b_C = 0.1$–2.0 m in water depth of 1.7–5.9 cm over a concrete surface with shallowness parameter $S = C_f b_{u,o}/2h = 0.004$–$0.23$. Velocities

were measured using timed photographs of surface particles, and temperature was measured with probes. The diffuser was located so it discharged perpendicular to a side wall, which served as a plane of symmetry. Once the individual ports had laterally merged and vertically mixed over depth, the experimental setup was equivalent to a shallow planar jet with initial width less than that of the entire diffuser. Both the centerline velocity and the centerline temperature excess within the diffuser flow were observed to decrease with distance downstream due to the effect of bottom friction in addition to lateral entrainment (Lee and Jirka, 1980). Lee and Jirka (1980) reported that an entrainment coefficient $\alpha_e = 0.068$ provided the best fit to their data.

Giger et al. (1991) and Dracos et al. (1992) used LDV to obtain detailed measurements of mean velocity and turbulent fluctuations in a shallow jet discharging from a 1-cm-wide orifice. The jet was observed spreading on a large horizontal glass-bottomed and glass-lidded water table of constant depth. The water depth was varied in the range 4–36 cm, such that $4 < h/b_{u,o} < 36$. The depth Reynolds number $Re_h = \frac{U_f b_f}{\nu} \approx 10^4$. To eliminate side-wall effects, water was supplied along both sides of the table at the estimated entrainment rate; no co-flow was present. Chen and Jirka (1999) performed detailed quantitative concentration measurements within this system using laser-induced fluorescence (LIF); qualitative flow visualizations were also performed using the continuous injection of a dark dye (Dracos et al., 1992).

The loss of energy to bottom friction was greater than lateral turbulent diffusive momentum exchange, so the flow depth, rather than the slot half-width, was the appropriate scaling variable for the shallow jet (Jirka, 1994). Within the near field ($x < 2h$), the jet had not yet spread to feel the boundaries and exhibited behavior similar to that of an unconfined jet (Giger et al., 1991). Within the middle field ($2h < x < 10h$), the presence of the free surface and the solid bed resulted in secondary currents perpendicular to the direction of jet propagation within the $x - z$ plane (Giger et al., 1991). These secondary currents transported momentum laterally and resulted in a local depression of up to 16% in the expected midline velocity. This secondary circulation was also observed to increase the lateral transport of dye within the middle field (Dracos et al., 1992). In the far field ($x > 10h$) the flow once

again became two-dimensional and, in the absence of secondary currents, the velocity returned to its expected value (Giger et al., 1991; Dracos et al., 1992). In the far field, the presence of bed and surface boundaries induced large-scale horizontal two-dimensional (2-D) instabilities, which caused large-scale jet meandering over the entire flow depth when $h/b_f \leq 12$ (Dracos et al., 1992; Jirka, 1994). The jet was still present (e.g., momentum dissipation was not complete) at the farthest measurement point at $x/h = 120$, although some breakdown of the meandering motion was present at that distance (Dracos et al., 1992).

Despite the development of three distinct flow zones, the jet exhibited self-similar velocity profiles and constant spreading and velocity decay (Dracos et al., 1992). The centerline velocity was observed to decay more rapidly than it would in a free jet: the average velocity decay rate within the jet was observed to be $\gamma_u = 2.21$–2.34 for $h/x \leq 40$ (Giger et al., 1991; Chen and Jirka, 1999). Over this same range, the jet half-width increased linearly as a function of x with $\beta_u = 0.095$–0.106 (Giger et al., 1991); note that these values of β_u are similar to those for a free jet. Giger et al. (1991) reported an average entrainment coefficient $\alpha_e = 0.054$ over their full range of slot half-widths ($h/b_f = 4$–36). The momentum flux m measured far downstream at $x/h = 40$ was within the range 0.74–$0.87 m_o$, confirming that momentum had been lost from the system due to bed drag (Giger et al., 1991).

Time-averaged concentration profiles remained self-similar and Gaussian in the jet for $x/h \geq 5$ (Chen and Jirka, 1999). The large-scale meanders within the far field did, however, increase the concentration half-width more rapidly than in a free jet, with $\gamma_C = 0.17$ and no clear dependence of the coefficient on the depth h (Jirka, 1994; Chen and Jirka, 1999). When temporally averaged, the concentration centerline concentration decayed with $\beta_C = 1.85$ (Chen and Jirka, 1999), which is slightly faster than expected for a free planar jet. The development of large coherent 2-D vortical structures decreased the mixing efficiency of the jet, as measured by its intermittency, from 95–99% to only 80% (Giger et al., 1991). When large-scale meandering was present, the maximum concentration in the center of the two-dimensional vortices was up to four times as high as the time-averaged value at the same location, which

created less dilution (Chen and Jirka, 1999).

Zhang and Chu (2003) used a video imaging method to track the motion of fluid marked with red dye injected vertically into fluid of the same density within a narrow space between two vertical walls separated by a distance of 0.6–4.4 cm. The jet was observed to stop some distance downstream of the nozzle, as a result of losses due to friction. Zhang and Chu (2003) observed the complete arrest of a jet (and cessation of concentration dilution and mixing) at a distance of $x_{diss} = 0.15(2h/C_f)$.

Chu and Baines (1989) studied the entrainment of a brine jet injected into a 1.7-cm-wide space between two plexiglass walls by noting the distance at which a known flow rate of co-flowing fresh water was fully entrained. During momentum-dominated test runs, the jet was observed to spread linearly, but volume flux was 25% less than expected for a free jet. Despite the development of secondary currents and complicated flow patterns, throughout the range $x < 160h$ the time-mean velocity profile $\bar{u}/u_m$ exhibited self-similar behavior that could be described by a Gaussian profile (Eq. 3.23; Chu and Baines, 1989).

Finally, Gaskin et al. (2004) used a photographic method to measure dye concentration within a shallow jet in co-flow in a water depth of $h = 2.5$ cm. To generate turbulence, 0.4-cm or 0.6-cm-high vertical walls were placed every 25 to 45 cm perpendicular to the flow direction. Velocity measurements were obtained using single wire hot-film anemometry, and dye concentrations were obtained using a color CCD camera. For $x < 16h$, the both the velocity and the concentration half-widths increased linearly. For $x > 16h$, jet spreading was reduced when low levels of background turbulence (i.e., relative strength of velocity fluctuations $u'/u_{pf} = 0.05$–0.10) were present. Velocity decay was increased and dilution was reduced over the case with no background turbulence (Gaskin et al., 2004).

These experimental observations can be used to develop a quantitative description of jet development in the presence of bed drag. When h is constant, the parameters C_f, b_u, and u_m are functions of x only. Substituting Eq. 3.8 into Eq. 3.6:

$$\frac{\mathrm{d}m}{\mathrm{d}x} = \frac{\mathrm{d}}{\mathrm{d}x}\left[\rho_w h u_m (u_m - u_c) b_u \int_0^\infty f_u^2(\eta_u)\ \mathrm{d}\eta_u\right]$$

$$= \quad -\rho_w C_f u_m (u_m - u_c) b_u \int_0^\infty f_u^2(\eta_u)\ \mathrm{d}\eta_u \tag{3.29}$$

Within the self-similar region of jet development, $I_{uu} = \int_0^\infty f_u^2(\eta_u)\ \mathrm{d}\eta_u$ depends on the self-similar velocity distribution only. Therefore:

$$\frac{\mathrm{d}}{\mathrm{d}x}\left[h u_m (u_m - u_c) b_u\right] = -\frac{C_f}{h}\left[h u_m (u_m - u_c) b_u\right] \tag{3.30}$$

which integrates to:

$$h u_m (u_m - u_c) b_u = h_m U_f (U_f - U_s) b_{u,o} \exp\left[-\frac{C_f}{h}(x - x_u)\right] \tag{3.31}$$

or, multiplying both sides by I_{uu}:

$$m = m_o \exp\left[-\frac{C_f}{h}(x - x_u)\right] \tag{3.32}$$

Thus, excess momentum is dissipated over an e-folding scale of length h/C_f, which agrees with experimental results (Jirka, 1994).

Lee and Jirka (1980) and Chu and Baines (1989) both note that Eq. 3.32 coupled with a constant value for the entrainment coefficient in Eq. 3.1 results in a prediction for an exponentially increasing jet width. However, observations of the growth of a shallow jet have shown that width increases linearly within the region of jet entrainment (Giger et al., 1991; Dracos et al., 1992). This implies that β_u is constant and that α_e is not constant. An equation for volume flux in the absence of co-flow under this assumption can be developed as follows. First, substitute the definitions for m (Eq. 3.3) and q_j (Eq. 3.2) into Eq. 3.19 to obtain:

$$\frac{\mathrm{d}}{\mathrm{d}x}\left(\frac{q_j^2}{m}\right) = \frac{\beta_u h I_u^2}{\rho_w I_{uu}} \tag{3.33}$$

where β_u is assumed constant and x_{ub} and x_u assumed equal to zero. Integrating with respect to x, substituting in the expression for m given in Eq. 3.32, and applying the boundary condition that $q_j = q_f$ at $x = 0$, an expression for the volumetric flux

within the jet is produced that accounts for momentum dissipation:

$$q_j = \sqrt{\left[\frac{m_o \beta_u h I_u^2}{\rho_w I_{uu}} x + q_f^2\right] \exp\left(-\frac{C_f}{h} x\right)} \tag{3.34}$$

Note that this expression indicates that jet volumetric flux (and therefore centerline velocity) are reduced over their values for a free jet, due to the presence of an additional momentum sink (Wright, 1994). Chu and Baines (1989) note that, when entrainment is large so q_f is small compared to the linear growth term, this expression predicts that the jet volumetric flow rate will increase, though at a slower and slower rate, until it reaches a maximum value at $x = h/C_f$. Downstream of this location, Eq. 3.34 predicts the physically unrealistic situation of jet detrainment, i.e., that the jet loses volumetric flux. By this position, however, the jet excess momentum m has decayed to 36% of its initial value, and the momentum-dominated assumptions used to develop Eq. 3.34 likely no longer apply.

As a result of the entrainment hypothesis (Eq. 3.1), dilution ceases after the point of momentum dissipation at a distance x_{diss} downstream of the jet initiation, and the jet flow rate q_j reaches a constant value that depends on the amount of drag. In general, the total dilution of a shallow jet will be reduced due to the reduction in turbulent entrainment caused by the presence of bed shear stress (Giger et al., 1991).

3.2.5 Jet over a bed of varying depth in the presence of drag

When the water depth is not uniform, jet velocity decreases due to vertical flow expansion in addition to lateral entrainment. Previous observations of fluid exiting a uniform dense array of simulated vegetation and entering a region of deeper water depth have shown that, for $Re_h > 800$ and no bed drag, the flow can separate and create vertical recirculation (Fox et al., 2002; Brunn and Nitsche, 2003; Lightbody et al., 2007). However, it is here assumed that vertical flow separation does not occur, which is reasonable if the expansion angle is less than 20° (White, 1991, p. 346). The presence of drag will also inhibit the development of recirculation (Negretti et al., 2005).

Previous work concerning the dilution and plunge point of dense surface discharges into lakes with sloping bottoms has investigated the effect of varying depth over a frictionless bed (e.g., Hauenstein and Dracos, 1984; Kassem et al., 2003). Johnson and Stefan (1988), Fang and Stefan (1991), and Fang and Stefan (2000) extended this analysis to consider a plunging discharge entering a lake with a constant entrance slope with bottom roughness. When depth is not constant, analytic solutions for jet parameters no longer exist, but results can be computed numerically.

When water depth varies in the longitudinal direction, $h = h(x)$, Eq. 3.6 can still be used to describe the effect of drag on jet momentum. The solution depends on the assumed type of drag. If periphyton or other elements distributed throughout the flow contribute drag, then a drag term must be included that depends on the element bulk drag coefficient C_d and the element volumetric frontal area fraction a, which are both assumed constant. This drag will add to contributions from a side wall and the bed. The total drag influencing the evolution of jet excess momentum will therefore be:

$$\begin{aligned}\langle F_{d,x}\rangle = \rho_w C_f \int_0^{b_j} \langle\bar{u}\rangle \left(\langle\bar{u}\rangle - u_c\right)\, \mathrm{d}y \;&+\; \rho_w C_w \int_0^{h} u_m(u_m - u_c)\, \mathrm{d}z \\ &+\; \rho_w C_d a h \int_0^{b_j} \langle\bar{u}\rangle \left(\langle\bar{u}\rangle - u_c\right)\, \mathrm{d}y \quad (3.35)\end{aligned}$$

where the terms on the right-hand side of the equation reflect the contributions of bed, wall, and distributed drag forces, respectively. When bed drag is the dominant term in Eq. 3.35, $\frac{\mathrm{d}m}{\mathrm{d}x} \sim \frac{C_f}{h}$ (Eq. 3.30), and drag decreases as the local water depth increases. On the other hand, when a distributed drag is the most important component, then $\frac{\mathrm{d}m}{\mathrm{d}x} \sim C_d a$.

One additional equation is required to complete the description of flow development. One possibility is the entrainment assumption, which holds that the entrainment coefficient α_e in Eq. 3.1 is constant. In this situation, Eq. 3.5 can be used directly to predict how jet volume flux will change. Note that this equation includes a dependency of $\frac{\mathrm{d}q_j}{\mathrm{d}x}$ on h, because the increased depth provides additional surface area through which the jet can entrain fluid. The equation also accounts for the

presence of a co-flow. Fang and Stefan (2000) used an assumption of constant entrainment and fourth-order Runge Kutta integration to show that b_u and q_j both increase nonlinearly in a jet over a constant downward slanting slope in the absence of co-flow; results are consistent with experimental results from Johnson and Stefan (1988), though the latter are also consistent with a linear increase.

An alternative, described above in Sec. 3.2.4, is to assume a constant value for $\beta_u = \frac{\mathrm{d}b_u}{\mathrm{d}x}$ in the region in which the co-flow can be neglected. Experimental observations have shown that jets spread linearly over a flat bed in the presence of bed drag and the absence of co-flow (Chu and Baines, 1989; Giger et al., 1991), and the few previous observations of a jet over a sloping rough bed do not contradict this assumption (Johnson and Stefan, 1988). For this situation, Eq. 3.19 will contain a constant β_u value. When a co-flow is present, in the absence of drag it is expected that when the jet excess velocity decays such that when the jet velocity is the same order of magnitude as the co-flow $[(u_m - u_c)/u_c \leq 1]$ the jet width will increase as $b_u \sim x^{1/2}$ (Rajaratnam, 1976); observations of a shallow jet in co-flow also observed a reduction in jet spreading downstream of the transition point between a strong and a weak jet (Gaskin et al., 2004). Within this regime, it would be expected that:

$$\frac{\mathrm{d}b_u}{\mathrm{d}x} = \frac{1}{2}\beta_u x^{-1/2} \tag{3.36}$$

where β_u may have a different value than it does in the region where the co-flow can be neglected.

A final possibility is to rearrange the continuity and momentum equations in the absence of drag, which produces $\frac{\mathrm{d}}{\mathrm{d}x}(hb_u) = 2\alpha_e h$ over a linearly sloping bed within the strong jet region. In analogy to the observation that $\frac{\mathrm{d}b_u}{\mathrm{d}x}$ is constant over a flat bed even in the presence of the drag, it is possible that over a bed of varying depth:

$$\frac{\mathrm{d}}{\mathrm{d}x}(hb_u) = \beta'_u h \tag{3.37}$$

where β'_u is a constant. Note that this equation predicts that flow depth and jet width are inversely proportionate: because an increase in flow depth will create vertical flow

expansion, it will reduce the peak velocity and therefore reduce jet entrainment. In addition, over a flat bed with $\frac{\mathrm{d}h}{\mathrm{d}x} = 0$, this equation predicts a linear growth in jet width, as expected. Eq. 3.37 can be solved for the predicted change in width when co-flow is negligible:

$$\frac{\mathrm{d}b_u}{\mathrm{d}x} = \beta'_u - \frac{b_u}{h}\frac{\mathrm{d}h}{\mathrm{d}x} \tag{3.38}$$

For a weak jet in co-flow [$(u_m - u_c)/u_c \leq 1$], the jet width would be expected to increase as:

$$\frac{\mathrm{d}b_u}{\mathrm{d}x} = \frac{1}{2}\beta'_u x^{-1/2} - \frac{b_u}{h}\frac{\mathrm{d}h}{\mathrm{d}x} \tag{3.39}$$

which will result in reduced spreading compared to the expectation for a strong jet (Eq. 3.38).

The present study predicts $b_u(x)$, $u_m(x)$, $q_j(x)$, and $m(x)$ by using a fourth order Runge Kutta technique to perform the numerical integration of Eqs. 3.2 and 3.3 with the drag force given by Eq. 3.35. One additional assumption is made. In the first model, a constant entrainment coefficient α_e is assumed in Eq. 3.5; note that this equation accounts for reduced entrainment as u_m decays and the jet transitions from a strong jet in weak co-flow to a weak jet in strong co-flow. In the second model, constant linear spreading is assumed, as predicted by Eq. 3.19 with a constant value for β_u. For $(u_m - u_c)/u_c \leq 1$, a modified spreading law was adopted, i.e., Eq. 3.36. In the third model, it is assumed that the rate of increase in jet cross-section depends on the local flow depth, Eq. 3.38 for $(u_m - u_c)/u_c > 1$ and Eq. 3.39 for $(u_m - u_c)/u_c \leq 1$. Predictions are then compared to experimental results obtained from a laboratory model of a jet spreading within a deep zone containing drag downstream of a fast flowpath through a short-circuiting marsh region.

3.3 Methods

A laboratory physical model (Fig. 3-2) was used to study the entrainment induced by a shallow jet discharging into an open deep area with flow resistance. This model was built to represent one segment within the Augusta wetland and included a marsh

region with a single fast flowpath followed by a deep zone and then a downstream marsh region. That is, the flume width represents the wetland width associated with a single flowpath $B_f = B/n_f$ and the flume flow rate $Q_f = \frac{B_f}{B}Q$, where Q is the wetland flow rate. The laboratory model did not need to mimic the full length, width, hydraulic loading rate (HLR), or inlet and outlet conditions of an entire field-scale wetland, because wetland vegetation is dense enough that flow in the middle of the wetland is largely independent of the wetland boundaries (e.g., Bolster and Saiers, 2002). Field and model parameters are compared in Table 3.2.

The model was constructed in a flat flume with glass bottom and sides and a width $B_f = 122$ cm. Water was recirculated through the flume at a flow rate of $Q_f = 85 \pm 1$ L/min. The upstream marsh section consisted of an elevated canopy of simulated vegetation, consisting of a regular hexagonal array of vertical wooden cylinders with a diameter of $d = 0.64$ cm at a packing density of $n_v = 3,200$ m^{-2}, for a volume density of $\phi = \frac{\pi}{4}n_v d^2 = 0.10$. To increase the drag within the simulated vegetation and to decrease the length scale associated with the elements within the vegetated region, fiberglass screening with 7 holes per cm was placed perpendicular to the flow every 3.5 cm. The upstream model vegetation zone was $L_m = 180$ cm long and had a flow depth of $h_m = 7.2$ cm. Fully developed flow was produced within 120 cm of the beginning of the marsh. At one edge of the model marsh was a fast flowpath, simulated by a narrow longitudinal gap of width $b_f = 4$ cm or 6 cm. The flow was allowed to naturally adjust between the flowpath and the cylinder array. The exact geometry (straightness) of the flowpath did not impact this velocity differential (Struve et al., 2003). In the model wetland, $Re_{j,o} = 7,000$–12,000; this range was sufficient to create a turbulent jet. The Froude number $Fr = U_f/\sqrt{gh_m} \approx 0.01$ in the model, where g is the gravitational acceleration.

Downstream of the vegetated area, there was a deep area with a depth of $h_{dz} = 26.6$ cm; the ratio between the marsh and deep zone depths was $h_m/(h_{dz} - h_m) = 0.4$. Plexiglass triangular prisms with a slope $\theta = 10°$ (i.e., a length of 70 cm) were placed at the upstream and downstream edges of the wetland; this slope was comparable to field conditions. The length of the deep zone varied in different trials, $L_{dz} = 140$–

635 cm. To mimic the length scale of momentum dissipation observed downstream of fast flowpaths in the field, in which at least 95% of the momentum was observed to dissipate within $7h_m$ (about 10 m), loose metal netting ($d = 0.25$ mm, $\phi \approx 0.002$) was added to the deep zone area to create momentum dissipation over the same nondimensional length scale, which is $7h \approx 200$ cm in the laboratory. Note that $d/h_m \ll 1$, so the turbulence produced by the netting is negligible. To hold the netting in place, a few 6 cm long dowels with $d = 0.64$ cm were placed vertically within an array of perforated PVC base boards (Ametco Manufacturing Corporation, Willoughby, Ohio) that covered the bottom of the deep zone. It is appropriate to add roughness to a physical prototype models to enhance agreement between model and field observations (Yalin, 1971, pp. 121ff; Sharp, 1981, pp. 97ff). Depending on deep zone length, the residence time within the deep zone was $T_{dz} = V_{dz}/Q_f \leq$ 23 min, where V_{dz} is the deep zone volume; at least this length of time passed between any changes to the flume flow configuration and the beginning any measurements. Downstream of the deep area was an additional elevated simulated marsh region identical to the one upstream. In some trials, no fast flowpath was present; in some, a fast flowpath of the same width as the upstream one ($b_f = 4$ or $b_f = 6$ cm) was placed either directly downstream of the upstream flowpath or at the opposite edge of the flume.

The transport of dye within this system was studied by looking at the evolution of dye that had been introduced into the fast flowpath through the vegetation to mark the water exiting through the jet. Dye injections occurred 120 cm downstream of the beginning of the model marsh. A syringe pump was used to inject dye into the fast flowpath; the dye velocity was matched to that of the passing water. The concentration of dye within the evolving jet within the deep zone was determined using three methods: laser-induced fluorescence (LIF) using Rhodamine WT, fluorometry using Rhodamine WT, and a photographic method using fluorescein.

In the LIF measurements, a 300-mW argon ion laser (Coherent, Santa Clara, California) was directed across the flume perpendicular to flow. Laser power was not modified over the course of the study. A charge-coupled device (CCD) camera (Pul-

nix, San Jose, California, 480 x 764 pixels) was mounted 116 cm above the flume and used to take continuous images of the laser line at $\approx$ 2 Hz. To block incident laser light, a 540-nm long-pass filter was placed on the camera. Because it was expected that the laser light is absorbed by Rhodamine across the width of the flume, *in-situ* calibration was performed at each lateral location across the flume as follows (see Fig. 3-3). In analogy to the method used by Chen and Jirka (1999), the CCD camera in its normal configuration was used to take images of a narrow plexiglass box containing different known concentrations of Rhodamine WT. Then, at each lateral location, a linear regression was performed between the measured pixel intensity in excess of the blank intensity and the known dye concentration. To calibrate pixel distance and physical distance, the camera was also used to take pictures of a coordinate grid inserted into the flume in the same plane as the light sheet. Each pixel corresponds to 2–3 mm of physical distance. Before starting each series of experiments, an image of the background concentration (i.e., image of water with no Rhodamine in it) was taken, and the pixel intensity from this image was subtracted from every image in the series prior to calculating concentration values. Within each experimental run, the concentration of the first picture (prior to that dye release) was subtracted from each subsequent image in the set.

Point measurements of Rhodamine WT concentration were taken using an *in-situ* fluorometer (Seapoint Sensors, Exeter, New Hampshire) connected to a Conductivity Temperature Depth probe (Ocean Sensors, San Diego, California) that was placed outside of the flume. The fluorometer sampled at 8 Hz and its voltage output was calibrated using known concentrations of Rhodamine stock solution diluted in fresh water (Fig. 2-4). The background concentration (i.e., the concentration emerging from the slow-flow marsh areas) was subtracted from all fluorometer measurements.

At least 300 individual measurements of tracer concentration (at least 5 min for LIF and at least 45 s for the fluorometer) during a continuous dye release at a particular depth and longitudinal position were averaged together and smoothed to produce distributions of concentration within a steady jet. Smoothed measurements of dye concentration $\bar{c}(y)$ were directly converted to a measurement of jet half-width $b_C(y)$,

which was defined as the location where the concentration reaches half of its centerline concentration. Uncertainty in the measurements of concentration half-width were calculated as the change in y necessary to change the value of $\bar{c}(y)$ by more than 5%. Velocity measurements were estimated from fluorometer and LIF measurements by observing the difference between the passage time t of the dye center of mass at different (x, y, z) locations for $x < 4$ m. At this location, visual inspection showed that the dye had not yet mixed over depth so it still retained the signature of a particular flow streamline. This observation is confirmed by time scale analysis. In an open channel flow, the vertical diffusivity can be estimated as $D_z = 0.067hu^*$ (Fischer et al., 1979), where the shear velocity $u^* \approx 0.07\langle\bar{u}\rangle$ over the perforated base boards (White, 2006), so the distance necessary to mix over depth in this flume would be approximately $h_{dz}^2\langle\bar{u}\rangle/D_z = h_{dz}/0.005 = 57$ m. Because distributed drag is present within the modeled deep zone so turbulence due to viscous drag is likely damped, the time scale to mix vertically within an open channel flow provides an upper limit on the vertical mixing time, so a lower limit on the distance to vertically mix. Therefore, the distance to mix vertically is ≥ 49 m. Total jet flow rate, momentum, and mass flux at various positions downstream were then calculated using discretized forms of Eqs. 3.2, 3.3, and 3.4.

In addition, point measurements of water velocity were obtained using acoustic Doppler velocimetry (ADV) using a three-dimensional (3-D) laboratory probe (SonTek/YSI, Inc.; accuracy $\pm$ 0.1 cm/s). The probe head was submerged in the water and oriented downward, with the sampling volume 3 cm above the bed. Two-minute-long velocity records were taken at 25 Hz; preliminary experiments showed 2 min was long enough for the mean value to stabilize. During ADV measurements, the flow was seeded with 0.18-μm diameter hollow glass spheres (Sphericel by Potters Industries Inc., Valley Forge, Pennsylvania).

Color photographs of continuous releases of fluorescein (Aldrich F245-6 powdered, dissolved in water at 7 g/L) were used to provide synoptic observations of the evolution of the half-width of the tracer jet with distance downstream. The bottom of the flume was covered with opaque gray plastic sheets to provide contrast with the

green fluorescein. The contrast was heightened by illumination from a black light mounted next to a color red, green, and blue (RGB) camera (Sony Cybershot) on a trolley above the flume; the camera was located 86 cm above the water surface. Each photograph was approximately 60 cm in the longitudinal location and 80 cm in the lateral direction. Photographs were taken approximately 20 cm apart to provide substantial overlap between successive images. Once during each run, the camera was used to take three photographs of a coordinate grid placed at the water surface and marked at 20-cm increments. The longitudinal location of each photograph was determined by noting the position of red tape pieces placed every 25 cm on the inside wall of the flume just above the water surface. Using these coordinates, photographs were merged to produce a composite image of fluorescein within the flume. To convert these observations to a measurement of concentration half-width, measurements of intensity half-width b_I were compared to LIF measurements of Rhodamine WT concentration plume half-width b_C (Fig. 3-4). A linear correlation was found between the two types of measurements, with $b_C = 1.11 b_I$ ($r^2 = 0.93$).

3.4 Results and discussion

3.4.1 Entrance conditions

Lateral ADV velocity profiles taken at the entrance to the deep zone indicated that a 4-cm-wide flowpath produced a peak velocity of $U_f = 16.7 \pm 0.1$ cm/s and an entrance velocity half-width of $b_u = 3.1 \pm 0.1$ cm; the 6-cm-wide flowpath produced a peak velocity of 9.4 ± 0.1 cm/s and initial velocity half-width of $b_u = 5.3 \pm 0.7$ cm(Fig. 3-5). The flow rates within the jet, which in this situation is defined as the region between the wall and the location $y = b_j$ where $\bar{u} = u_c$, were $q_f = \int_0^{b_j} h_m \bar{u}\, \mathrm{d}y = 340 \pm 12$ cm^3/s for $b_f = 4$ cm and 480 ± 16 cm^3/s for $b_f = 6$ cm. These flow rates correspond to a fraction $q_f/Q_f = 0.24 \pm 0.01$ and 0.34 ± 0.01 of the total flow rate through the flume, which was comparable to field measurements (Table 2.2). ADV measurements of flow exiting the simulated vegetation were similar between the two cases: $U_s =$

1.6 ± 0.2 cm/s for $b_f = 4$ cm and 1.1 ± 0.4 cm/s for $b_f = 6$ cm. From continuity, the slow-flow velocity was expected to be $U_s = 1.4 \pm 0.3$ cm/s and 0.8 ± 0.2 cm/s, respectively. The initial excess momentum flux through the fast flowpath was found to be $m_o = \int_0^{b_j} \rho_w h_m \langle\bar{u}\rangle(\langle\bar{u}\rangle - U_s)\ \mathrm{d}y = 1,200 \pm 100$ g cm/s^2 for $b_f = 4$ cm and $7,000 \pm 200$ g cm/s^2 for $b_f = 6$ cm; the largest source of uncertainty was the numerical integration. Fig. 3-6a,b shows the velocity distribution over width and depth at the entrance to the deep zone. Note that the velocity is reduced in both the bottom and surface boundary layers within 1 cm of the bed and surface.

Fig. 3-7 shows lateral concentration profiles of water entering the deep zone. Dye had been released into the center of the fast flowpath 60 cm upstream. Concentration profiles over depth show that the tracer was mixed over depth and width within the flowpath when it entered the deep zone (Fig. 3-8a,b). The half-width of the concentration curve entering the deep zone was $b_{c,o} = 7.1 \pm 0.1$ cm for $b_f = 4$ cm and $b_{c,o} = 11.6 \pm 0.1$ cm for $b_f = 6$ cm. Thus, the entering fast-flowing water was successfully marked with dye prior to entering the deep zone, where its spreading was observed. Note that the tracer spread into the adjacent vegetation over a width comparable to the fast flowpath width, which is similar to previous observations in both the laboratory and the field even within much longer vegetated areas (Pasche and Rouvé, 1985; Su and Li, 2002; White, 2006).

3.4.2 Jet development within the deep zone

First consider jet development within the near-field region of the deep zone, for $x < 200$ cm. The maximum velocity within the jet was observed to decrease as the jet traveled across the deep zone (Fig. 3-9). The uncertainties associated with these observations are primarily caused by the uncertainty in subtracting travel times to different longitudinal positions. No initial zone of constant midline velocity was observed (i.e., $\hat{x}$ was indistinguishable from zero), which is consistent with the presence of drag, which will begin to decrease the velocity throughout the jet immediately after jet initiation. Also note that the presence of a porous flowpath boundary within the marsh region creates an entrance velocity profile that already has an inflection

point, which will tend to result in faster initiation of the shear instability that forms the jet. For the 6-cm-wide flowpath, the decay exceeded that expected from vertical expansion within the deeper area. Note that the maximum contribution of vertical expansion is given by $\langle\bar{u}\rangle(x) = U_f h_m/h(x)$ but the actual contribution of vertical expansion is likely less, because the jet did not expand fully over depth and the near-bed velocity remained low (Fig. 3-6). For both flowpath widths, the velocity at $x > 70$ cm was much lower than what would be predicted from vertical expansion over the whole flow depth. By $x = 200$ cm, the jet velocity was indistinguishable from the plug flow velocity within the flume, $u_{pf} = Q_f/B_f h$. The evolution of jet velocity for $x < 200$ cm is consistent with an initial linear decay of $(U_f/u_m)^2$ (Fig. 3-10), as is expected within the self-similar region of a planar free jet. The values of the decay coefficient, $\gamma_u = 0.8 \pm 0.2$ for $b_f = 4$ cm and $\gamma_u = 2.1 \pm 0.7$ for $b_f = 6$ cm, are lower than previous measurements within a free planar jet, suggesting that the velocity is decreasing more rapidly than due to entrainment alone. Similarly, Gaskin et al. (2004) observed that the presence of bed drag decreased the velocity of a shallow co-flowing planar jet more rapidly than was observed in a co-flowing planar jet without background turbulence. Releases of a tracer dye showed that vertical recirculation (reverse flow below the surface) did not develop during any trial within any portion of the flow.

The rapid decay of fast flowpath momentum was not observed in previous physical models of wetlands that did not include drag within deep zone areas (e.g., Arzabe, 2000; Lightbody et al., 2007, see Sec. 1.6.2). Lightbody et al. (2007) did not quantify velocity decay but presented velocity vector plots that indicate at most a 25% decay in the midline velocity over the entrance slope, whereas here 81% (for $b_f = 4$ cm) and 87% (for $b_f = 6$ cm) of the initial velocity was observed to decay over the initial 70-cm-long entrance slope. Arzabe (2000) observed that 40% of vorticity decayed within 1.2–7 h_{dz} of the start of the modeled deep zone and attributed the loss to vortex dissipation following stretching over depth, i.e., the decay of excess jet momentum was attributed to the flow expansion associated with the inlet slope. Vorticity scales on $(u_m - u_c)/b_u$; observations here show that 40% of $(u_m - u_c)/b_u$ decays within 20 cm

(i.e., $< h_{dz}$) of the beginning of the deep zone and that nearly 100% of excess velocity decays within 8 h_{dz}, confirming that a mechanism that relies only on spreading over depth is not sufficient to explain the observed momentum decay.

Measurements of maximum concentration within steady flow were also consistent with an initial linear decay with $\gamma_C = c_o/c_m = 0.14 \pm 0.01$ (Fig. 3-11). The observed decay was much smaller than previous observations within free and shallow planar jets (Table 3.1). Although not enough data points were obtained to confirm a linear relationship between $(c_o/c_m)^2$ and x, such a relationship is expected within the self-similar region of a planar free jet (Eq. 3.22).

After entering the deep zone, the jet velocity half-width b_u initially ($x < 200$ cm) increased (Fig. 3-12). Assuming a linear growth, the distance between the wall and the location where the jet velocity was half its midline value increased as $\frac{\mathrm{d}b_u}{\mathrm{d}x} = 0.22 \pm 0.05$ for the 4-cm-wide flowpath and $\frac{\mathrm{d}b_u}{\mathrm{d}x} = 0.24 \pm 0.04$ for the 6-cm-wide flowpath. In addition, due to the growing boundary layer at the flume wall ($y = 0$), the jet migrated away from the near wall with a linear increase with distance downstream: for both flowpath widths and $x < 200$ cm, the maximum velocity moved away from the wall at a rate $\frac{\mathrm{d}b_m}{\mathrm{d}x} = 0.08 \pm 0.02$. Therefore, the width of the outer region of the jet, between the peak velocity and where the velocity declined to half its peak, increased as $\beta_u = \frac{\mathrm{d}(b_u - b_m)}{\mathrm{d}x} = 0.14 \pm 0.05$ for the 4-cm-wide flowpath and $\beta_u = 0.16 \pm 0.04$ for the 6-cm-wide flowpath; this spreading rate is comparable to measurements obtained in previous studies of a free planar jet and a planar jet in shallow water (cf. Table 3.1).

Detailed synoptic from the photographic method indicate that for $x < 30$ cm the distance between the wall and the jet concentration half-width increased slowly, at a rate of $\frac{\mathrm{d}b_C}{\mathrm{d}x} = 0.13 \pm 0.02$, then spread laterally much more rapidly at $\frac{\mathrm{d}b_C}{\mathrm{d}x} = 0.40 \pm 0.01$ for 30 cm $\leq x \leq$ 110 cm for $b_f = 4$ cm and $\frac{\mathrm{d}b_C}{\mathrm{d}x} = 0.45 \pm 0.01$ for 30 cm $\leq x \leq$ 150 cm for $b_f = 6$ cm, (Fig. 3-13). It is likely that the initially slow spreading resulted from the upstream porous canopy, which allowed the concentration to spread one flowpath width outside of the high-momentum fluid within the flowpath (Figs. 3-5 and 3-7). Within the deep zone, spreading depends on jet entrainment, which eventually but not immediately engulfs this small width of marked co-flow. Measurements of jet

velocity half-width (Fig. 3-12) indicated that the velocity half-width had spread to twice the initial flowpath width at $x = 24 \pm 2$ cm downstream for $b_f = 4$ cm and $x = 29 \pm 2$ cm for $b_f = 6$ cm, so would have been expected to entrain the marked co-flow by $x \approx 30$ cm, consistent with the position at which the change in growth occurs. It is also possible that lateral spreading was initially reduced due to flow expansion over depth or the presence of drag (e.g., Dracos et al., 1992).

Because the initial slow spreading likely results from the upstream boundary condition, the observed spreading for 30 cm $\leq x \leq$ 150 cm provides the best estimate of concentration spreading due to jet entrainment. If the center of the tracer distribution is located at the center of the velocity distribution, then the observed spread of the jet centerline ($\frac{\mathrm{d}b_m}{\mathrm{d}x} = 0.08 \pm 0.02$) can be subtracted, and downstream of $x = 30$ cm the spreading coefficient is found to be $\beta_C = \frac{\mathrm{d}(b_C - b_m)}{\mathrm{d}x} = 0.33 \pm 0.02$ for $b_f = 4$ cm and $\beta_C = 0.37 \pm 0.02$ for $b_f = 6$cm. These values show that $\beta_C > \beta_u$, which is consistent with previous studies; the ratios between the spreading coefficients, $\beta_C/\beta_u = 2.4 \pm 0.9$ for $b_f = 4$ cm and $\beta_C/\beta_u = 2.3 \pm 0.6$ for $b_f = 6$ cm, are greater than prior work (Table 3.1). Meandering acts to increase β_C/β_u, but large-scale meanders were not observed in the present study, which occurred in relatively deep water.

Further downstream ($x > 100$ cm for $b_f = 4$ cm and $x > 150$ cm for $b_f = 6$ cm), jet spreading was reduced. Theory predicts that the transition between a strong jet and a weak jet was located at $x \approx 168$ cm, at which point the jet excess momentum had decayed to $u_m - u_c = u_c$. For $(u_m - u_c)/u_c \ll 1$ it is expected that spreading is reduced and $b_C \sim x^{-1/2}$ (Rajaratnam, 1976, p. 248), which likely contributes to the decrease in observed jet spreading. The time-averaged distributions of concentration at various longitudinal positions (Fig. 3-8) confirmed that the jet ceased spreading laterally well before touching the far edge of the flume.

Now consider jet development in the far-field region for $x > 200$ cm. Fig. 3-9 shows that, by $x = 200$ cm, the excess momentum initially present within the fast-flowing jet water was dissipated. At this location, the distance of the maximum velocity from the wall was $b_m = 16 \pm 1$ cm, and the velocity jet had a half-width (distance from wall) of $b_u = 45 \pm 2$ cm for $b_f = 4$ cm and $b_u = 50 \pm 2$ cm for and $b_f = 6$ cm, or an

outer jet half-width of $b_u - b_m = 29 \pm 2$ cm for $b_f = 4$ cm and $b_u - b_m = 34 \pm 1$ cm for $b_f = 6$ cm (Fig. 3-12). Downstream of x_{diss} the jet velocity distribution and the locations of b_m and b_u were poorly defined, because the entire flow outside of the side- and bottom-boundary layers traveled at the background velocity u_{pf}. The concentration half-width was observed to reach a constant value, $b_C = 59 \pm 3$ cm for $b_f = 4$ cm and $b_C = 69 \pm 2$ cm for $b_f = 6$ cm, with a constant maximum value, $c_m/c_o = 0.49 \pm 0.01$.

Previous studies of jet development in the presence of friction have also observed that lateral growth is reduced or eliminated due to the enhanced momentum dissipation. When the jet discharges into still water, its forward progression ceases after its momentum is dissipated (Zhang and Chu, 2003). When a co-flow is present, the marked fluid is advected downstream even after its excess momentum is dissipated. In a study of a shallow jet over a rough bed, velocity half-width and concentration half-width were both observed to initially spread like that of a free planar jet, but β_u approached zero and β_C decreased to 0.03 downstream of $x = 16h$; the location of momentum dissipation was not estimated in that study (Gaskin et al., 2004). To date measurements have not been obtained of jet growth in a totally quiescent ambient fluid with no residual tank-wide circulation.

Within the laboratory model, the possible mechanisms for lateral mixing downstream of $x = 200$ cm were turbulent diffusion and mechanical dispersion; molecular diffusion is so small that it will not be considered. When turbulence primarily results from the bottom boundary layer, a robust estimate for the lateral eddy viscosity is $\nu_t = 0.2u^*h$, where the shear velocity $u^* = \sqrt{C_f/2}U_f \approx \frac{1}{10}\langle\bar{u}\rangle$ (Fischer et al., 1979). The jet width would then be expected to increase $\Delta b_u \sim \sqrt{\Delta x \nu_t/\langle\bar{u}\rangle} \approx \sqrt{0.02h\Delta x} \approx$ 10 cm in width in a 26-cm-deep system over a length scale of $\Delta x = 200$ cm. Here, the flow was transitional ($Re_h = u_{pf}h/\nu \approx 1200$), and the contribution of bed-generated turbulence was likely reduced below this expectation due to the presence of elements throughout the fluid volume (Nepf et al., 1997). Note that the netting itself did not create turbulent diffusion or mechanical lateral dispersion because the element Reynolds number $Re_d = u_m d/\nu < 40$ and the volume fraction $\phi \approx 0.002$ (Nepf,

1999; White and Nepf, 2003). Therefore, due to the quiescent laboratory conditions, the marked fluid was not observed to spread laterally once the jet momentum had dissipated. Within a constructed wetland in the field, other forces such as wind or biological activity (e.g., fish) could contribute to lateral mixing within the deep zone downstream of x_{diss} and may overwhelm the contribution of jet entrainment. For example, Gaskin et al. (2004) observed that when 12–15% background bed-generated turbulence was present in a shallow jet system, once the jet had decayed from a strong jet to a weak jet lateral spreading was tripled over the case with no turbulence.

Throughout the region of flow development, normalized velocity and concentration transverse profiles collapsed onto a self-similar profile, which was expected within a momentum-dominated jet. The observed shape of the excess velocity profile, $[\bar{u}(y) - u_{pf}]/[u_m - u_{pf}] = f_u(\eta_u)$, agreed quite well with the expected distribution from theory, $\exp(-0.593\eta_u)$, except for the near-wall region where the velocity became zero at the wall ($\langle\bar{u}\rangle = 0$ at $y = 0$) to satisfy the no-slip boundary condition (Fig. 3-14). The shape of the normalized concentration profiles fit a Gaussian profile less well; the concentration profiles fell off more sharply at the edge of the jet than the velocity profiles did (Figs. 3-14 and 3-15). Even as the dye moved downstream within the quiescent far-field region, the gradient between marked jet fluid and the co-flow remained relatively sharp (Fig. 3-8). Also note that the velocity and concentration profiles exhibited different wall boundary conditions: the velocity became zero at the wall to satisfy the no-slip boundary condition, whereas the concentration profiles were normal to the wall ($\frac{\mathrm{d}\langle\bar{c}\rangle}{\mathrm{d}y} = 0$ at $y = 0$), which is consistent with a no-flux boundary condition.

Fig. 3-16 shows a sample vertical velocity profile within the region of developing flow. Note that, due to the bottom boundary layer, the maximum velocity was located within the top half of the water column. The maximum concentration was also observed within the top half of the water column (Fig. 3-8), indicating that the flow was not fully mixed over depth. Therefore, the fluid close to the bed likely has a longer residence time within the deep zone than the fluid higher in the water column.

3.4.3 Jet development with different downstream conditions

Fig. 3-17 shows the width of the concentration within the jet $b_C(x)$ as it traveled along the deep zone. In both panels, flow is from left to right, and the jet was observed to spread as it traveled downstream within deep zones of different lengths; the length of the deep zone is shown by a vertical line. The length of the deep zone did not affect the initial evolution of jet width (Fig. 3-17). Regardless of deep zone length, jet development was indistinguishable until a distance of $x \approx 100$ cm. Downstream of this location, the final amount of lateral spreading was inhibited within jets within 140-cm-long and 202-cm-long deep zones, in comparison to 635-cm-long deep zone, because the jet did not have as long a travel distance before entering the shallow water and then downstream simulated marsh at the end of the deep zone.

The length of the deep zone also did not affect the momentum dissipation length. Note that, due to the downstream exit slope, the expected plug flow time of travel to a particular x location is reduced over the expectation for a longer deep zone. When transit times are compared to the plug flow expectation, however, the velocity decayed toward this baseline at the same rate within a 140-cm-long and a 635-cm-long deep zone (Fig. 3-19), suggesting that momentum dissipation was unaffected. By approximately $x = 200$ cm downstream, the linear slope of the time of travel measurements for the jet in the long deep zone was the same as that of the expected plug flow velocity, indicating that the jet had slowed to the background plug-flow velocity. Note that, for all deep zone lengths, dye was expected to accelerate as it traveled over the downstream upslope and entered the downstream marsh; the toe of the downstream entrance slope was located at $x = 70$ cm for the shortest deep zone considered.

In some runs, a fast flowpath of the same dimensions and flow rate as the one upstream was introduced into the downstream marsh. In some runs, it was located directly downstream of the upstream flowpath; in some runs, it was located on the opposite side of the flume. The presence and location of this downstream flowpath did not influence jet spreading within the first 100 cm of jet development. Fig. 3-18

shows, for three different deep zone lengths, that there is little difference between jet width profiles until within 30–60 cm of the downstream edge of the deep zone. As a result of rapid momentum dissipation, and the drag present within the system, the downstream end condition did not affect the jet within most of the deep zone. Regardless of deep zone length and position of downstream flowpath, the influence of the downstream edge affected the jet only $< 2h$ from the downstream edge, which was less than the length of the downstream exit slope. The length of the region of influence likely depends on the amount of drag in the system. Therefore, the downstream flowpath did not change the orientation of streamlines throughout most of the deep zone area. Because the dominant factors controlling flow patterns within this system are likely to be co-flow and drag, both of which were matched to the field, the downstream flowpath does not behave as a potential sink (e.g., Granger, 1985, pp. 587ff.) and instead has a limited range of influence.

Transit times (and therefore velocities) were also unaffected by the presence and location of a downstream flowpath (Fig. 3-19). Neither the presence nor position of the flowpath created a consistent difference in travel times, even when the length of the deep zone was less than the momentum dissipation length. In particular, the alignment of the flowpaths directly upstream and downstream from each other was not observed to create an enhanced connection between them, which would have resulted in reduced entrainment within the deep zone.

3.4.4 Jet integral quantities

Measurements of velocity and concentration distributions over width and depth (e.g., data in Figs. 3-6 and 3-8) can be integrated to provide measurements of the evolution of jet integral parameters over distance. Fig. 3-20 shows these integral quantities within the jet as a function of distance along the deep zone. Initially, mass flux was $J = 420 \pm 120$ cm^3/s for $b_f = 4$ cm and $J = 930 \pm 450$ cm^3/s for $b_f = 6$ cm.

The flow rate within the jet increased within the first 200 cm of jet evolution, due to the entrainment of co-flow from outside of the jet, before reaching a constant value of $q_j = 830 \pm 40$ cm^3/s for the 4-cm-wide flowpath and $q_j = 950 \pm 60$ cm^3/s for the

6-cm-wide flowpath (Fig. 3-20a). These averages are calculated from the five circled points within Fig. 3-20a. The higher values of q_j are close to the total flume flow rate Q_f, which contradicts observations that the jet spread only part-way across the flume (e.g., Figs. 3-12 and 3-13) and highlights the uncertainty associated with this method of calculation. The observed increase in flow was $q_j - q_f = 490 \pm 40$ cm^3/s for the 4-cm-wide flowpath and $q_j - q_f = 470 \pm 60$ cm^3/s for the 6-cm-wide flowpath, which represents $45 \pm 4\%$ and $50 \pm 6\%$ of the flow outside of the flowpath, $Q_f - q_f$. Thus, much of the jets' flow expansion is due to continuity and its adjustment to the plug flow velocity.

Based on the integrated jet flow rate, it is possible to use continuity to predict the streamline expansion when a flowpath is present within the downstream marsh region. For the flow rates considered here, $q_j/Q_f \leq 1 - q_f/Q_f$ and it is expected that no fluid should pass through both the upstream and downstream flowpaths when they are located on opposite edges of the flume. The dividing streamline, which sets the edge of the tracer-bearing fluid that passed through the upstream flowpath, would be expected to be deflected laterally a distance $y \approx 22$ cm for $b_f = 4$ cm and $y \approx 34$ cm for $b_f = 6$ cm once full flow expansion is achieved downstream. Here, due to the porous nature of the downstream marsh, flow expansion was not complete until some distance within the downstream marsh, so the observed deflection of 20 cm or less was consistent with the prediction from continuity (Fig. 3-18. For a flowpath located on the near side of the flume, it was expected that the dividing streamline should be deflected laterally a distance $y \approx 17$ cm for $b_f = 4$ cm and $y \approx 23$ cm for $b_f = 6$ cm once full flow expansion is achieved downstream. Again, this is consistent with observations, which showed a deflection distance of 20 cm or less (Fig. 3-18).

Jet momentum decreased over distance and reached a background level comparable with that of the co-flowing region by a distance of $x = 200$ cm (Fig. 3-20b). The momentum decay was consistent with an exponential decline, with $\frac{h_{dz}}{x} \ln(\frac{m_o}{m}) = 0.12 \pm 0.03$ for $b_f = 4$ cm and $\frac{h_{dz}}{x} \ln(\frac{m_o}{m}) = 0.32 \pm 0.08$ for $b_f = 6$ cm. An exponential decline is expected within a shallow system with losses due to bottom friction (Jirka, 1994). The value of the coefficient within the exponential expression is higher than

the expected value for a smooth earthen channel (Mannings coefficient $n_M \approx 0.020$, so $C_f \approx h_{dz}^{2/3} n_M^2 = 0.0005$; Henderson, 1966, p. 99) but is within the range of bed drag coefficient values suggested by previous studies of flow through wetlands. For example, Tsihrintzis and Madiedo (2000) suggested using a Darcy-Weisbach drag coefficient $f_o = 0.1$–1000 to simulate marsh wetlands; this corresponds to $C_f = 0.01$–100. This large range in possible values indicates why more work is necessary to measure flow through wetlands containing deep zones.

Finally, the scalar mass flux remained approximately constant with distance downstream, at $J = 600 \pm 50 \mu$g/s and $J = 1000 \pm 150$ μg/s for the 4-cm-wide and 6-cm-wide flowpaths, respectively (Fig. 3-20c). This result confirms that Rhodamine WT behaved as a conservative tracer within the jet. In addition, the scatter in the data points reveals the imprecision in the calculation of these integrated jet quantities using this method of integrating line measurements.

3.4.5 Comparison between theoretical, laboratory, and field observations of jet development

These experimental measurements of q_j, m, b_u, and u_m are now compared to the predictions presented above in Sec. 3.2.5. In the present study, the bed, the flume wall adjacent to the discharging jet, and the netting distributed throughout the depth all contributed drag to the system. The sidewall of the flume was glass, which for $Re_h = 4000$ produces a Darcy-Weisbach friction factor $f_o = 0.042$ (e.g., Mott, 2000, pp. 243-244), so $C_w = f_o/8 = 0.0053$. The bottom of the flume was covered by perforated plastic, with measured bed drag coefficient $C_f = 0.001$–0.012 (White, 2006, Table 2-1); because the current set-up included a few additional near-bed roughness elements (a few short dowels to hold the netting in place), the maximum measured value of $C_f = 0.012$ was selected for simulations. The values $I_u = 1.01$ and $I_{uu} = 1.47$ are chosen based on work by Patel (1971) and Bradbury and Riley (1967). Six different simulations were produced, using combinations of three different assumptions for the jet entrainment, as explained in Sec. 3.2.5, and two different assumptions for drag

(bed and wall drag only, and bed and wall drug plus distributed drag). Figs. 3-21 and 3-22 compare the predictions from these different assumptions to measured data.

For those simulations in which only bed and wall drag were present, model fits were obtained by optimizing the relevant entrainment parameter (either α_e, β_u, or β_u') to obtain the best fit (that is, smallest sum of squared residuals) to velocity half-width for 25 cm $\leq x \leq$ 150 cm and centerline velocity measurements, which were the two measured parameters with the greatest number of measurements. The width measurements were estimated from observations of jet concentration width shown in Fig. 3-13, scaled by $\beta_u/\beta_C = 0.55$; this approach assumes constant turbulent Prandtl and Schmidt numbers. For those simulations in which bed, wall, and distributed drag were present, model fits were obtained by simultaneously optimizing the distributed drag coefficient $C_d a h_m$ and the relevant entrainment parameter. Table 3.3 reports the best-fit parameter values and their uncertainties.

All six models are able to represent the observations of jet flow rate increase, jet momentum loss, jet width increase, and jet velocity decay relatively well (Figs. 3-21 and 3-22). In addition, the model predictions for $x < 150$ cm are relatively similar. On the other hand, downstream of the position of maximum entrainment, all three of the models with distributed drag predict a decrease in jet flow rate q_j, i.e., detrainment, which is physically unrealistic and is not shown in Figs. 3-21a and 3-22a. Similarly, in a shallow jet in a region of constant depth, the equations that predict jet entrainment cease to have physical meaning for $x > h/C_f$ (Chu and Baines, 1989). Downstream of $x = 150$ cm, the model with constant α_e as currently formulated does not represent the reduction in jet width growth associated with the transition from a strong jet to a weak jet. Also note that both the model with constant β_u and the model with constant β_u' were integrated assuming a sudden change in spreading behavior from $b_u \sim x$ to $b_u \sim x^{1/2}$ when $(u_m - u_c)/u_c = 1$. Such an abrupt transition between strong and weak jet behavior is not realistic. More work is therefore necessary to develop a model that fully describes jet behavior in the far-field region, though these observations should provide an important step in the modeling and an analytical check on future detailed numerical models.

The studied system contained drag distributed throughout the flow volume in addition to the drag contributed by the flume bed and side walls. Not surprisingly, Figs. 3-21b and 3-22b clearly show that the models that lack distributed drag predict a slower decline in jet momentum than was observed. This reduced momentum decay delays the transition to a weak jet and results in a large predicted maximum jet flow rate. The additional drag within the laboratory system therefore has a large effect in limiting the predicted entrainment.

Fig. 3-23 uses these numerical models to predict jet spreading within a field wetland such as the Augusta wetland. Because no model is clearly superior, all three are used and the results compared. Variables are chosen based on characteristic values obtained from the field study of the Augusta wetland (Tables 2.1 and 2.2): $b_f = 2$ m, $u_{m,o} = u_{peak} = 3$ cm/s, $u_c = U_s \approx u_{pf} = 0.1$ cm/s, $h_m = 0.4$ m, $h_{dz} = 1.4$ m, and $L_{slope} = 6$ m. The entrainment coefficient was set at $\alpha_e = 0.35$ and the jet spreading coefficients at $\beta_u = 0.22$ and $\beta'_u = 0.29$, which are the average best-fit entrainment coefficient observed in the laboratory study. When present, simulated distributed drag was chosen to be $C_d ah = 1$; because $C_d \approx 1$ for rigid elements with $ad < 0.10$ and element Reynolds number $10 < Re_d < 10,000$ (Koch and Ladd, 1997; Nepf, 1999; Stone and Shen, 2002), this value would be produced by the inclusion of a volume fraction $\phi \approx 0.001$ of 1-mm-wide *Nymphaea* spp. (water lily) roots. In some wetlands, additional drag may not be distributed throughout the fluid volume and may instead result from submerged aquatic vegetation and wrack at the bed surface. In that situation, the drag elements would elevate C_f rather than creating a distributed drag force. Three values of the bed drag coefficient C_f were selected for comparison: $C_f = 0.04$ to represent flow discharging over a relatively smooth bed Fang and Stefan (e.g., $0.03 \leq C_f \leq 0.06$ for a reservoir inflow 1991), $C_f = 0.42$ to represent flow over a periphyton bed as in the Augusta wetland (recall that over 95% of momentum was dissipated over a length scale of $x_{diss} \approx 10$ m, so $C_f \approx 3h_{dz}/x_{diss} \approx 0.42$), and $C_f = 1$ for comparison with the case with distributed drag.

As shown in Fig. 3-23a, the assumed amount of drag determines the length of the momentum dissipation length x_{diss}. Whether the drag is contributed by bed

drag or distributed elements, jet momentum decay increases as C_f or $C_d ah$ increases. The amount of drag present within the system is therefore important in determining the length scale of momentum dissipation x_{diss}. Fig. 3-24 shows the predicted lengths scale of dissipation x_{diss} for various combinations of bed drag C_f and distributed drag $C_d ah$, using parameters appropriate for the field as shown in Fig. 3-23. The amount and type of entrainment does not affect these results. Increasing either type of drag is predicted to shorten the dissipation distance considerably, from over 50 m to less than 3 m. Note that high levels of bed and/or distributed drag are necessary to achieve the dissipation distance of $symXdissipation = 10$ m observed in the Augusta wetland. Because the momentum dissipation distance sets the minimum length of the deep zone, the amount of drag within the system is an important parameter. As shown in Fig. 3-23b, however, there is a tradeoff associated with increasing the amount of drag: when drag is high, jet entrainment is reduced, and less dilution is achieved. When $C_f = 0.01$ and $C_d ah = 0$, the maximum value of $(q_j - q_f)/q_f = 2.1$–3.3; this ratio decreases to $(q_j - q_f)/q_f = 0.1$–0.4 for $C_f = 0.14$ and $C_d ah = 0$ and to $(q_j - q_f)/q_f = 0$–0.02 for $C_f = 1$ or $C_d ah = 1$. Therefore, the ability of the jet to create lateral mixing depends on the amount of drag present in the system.

3.5 Conclusion

Within the laboratory model, the water that passed through an upstream fast flowpath initially spread like a strong free jet. Initially, jet velocity and concentration half-widths both increased approximately linearly, the centerline concentration and velocity both decayed in proportion to $x^{-1/2}$, and velocity and concentration profiles were self-similar, as is expected for a free jet. Due to the drag present within the system, however, by $x \approx 200$ cm the excess momentum within the jet was dissipated. Downstream of this location, the marked fluid that had initially traveled within the fast flowpath traveled at the plug flow average velocity and did not exhibit additional lateral spreading. Within a constructed wetland in the field, other forces such as wind or biological activity (e.g., fish) could contribute to lateral mixing within the deep

zone downstream of x_{diss} and may overwhelm the contribution of jet entrainment.

These observations suggest that the relative length of momentum dissipation, x_{diss}/L_{dz}, is likely to be an important factor in determining flow patterns within a constructed wetland deep zone. When $L_{dz} > x_{diss}$, as occurred in this laboratory study, the deep zone disconnected upstream and downstream flowpaths, which is shown in Chap. 4 to play an important role in the mitigation of short-circuiting. On the other hand, when $L_{dz} < x_{diss}$, it is likely that the deep zone will not be able to fully uncorrelated the location of flowpaths in successive marsh sections. The length of momentum dissipation in turn depends on the amount of drag present within the system. Within a system with bed drag, the dissipation length scale x_{diss} has been shown by both experimental and numerical results to depend on the shallowness parameter $S = C_f \frac{2b_f}{h_m}$, which also governs both the decay rate of momentum and the maximum dilution attained (Chu et al., 1991; Chen and Jirka, 1998). Within a system with distributed drag, a comparable formulation is $S = C_d a b_f$. When $S > 1$, drag would be expected to play an important role in dissipating momentum within the deep zone.

Finally, note that only one fast flowpath was considered in this study. The existence of multiple parallel fast flowpaths entering a deep zone within a wetland, as was found in the Augusta wetland (Sec. 2.3.1), presents the possibility of jets interacting with each other within the deep zone. To first approximation, the distance at which parallel jets will merge is the distance at which the jet half-width becomes equal to half the jet spacing, and the jets do not interact prior to this location (Jirka, 2006). Wang and Davidson (1997) performed detailed velocity measurements during the merging of jets in a weak co-flow and found that they closely agree with an additive model that does not include any jet interactions. Therefore, as long as parallel jets are separated by a distance $b_\delta > \beta_u L_{dz}$, where L_{dz} is the length of the deep zone, interactions between them can be neglected. Within the Augusta wetland, flowpaths were separated by $b_\delta \approx B/n_f = 34$–$71$ m, which is much larger than 10–20% of $L_{dz} = 45$ m, so it was appropriate to neglect jet interactions in a model of this system. Interactions between adjacent fast flowpaths may be important in wetlands

with a greater density of flowpaths. When interaction occurs, it is likely to reduce jet dilution even further, because the presence of parallel jets reduces the volume of unmarked co-flow.

Table 3.1: Experimental values of constants in previous studies of free planar, shallow planar, co-flowing, and wall jets. Sources are shown in the table. Table continued on next page.

Parameter	Value	Jet type	Source
ξ_u	0.693	Planar	Rajaratnam (1976)
I_u	2.025	Planar in co-flow	Bradbury and Riley (1967)
I_u	1.01	Wall in co-flow	Patel (1971)
I_{uu}	1.467	Planar in co-flow	Bradbury and Riley (1967)
α_e	0.053	Free planar	Rajaratnam (1976)
α_e	0.057	Free planar	Literature review in Giger et al. (1991)
α_e	0.059	Free planar	Recommended value in Chen and Rodi (1980)
α_e	0.052	Free planar	Abramovich (1963)
α_e	0.068	Free planar	Albertson et al. (1950)
α_e	0.051–0.053	Free planar	Zijnen and Van der Hegge (1958)
α_e	0.057	Planar in co-flow	Bradbury and Riley (1967)
α_e	0.068	Shallow planar	Lee and Jirka (1980)
α_e	0.054	Shallow planer	Giger et al. (1991)

Table 3.1, cont.

Parameter	Value	Jet type	Source
γ_u	3.1–3.7	Free planar	Rajaratnam (1976)
γ_u	3.36	Free planar	Jirka (2006)
γ_u	2.58	Free planar	Davies et al. (1975)
γ_u	3.22	Free planar	Albertson et al. (1950)
γ_u	3.13–3.51	Free planar	Zijnen and Van der Hegge (1958)
γ_u	3.78	Free planar	Abramovich (1963)
γ_u	3.50	Planar wall	Rajaratnam (1976, p. 218)
γ_u	4.00	Planar wall in opposing flow	Ead and Rajaratnam (2002)
γ_u	3.43	Planar in co-flow	Rajaratnam (1976)
γ_u	2.23	Shallow planar	Gaskin et al. (2004)
γ_u	2.21–2.34	Shallow planar	Giger et al. (1991), Dracos et al. (1992)
β_u	0.097–0.114	Free planar	Rajaratnam (1976)
β_u	0.0991	Free planar	Chu and Baines (1989)
β_u	0.128	Free planar	Albertson et al. (1950)
β_u	0.096–0.0991	Free planar	Zijnen and Van der Hegge (1958)
β_u	0.097	Free planar	Abramovich (1963)
β_u	0.106	Free planar	Literature review in Giger et al. (1991)
β_u	0.11	Free planar	Recommended value in Chen and Rodi (1980)
β_u	0.116	Free planar	Recommended value in Fischer et al. (1979, p. 328)
β_u	0.14	Free planar	Jirka (2006)
β_u	0.068	Wall	Schwarz and Cosart (1961)
β_u	0.073	Wall	Kruka and Eskinazi (1964)
β_u	0.068	Wall	Rajaratnam (1976, p. 219)
β_u	0.068	Planar wall	Rajaratnam (1976)
β_u	0.064	Planar wall in co-flow	Patel (1971)
β_u	0.076	Planar wall in opposing flow	Ead and Rajaratnam (2002)
β_u	0.20-0.35	Shallow planar	Ead and Rajaratnam (2002)
β_u	0.095–0.106	Shallow planar	Giger et al. (1991), Dracos et al. (1992)
β_u	0.12	Shallow with background turbulence	Gaskin et al. (2004)

Table 3.1, cont.

Parameter	Value	Jet type	Source
γ_C	1.92	Free planar	Bashir and Uberoi (1975)
γ_C	1.98	Free planar	Davies et al. (1975)
γ_C	1.96	Free planar	Abramovich (1963)
γ_C	2.46	Shallow planar	Zhang and Chu (2003)
γ_C	0.82	Shallow planar	Gaskin et al. (2004)
γ_C	1.83	Shallow planar	Chen and Jirka (1999)
γ_C	1.11	Shallow with background turbulence	Gaskin et al. (2004)
β_C	0.135	Free planar	Recommended value in Chen and Rodi (1980)
β_C	0.157	Free planar	Recommended value in Fischer et al. (1979, p. 328)
β_C	0.168–0.177	Shallow planar	Chen and Jirka (1999)
β_C	0.17	Shallow planar	Jirka (1994)
β_C	0.08	Shallow with background turbulence	Gaskin et al. (2004)
β_m	0.011	Wall	Kruka and Eskinazi (1964)

Table 3.2: Comparison between parameters in the Augusta wetland and in laboratory experiments.

Parameter	Field	Lab
Marsh & deep zone depth ratio, h_m/h_{dz}	0.28	0.27
Vegetation & flowpath length ratio,d/h_m	0.05–0.2	0.09
Flowpath height, b_f/h_m	3.75	06–0.8
Flowpath width, b_f/B_f	0.02	0.03–0.05
Vegetation volume fraction, ϕ	0.05–0.2	0.1
Velocity ratio, U_f/U_s	14–20	6–15
Fraction of flow in flowpath, q_f/Q	0.2–0.7	0.25–0.35
Jet Reynolds number, $Re_j = U_f h_m/\nu$	20,000	7,000–12,000
Marsh Reynolds number, $Re_m = Q/B_f\nu(1-\phi)$	4000	1000
Froude number, $Fr = symUjet/\sqrt{gh}$	0.01	0.01–0.02

Table 3.3: Best-fit parameter values for numerical simulations of jet development parameters, calculated as the value that produces the lowest sum of squared residuals when compared to measurements of jet width and centerline velocity (Figs. 3-21 and 3-21). The reported uncertainty is the change that creates a 5% change in the sum of squared residuals.

	$b_f = 4$ cm		$b_f = 6$ cm	
No distributed drag				
Constant α_e	-	$\alpha_e = 0.38 \pm 0.02$	-	$\alpha_e = 0.35 \pm 0.02$
$\frac{db_u}{dx} = \beta_u$	-	$\beta_u = 0.19 \pm 0.01$	-	$\beta_u = 0.24 \pm 0.02$
$\frac{db_u h}{dx} = \beta_u h$	-	$\beta'_u = 0.28 \pm 0.02$	-	$\beta'_u = 0.31 \pm 0.01$
Distributed drag present				
Constant α_e	$C_d a h_m = 0.002 \pm 0.001$	$\alpha_e = 0.34 \pm 0.02$	$C_d a h_m = 0.002 \pm 0.001$	$\alpha_e = 0.30 \pm 0.02$
$\frac{db_u}{dx} = \beta_u$	$C_d a h_m = 0.002 \pm 0.001$	$\beta_u = 0.23 \pm 0.03$	$C_d a h_m = 0.006 \pm 0.004$	$\beta_u = 0.24 \pm 0.02$
$\frac{db_u h}{dx} = \beta_u h$	$C_d a h_m = 0.002 \pm 0.001$	$\beta'_u = 0.34 \pm 0.02$	$C_d a h_m = 0.007 \pm 0.002$	$\beta'_u = 0.31 \pm 0.02$

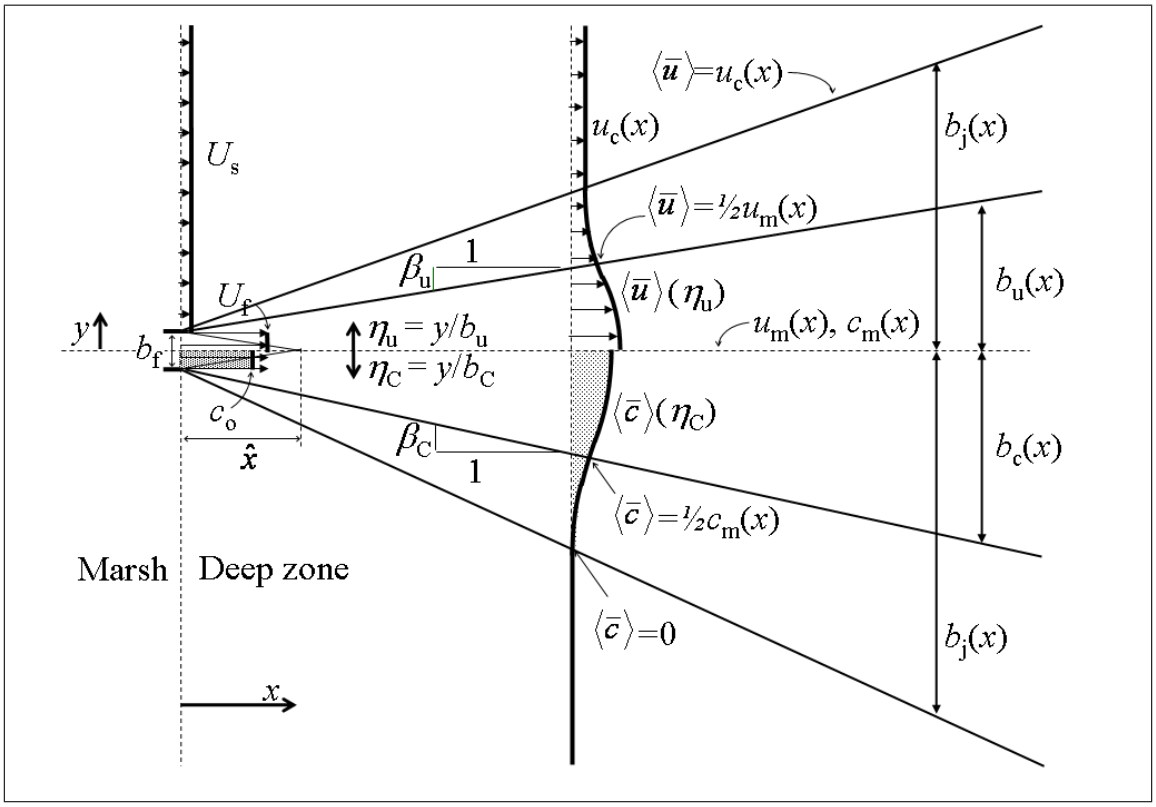

Figure 3-1: Definition sketch for variables within the planar jet created when a fast flowpath enters a deep zone. The origin of the coordinate system is located at the center of the flowpath exit. Variables pertaining to jet velocity are shown above the jet centerline; variables pertaining to jet concentration are shown below the centerline.

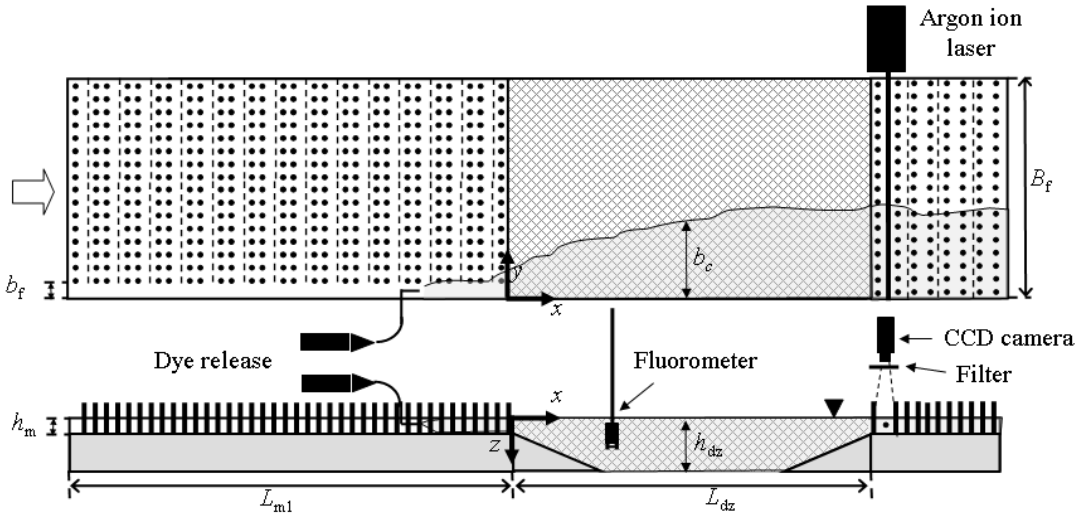

Figure 3-2: Laboratory model setup. Flow within a 1.2-m-wide flume passes through an array of vegetation mimics on a false bed; a narrow gap of width b_f is left between the array and one wall. The flow then travels down an entrance slope and into a deeper area of variable length, before flowing up an exit slope and leaving the model through another elevated array. Hatching indicates the location of added roughness. Dye is used to mark the water traveling within the fast flowpath within the upstream marsh region. A line laser source illuminates the dye within the flow for lateral LIF measurements.

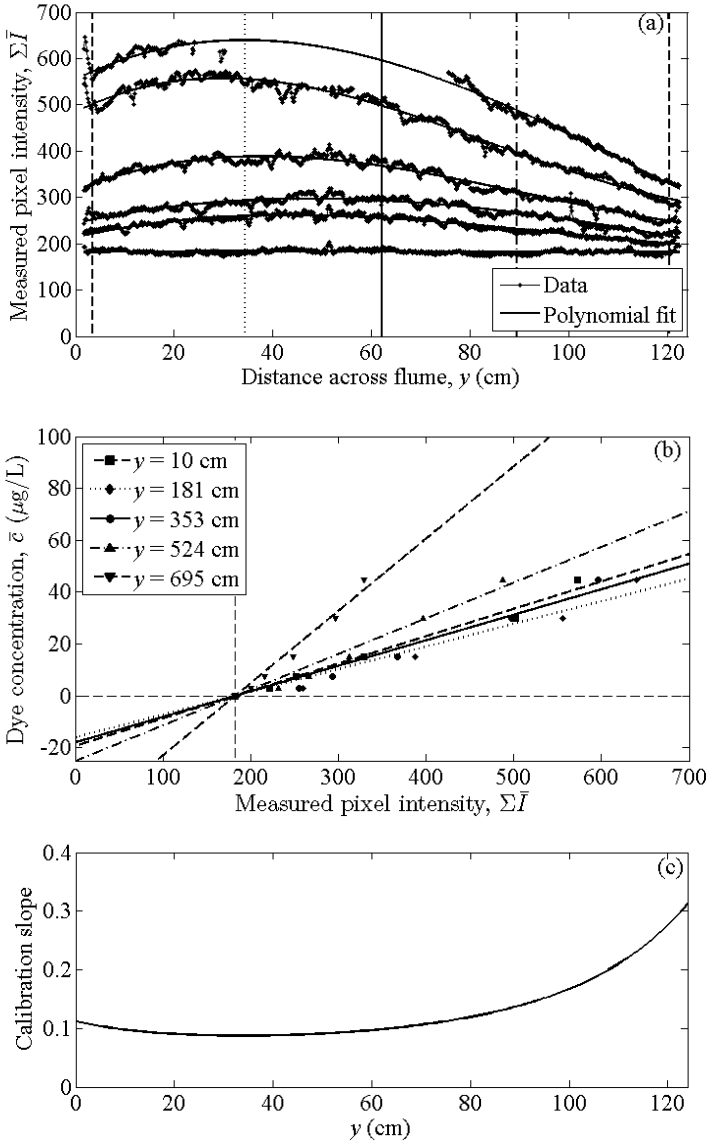

Figure 3-3: Calibration of laser-induced fluorescence method. (a) Intensity profiles of the excitation $0 \leq \bar{I}(y) \leq 256$ of different concentrations of Rhodamine WT measured by a downward-looking CCD camera. Intensity measurements are summed across four rows of pixels; the laser beam is less than one pixel wide. The raw data and a smooth polynomial fit to the data are shown. (b) Comparison between dye concentration and smoothed pixel intensity at several locations across the flume, which are shown as vertical lines in Fig. 3-3a. Thin vertical and horizontal dashed lines indicate the position of the background intensity. The straight lines are best-fit regressions to these data. (c) Slope of the straight lines in Fig. 3-3b as a function of distance across the flume. These slopes were used to calculate the dye concentration for a measured intensity above background.

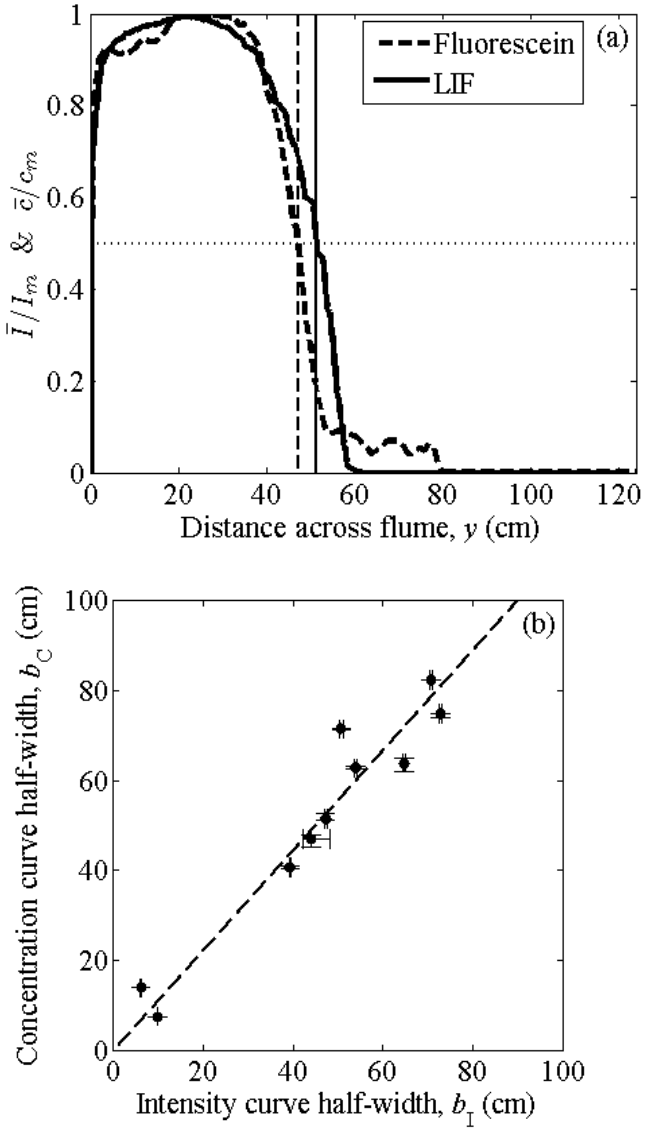

Figure 3-4: Calculation of concentration half-width from photographs of fluorescent dye. (a) Sample profiles of fluorescein dye intensity $\bar{I}(y)$ from color photographs and LIF measurements of Rhodamine concentration $\bar{c}(y)$, both normalized by their respective maximum values at this longitudinal position. The locations of the intensity half-width b_I and the concentration half-width b_C are marked by vertical lines. (b) Comparison between the half-width measured from fluorescein dye intensity and the half-width measured from LIF with Rhodamine. Horizontal and vertical lines indicate uncertainty in the width measurements. The dashed line shows the best-fit linear correlation between the two measurements, $b_C = 1.11 b_I$ ($r^2 = 0.93$).

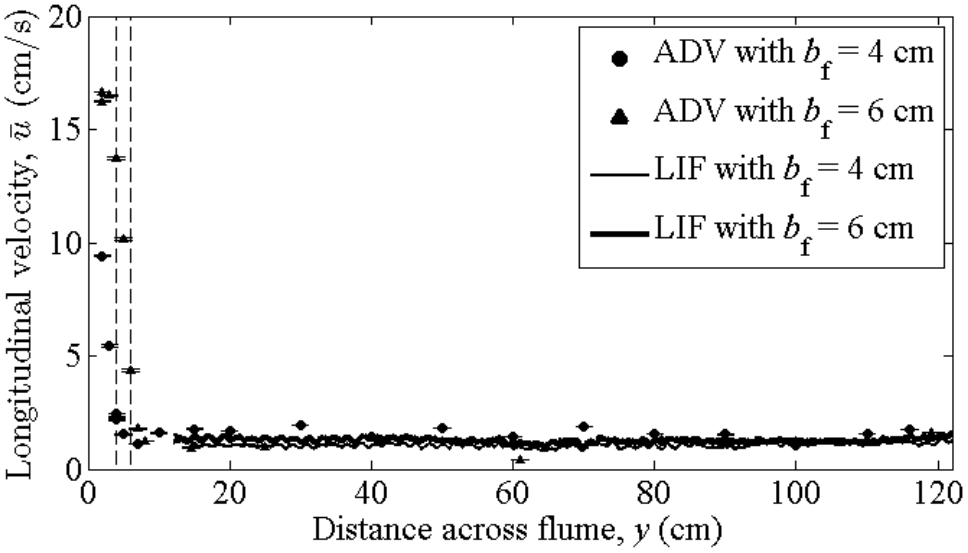

Figure 3-5: Profiles of cumulative travel time distributions within a laboratory deep zone. LIF velocity measurements for $y < 8$ cm are not shown, due to their high relative error. Vertical bars indicate standard deviation of the ADV velocity measurements. Thin lines indicate uncertainty in LIF dye travel time measurements.

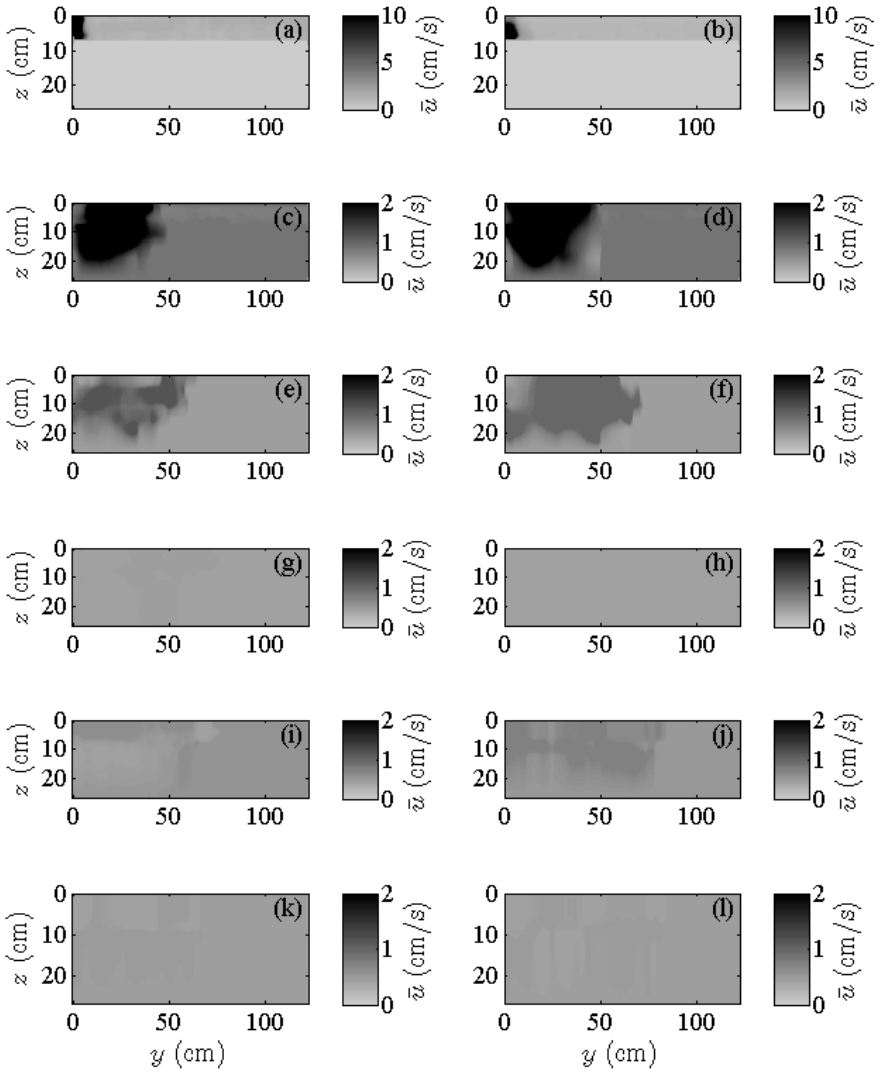

Figure 3-6: Distribution of flow velocity over flume depth and width. Color indicates flow speed as measured by dye travel time. (a) $x = 0, b_f = 4$ cm; (b) $x = 0, b_f = 6$ cm; (c) $x = 50$ cm, $b_f = 4$ cm; (d) $x = 50$ cm, $b_f = 6$ cm; (e) $x = 130$ cm, $b_f = 4$ cm; (f) $x = 130$ cm, $b_f = 6$ cm; (g) $x = 190$ cm, $b_f = 4$ cm; (h) $x = 190$ cm, $b_f = 6$ cm;(i) $x = 260$ cm, $b_f = 4$ cm; (j) $x = 260$ cm, $b_f = 6$ cm; (k) $x = 350$ cm, $b_f = 4$ cm; (l) $x = 350$ cm, $b_f = 6$ cm. Note that in panels (a) and (b) the flume depth is only 7.2 cm and the velocity scale is 0–10 cm/s. Thin horizontal lines indicate the vertical locations of LIF measurements.

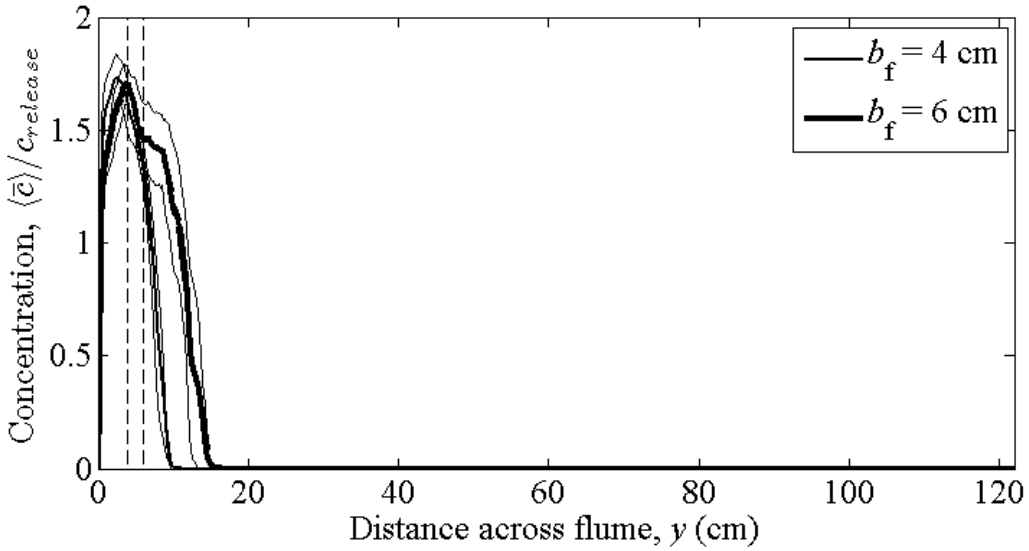

Figure 3-7: Depth- and time-averaged concentration profiles entering the laboratory deep zone, normalized by the expected release concentration $c_{release} = j_{release}/q_f$. Thin lines indicate uncertainty in these LIF measurements.

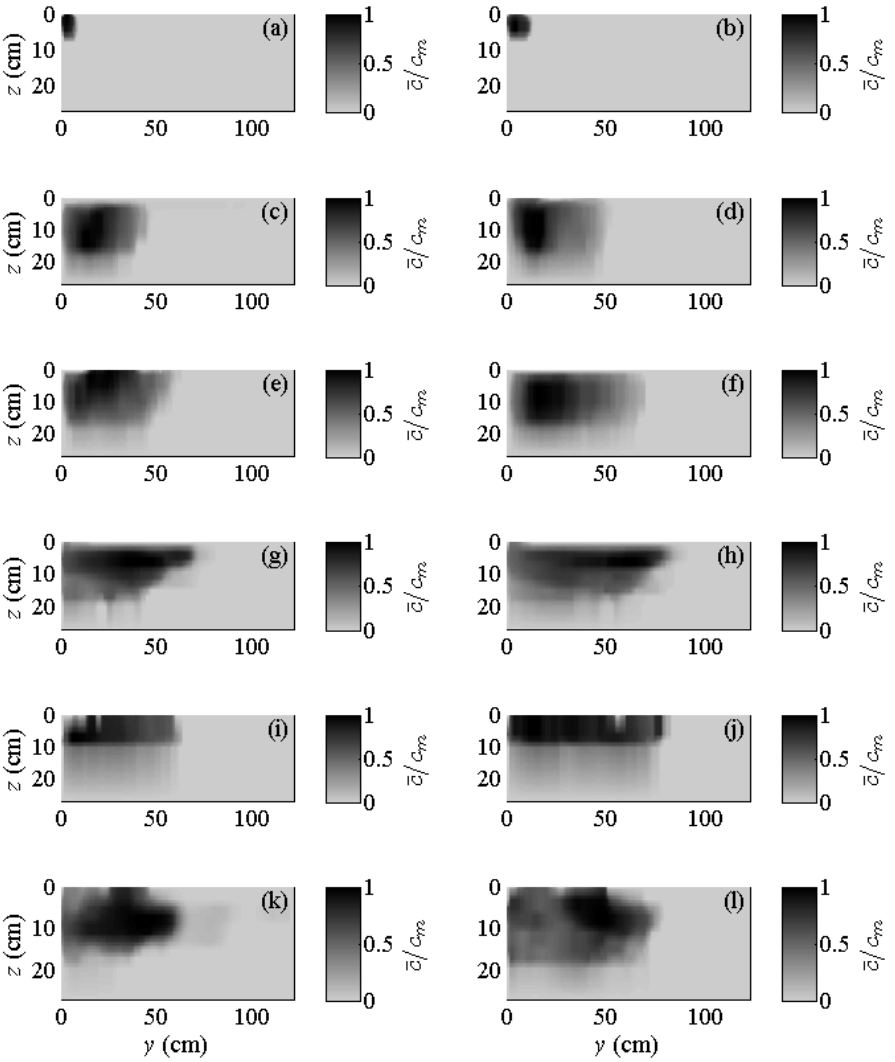

Figure 3-8: Distribution of tracer concentration over flume depth and width at the entrance to the deep zone. Color indicates concentration, normalized by the peak concentration measured at that longitudinal location. (a) $x = 0, b_f = 4$ cm; (b) $x = 0, b_f = 6$ cm; (c) $x = 100$ cm, $b_f = 4$ cm; (d) $x = 100$ cm, $b_f = 6$ cm; (e) $x = 160$ cm, $b_f = 4$ cm; (f) $x = 160$ cm, $b_f = 6$ cm; (g) $x = 220$ cm, $b_f = 4$ cm; (h) $x = 220$ cm, $b_f = 6$ cm; (i) $x = 300$ cm, $b_f = 4$ cm; (j) $x = 300$ cm, $b_f = 6$ cm; (k) $x = 390$ cm, $b_f = 4$ cm; (l) $x = 390$ cm, $b_f = 6$ cm. Note that the flume depth is only 7.2 cm in panels (a) and (b). Panels (a), (b), (g), (h), (k), and (l) were taken during continuous releases; panels (c), (d), (e), (f), (i), and (j) were taken during instantaneous releases. Note that the flume depth is only 7.2 cm in panels (a) and (b). Thin horizontal lines indicate the vertical locations of LIF measurements.

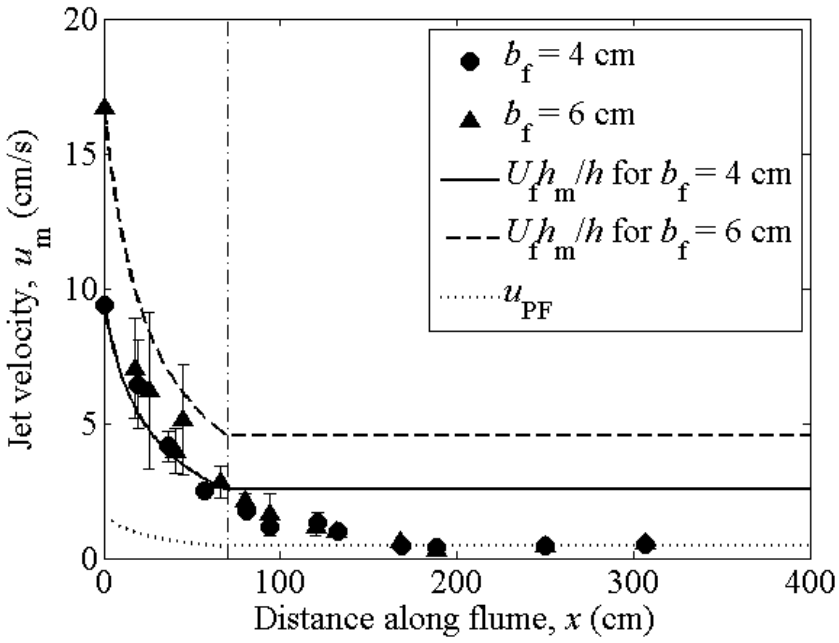

Figure 3-9: Measurements of the maximum dye travel velocity at various longitudinal positions within the deep zone. The measurements at $x = 0$ cm were obtained by ADV; all others were obtained using dye travel times. Vertical bars indicate uncertainty associated with the velocity measurements. The thin solid and dashed lines show the expected velocity due to vertical flow expansion. The thin dotted line is the plug flow velocity, u_{pf}. The vertical dash-dot line shows the end of the deep zone entrance slope at $x = 70$ cm.

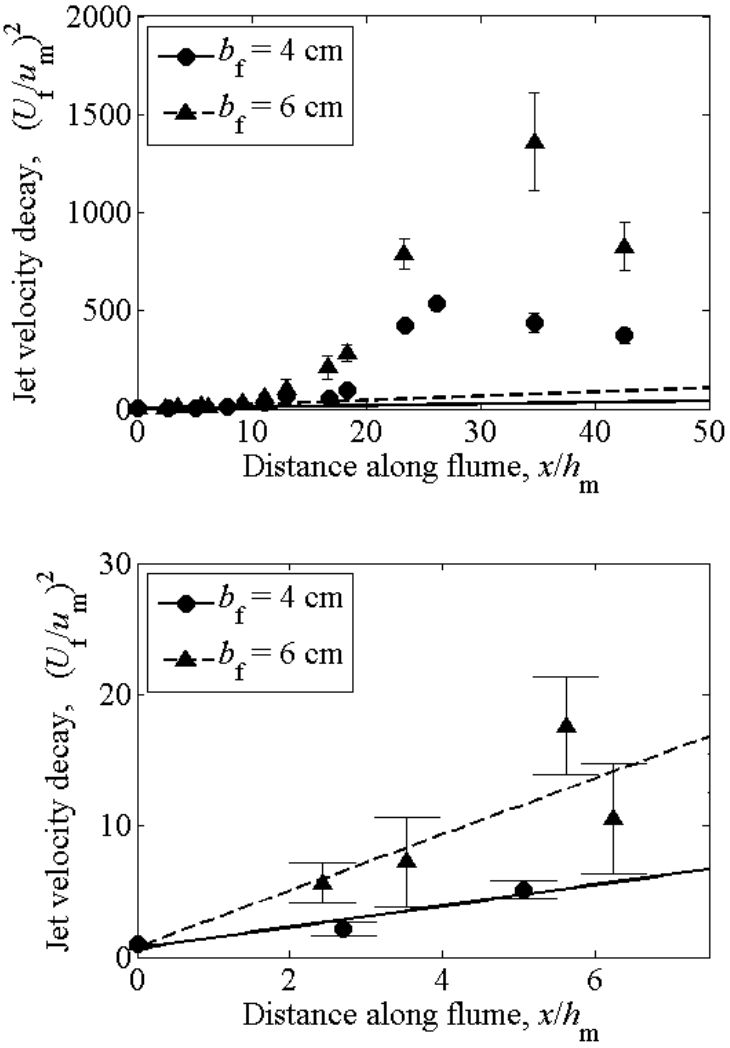

Figure 3-10: Decay of maximum velocity within the deep zone. (a) Data from Fig. 3-9, replotted in a manner that is expected to show a linear increase within a free planar jet. It is assumed that $\hat{x} = 0$. (b) Close-up of the linear region of the plot. The dashed straight lines in both plots are the best-fit lines to the subset of data shown in (b).

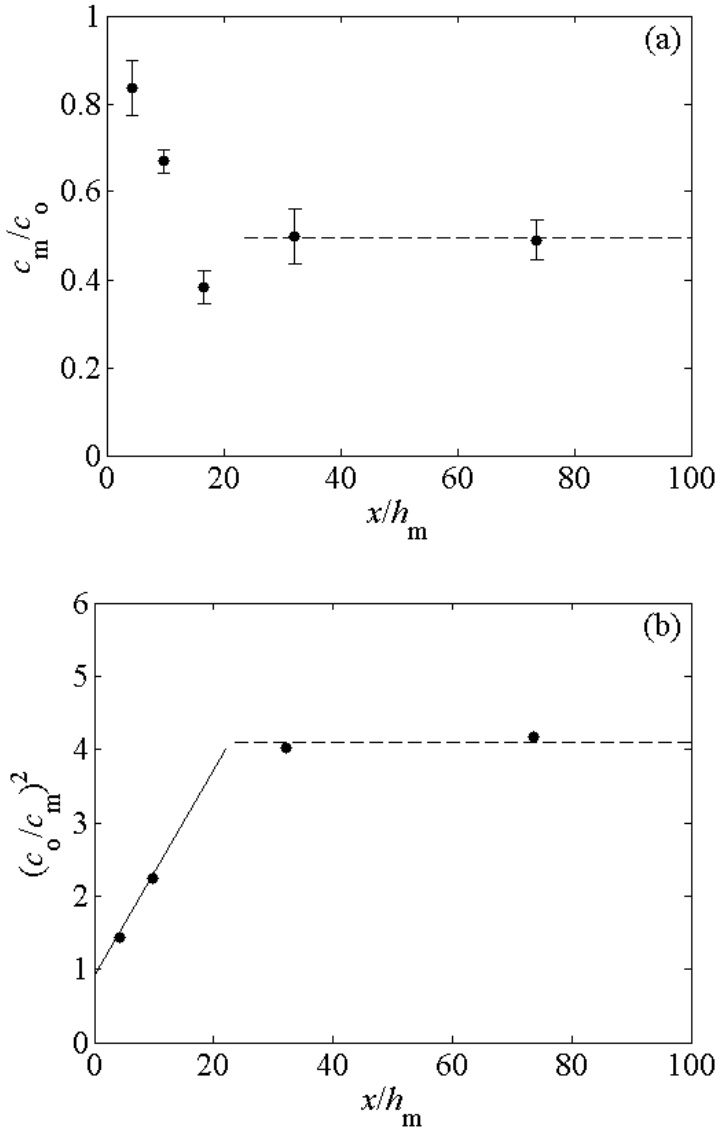

Figure 3-11: Decay of maximum concentration within the deep zone downstream of a continuous dye release. (a)Fluorometer measurements of the maximum concentration measured at various locations downstream of a continuous dye release. Vertical bars indicate uncertainty associated with the measurements. The dashed line is the average value for $x > 200$ cm. (b) Data from Fig. 3-11, replotted in a manner that is expected to show a linear increase within a free planar jet. The solid line is the best linear fit to the initial concentration increase; the dashed line is the average value for $x > 200$ cm.

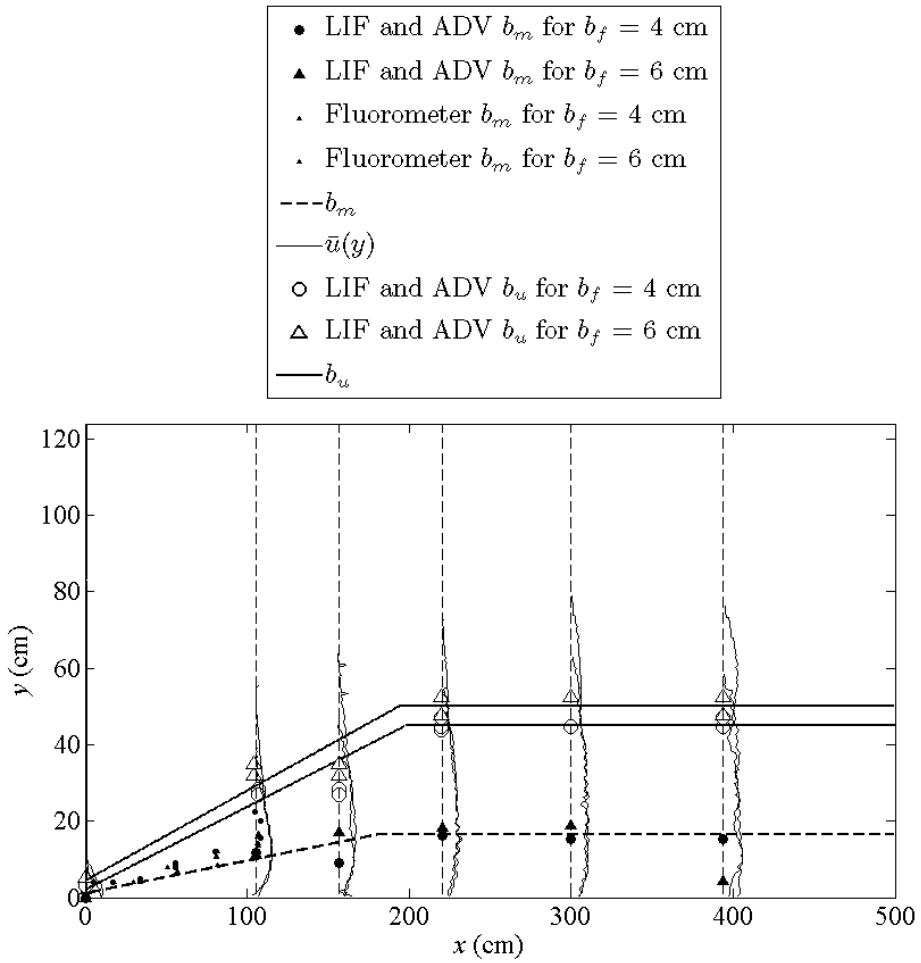

Figure 3-12: Average velocity profiles inferred from cumulative LIF travel time measurements at various locations (marked by vertical dashed lines) within the deep zone. The profiles are shown from the depth with the fastest maximum flow speed. Also shown are the lateral positions of the velocity maximum (b_m) and the velocity half-width of the jet (b_u) from various measurement techniques.

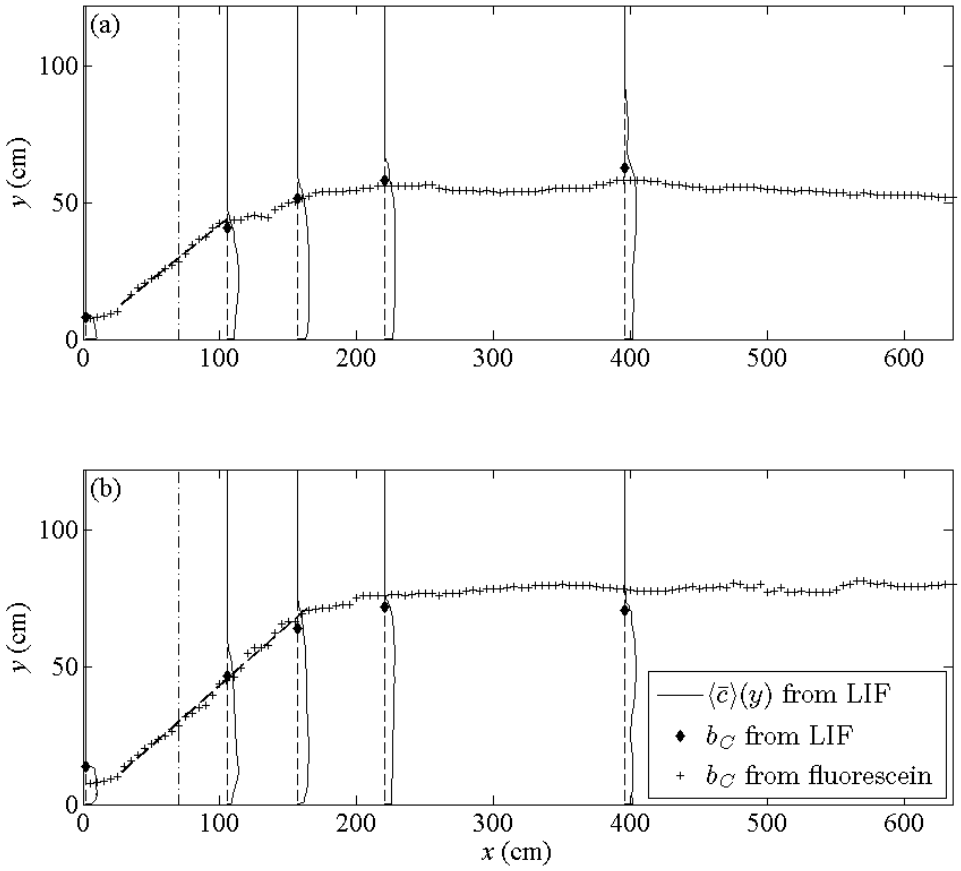

Figure 3-13: Concentration profiles at various locations (marked by vertical dashed lines) within the deep zone. The profiles are shown from the depth with the highest maximum concentration. Also shown are the lateral positions of the concentration half width b_C from both LIF and fluorescein photographs. Results are shown for both upstream flowpath widths: (a) $b_f = 4$ cm and (b) $b_f = 6$ cm. The vertical dash-dot line shows the end of the deep zone entrance slope at $x = 70$ cm. The diagonal dashed lines are the best linear fits to fluorescein b_C data.

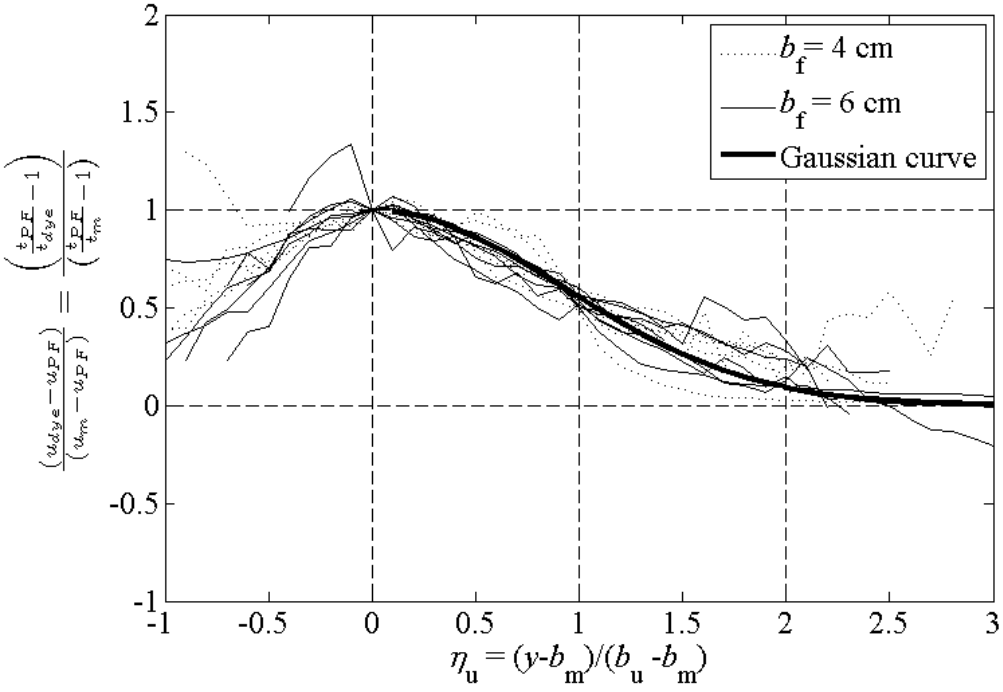

Figure 3-14: Normalized velocity profiles from cumulative travel times of instantaneous dye releases, plotted against a transverse distance normalized by the scaling expected within the outer region of the flow. The 16 profiles are from the depth with maximum velocity at x = 2–394 cm. The Gaussian profile compared to the velocity profiles within the outer region of the flow is $(\bar{u}(y)-u_{pf})/(u_m-u_{pf}) = \exp(-0.593\eta_u)$, which is the theoretical expectation for a free planar jet. Within the inner region of the flow, it is expected that $u_{dye} = 0$ at the wall.

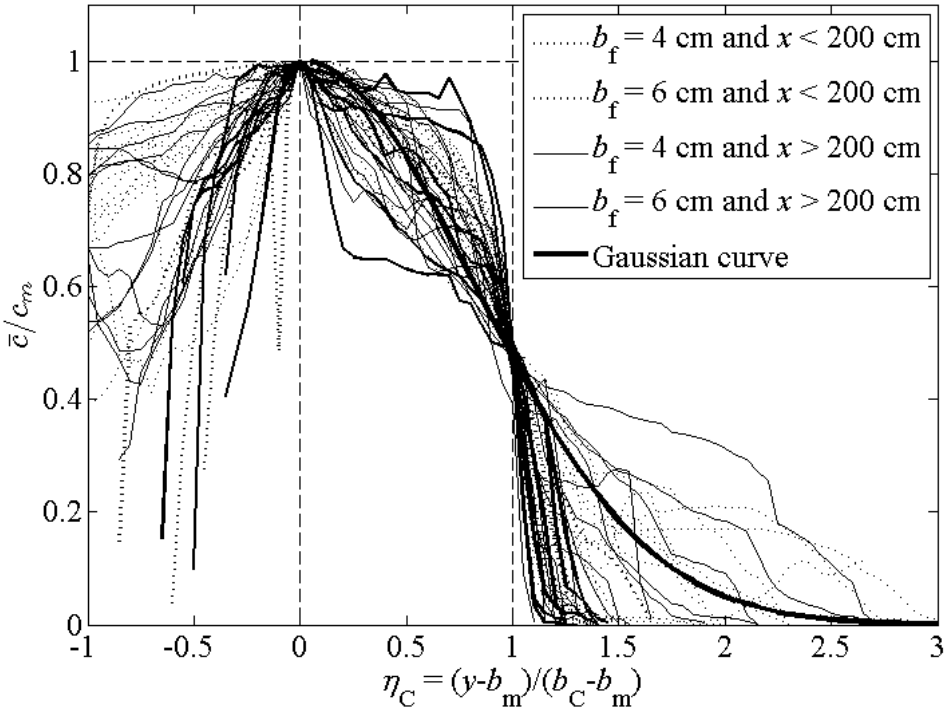

Figure 3-15: Normalized concentration profiles from continuous releases, plotted against a transverse distance normalized by the scaling expected within the outer region of the flow. The 43 profiles are from positions with $x = 2$–394 cm and $z = 1$–15 cm. The Gaussian profile compared to the concentration profiles within the outer region of the flow is $\bar{c}/c_m = \exp(-0.75\eta_C)$. Within the inner region of the flow, it is expected that $\frac{\mathrm{d}\bar{c}}{\mathrm{d}y} = 0$ at the wall.

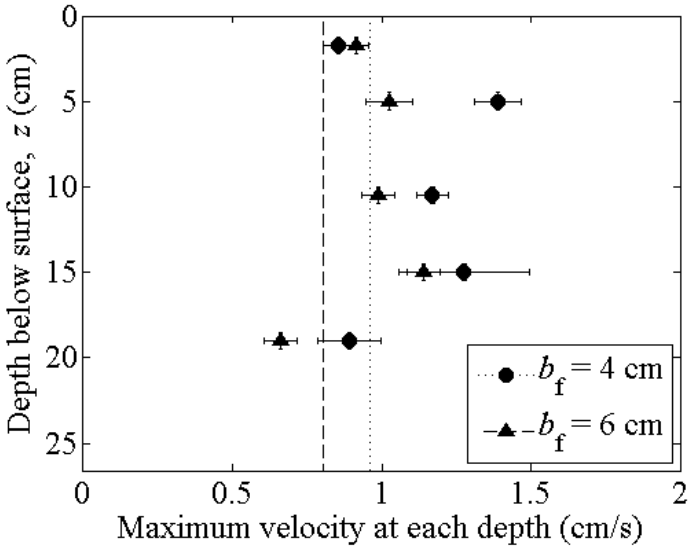

Figure 3-16: Sample vertical velocity profile within the jet. Each marker represents the lateral maximum velocity measured between $x = 105$ cm and $x = 150$ cm. Horizontal bars indicate the uncertainty associated with the subtraction of ensemble means. The vertical dashed lines indicate the depth-averaged velocity $\langle \bar{u} \rangle$, calculated assuming $\bar{u} = 0$ at $z = h_{dz}$.

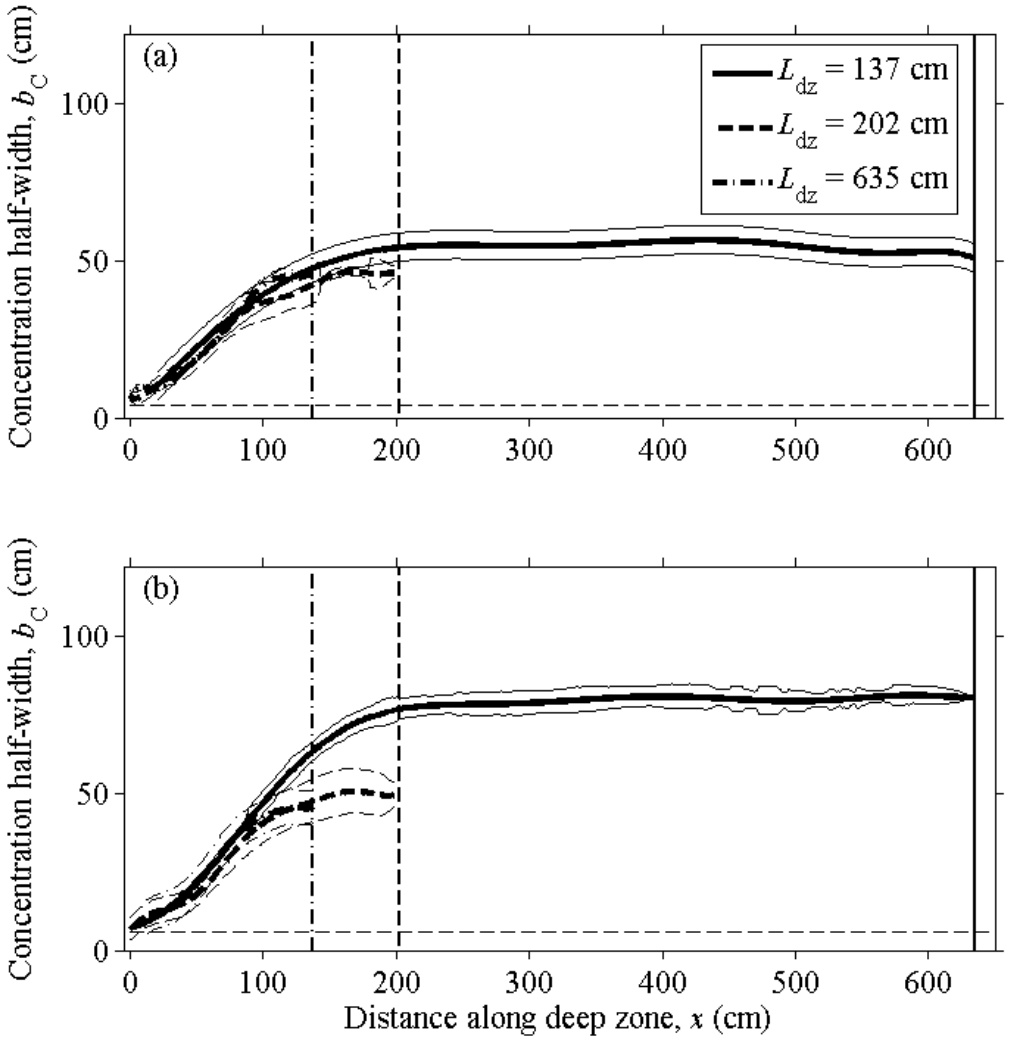

Figure 3-17: Half-width of the concentration jet from synoptic photographs of fluorescein dye for deep zones of different lengths, which are marked by vertical dashed lines. Narrow lines indicate error associated with each width measurement. There is no flowpath located within the marsh area downstream. The width of the upstream flowpath is shown as a horizontal dashed line. (a) $b_f = 4$ cm and (b) $b_f = 6$ cm.

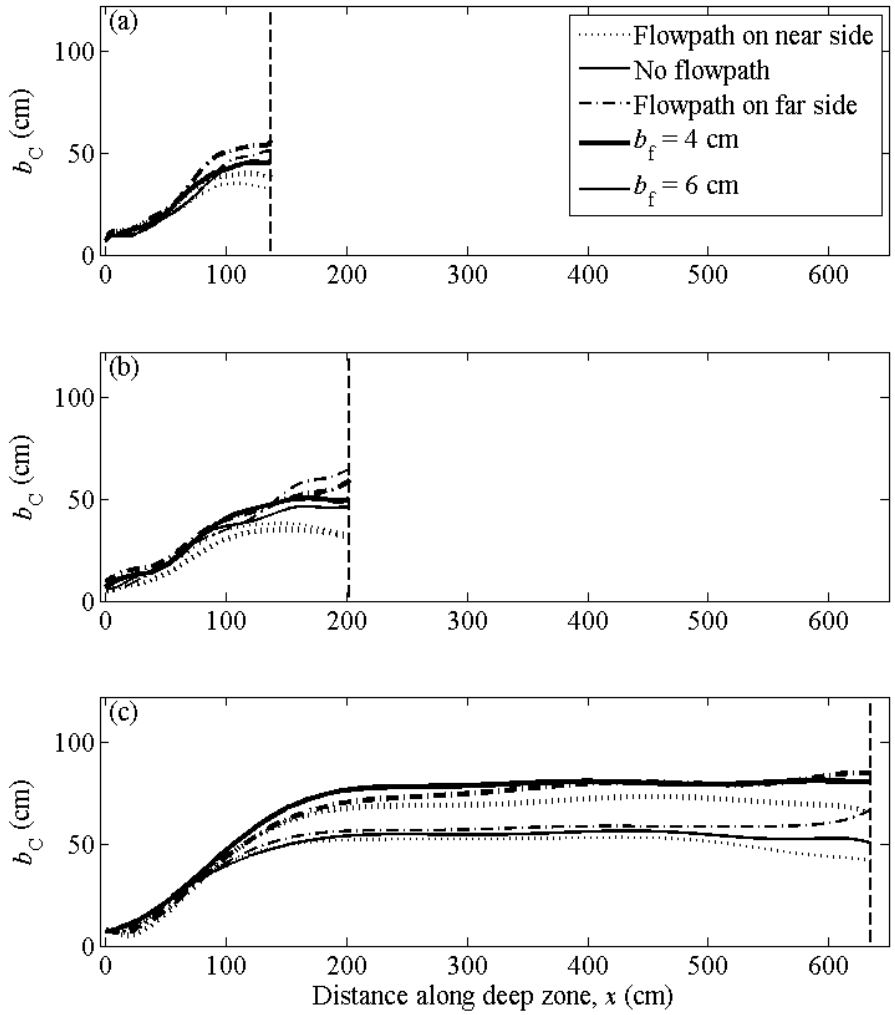

Figure 3-18: Half-width of the concentration jet from synoptic photographs of fluorescein dye for deep zones of different lengths: (a) $L_{dz} = 140$ cm, (b) $L_{dz} = 200$ cm, and (c) $L_{dz} = 635$ cm. The lines show results for different upstream flowpath widths and different downstream flowpath locations. In all cases the width of the downstream flowpath matches that of the upstream flowpath. Uncertainty in concentration half-widths is ± 4 cm.

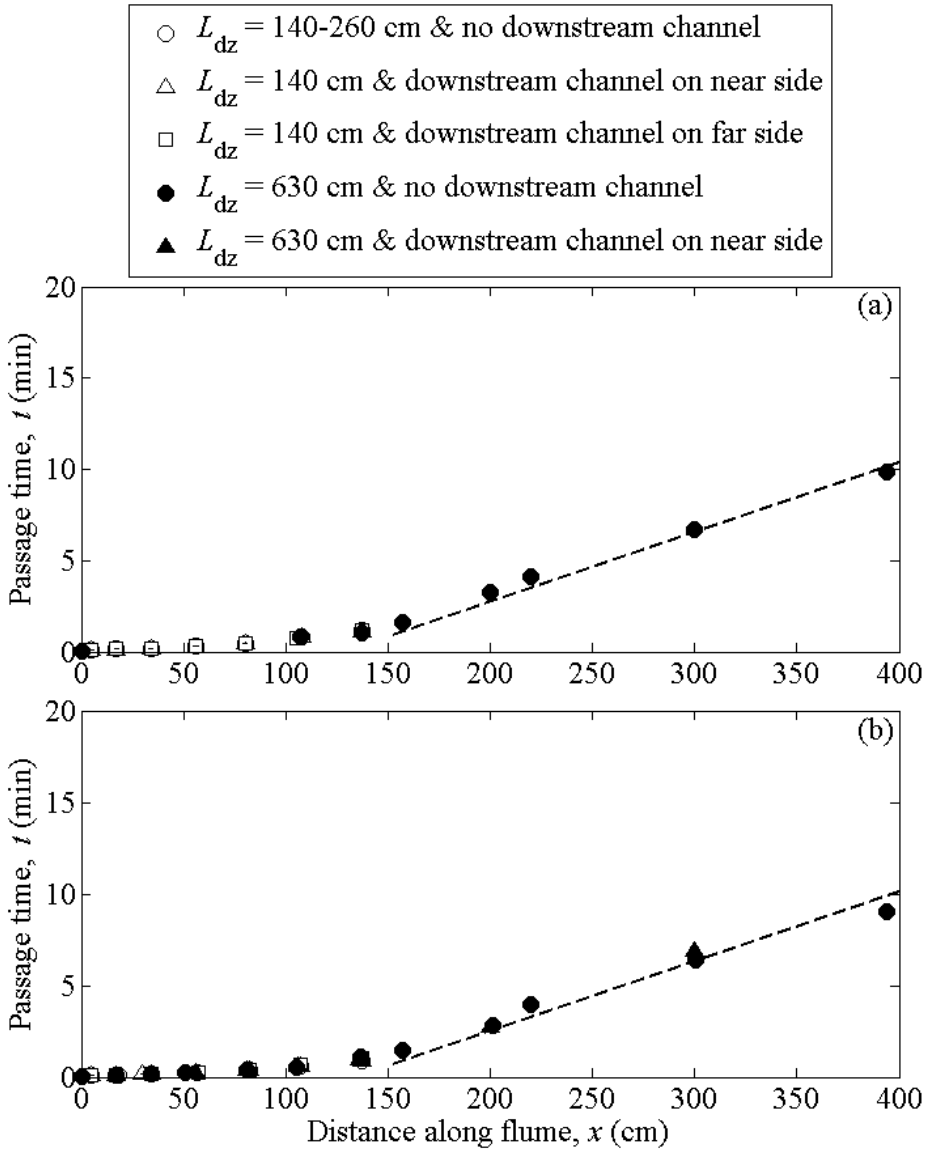

Figure 3-19: Data from both fluorometer and LIF measurements of dye passage time to various longitudinal locations within the model deep zone. Standard error of the means are smaller than the size of the markers. Measurements are shown for different lengths of deep zones and for different downstream flowpath positions. The slope of the diagonal dashed lines indicates the plug flow time of travel based on the flume flow rate.

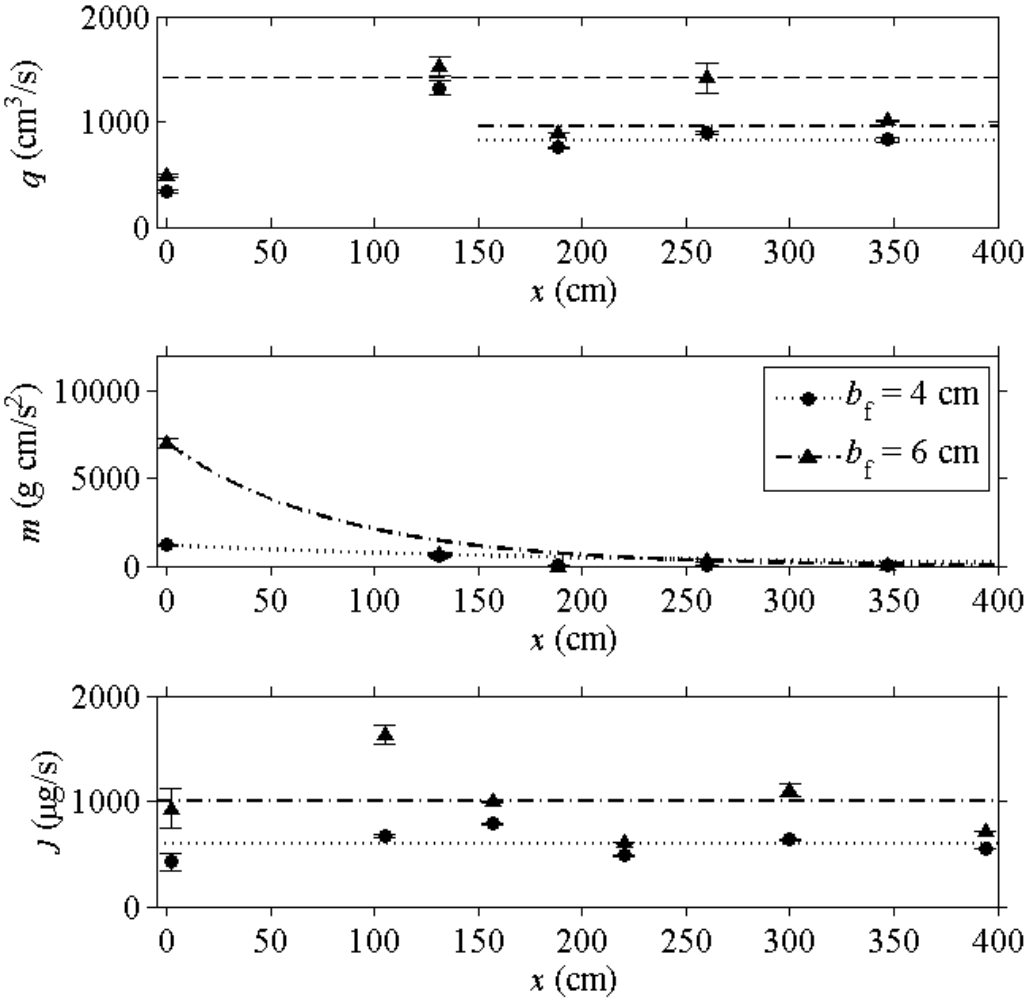

Figure 3-20: Measurements of integral jet parameters at various locations downstream, integrated from the wall to where the jet velocity is indistinguishable from the co-flow velocity. Velocity measurements at $x = 0$ cm were obtained by ADV; all others were obtained using dye travel times. (a) Jet volumetric flow rate, $q_j = \int_0^{b_j} h\langle\bar{u}\rangle \, \mathrm{d}y$. The circled data points are used to calculate the far-field jet flow rates, which are shown by horizontal lines. The thin horizontal dashed line is the total flume flow rate Q_f. (b) Jet excess momentum flux, $m = \int_0^{b_j} \rho_w h\langle\bar{u}\rangle(\langle\bar{u}\rangle - u_c) \, \mathrm{d}y$. The two lines are $m = (1200 \text{ g cm/s}^2)\exp(-0.12x/h)$ and $m = (7000 \text{ g cm/s}^2)\exp(-0.32x/h)$. (c) Jet mass flux, $J = \int_0^{b_j} h\langle\bar{u}\rangle\langle\bar{c}\rangle \, \mathrm{d}y$. The horizontal lines are the mean mass fluxes for each flowpath width. Vertical bars indicate uncertainty associated with the numerical integration.

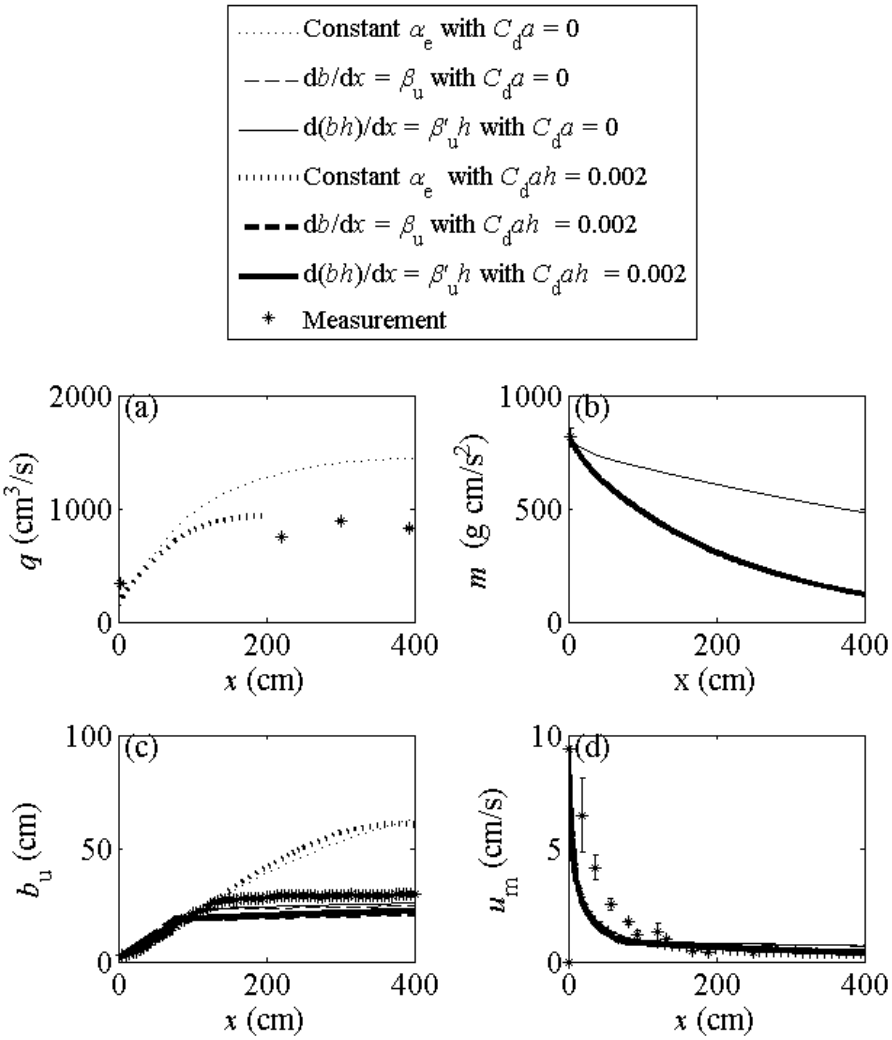

Figure 3-21: Comparison between laboratory measurements and theoretical predictions of jet parameters for an upstream flowpath width $b_f = 4$ cm. For each drag assumption, three model predictions are shown based on different entrainment assumptions. Vertical bars indicate uncertainty in the measured parameters. (a) Jet volumetric flow rate $q_j = \int_0^\infty h\langle\bar{u}\rangle \, dy$. Lines are drawn only for regions where predicted $\frac{dq_j}{dx} > 0$. (b) Jet excess momentum flux, $m = \int_0^\infty \rho_w h\langle\bar{u}\rangle(\langle\bar{u}\rangle - u_c) \, dy$. (c) Jet velocity half-width b_u, calculated from the jet concentration half-width measurements. (d) Jet centerline velocity u_m. It was assumed that $C_f = 0.012$, $C_w = 0.0053$, $I_u = 1.01$, and $I_{uu} = 1.47$. The best-fit parameter values are shown in Table 3.3.

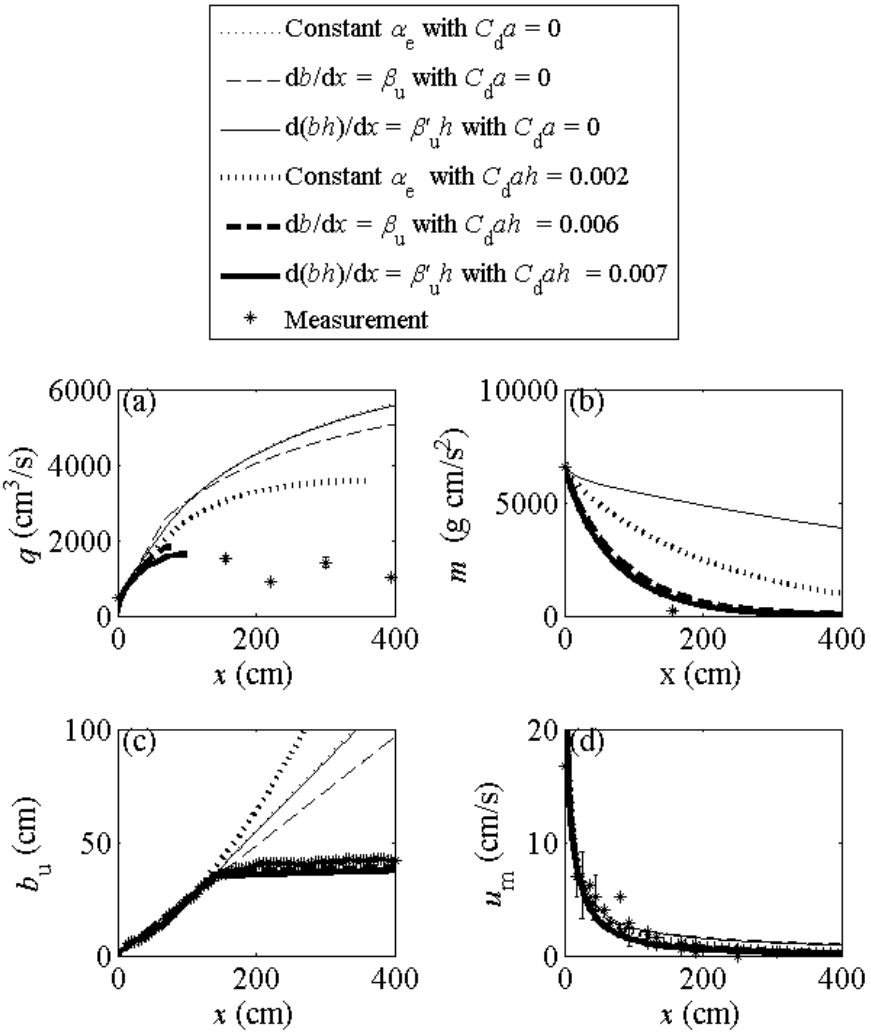

Figure 3-22: Comparison between laboratory measurements and theoretical predictions of jet parameters for an upstream flowpath width $b_f = 4$ cm. For each drag assumption, three model predictions are shown based on different entrainment assumptions. Vertical bars indicate uncertainty in the measured parameters. (a) Jet volumetric flow rate $q_j = \int_0^\infty h\langle\bar{u}\rangle \, dy$. Lines are drawn only for regions where predicted $\frac{dq_j}{dx} > 0$. (b) Jet excess momentum flux, $m = \int_0^\infty \rho_w h\langle\bar{u}\rangle(\langle\bar{u}\rangle - u_c) \, dy$. (c) Jet velocity half-width b_u, calculated from the jet concentration half-width measurements. (d) Jet centerline velocity u_m. It was assumed that $C_f = 0.012$, $C_w = 0.0053$, $I_u = 1.01$, and $I_{uu} = 1.47$. The best-fit parameter values are shown in Table 3.3.

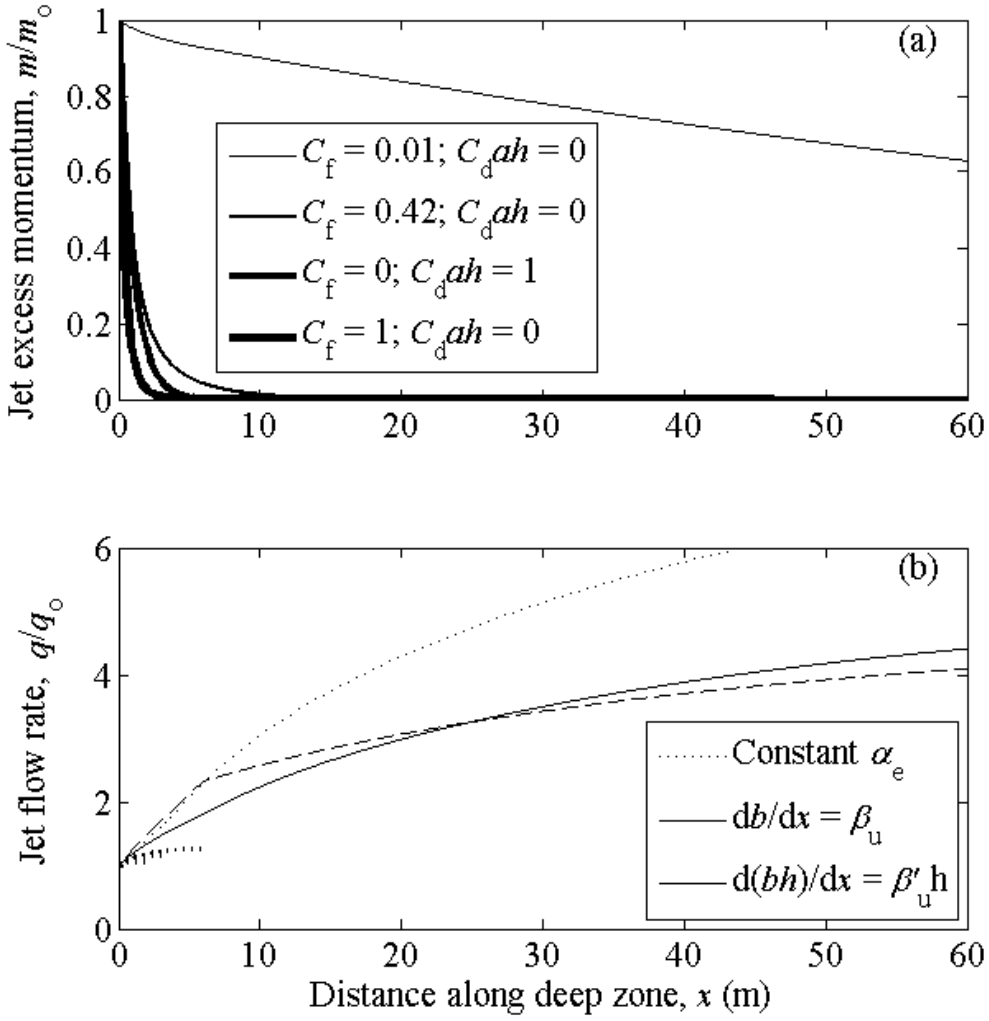

Figure 3-23: Comparison of the predicted behavior of the jet formed by a fast flowpath within a downstream deep zone under various drag conditions. (a) Momentum losses with different values of bed drag and in the presence and absence of a distributed drag. Results from the three different entrainment scenarios are indistinguishable. (b) Jet volumetric flux for the same drag scenarios, which are indicated by the same line widths. Results from three different entrainment scenarios are presented. It is assumed that $\alpha_e = 0.35$, $\beta_u = 0.22$, $\beta'_u = 0.29$, $b_f = 2$ m, $u_{m,o} = 3$ cm/s, $u_c = 0.1$ cm/s, $h_m = 0.4$ m, $h_{dz} = 1.4$ m, and $L_{slope} = 6$ m.

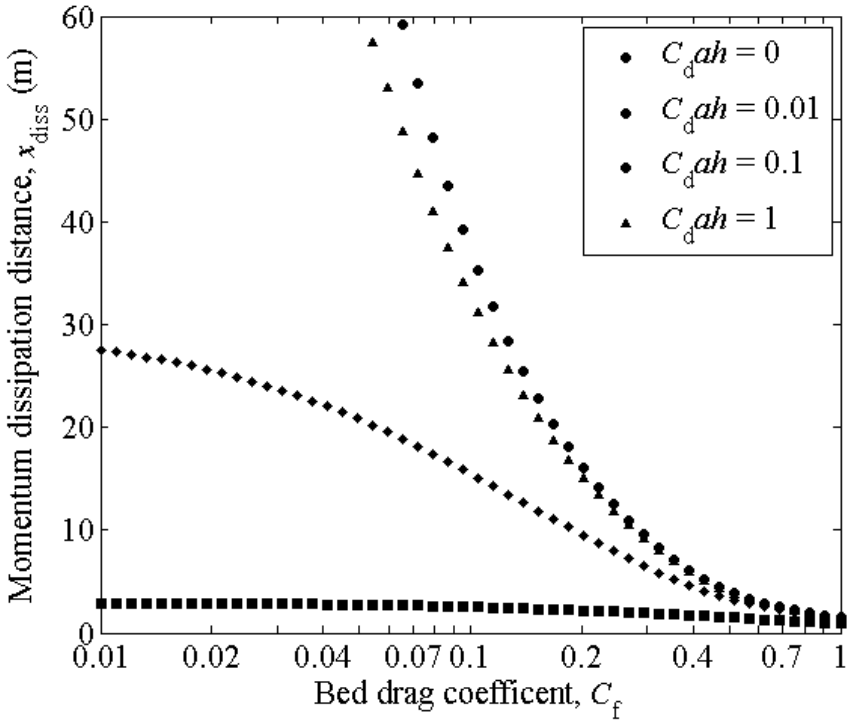

Figure 3-24: Predicted momentum dissipation distance as a function of drag within the deep zone. The dissipation distance x_{diss} is estimated as the longitudinal location where $m/m_o < 0.05$ using the model parameters shown in Fig. 3-23. Note that the x-axis has a logarithmic scale.

Chapter 4

Mathematical simulation of the effect of deep zones on the performance of short-circuiting constructed treatment wetlands

In this chapter, a mathematical model is developed to explore the effect on the outlet concentration of replacing a portion of a wetland marsh with deep water. The presence of one or more deep zones may in some circumstances improve the performance of a wetland segment; in other circumstances, performance may decrease. The Damkohler number of the wetland, the dimensions and number of deep zones, the amount of short-circuiting that is present, the location of fast flowpaths, and the removal rate within and the location and number of deep zones affect whether the deep zones. First, the model developed by Lightbody et al. (2007) is explained; this model assumes a single laterally mixed deep zone. This model is then extended to consider incomplete lateral mixing and the presence of multiple deep zones.

4.1 Conceptual basis for model

Observations of flow within the Augusta wetland found that two distinct flow speeds were present within dense marsh regions, and that the fast flow was carried by narrow, continuous fast flowpaths that exhibited only limited exchange with the surrounding vegetation (Sec. 2.3.1). Dispersion was present within the fast flowpaths (Fig. 2-9b), likely caused by retardation of fluid in the dense vegetation on either side of the flowpath, but laboratory observations confirm that such exchange is limited to a small region immediately adjacent to a fast flowpath so is unlikely to affect the majority of flow through a marsh (Sec. 3.4.1 and Su and Li, 2002). As a result of these observations, the model presented here uses parallel and non-interacting systems of tanks in series (TIS) to explicitly represent the fast and slow flow within a short-circuiting marsh region of a wetland under steady flow conditions (cf. Sec. 1.6.7 and Fig. 1-2f). Several previous models of flow through wetlands have also used parallel trains ofTIS or, equivalently, parallel plug flow reactors with dispersion (Kadlec and Knight, 1996; Kadlec, 2000; Dierberg et al., 2005; Wörman and Kronnäs, 2005; Wang and Jawitz, 2006). Two parallel non-interacting flowpaths is a simplification of the infinite number of stream tubes that Carleton (2002) used in his stochastic-convective flow representation of the travel time through a marsh system. Similarly, simplification of a complex flow-field into two characteristic flow speeds has been found to represent observed flow patterns in heterogeneous groundwater flows (Rubin, 1995). Some wetlands may exhibit more than two flow speeds (e.g., Kadlec, 2000); the approach presented here could be extended with additional parallel compartments to represent these additional flows.

In the Augusta wetland, grading was used to remove site microtopography, plant species were planted in uniform distributions throughout marsh regions, marsh vegetation appeared uniform, and the marsh had a uniform flow depth (Sec. 2.1). However, observations four to six years after the wetland cells began operation revealed that narrow fast flowpaths had developed and carried a large fraction (20–70%) of the flow through marsh regions (Sec. 2.3.1). In analogy to tidal creek evolution, in which

tidal fluxes enhance small perturbations in the topography of the marsh platform (D'Alpaos et al., 2006), it is assumed that the development of velocity heterogeneity and fast flowpaths is inevitable and spontaneous but random, so it is impossible to predict the locations of the flowpaths in advance. These flowpaths are moreover assumed to be narrow, to have the same depth as the slow-flow zones, and to carry an equal fraction of the flow in all marsh sections. For simplicity, fast flowpaths are assumed to be evenly distributed across the wetland, and the model represents a narrow subfraction of a wide wetland; this subfraction consists of a single flowpath and the surrounding vegetation with periodic lateral boundary conditions.

This model also assumes that the excess momentum within the flow exiting a short-circuiting flowpath completely dissipates before impinging on the downstream marsh section, as was found in the Augusta wetland (Sec. 2.3.2). Similarly, Brueske and Barrett (1994) report that water velocities within a small constructed wetland rapidly decayed to background levels within 20 m of the inlet. Detailed studies of flow patterns in the laboratory model show that downstream of the momentum dissipation distance a jet ceases to entrain fluid and is advected at the mean flow speed (Sec. 3.4.2). It was also observed that, except close to the downstream end of the deep zone, the location of downstream fast flowpaths does not affect jet width or flow velocities (Sec. 3.4.3). Therefore, the deep zone is assumed long enough that the location of the fast flowpath within any marsh section is independent of the location of flowpaths upstream or downstream. In addition, because the jet momentum is dissipated quickly, the residence time within the deep zone for all water can be approximated by the nominal hydraulic residence time (HRT). In addition, the flow rate through the jet and the non-jet water is simply related to their relative width within the bulk of the deep zone.

In the field, the wind produced lateral mixing, such that the water that passed through fast flowpaths was nearly completely mixed with the slow-flowing water exiting from the remainder of the marsh region before it exited the deep zone (Sec. 2.3.2). In the laboratory setup, in which wind was not present, lateral mixing was also present but was reduced to that provided by jet entrainment (Sec. 3.4.4). The model will con-

sider a range of mixing to represent both wind and non-wind conditions. Further, it is assumed that mixing is complete within the jet, so that by the time the jet fluid exits the deep zone it can be characterized by a single concentration. Detailed laboratory measurements of the concentration profile across an evolving jet exiting a fast flowpath showed that the concentration gradient at the edge of the jet is relatively high and so an assumption of a uniform concentration within the interior of the jet is relatively good (Fig. 3-8). In addition, it is assumed that all mixing occurs instantaneously at the entrance to the deep zone; when no removal is present within the deep zone it does not matter where mixing is assumed to occur. Finally, it is assumed that, unless they are entrained into the jet, streams of non-jet water do not mix as they flow through successive marsh and deep zone areas.

First-order removal will be considered here, since previous observations have found that it can describe the removal of many wetland contaminants (Sec. 1.4). When the removal rate is uniform across the wetland, then for a first-order removal process for a given residence time distribution (RTD) the expected outlet concentration will be equal no matter how the internal flow patterns are represented (Danckwerts, 1953; Werner and Kadlec, 2000). However, knowledge of the RTD is not sufficient if the removal rate is spatially homogeneous. The model here considers different removal rates in three different portions of the wetland (fast flowpaths, slow flow regions, and deep zones); other removal rates could be incorporated by designating more flow areas or applying a stochastic removal rate to different sections of marsh (cf. Kadlec, 2000).

4.2 Model development

4.2.1 Short-circuiting flow with no deep zones

First, consider a continuously vegetated marsh region of total length L with a constant total flow Q_f and first-order removal with inlet concentration c_o and background concentration $c*$ (cf. Fig. 4-1a). The marsh has average velocity $U_m = Q_f/B_f h_m(1-\phi)$, where B_f is the width of the marsh section, h_m the marsh water depth, and

ϕ the volume fraction of vegetation. The marsh residence time $T_m = L/U_m$ and the Damkohler number $Da = k_s T_m/h_m$, where k_s is the first-order areal removal rate in the slowly flowing marsh region. If no velocity heterogeneity is present, the outlet concentration c_e will be given by Eq. 1.16. Note that, as expected, Eq. 1.16 predicts that c_e will decrease as the number of equivalent TIS increases, indicating that performance improves as marsh longitudinal dispersion decreases.

When two flow speeds are present within the marsh, a portion, q_f, of the total flow Q_f travels in a fast flowpath of width b_f at speed U_f, while the remainder of the flow $q_s = Q_f - q_f$ travels through dense vegetation at a slower speed U_s. Let $T_f = L/U_f$ be the residence time of a parcel that enters a fast flowpath and $T_s = L/U_s$ the residence time of the water that flows through a slowly flowing vegetated zone. It can be shown algebraically that:

$$T_f = \frac{T_m}{\frac{q_f}{Q_f} + \left(1 - \frac{q_f}{Q_f}\right)\frac{U_f}{U_s}} \tag{4.1}$$

and:

$$T_s = \frac{T_m\left(\frac{U_f}{U_s}\right)}{\frac{q_f}{Q_f} + \left(1 - \frac{q_f}{Q_f}\right)\frac{U_f}{U_s}} \tag{4.2}$$

where:

$$\frac{q_f}{Q_f} = \frac{\frac{U_f}{U_s}}{\frac{U_f}{U_s} + \left(\frac{1}{b_f/B_f} - 1\right)} \tag{4.3}$$

is the fraction of flow in the fast flowpath. The exit concentration from the fast flowpath $c_{e,f}$ is given by:

$$c_{e,f} = (c_o - c*)\left(1 + \frac{k_f T_f}{h_m N_f}\right)^{-N_f} + c* \tag{4.4}$$

and the exit concentration from the slow-flow zone $c_{e,s}$ is:

$$c_{e,s} = (c_o - c*)\left(1 + \frac{k_s T_s}{h_m N_s}\right)^{-N_s} + c* \tag{4.5}$$

where k_f is the areal removal rate constant in the fast flowpath, N_f the equivalent number of TIS for the fast flowpath, and N_s the equivalent number of TIS for the slow-flow zone. The flow-weighted average concentration at the exit of the short-circuiting marsh region is then given by:

$$\begin{aligned} c_e &= \frac{q_f c_{e,f} + q_s c_{e,s}}{Q_f} \\ &= (c_o - c*)\left[\left(\frac{q_f}{Q_f}\right)\left(1+\frac{k_f T_f}{h_m N_f}\right)^{-N_f} + \left(1-\frac{q_f}{Q_f}\right)\left(1+\frac{k_s T_s}{h_m N_s}\right)^{-N_s}\right] + c* \end{aligned} \tag{4.6}$$

4.2.2 Short-circuiting marsh containing one laterally mixed deep zone with no removal

Next, consider what occurs when a portion of this marsh region is replaced by a deep zone of depth h_{dz} and length L_{dz} that stretches completely across the wetland (e.g., Fig. 4-1a). The residence time of the deep zone is $T_{dz} = V_{dz}/Q_f$, where $V_{dz} = h_{dz} L_{dz} B_f$ is the volume of the deep zone neglecting the entrance and exit slopes. This deep zone serves to separate the vegetated portion of the wetland into two regions, creating an upstream marsh of length L_{m1} and residence time $T_{m1} = L_{m1}/U_m$ and a downstream marsh of length L_{m2} and residence time $T_{m2} = L_{m2}/U_m$. The flowpath velocities U_f and U_s are unchanged, as is the average velocity U_m. If the deep zone immediately and completely mixes laterally and no removal occurs within the deep zone, then the concentration of water exiting the deep zone $c_{e,dz}$ is the mixed concentration leaving the marsh, i.e., $c_{e,dz} = c_e$ given above in Eq. 4.6. The water entering a subsequent downstream short-circuiting marsh will have the concentration exiting from the deep zone. Eq. 4.6 can be adapted to provide the average concentration at the end of a downstream short-circuiting marsh region:

$$c_e = (c_{e,dz} - c*)\left[\left(\frac{q_f}{Q_f}\right)\left(1+\frac{k_f T_{f2}}{h_m N_f}\right)^{-N_f} + \left(1-\frac{q_f}{Q_f}\right)\left(1+\frac{k_s T_{s2}}{h_m N_s}\right)^{-N_s}\right] + c* \tag{4.7}$$

where T_{f2} and T_{s2} are, respectively, the residence times of the fast and slow flow zones within the second marsh section. Eqs. 4.1, 4.2, 4.6, and 4.7 allow the computation

of the exit concentration from a wetland containing a fully laterally mixed interior deep-zone area bracketed by two marsh regions.

4.2.3 Short-circuiting marsh containing one deep zone with incomplete lateral mixing and no removal

When the deep zone is only partially laterally mixed, then only a portion of the slow-flowing water mixes with the water that traveled through the fast flowpath (Fig. 4-3). To parameterize the mixing present within the deep zone, the mixing coefficient λ is used to represent the fraction of water that traveled through the vegetated slow-flow zone that is mixed with the water that traveled through the fast flowpath; for simplicity, the mixed flow will be called the jet even after its excess momentum is dissipated. The total flow rate associated with the jet is $q_j = q_f + \lambda q_s$. When no mixing is present, $\lambda = 0$; when complete lateral mixing is present, $\lambda = 1$. Since it is assumed here that the flow is mixed over depth and reaches the background plug flow velocity before it enters the downstream marsh section, from continuity the width of the jet within the deep zone depends on the lateral mixing, and the final jet width $b_j/B_f = q_j/Q_f = q_f/Q_f + \lambda\,(1 - q_f/Q_f)$. When no biogeochemical processes occur within the deep zone, the concentration $c_{e,j}$ of the jet water when it exits the deep zone is the flow-weighted average of the concentration exiting the fast- and slow-flow zones:

$$c_{e,j} \;=\; \frac{q_f c_{e,f1} + \lambda q_s c_{e,s1}}{q_j} \tag{4.8}$$

where $c_{e,f1}$ and $c_{e,s1}$ are given by Eqs. 4.4 and 4.5. The water in the remainder of the deep zone exits with a concentration of

$$c_{e,k} = c_{e,s1} \tag{4.9}$$

when no removal occurs within the deep zone. The flow rate at this concentration is $q_k = (1 - \lambda)q_s$, where the subscript k indicates that this water is not in the jet.

When this flow reaches the downstream edge of the deep zone, a fraction q_f/Q_f enters a fast flowpath within the downstream marsh section. The parameter $0 \leq \psi \leq 1$ is introduced to represent the fraction of water from the jet that enters this downstream flowpath (Fig. 4-1). That is, the flow rate of jet water that enters the downstream flowpath is ψq_j and the flow rate of jet water that enters the slow-flow zone downstream is $q_{kb} = (1-\psi)q_j$ (Fig. 4-3). When $\psi = 1$, the flowpaths perfectly align; when $\psi = 0$, all the water that passed through the upstream fast flowpath enters dense vegetation downstream.

Because all momentum is rapidly dissipated within the deep zone, continuity dictates that there is a simple geometric relationship between the separation distance between two fast flowpaths and the amount of flow between them. Consider two fast flowpaths with centerlines at the lateral locations of y_1 and y_2 with a minimum separation distance $b_\delta = |y_1 - y_2|$ (see Fig. 4-1). The nondimensional variable $\delta = \frac{b_\delta}{B_f}$ is introduced to parameterize the separation distance between the flowpaths, where $0 \leq \delta \leq 0.5$ due to the periodic boundary conditions. (In a narrow wetland with only one short-circuiting flowpath then periodic boundary conditions would not be needed and $0 \leq \delta \leq 1$.) When all momentum is rapidly dissipated within the deep zone, then there is a simple linear relationship between the separation distance between these flowpaths and the amount of flow between them:

$$\psi = \begin{cases} \frac{q_f}{q_j}, & 0 \leq \delta \leq \frac{1}{2}\frac{q_j - q_f}{Q_f} \\ \frac{Q_f}{q_j}\left(\frac{1}{2}\frac{q_j+q_f}{Q_f} - \delta\right), & \frac{1}{2}\frac{q_j-q_f}{Q_f} < \delta \leq \frac{1}{2}\frac{q_j+q_f}{Q_f} \\ 0, & \frac{1}{2}\frac{q_j+q_f}{Q_f} < \delta \leq 0.5 \end{cases} \tag{4.10}$$

with the additional constraint from continuity that $(q_f - q_k)/q_j \leq \psi \leq q_f/q_j$. In particular, the value of ψ when $\lambda = 1$ must be q_f/Q_f. Figure 4-4 shows these relationships graphically. Note that if $\delta = 0$, then fast flowpaths perfectly align, and the maximum amount of water flows from one into the next. On the other hand, if $\delta \geq \frac{1}{2}\frac{q_j+q_f}{Q_f}$, the fast flowpaths do not interact and $\psi = 0$. The amount of interconnection between fast flowpaths upstream and downstream of a deep zone therefore depends on both their relative position and the amount of lateral mixing

within the deep zone. Note that, if complete momentum dissipation does not occur before the end of the deep zone, then Eq. 4.10 will not be valid, but the separation distance between the flowpaths and the amount of mixing within the deep zone will still be important.

When q_s and q_f are the same in all marsh zones and the jet is fully mixed by the time it exits the deep zone, when it has a uniform concentration of $c_{e,j}$ (Eq. 4.8), the concentration exiting the downstream fast flowpath $c_{e,f2}$ is given by:

$$c_{e,f2} = \left[\frac{\psi q_j c_{e,j} + (q_f - \psi q_j) c_{e,k}}{q_j} - c*\right]\left(1 + \frac{k_f T_{f2}}{N_f}\right)^{-N_f} + c* \qquad (4.11)$$

where $c_{e,j}$ is the concentration within the jet water as it exits from the deep zone, $c_{e,k}$ is the concentration within the non-jet water as it exits from the deep zone, and T_{f2} is the residence time of the fast flowpath within the second marsh section (see Fig. 4-3). Similarly, the downstream slow-flow zone receives some water that passed through the upstream fast flowpath and some water that did not. Due to the minimal lateral mixing within the densely vegetated slow-flow areas, these two flows must be treated separately. The two exit concentrations $c_{e,s2,a}$ and $c_{e,s2,b}$ (see Fig. 4-3) are equal to:

$$c_{e,s2,a} = (c_{e,k} - c*)\left(1 + \frac{k_s T_{s2}}{N_s}\right)^{-N_s} + c* \qquad (4.12)$$

$$c_{e,s2,b} = (c_{e,j} - c*)\left(1 + \frac{k_s T_{s2}}{N_s}\right)^{-N_s} + c* \qquad (4.13)$$

Within a wetland with one deep zone, the flow-weighted concentration at the wetland exit is the exit concentration from the second marsh section, which is:

$$c_e = \frac{q_f c_{e,f2} + [(1-\lambda)q_s - q_f + \psi q_j] c_{e,s2,a} + (1-\psi) q_j c_{e,s2,b}}{Q_f} \qquad (4.14)$$

Confirming the consistency of this approach, Eq. 4.7 is a special case of Eq. 4.14, which results when $\lambda = 1$ and therefore $\psi = q_f/Q_f$.

4.2.4 Short-circuiting marsh containing multiple deep zones with incomplete lateral mixing and no removal

When multiple sequential deep zones are present, the outlet concentrations from one wetland section (Eqs. 4.11, 4.12, and 4.13) serve as the inlet concentrations for the next downstream. An unlimited number of marsh–deep-zone sections can be concatenated in this manner, though, each time a deep zone is added, another flow stream is added to account for the fact that different fractions of water have passed through different numbers of flowpaths. As more deep zones are added, the situation becomes complicated, because it necessitates tracking an additional mass of water, which will likely have passed through a different number of fast flowpaths than other masses and therefore have received a different amount of treatment.

The most complicated parameter to determine is the connection between various flowpaths, denoted by $\psi_{\imath\ell}$, which refers to the fraction of water that flowed through a fast flowpath in the $\imath^{th}$ marsh section that next travels through a fast flowpath within the ℓ^{th} marsh section. Eq. 4.10 can be used to calculate $\psi_{\imath\ell}$ for an arbitrary pair of fast flowpaths, when $\delta_{\imath\ell}$ refers to their lateral separation distance, but must be reduced when they both interact with an intervening flowpath. Eq. 4.10 can also be extended to calculate $\psi'_{\imath\ell}$, which is the fraction of flow through the fast flowpath in the $\imath^{th}$ marsh section that within the ℓ^{th} deep zone is mixed with water that traveled through the fast flowpath within the ℓ^{th} marsh section.

4.2.5 Short-circuiting wetland containing one or more deep zones that provide contaminant removal

When algae, floating aquatic vegetation, or other biological matter are present within the deep zone, then biogeochemical processes are likely to occur within the deep zone and change the concentration of the contaminant of interest. In this case, the areal removal rate within the deep zone k_{dz} may be either positive or negative. As a first approximation, it is assumed that the deep zone is long enough that all water experiences the same RTD within the deep zone, even though observations of transport

within the deep zone within the Augusta wetland and other pond systems suggest that short-circuiting occurs within the deep zone (Sec. 2.3.1 and Thackston et al., 1987). It is also assumed that the minimum amount of time that a water parcel can remain within the deep zone is $T_{dz,min} = L_{dz}/U_f = T_{f1}(h_m/h_{dz})(T_{dz}/T_{m1})$, where T_{f1} is the residence time within the upstream fast flowpath and U_f represents the maximum velocity possible within the deep zone. When removal is present within the deep zone, Eqs. 4.8 and 4.9 are modified to become:

$$c_{e,j} = \frac{q_f(c_{e,f} - c*) + \lambda q_s(c_{e,s} - c*)}{q_j} \exp(-k_{dz}T_{dz,min}) \left[1 + \frac{k_{dz}(T_{dz} - T_{dz,min})}{h_m N_{dz}}\right]^{-N_{dz}} + c* \tag{4.15}$$

and:

$$c_{e,k} = (c_{e,s1} - c*) \exp(-k_{dz}T_{dz,min}) \left[1 + \frac{k_{dz}(T_{dz} - T_{dz,min})}{h_m N_{dz}}\right]^{-N_{dz}} + c* \tag{4.16}$$

where N_{dz} is the equivalent number of TIS for the deep zone. These concentrations then provide the input concentration to the downstream marsh section in Eqs. 4.11, 4.12, and 4.13, and other analysis proceeds unchanged.

4.3 Numerical methods and parameter values

The above model is deterministic, and for a given distribution of fast flowpaths located at positions $\{y_1, y_2, y_3, \ldots\}$ will produce a single exit concentration. The simulations presented here were calculated using Matlab (The MathWorks, Natick, Massachusetts), but a spreadsheet (e.g., Microsoft Excel) would produce the same results. Different wetlands are expected to have different distributions of short-circuiting flowpaths. To quantify the stochastic nature of short-circuiting within a marsh and deep zone system, Monte Carlo techniques are used to simulate the exit concentration from 10,000 wetlands with different distributions of flowpaths. Previously, Monte Carlo simulations with a one-dimensional (1-D) TIS model have been used to predict the outlet concentration from a combined pond-wetland system (Buchberger and Shaw,

1995) and from a groundwater system with an interlacing channel network (Moreno et al., 2006). In the simulations performed here, there is one fast flowpath within each marsh section within each wetland and located at a lateral position y/B_f, which is chosen from a uniform probability distribution over the interval {0–1}. Then, for each wetland, the blended exit concentration from the entire wetland is calculated from Eq. 4.14. The mean and standard deviation of the 10,000 simulations indicate the ensemble mean performance and expected variability in different constructed wetlands.

Throughout this analysis, the wetland area for a given simulation is kept constant. When a deep zone is added, it replaces marsh, such that the wetland area does not increase when the deep zone is added. To avoid an apparent residence time increase due to the added volume of the deep zone, results are presented in terms of the HRT and Damkohler number that correspond to a full marsh with the same footprint but no deep zones. Note that, as additional deep zones are added, the length and therefore HRT of each marsh section decreases.

Table 4.1 lists the independent variables that must be specified for this numerical model. For each variable, the table shows the range of values considered and the value selected for most model simulations; unless otherwise specified, these default values will be used. The choice of these values is now explained.

Damkohler number values $Da = k_s\tau/h_m = \{0.2, 1, 5\}$ are considered, where $\tau = h_m A_{cell}$ is the HRT of a continuously vegetated marsh section with surface area A_{cell}; this range brackets most of the contaminants of interest for the field studies discussed in Sec. 1.3 above. Estimates of nutrient removal in emergent wetlands and open water suggest that the removal rate within faster flow through less dense areas k_f is smaller than the removal associated with flow through dense vegetation k_s (Kadlec and Knight, 1996; Kadlec, 2000; Carleton, 2002; Li et al., 2003; Dierberg et al., 2005); both $k_f = k_s$ and $k_f = 1/10k_s$ will be considered here. It is expected that the removal rate within an unvegetated deep zone is different than in marsh areas. In some wetlands, floating aquatic vegetation, submerged aquatic vegetation, and periphyton within open water areas have been able to reduce contaminant levels (Bonomo et al.,

1997; Dierberg et al., 2005; Pietro et al., 2006), but in general previous studies have found that removal is reduced within a deep zone area (Kadlec, 2005*b*). For sensitivity analysis, $-1 \leq k_{dz}/k_s \leq 1$ are considered. To be conservative, a value of $k_{dz} = 0$ is adopted in most simulations; when no removal is present, the addition of a deep zone does not increase the effective volume of the wetland, so any performance improvements observed are due to their hydraulic effects alone. Results are presented as the normalized outlet concentration $(c_e - c*)/(c_o - c*)$, so it is not necessary to specify values for c_o or $c*$.

Values for λ are selected based on field and laboratory observations of mixing within constructed wetland deep zones. When strong wind was directed laterally across the deep zone in Cell 12 of the Augusta wetlands, by the time the fast-flow water touched the downstream edge of the deep zone at 5.3 hr after release, it had spread laterally across approximately 95% of the wetland (Figs. 2-11 and 2-14), so $q_j/Q_f \approx 0.95$. As shown in Table 2.2, the flow rate within the fast flowpaths was $q_f/Q_f = 0.7$, so $\lambda = (q_j/Q_f - q_f/Q_f)/(1 - q_f/Q_f) \approx 0.8$. In the lab, jet entrainment resulted in the incorporation of $0.45 \leq (q_j - q_f)/(Q_f - q_f) \leq 0.50$ of the fluid initially not within the jet. Therefore, $0.45 \leq \lambda =\leq 0.50$. To represent a wide range of possible conditions, $\lambda = \{0, 0.2, 0.5, 0.8, 1\}$ will be considered in this study.

In the Augusta wetland, the length of deep zone necessary for momentum dissipation and the minimum constructable length were both $L_{dz,min} \approx 15$ m. Based on construction and momentum dissipation constraints (Secs. 1.3 and 2.3.2), the minimum full-scale deep zone length probably differs between different wetlands; the range $L_{dz} = 5$–60 m will be considered. Based on field observations in the Augusta wetland (Table 2.2) and studies in other wetlands (e.g., Martinez and Wise, 2003*b*), the ratio of fast-flow and slow-flow transport speeds is $1 \leq U_f/U_s \leq 100$, and the fraction of flow within fast flowpaths $0 \leq q_f/Q_f \leq 0.85$. In later comparisons, intermediate values of $U_f/U_s = 20$ and $q_f/Q_f = 0.45$ are considered; these values correspond to an intermediate value for the normalized fast-flowpath width, $b_f/B_f = 0.045$ (cf. Table 2.2).

Previous work has suggested that longitudinal dispersion within a continuous

swath of homogeneous vegetation is low and induces near-plug-flow conditions with $N_s \approx 100$ (cf. Lightbody and Nepf, 2006*b*). The equivalent number of TIS for a fast flowpath within the Augusta wetland was observed to be between 4.9 and 12.1 (Sec. 2.3.1), so an intermediate value of $N_f = 10$ was adopted; measurements of longitudinal dispersion in natural streams also suggest that the mixing in a fast channel is an order of magnitude larger than that in the slow-flow zones (Fischer et al., 1979). Finally, it is assumed that $N_{dz} = 3$, which provides a good approximation to many natural wetland systems (Kadlec and Knight, 1996).

4.4 Results and discussion

4.4.1 Short-circuiting flow with no deep zones

First, consider the performance of a short-circuiting marsh. Fig. 4-5 compares the exit concentration from uniform and short-circuiting marsh regions as predicted by Eq. 4.6. In the plot, a normalized exit concentration $(c_e - c*)/(c_o - c*)$ (vertical axis) of 1 indicates no removal, and the value 0 indicates complete removal. In this simulation the flow rate Q_f through the wetland section, the length L, and the width ratio $b_f/B_f = 0.045$ are fixed, and the velocity ratio U_f/U_s is adjusted to create different fast-flow ratios q_f/Q_f. Note that when $U_f/U_s = 1$ no velocity heterogeneity is present. As U_f/U_s increases, the fraction of flow in the fast flowpath q_f/Q_f increases. This trend is supported by previous field studies (Dal Cin and Persson, 2000) and numerical simulations (Jenkins and Greenway, 2005), which have found that a greater difference in vegetation density and therefore flow speed between the fast- and slow-flow zones increases the amount of short-circuiting present in the RTD. When short-circuiting is not present ($U_f/U_s = 1$ and $k_f/k_s = 1$), the wetland section produces a normalized exit concentration of $(c_e - c*)/(c_o - c*) = 0.37$. When short-circuiting is present, the exit concentration is predicted to be higher, indicating a reduction in performance. For example, when $U_f/U_s = 20$ and $k_f/k_s = 1$, the normalized outlet concentration increases to 0.55.

Moreover, when the removal rate is lower in the fast flowpaths than in the vegetation, as would be expected in a wetland, the negative impact of vegetation heterogeneity is increased. For example, maintaining $U_f/U_s = 20$ but decreasing the removal rate in the fast flowpaths to $k_f/k_s = 0.1$ results in a further decrease wetland performance such that the outlet concentration becomes $(c_e - c*)/(c_o - c*) = 0.58$. The negative impact of short-circuiting grows as the velocity ratio U_f/U_s and the fraction of flow within them q_f/Q_f increase. In the limit of nearly all flow in the fast flowpath ($U_f/U_s \rightarrow \infty$ and $q_f/Q_f \rightarrow 1$), the outlet concentration $(c_e - c*)/(c_o - c*) = 0.96$ when $k_f/k_s = 1$ and $(c_e - c*)/(c_o - c*) = 0.99$ when $k_f/k_s = 0.1$. Recall that field observations suggest U_f/U_s can be as high as 50 (Sec. 2.3.1), and note that for these conditions Fig. 4-5 predicts that the nondimensional outflow concentration will be nearly doubled (from 0.37 to 0.7) in the likely case of short-circuiting.

Fig. 4-5 shows that the exit concentration is much more sensitive to the existence of fast flowpaths rather than the removal rate within them. In addition, the width of the fast flowpaths is not as important as their presence. For example, when $U_f/U_s = 20$ and $k_f/k_s = 0.1$, increasing or decreasing b_f/B_f by 50% changes the results by $\leq 15\%$ (Fig. 4-6). Finally, it is useful to note that the model is not very sensitive to the amount of longitudinal dispersion within either the fast flowpaths or the slow-flow zones. Recall that $N_s = 100$ and $N_f = 10$. For sensitivity analysis, all combinations of $N_s = \{1, 3, 10, 100, 1000\}$ and $N_f = \{1, 3, 10, 100, 1000\}$ are considered. When $b_f/B_f = 0.045$, $U_f/U_s = 20$, and $k_f/k_s = 0.1$, changing N_s changed the predicted outlet concentration by $\leq 14\%$ and changing N_f changed the predicted outlet concentration by $\leq 0.01\%$ (Fig. 4-7). Previous work suggests that the longitudinal amount of mixing (e.g., N_f and N_s) becomes important only for $Da \geq 5$ (Wörman and Kronnäs, 2005).

4.4.2 Short-circuiting marsh containing one laterally mixed deep zone with no removal

Fig. 4-8 demonstrates the impact of replacing a portion of a short-circuiting wetland by a transverse deep zone. The thin lines show the baseline case of a short-circuiting wetland ($b_f/B_f = 0.045$ and $U_f/U_s = 20$) without a deep zone (number of deep zones $n_{dz} = 0$). The thicker lines show the expected outlet concentration when the total wetland length L is held constant but a portion of the wetland is replaced by a laterally-mixed transverse deep zone of length $L_{dz}/L = 0.2$. The total marsh length, L_m, is the sum of the lengths of the marsh sections upstream (L_{m1}) and downstream (L_{m2}) of the deep zone. In the plot, the x-axis shows the fraction of the marsh that is upstream of the deep zone: when $L_{m1}/L_m = 0$ the deep zone is located at the beginning of the wetland section, and when $L_{m1}/L_m = 1$ it is located all the way at the end (cf. Fig 4-1b). For the cases with $n_{dz} = 1$, the reported Damkohler number is the same as that reported as when $n_{dz} = 0$, even though the total wetland HRT τ increases to reflect the additional volume that the deep zone adds to the wetland. It is also assumed that no contaminant removal occurs within the deep zone ($k_{dz} = 0$).

Fig. 4-8 shows that, when $Da = 1$, the addition of a deep zone at the beginning or end of a wetland section decreases contaminant removal, because the deep zone is not able to counteract short-circuiting yet reduces the fraction of time that the flow contacts the highly active vegetated zones. However, when the deep zone is located in the middle of the wetland (e.g., $0.3 < L_{m1}/L_m < 0.7$), its presence improves wetland performance even though it reduces the volume of the wetland that is actively removing contaminants. The complete lateral mixing within this simulated deep zone ensures that the same water does not short-circuit the entire wetland, and this improves the overall wetland performance. Thus, the performance of a wetland with periodic well-mixed sections is less than a wetland exhibiting plug flow and better than a wetland with short-circuiting. Note that, because no removal occurs within the deep zone in this simulation, this observed benefit associated with adding a deep zone is due to its effect on flow patterns and not an increase in wetland volume.

The relationship between the removal rate and the HRT affects the performance of a wetland section and the ability of a deep zone to mitigate short-circuiting within it. Fig. 4-8 also shows that, when the vegetation Damkohler number $Da = k_s\tau/h_m$ is increased from 1 to 5, the beneficial effect of the deep zone is dramatically increased. Furthermore, the deep zone can be situated nearly anywhere in the wetland and still provide greater removal than if no deep zone were present. Conversely, when Da decreases to 0.2, the presence of a deep zone decreases performance regardless of where it is located in the wetland section. Note that, for all cases examined here, locating the deep zone in the middle of the wetland section provides the best removal.

Because $k_{dz} = 0$, the results shown in Fig. 4-8 do not depend on the value of N_{dz}. Increasing the value of N_{dz} from 3 to 1000 or decreasing it to 1 does not change the outlet concentration. The insensitivity of the modeled results to the value of N_{dz} indicates that transport is affected more by the assumption of complete lateral mixing than by the assumed degree of longitudinal mixing.

In Fig. 4-8, the difference in fast- and slow-flow zone velocities is $U_f/U_s = 16$. That is, if the marsh section has mean residence time $T_m = 5$ d the water that travels through the fast flowpaths will exit $T_f - T_s = 7.5$ d before the water that travels through the slow-flow zones. In practice a range of different values of U_f/U_s is possible, and the exact value of this ratio will determine just how well a downstream deep zone can mix out the short-circuiting signal. If the difference between the time it takes water to travel through fast flowpaths and the time it takes water to travel through slow-flow zones is large relative to the HRT of the deep zone [i.e., $(T_f - T_s)/T_{dz} \gg 1$], then transport through the marsh region dictates the shape of the RTD (Fig. 4-9a). In this case, even though the mean HRT is still τ, the RTD is bimodal with one peak at $(T_f + T_{dz})/\tau$ and another at $(T_s + T_{dz})/\tau$, and the width of each peak is determined by mixing in the marsh and deep zone. If, however, U_f/U_s decreases such that $(T_f - T_s)/T_{dz} \ll 1$, then the two peaks in the RTD merge, forming a single peak centered at time $t/\tau = 1$ (Fig. 4-9b). In this case, the longitudinal mixing in the deep zone alleviates the short-circuiting associated with the fast flowpaths.

Fig. 4-10 summarizes the role of the velocity difference $T_s - T_f$ on the exit concen-

tration from a wetland section. First consider the case with no deep zone ($n_{dz} = 0$). As the degree of short-circuiting in the marsh $(T_s - T_f)/T_m$ increases, the wetland exit concentration increases as well. Note that $T_s - T_f$ is normalized by T_m because when a portion of a wetland is replaced by a deep zone both $T_s - T_f$ and T_m will decrease but the ratio $(T_s - T_f)/T_m$ will remain constant. Now consider the impact of replacing a portion of the marsh with a deep zone. When not much short-circuiting is present [i.e., $(T_s - T_f)/T_m < 1$], replacing marsh vegetation with a deep zone of length $L_{dz}/L = 0.2$ decreases wetland performance. However, when there is a large degree of short-circuiting in the wetland [i.e., $(T_s - T_f)/T_m > 1$], the presence of a laterally mixed deep zone located at the midpoint of the wetland ($L_{m1}/L_m = 0.5$) can mitigate the effect of short-circuiting. However, if the deep zone is located at the end of the wetland ($L_{m1}/L_m = 1$), the deep zone cannot improve wetland performance. Note that regardless of whether a deep zone is included or not, if the degree of short-circuiting is very large [i.e., $(T_s - T_f)/T_m > 10$], wetland removal approaches zero. A wetland designer could use Fig. 4-10 to determine whether adding a deep zone would improve the performance of a surface flow wetland with complete lateral mixing within its deep zone. First, measure or estimate the degree of short-circuiting in a wetland without a deep zone using a tracer study or direct measurements of fast-flowpath velocity. If $1 \leq (T_s - T_f)/T_m \leq 10$ and $k_s T_m \geq 1$, then the addition of a transverse deep zone could help offset the effect of short-circuiting.

4.4.3 Short-circuiting marsh containing one deep zone with incomplete lateral mixing and no removal

Now consider the effect of partial mixing within the single deep zone. The worst-case scenario, which occurs when fast flowpaths align upstream and downstream of the deep zone, is first considered. In this situation, mixing within the deep zone results in an increase in performance. Fig. 4-11 shows the predicted outlet concentration for various amounts of lateral mixing, λ, within a wetland containing a single deep zone with fast flowpaths aligned upstream and downstream of it. For a Damkohler number

$Da = 1$, mixing in excess of $\lambda = 0.7$ results in an improvement in performance over the case with no deep zone. For a Damkohler number $Da = 5$, any amount of lateral mixing provides an improvement; for a Damkohler number $Da = 0.2$, better performance is obtained without a deep zone, regardless of the amount of mixing within it. Note that Fig. 4-11 also suggests that deep zones should stretch completely across the wetland. For example, a deep zone that only comprises 45% of the wetland width will reduce the maximum value of λ to 0.45, which will prevent wetland performance from ever surpassing the performance expected when no deep zone is present. Because the main benefit of the deep zones is lateral flow redistribution, if they are included they should be constructed to intercept all of the water traveling through the wetland.

Next, consider the role of fast-flowpath alignment. Fig. 4-12 illustrates the role of lateral mixing (λ) and flowpath alignment (δ) on wetland performance when $Da = 1$ and $L_{dz}/L = 0.2$. First, consider the situation that results when lateral mixing is low ($\lambda < 0.25$). When one fast flowpath is located directly downstream of another ($\delta = 0$), it receives a large fraction of the water that passed through that upstream flowpath, and the deep zone provides little hydraulic benefit. On the other hand, if lateral mixing is low ($\lambda < 0.25$) and flowpaths are laterally offset ($\delta = 0.5$), water that travels down one fast flowpath must travel through a slow-flow zone in the next marsh region; because all water travels through at least a portion of the dense vegetation within the wetland, removal is predicted to be higher. Thus, when mixing is low (λ small), flowpath alignment plays a large role, and staggered fast flowpaths can dramatically improve removal over the expectation when deep zones are not present. As lateral mixing increases ($\lambda \rightarrow 1$), the difference between different flowpath alignments is reduced. Regardless of whether the flowpaths are aligned or not, some of the short-circuiting water is shunted into the downstream fast flowpath, and some enters dense vegetation. Thus, the outlet concentrations for all values of δ approach the same value. This value is less than that that obtained when mixing is low and the flowpaths are aligned ($\lambda = \delta = 0$) and greater than the value predicted when mixing is low and the flowpaths are offset ($\lambda = 0$, $\delta = 0.5$). Recall, however, that the distribution of fast flowpaths is unknown prior to wetland constructed, so wetland

designers cannot be certain of the value of δ in advance.

To illustrate how stochastic variation in the value of δ affects wetland performance, effluent concentrations from many different wetlands can be simulated. Fig. 4-13 shows a Monte Carlo simulation of the outlet concentration from a marsh downstream of a single deep zone with different amounts of lateral mixing λ. It is assumed that $Da = 1$ and $L_{dz}/L = 0.2$. The upstream marsh has a fast flowpath located at lateral position y_1/B_f and the downstream marsh has a fast flowpath located at y_2/B_f, both of which are chosen randomly from a uniform probability distribution over the interval {0–1}; δ is the difference between these values (Fig. 4-13a). Note that, due to the periodic boundary condition, $0 \leq \delta \leq 0.5$. The simulations show that, when lateral mixing is not present ($\lambda = 0$), there is a wide range of performance in different wetlands (Fig. 4-13b). That is, 67% of wetlands will experience better removal than what is predicted in the absence of a deep zone (in fact, 1% of wetlands will exhibit 11% better removal than the baseline situation of the same wetland area completely filled with a short-circuiting marsh; see Fig. 4-1a); however, the remaining 33% of wetlands will perform worse than this baseline expectation. The portion of Fig. 4-12 with $\lambda = 0$ (i.e., small values on the x-axis) reveals the difference between these different wetlands: the wetlands that perform better than the baseline expectation have large separation between their flowpaths ($\delta \geq 0.2$), whereas the wetlands that perform poorly have aligned flowpaths ($\delta \leq 0.15$). A wetland designer does not know in advance where the fast flowpaths will develop, so including a single deep zone within a wetland where lateral mixing is low (e.g., the wetland is sheltered from the prevailing winds) means risking poor performance. The presence of lateral mixing ($0 < \lambda < 1$; Figs. 4-13c–e) reduces the variability in wetland removal, though it also eliminates the possibility of obtaining very high performance due to a favorable staggered flowpath configuration. Finally, when $\lambda = 1$, the alignment of the flowpaths is unimportant and all configurations perform identically (Fig. 4-13f).

Fig. 4-14 shows the ensemble mean of the exit concentration from Monte Carlo simulations of flow through a short-circuiting wetland with a single interior deep zone located in the middle ($L_{m1}/L_m = 0.5$) of a 75-m-long wetland. To generate this

figure, it is assumed that the deep zone length is sufficient to allow construction and also to allow complete momentum dissipation, which is almost certainly unrealistic for the shortest deep zone considered here (L_{dz} = 1 m). Fig. 4-14 shows that, on average, adding a deep zone of length L_{dz} = 15 m (so L_{dz}/L = 0.2) will improve wetland performance over that expected for the baseline case of a short-circuiting wetland of the same size with no deep zone. Although the amount of lateral mixing λ does not affect the mean concentration observed from many different wetlands each containing a single deep zone, the amount of mixing does affect the distribution of wetland exit concentrations about the mean; when less mixing is present, the range of wetland performances is larger. The vertical bars indicate the standard deviation σ associated with the ensemble average so encompass the performance of 68% of all wetlands. To ensure that 97.5% of all wetlands perform better than the baseline exit concentration, the ensemble mean must be 2σ smaller than the exit concentration for the baseline case. For L_{dz} = 15 m, the exit concentration is 2σ below the baseline exit concentration for $\lambda = 0.8$ but not for $\lambda = 0.2$ or 0.5. Therefore, when $Da = 1$, $L_{dz}/L = 0.2$, and $\lambda \leq 0.5$, adding a deep zone will on average improve wetland performance, but some wetlands that develop aligned flowpaths and are sheltered from the wind may develop aligned flowpaths and exhibit reduced performance.

Now consider the effect of deep zone length L_{dz} on wetland performance. When no removal or other benefit occurs within the deep zone, average performance is reduced (c_e increases) as the length of the deep zone increases (Fig. 4-14). In fact, adding a deep zone longer than L_{dz} = 15 m to this 75-m-long wetland would on average increase the exit concentration above what would be expected in a short-circuiting wetland with no deep zone. On the other hand, decreasing the deep zone length improves removal, as long as the deep zone is still able to provide momentum dissipation. For a particular wetland, the minimum deep zone length necessary for complete momentum dissipation will be determined by site-specific drag within the deep zone; construction constraints also create a minimum practical deep zone width. Therefore, within a particular wetland, deep zones must be larger than a certain width, which is estimated to be $L_{dz,min}$ = 15 m within the Augusta wetland. From a hydraulic

perspective, wetland designers should make internal deep zones just long enough to result in complete momentum dissipation. In certain situations, however, chemical or biological considerations may necessitate excess deep zone length, for example for denitrification or mosquito control (U. S. Environmental Protection Agency, 2000; Thullen et al., 2005). Those situations complicate the simple application of Fig. 4-14 and are discussed below in Sec. 4.4.5.

4.4.4 Short-circuiting marsh containing multiple deep zones with incomplete lateral mixing and no removal

Now consider wetland performance when multiple deep zones are present. First, model predictions are compared for a 200-m-long wetland, which can fit up to thirteen 15-m-long deep zones, which is estimated to be the shortest width practical in the Augusta wetland. Each point within Fig. 4-15 represents the ensemble average exit concentration from Monte Carlo simulations of flow through 10,000 wetlands. For each wetland, the locations of the fast flowpaths $\{y_1/B_f, y_2/B_f, y_3/B_f, \ldots\}$ are chosen randomly from a uniform probability distribution over the interval {0–1}. First consider the results for $Da = 1$. The best average removal is provided by the wetlands that include two deep zones ($n_{dz} = 2$). The level of lateral deep zone mixing λ does not affect the mean behavior, but it does impact the range of individual results. For example, low lateral mixing ($\lambda = 0.2$) results in some wetlands with zero, one, three, and four deep zones outperforming some of the wetlands with two deep zones. Further increasing the number of deep zones within this 200-m-long wetland decreases the fraction of marsh that provides contaminant removal and, for total deep zone length $n_{dz}L_{dz}/L_{dz} > 0.4$, results in worse performance than a short-circuiting marsh without a deep zone. This trend is analogous to that for a single deep zone shown in Fig. 4-14. Now consider the different Damkohler numbers shown. When the marsh is undersized ($Da = 0.2$), all marsh area is valuable for treatment and deep zones cannot improve performance over a short-circuiting marsh with no deep zone, so removal declines (c_e increases) no matter how many deep zones are added. On the

other hand, when the marsh is oversized ($Da = 5$), the optimal number of deep zones increases on average to $n_{dz} = 4$, although the differences in removal expected within different wetlands with different flowpath alignments make the optimal number of deep zones $1 \leq n_{dz,opt} \leq 7$ when $\lambda < 1$. In addition, Fig. 4-15 shows that the value of Da (i.e., relative wetland size) has a larger impact on wetland performance than the amount of lateral mixing within the deep zone. The amount of lateral mixing within the deep zone does not substantially affect the ensemble mean performance that is achieved, but it does affect the distribution about the mean.

As shown in Fig. 4-16, the number of deep zones that produces the minimum exit concentration depends on the length of the deep zones. As $L_{dz,min}$ increases, the number of deep zones that produces the minimum outlet concentration (i.e., the optimal number of deep zones) shifts toward fewer deep zones. Fig. 4-16 shows that, for a 200-m-long wetland, the optimal number of deep zones $n_{dz,opt} = 4$ for $L_{dz,min} = 5$ m, $n_{dz,opt} = 3$ for $L_{dz,min} = 10$ m, $n_{dz,opt} = 2$ for $L_{dz,min} = 15$ m, and $n_{dz,opt} = 1$ for $L_{dz,min} = 30$ m and $L_{dz,min} = 60$ m. This trend is not surprising, because large deep zones take away more of the productive marsh area, so including more would be expected to hinder removal. Because only integer quantities of deep zones can be included, the optimum fraction of wetland area to commit to deep zones also differs for different deep zone lengths. As shown in Fig. 4-16, the optimum deep zone fraction $n_{dz,opt}L_{dz}/L = 0.24$ for a 60-m-long deep zone, which is higher than the optimal fraction $n_{dz,opt}L_{dz}/L = 0.08$ for a 5-m-long deep zone. Finally, note that, regardless of whether one deep zone is present (Fig. 4-14) or many (Fig. 4-16), shorter deep zones provide lower outlet concentrations, as long as the deep zones are each long enough to prevent alignment between fast flowpaths within successive marsh sections (i.e., $L_{dz} \geq L_{dz,min}$).

Next, consider the case of constant deep zone fraction, in which both n_{dz} and L_{dz} are allowed to change but $n_{dz}L_{dz}/L$ is kept constant. The removal rate k_s is assumed constant, such that Da does not change depending on wetland length and the number of deep zones. Fig. 4-17 shows the average exit concentration from Monte Carlo simulations of flow through wetlands with different numbers of deep zones

but constant total deep zone fraction $n_{dz}L_{dz}/L = 0.2$. Each point represents the ensemble average exit concentration from 10,000 different wetland realizations. For each wetland, the locations of the fast flowpaths $\{y_1/B_f, y_2/B_f, y_3/B_f, \ldots\}$ are chosen randomly from a uniform probability distribution over the interval {0–1}. Partial mixing within the deep zones ($\lambda = 0.2$, which is reflective of the calm conditions observed in the laboratory) is assumed. The figure illustrates that a greater number of deep zones results in a decrease in average wetland exit concentration. In addition, the first deep zone provides the most benefit, and the added benefit of each subsequent one declines, such that the presence of four or more deep zones ($n_{dz} \geq 4$) provides within 5% of the performance achieved by $n_{dz} = 20$. Also note that the range of outlet concentrations decreases as the number of deep zones increases. The two limiting cases shown in the figure help to illustrate the bounds on possible wetland performances. The aligned configuration, in which all fast flowpaths are located at the same lateral location ($y_1/B_f = y_2/B_f = y_3/B_f = \ldots$), provides the worst-case alignment scenario. At the other extreme, when flowpaths are staggered ($y_1/B_f = y_3/B_f = \ldots = 0$ and $y_2/B_f = y_4/B_f = \ldots = 0.5$), performance is highest. As the number of deep zones increases, the probability that all flowpaths are perfectly aligned becomes vanishingly small, thus ensuring that all water receives some treatment, and average wetland performance improves.

Now consider the removal expected within wetlands of different lengths (Fig. 4-18). The contaminant removal rate k_s and flow rate Q_f are assumed fixed such that $Da = 1$ when $L = 200$ m. Therefore, wetlands smaller than $L = 200$ m will have shorter residence times and $Da < 1$; wetlands longer than $L = 200$ m will have $Da > 1$. The deep zone length is also fixed at $L_{dz} = 15$ m. Fig. 4-18 shows the average exit concentration from Monte Carlo simulations of 10,000 wetlands with various combinations of wetland length L and number of deep zones n_{dz}. The figure shows a series of lines connecting results for the same number of deep zones. The all-marsh baseline ($n_{dz} = 0$) is shown as a dashed line. This line reflects the effect of residence time on performance; when k_s and Q_f are fixed, simply enlarging the wetland will improve removal even though unmitigated short-circuiting is still present.

Now, partially mixed ($\lambda = 0.5$) deep zones are added to these wetlands. In the upper left corner, the first solid line to its right indicates $n_{dz} = 1$, the next solid line indicates $n_{dz} = 2$, and so on. As the wetland length L increases, the lines begin to cross each other, indicating that a greater number of deep zones produces a lower exit concentration. For example, a wetland that is 25 m long can contain one 15-m-long deep zone. This large deep zone, which comprises $L_{dz}/L = 60\%$ of its length, results in a higher outlet concentration (worse performance) than if no deep zone were present. On the other hand, a wetland with $L = 150$ m can contain up to ten deep zones. No removal is expected, of course, when $n_{dz}L_{dz}/L = 1$, but when one or two deep zones are included performance is improved over the baseline case of no deep zone. Note that, for wetlands with $L \geq 100$ m, it is beneficial to include at least one deep zone. As wetland size increases, so does the optimal number of 15-m-long deep zones $n_{dz,opt}$, which is the value of n_{dz} that produces the lowest normalized outlet concentration.

The optimal number of deep zones for each wetland length considered in Fig. 4-18 is plotted in Fig. 4-19. Note that $L_{dz} = 15$ m in these simulations; as shown in Fig. 4-14, wetland performance depends on the length of each individual deep zone. The left-hand y-axis and the circular data points indicate the value of $n_{dz,opt}$ for each wetland length L. Since the number of deep zones must be an integer, the value of $n_{dz,opt}$ increases stepwise. The right-hand y-axis and the triangular data points compare the optimal deep zone fraction $n_{dz,opt}\ L_{dz}/L$ for each wetland length. The figure shows that for a 150-m-long wetland, including only one deep zone ($n_{dz}L_{dz}/L = 0.1$) produces the best performance. When wetland size increases to $L = 300$ m, though, the optimal number of deep zones increases, and three deep zones ($n_{dz}L_{dz}/L = 0.15$) provides the best removal. For very long wetlands ($L \geq 500$ m), the optimal deep zone fraction reaches a value of 0.16 for the parameter values considered here ($Da = 1$ when $L = 200$ m, $\lambda = 0.5$, $L_{dz} = 15$ m, and other values shown in Table 4.1).

Next consider the sensitivity of the optimal number of deep zones within short-circuiting wetlands to the wetland Damkohler number, the deep zone length, and the amount of short-circuiting flow. Figs. 4-20 and 4-21, unlike Fig. 4-19, show

the ensemble mean of the optimum number of deep zones for 10,000 simulations of wetlands with randomly located flowpaths; even though the optimum value of $n_{dz,opt}$ is still an integer for any particular wetland, the mean value across all the different wetlands is not necessarily an integer. For both values of the lateral mixing coefficient λ examined, wetlands with higher values of Da benefit from more deep zones (Figs. 4-20a and 4-21a). The optimal deep zone fraction $n_{dz,opt}L_{dz}/L$ is also higher in wetlands with higher Da (Figs. 4-20b and 4-21b). The minimum size wetland that could benefit from deep zones is also a function of Damkohler number (Figs. 4-20c and 4-21c).

The optimal number of deep zones also depends on the length of each deep zone (Fig. 4-22). Here is assumed that $L_{dz} \geq L_{dz,min}$, so that momentum dissipation is achieved within each deep zone. For both values of the lateral mixing coefficient λ examined, wetlands with shorter deep zones should include more deep zones (Fig. 4-22a). The optimal deep zone fraction also depends on the value of L_{dz}; wetlands with longer deep zones should include a larger deep zone fraction $n_{dz,opt}L_{dz}/L$ (Fig. 4-22b).

Finally consider the effect of the fraction of flow within the fast flowpaths on the optimal number of deep zones. Fig. 4-23a shows that $n_{dz,opt}$ increases from 0 to 3.3 as q_f/Q_f increases from 0.1 to 0.8 for $Da = 1$, $L = 200$ m, and $L_{dz} = 15$ m. The value of the fast-flowpath width, which determines the value of the ratio U_f/U_s, has a more modest effect, resulting in a difference of less than 10% in the value of $n_{dz,opt}$. Fig. 4-23b shows that the exit concentration associated with the optimal number of deep zones increases as the fraction of short-circuiting flow increases. In addition, it compares the exit concentration produced by the optimal number of deep zones to the value produced when no deep zone is present. Figs. 4-23a and Figs. 4-23b both show that, when only a small amount of short-circuiting flow is present (q_f/Q_f le0.1), adding a deep zone does not improve wetland performance over the short-circuiting baseline. However, as the amount of short-circuiting increases, the potential benefit of the deep zone increases. Moreover, Fig. 4-24 shows that the optimal number of deep zones is more sensitive to the value of q_f/Q_f than to the value of U_f/U_s as long as $U_f/U_s \geq 10$. The amount of lateral mixing does not affect this observation.

Throughout this discussion, periodic boundary conditions with constant B_f are

assumed; this assumption is equivalent to assuming that fast flowpaths are distributed a constant distance apart within each marsh section. In a real system, however, flowpaths are not evenly distributed throughout the wetland (Sec. 2.3.1). This model could be extended to consider the impact of flowpaths distributed randomly within each marsh section. When complete lateral mixing is present, simulated results would not change. When incomplete lateral mixing is present, results would likely have the same mean value but increased variability around that mean, as long as there is no correlation between flowpath locations among different marsh sections.

4.4.5 Short-circuiting wetland containing one or more deep zones that provide contaminant removal

Now consider the presence of removal processes within the deep zone. Fig. 4-25 shows the analytic outlet concentration from a 75-m-long short-circuiting wetland containing a single centrally located 15-m-long deep zone, which is assumed to be fully laterally mixed and long enough to allow complete momentum dissipation. The RTD is assumed to be identical for all water parcels passing through the deep zone; this is a simplification of the actual flow patterns present within the deep zone. The vertical dotted line indicates the removal expected when $k_{dz} = 0$, which has been assumed in the above plots. This value is compared to the exit concentration expected when $k_{dz} \neq 0$, which results when the deep zone adds contamination, for example by allowing wind shear that suspends sediments or by harboring algal populations, or removes contamination, which may occur if floating aquatic vegetation or periphyton is present. Note that the relative removal within the deep zones, k_{dz}/k_s, is a comparison on an areal basis, which takes into account the relative depths and therefore volumes of the marsh and deep zone areas. To compare different wetlands on a volumetric basis, the x-axis could be rescaled by multiplying by the relative marsh depth, which is $h_m/h_{dz} = 0.3$ in the Augusta wetland (Table 3.2). Not surprisingly, the exit concentration increases for $k_{dz} < 0$ and decreases for $k_{dz} > 0$, compared to the exit concentration expected when $k_{dz} = 0$. For $Da = 1$, adding a deep zone is beneficial

when $k_{dz}/k_s > -0.19$. For $Da = 0.2$, this value increases to 0.69; for $Da = 5$ it decreases to -0.62. Therefore, for $Da \geq 1$, it can be advantageous to add a deep zone even if it contributes contamination to the wetland at a modest rate. For $k_{dz} \geq 0.7k_s$, wetland performance is improved over the baseline case with no deep zone even for $Da = 0.2$.

The presence of either positive or negative removal within the deep zone also affects the optimal number of deep zones (Fig. 4-26). For all three Damkohler numbers considered, when $k_{dz} = k_s$ the optimal removal occurs when deep zones encompass the entire wetland area, because the deep zones, unlike the marsh areas, are assumed not to exhibit short-circuiting, which is a simplification of actual flow paths within open ponded areas (Thackston et al., 1987). For $Da = 0.2$ and $k_{dz}/k_s \leq 0.1$, exit concentrations are higher than the baseline case of no deep zone, so the optimal deep zone number is still $n_{dz} = 0$ (Fig. 4-26a). For $Da = 1$ and $k_{dz}/k_s \leq 0$, the optimal deep zone number is still $n_{dz} = 1$, but for $k_{dz}/k_s \geq 0.1$ better performance is predicted when more deep zones are included (Fig. 4-26b). For $Da = 5$ and $Da = 0.2$, the optimal number of deep zones also increases as the removal within the deep zones increases. However, the presence of moderate removal within the deep zones ($-0.6 \leq k_{dz}/k_s \leq 0.4$) does not change the optimal number of deep zones by more than one deep zone so is not expected to substantially affect wetland design. Fig. 4-27 shows the exit concentrations that correspond to different removal rates.

4.5 Comparison of model conclusions to field studies

The approach presented here provides predictions for how performance should vary within field wetlands. In particular, for a Damkohler number $Da = 1$, the best performance should be observed within wetlands with $0.05 \leq A_{dz}/A \leq 0.25$ (cf. Fig. 4-22) and deep zones that fully dissipate momentum, so $L_{dz} \geq L_{dz,min}$. Previous studies have examined the effect on performance of wetland open area, which may

or may not be deeper than the surrounding marsh areas. The U. S. Environmental Protection Agency (2000) reviewed several case studies of free-water-surface wetlands providing secondary treatment and found that all eight wetlands with "significant open area" produce effluent 5-day biological oxygen demand (BOD_5) concentrations of less than 20 mg/L, whereas only three of twelve "fully vegetated" systems are able to do so. In addition, in a comparison between different wetlands with the same length but different sizes of deep zones, Knight et al. (1994) report that a wetland with two centrally located deep zones with total $L_{dz}/L = 0.25$ was able to achieve an average normalized total nitrogen outlet concentration of $c_e/c_o = 0.27$, whereas a wetland of the same size but no deep zones ($L_{dz}/L = 0$) could only achieve $c_e/c_o = 0.39$, so the addition of deep zones provided 30% better removal (see Champion data in Table 1.3). Similarly, six of seven wetlands with "significant open area" produced effluent total suspended solids (TSS) concentrations of less than 20 mg/L but only five of twelve "fully vegetated" systems, even though there is no apparent correlation between TSS load and amount of vegetation (U. S. Environmental Protection Agency, 2000). Likewise, in a comparison of forty-six wetlands with no deep zones, fifty-eight wetlands with some open water, and seventy-two ponds, Kadlec (2005*b*) presented data that show that the average removal rate is highest for wetlands with between 5 and 35% open water.

Figs. 4-28 and 4-29 can be used to test these predictions. Within each plot, the y-axis shows the fraction of internal wetland area (that is, wetland area excluding inlet and outlet deep zones) that is a deep zone without emergent macrophytes. The x-axis shows the removal $(1 - c_o/c_e)$ for different contaminants within the wetlands listed in Table 1.3; higher removal indicates better performance. Note that, due to space limitations, negative removals (i.e., $c_e > c_o$), are plotted as having a removal of 0.

First, consider the effect of deep zone area. For seven (total nitrogen, ammonia nitrogen, nitrate nitrogen, organic nitrogen, total phosphorus, biological oxygen demand, total suspended sediments) out of the eight contaminants with more than one data point for a deep zone areal fraction $0 < A_{dz}/A \leq 0.2$, there is a positive

correlation between deep zone fraction and removal, suggesting that adding a relatively small deep zone improves deep zone performance. As the size of the deep zone increases, however, removal is seen to decrease again. For eight (total nitrogen, ammonia nitrogen, nitrate nitrogen, organic nitrogen, total Kjeldahl nitrogen, total phosphorus, biological demand, and total suspended solids) out of the eleven contaminants with more than one data point for $A_{dz}/A > 0.2$, there is a negative relationship between deep zone area and removal. That is, the larger the pond in excess of what is necessary for hydraulic reasons, the lower the removal.

Second, consider the effect of deep zone length. It is assumed here, based on laboratory experiments (Sec. 3.5), that when $L_{dz} < L_{dz,min}$ the deep zone will not be able to fully uncorrelate the location of flowpaths in successive marsh sections. In this situation, flowpaths may be aligned between different marsh sections, which will decrease performance (cf. Fig. 4-17). The minimum deep zone length $L_{dz,min}$ will depend on the particular wetland characteristics but is likely to be $L_{dz,min} \geq 10$ m in most wetlands. The total nitrogen results support the expectation that L_{dz} should be longer than $L_{dz,min}$: when $A_{dz}/A \approx 0.2$, the best performance is obtained from wetlands with $L_{dz} > 10$ m. Overall, however, the data neither support nor deny this trend: the removal for wetlands with $L_{dz} > 10$ m is $26 \pm 10\%$ (mean $\pm$ standard error of the mean) and the overall removal for wetlands with $L_{dz} < 10$ m is $31 \pm 12\%$, which is statistically indistinguishable. More studies, and in particular more controlled studies comparing the performance of wetlands with and without deep zones and with deep zones of various sizes, are necessary before it can be established whether this model has predictive power.

Thus, existing data tend to agree with model assumptions and results. Note, however, that the presence of this correlation does not fully validate the model. Other processes may also be promoted by multiple narrow deep zones; for example, the U. S. Environmental Protection Agency (2000) recommends including open areas to enhance aerobic environments to promote nitrification and BOD_5 removal, and suggests that deep zones have a residence time of less than 2 d to prevent algal blooms, which results in a design recommendation for multiple narrower deep zones

in large wetlands.

4.6 Conclusion

An analytical model was here developed based on current understanding of flow through the Augusta wetland. The model is built on the assumption that the development of short-circuiting is unavoidable in vegetated systems but the position of fast flowpaths is impossible to predict in advance or control. The model is used to explore the effect on wetland performance of including transverse deep zones, which eliminate the correlation between the position of fast flowpaths in different sections of marsh. For sufficiently large wetlands ($Da = k_s\tau/h_m \geq 1$ and $L > 100$ m), including at least one deep zone will improve wetland performance even though the deep zones provide no removal themselves, because the deep zone reduces the probability that any water parcels will short-circuit the wetland and avoid all dense marsh vegetation. Because it is assumed that deep zones are long enough to allow complete momentum dissipation, this result is independent of the amount of lateral mixing within the deep zone. When lateral mixing is high, then the mixing redistributes the flow that passes through one fast flowpath into a productive slow-flow zone within the next marsh section. When lateral mixing is low, then it is unlikely that fast flowpaths will perfectly align, so in most cases water that short-circuits one marsh region will pass through dense vegetation within the next. The probability of flowpath alignment decreases as the number of deep zones (and hence independent marsh sections) increases, though increasing the deep zone fraction above $n_{dz}L_{dz}/L = 0.35$ reduces performance for all deep zone lengths and Damkohler numbers considered here. Supporting this conclusion, field data show that wetlands with a moderate fraction ($0 < A_{dz}/A \leq 0.2$) of long deep zones ($L_{dz} > 10$ m) tend to remove more nitrogen than wetlands with either no deep zones, shorter deep zones, or a greater fraction of deep zone area.

Observations in both the field and the laboratory were at the scale of individual fast flowpaths and individual marsh sections, and this model is designed to capture flow patterns at that length scale. In wetlands with multiple marsh sections, other

large-scale effects may become important. For example, a constant flow depth h_m is assumed in all marsh regions, which is likely to be a good approximation in a small graded wetland, but microtopography and deviations from normal flow can create differences of up to 50% in marsh water depth in a large wetland (Guardo and Tomasello, 1995). Large wetlands may also exhibit large-scale vegetation patchiness (Swain et al., 2004), which could alter the distribution of fast flowpath velocities throughout the wetland. Therefore, more work must be done to validate this model within additional wetlands.

One of the primary effects of the deep zones is to uncorrelate the positions of the fast flowpaths. Studies of flow within groundwater (drag-dominated) systems have also found that a reduction in the correlation length associated with the velocity field results in increased removal. For example, a comparison of removal achieved within two-dimensional flow fields with identical total velocity heterogeneity revealed that first-order removal was highest in flow fields in which regions of high velocity were the least connected (Zinn and Harvey, 2003). This effect allow deep zones to provide lateral redistribution of flow regardless of the amount of mixing present.

Table 4.1: Nondimensional variables used by the numerical model, along with values considered in model runs. The listed default value is the one used in simulations unless otherwise specified. †When more than one deep zone is present, it is assumed that they are spaced evenly. ‡Two of the three variables U_f/U_s, b_f/B_f, and q_f/Q_f must be specified.

Variable	Symbol	Value(s) considered	Default value
Damkohler number based on slow-flow zone removal	$Da = k_s\tau$	0.2,1,5	1
Removal rate within fast flowpath	k_f/k_s	0–0.1	0.1
Removal rate in deep zone	k_{dz}/k_s	-1–1	0
Lateral mixing within the deep zone	λ	0,0.2,0.5,0.8,1	0.2, 0.8
Minimum deep zone length	L_{dz}	5–30 m	15 m
Wetland length	L	25–500 m	75 m
Number of deep zones	n_{dz}	0–20	1
Position of first deep zone†	L_{m1}/L	0–1	0.5
Flow speed ratio‡	U_f/U_s	1–100	20
Fast-flowpath width‡	b_f/B_f	0.045	0.045
Fast-flowpath flow rate‡	q_f/Q_f	0–0.85	0.4
Equivalent TIS within the fast flowpath	N_f	1,3,10,100,1000	10
Equivalent TIS within the slow-flow zone	N_s	1,3,10,100,1000	100
Equivalent TIS within each deep zone	N_{dz}	1,3,1000	3
Lateral positions of fast flowpaths	$y_1/B_f, y_2/B_f \ldots$	0–1	0–1

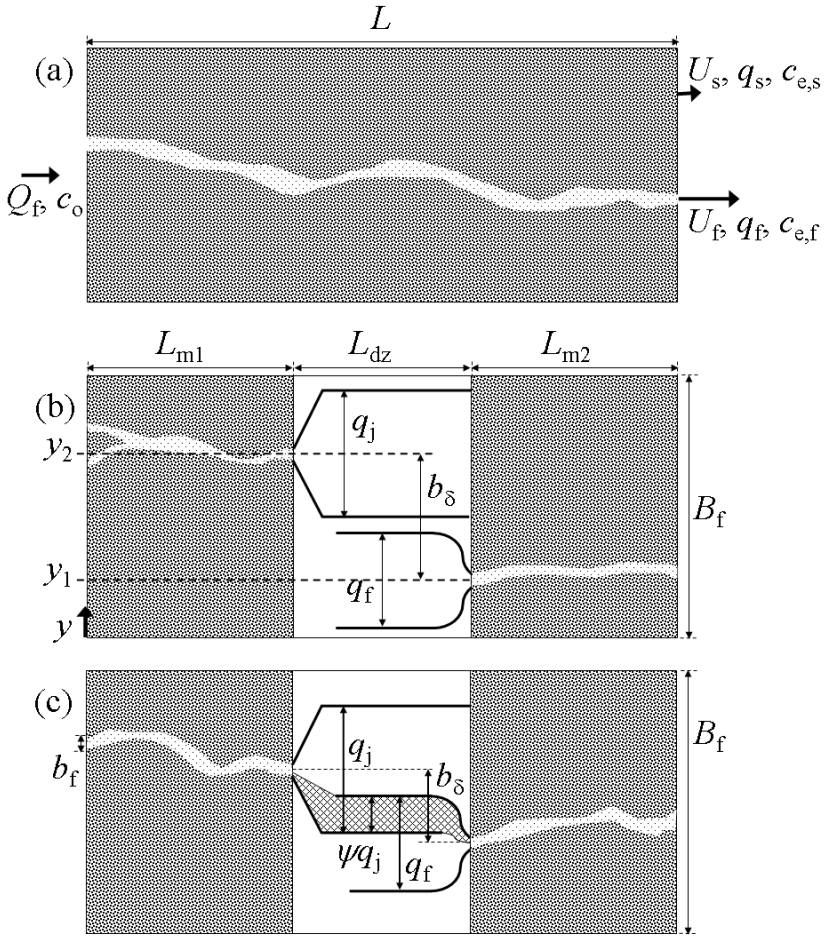

Figure 4-1: Conceptual representations of short-circuiting flowpaths through a portion of a marsh. (a) Top view of a short-circuiting marsh section, showing the resulting velocities in the fast flowpath, U_f, and slow-flow zone, U_s. (b) When a fast flowpath with flowrate q_f exits into a deep zone, it entrains a fraction λ of the adjacent slow flow exiting the marsh, so the total amount of flow associated with the jet is $q_j = q_f + \lambda q_s$. The deep zone is assumed to remove the correlation between the lateral position of an upstream fast flowpath and a downstream flowpath. When the normalized distance between the flowpath centerlines $b_\delta/B_f \geq \frac{1}{2}(q_j + q_f)$, the flowpaths are far enough apart that they do not interact. (c) When $b_\delta/B_f < \frac{1}{2}(q_j + q_f)$, an amount of water ψq_j travels directly from the upstream to the downstream fast flowpath. Additional deep zones may be located upstream or downstream of this marsh section.

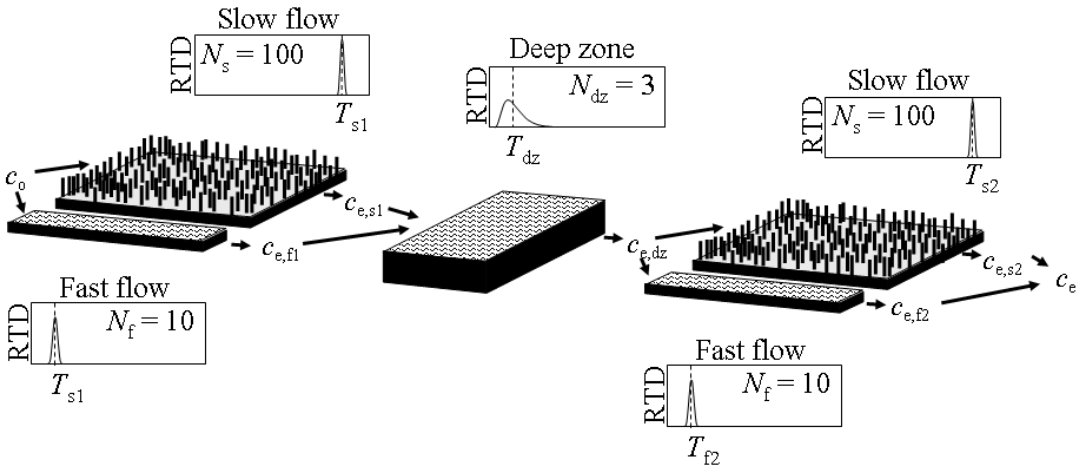

Figure 4-2: Conceptual sketch of a one-dimensional model representing transport within a wetland segment containing a laterally mixed deep zone. Water with initial concentration c_o enters a marsh region and then travels through either a fast- or slow-flow zone, each with its own residence time distribution. The water exiting the deep zone has a blended concentration of $c_{e,dz}$. The final exit concentration after another short-circuiting marsh segment is c_e.

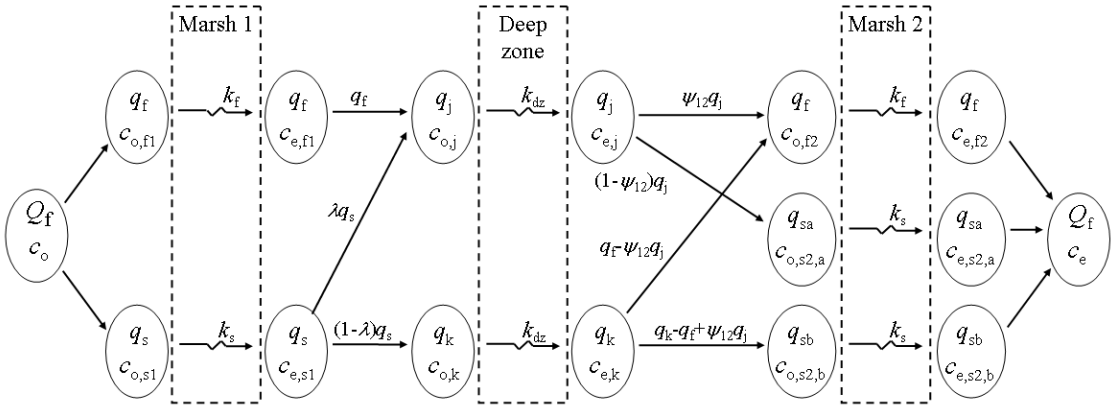

Figure 4-3: Extension of the one-dimensional box model to account for partial mixing within a single deep zone. Arrows indicate water movement between different compartments within the model; water is assumed fully mixed within each compartment.

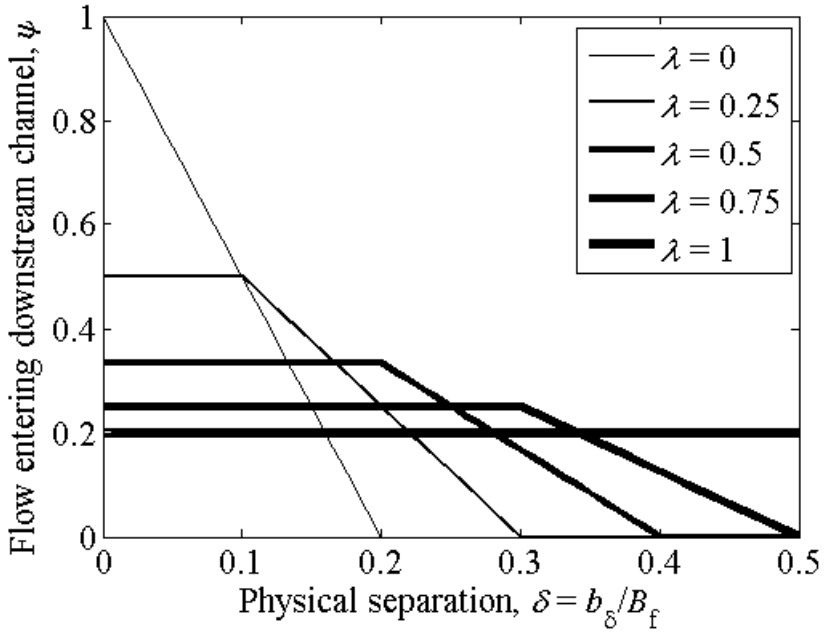

Figure 4-4: Relationship between the fraction of jet water that enters downstream vegetation, ψ, and the normalized physical separation between fast flowpaths, δ. In this plot it is assumed that $q_f/Q_f = 0.2$, which limits the value of ψ as $\lambda \rightarrow 1$.

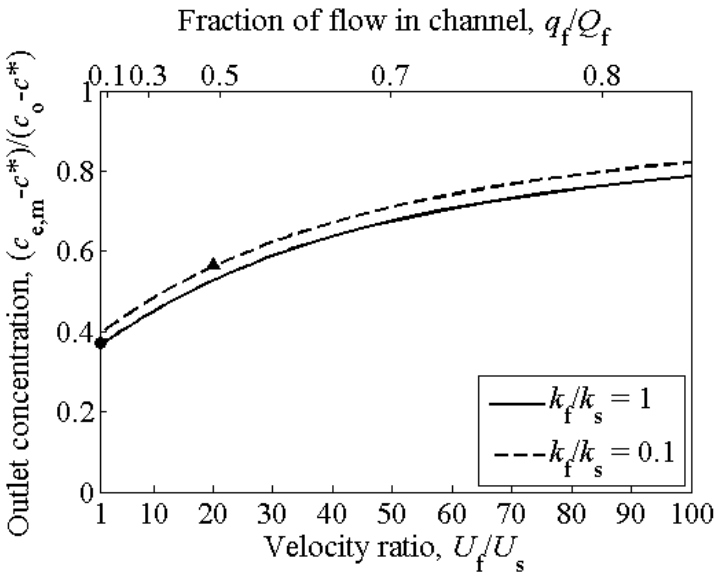

Figure 4-5: Analytic calculation of normalized exit concentration from a marsh region with short-circuiting. The black circle indicates the exit concentration when no short-circuiting is present ($U_f = U_s$ and $k_f = k_s$). The black triangle indicates the exit concentration of the short-circuiting baseline wetland, which has $U_f/U_s = 20$ and $k_f/k_s = 0.1$. It is assumed that $b_f/B_f = 0.045$.

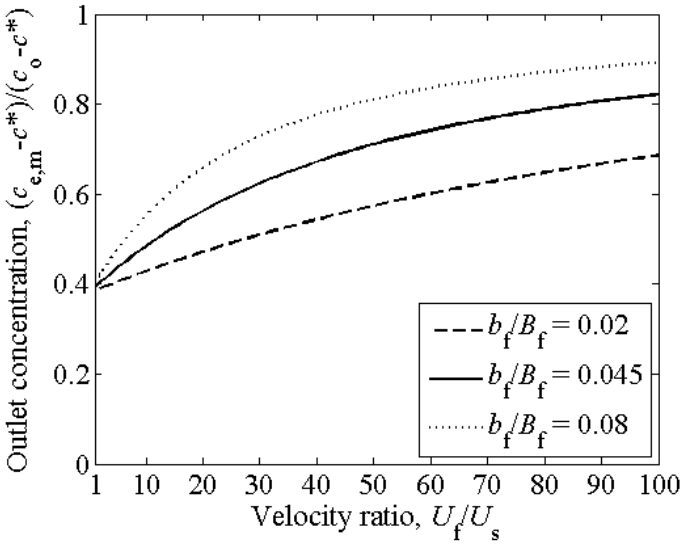

Figure 4-6: Comparison of normalized exit concentration from a short-circuiting marsh region with different fast-flowpath widths. Results are shown for $b_f/B_f = 0.02$, for which $0.02 \leq q_f/Q_f \leq 0.67$ for $1 \leq U_f/U_s \leq 100$; $b_f/B_f = 0.045$ (as in Fig. 4-5), for which $0.05 \leq q_f/Q_f \leq 0.82$; and $b_f/B_f = 0.08$, for which $0.08 \leq q_f/Q_f \leq 0.90$. It is assumed that $k_f/k_s = 0.1$.

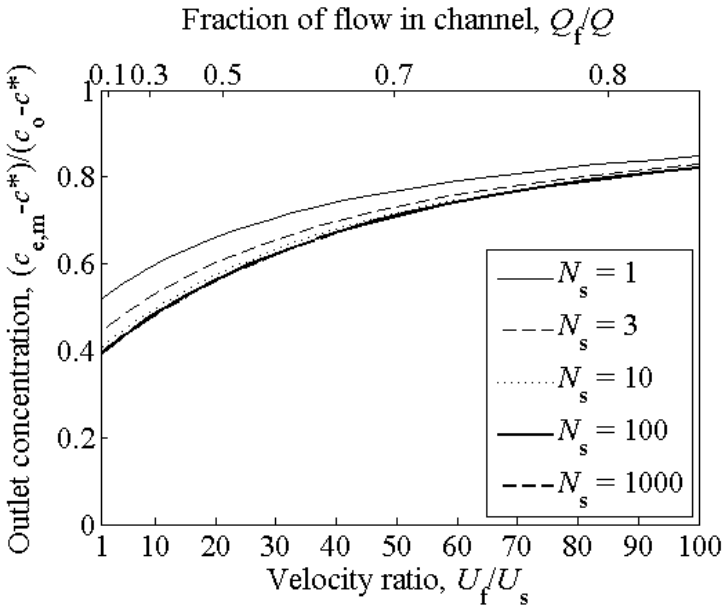

Figure 4-7: Comparison of normalized exit concentration from a short-circuiting marsh region with different amounts of longitudinal mixing. Results are shown for different values of N_s; different values of N_f do not change the displayed results. It is assumed that $k_f/k_s = 0.1$ and $b_f/B_f = 0.045$.

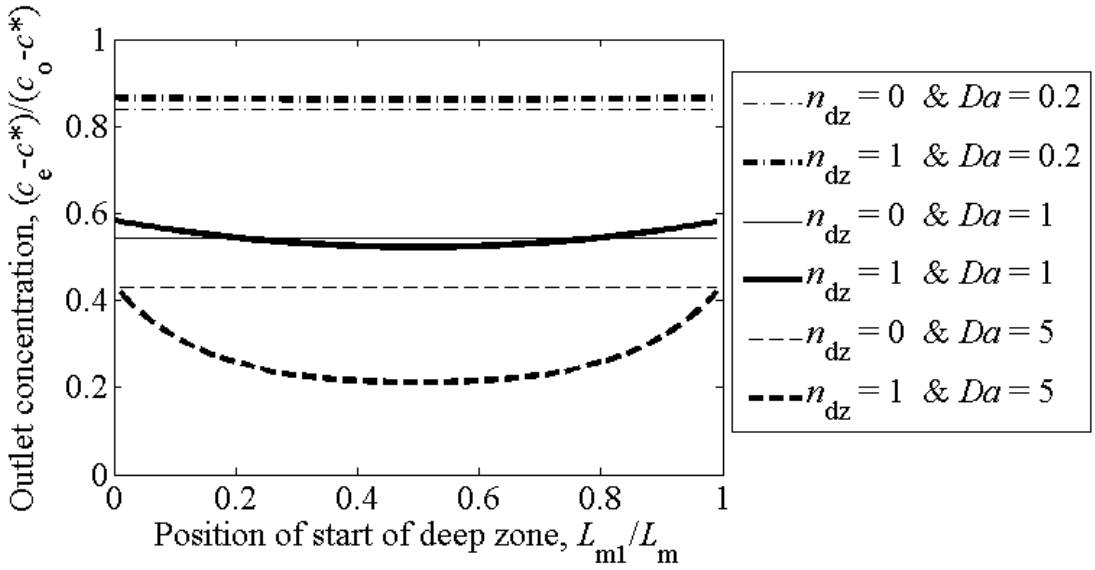

Figure 4-8: Analytic calculation of normalized exit concentration from a short-circuiting wetland without ($n_{dz} = 0$) and with ($n_{dz} = 1$) a laterally mixed transverse deep zone ($\lambda = 1$). When present, the normalized deep zone length $L_{dz}/L = 0.2$.

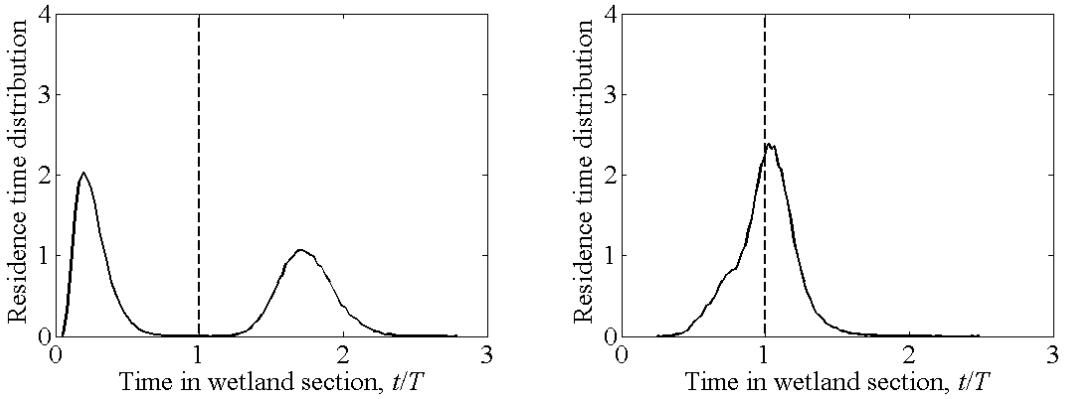

Figure 4-9: Sample residence time distributions for water parcels traveling through a marsh area followed by a deep zone. In (a), the degree of short-circuiting is large ($U_f/U_s = 20$), so that $(T_f - T_s) \gg T_{dz}$ and the deep zone cannot erase the short-circuiting signature, whereas in (b) the reduced short-circuiting [$U_f/U_s = 1.2$, so $(T_s - T_f) \ll T_{dz}$] leads to mixing of water that traveled through the fast- and slow-flow zones.

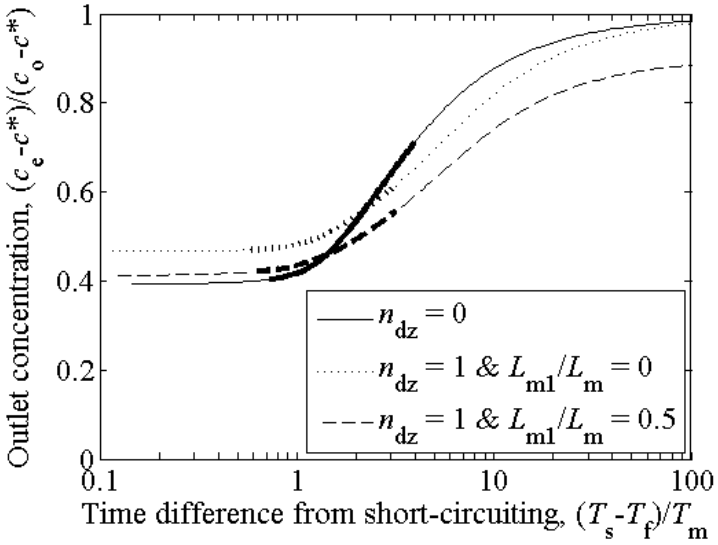

Figure 4-10: Analytic calculations of the effect of deep zone position on wetland performance for different velocity differences between fast- and slow-flow zones. It is assumed that $Da = k_s\tau = 1$ when $n_{dz} = 0$, and $b_f/B_f = 0.045$ is fixed. The thick portions of the lines indicate regions for which $2 < U_f/U_s < 50$, which would be expected in field situations.

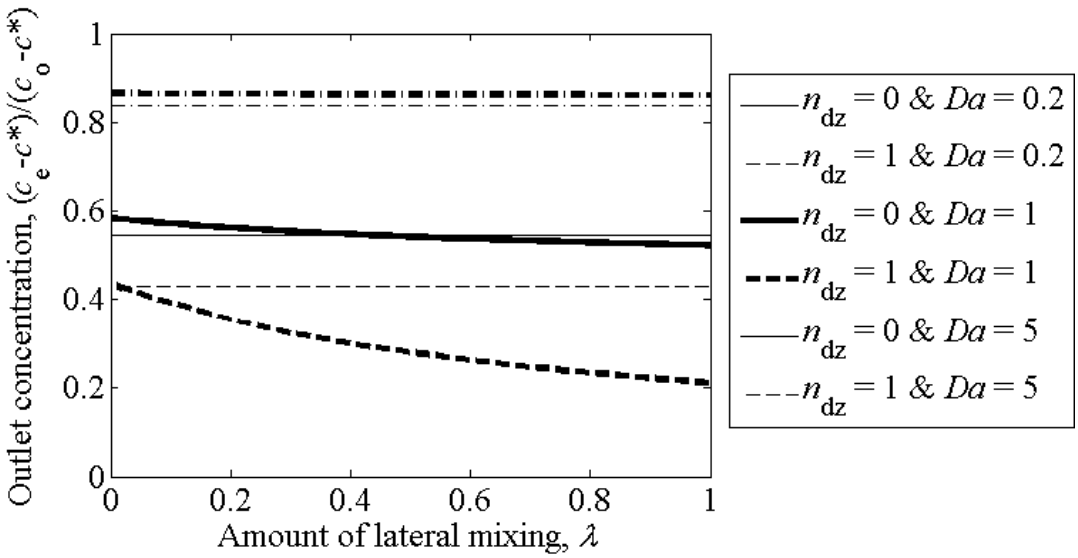

Figure 4-11: Analytic calculations of wetland performance depending on lateral mixing within a single deep zone located in the middle of a wetland with aligned fast flowpaths. Results are shown for three different Damkohler numbers. It is assumed that $L_{dz}/L = 0.2$, $L_{m1}/L_m = 0.5$, and $U_f/U_s = 20$.

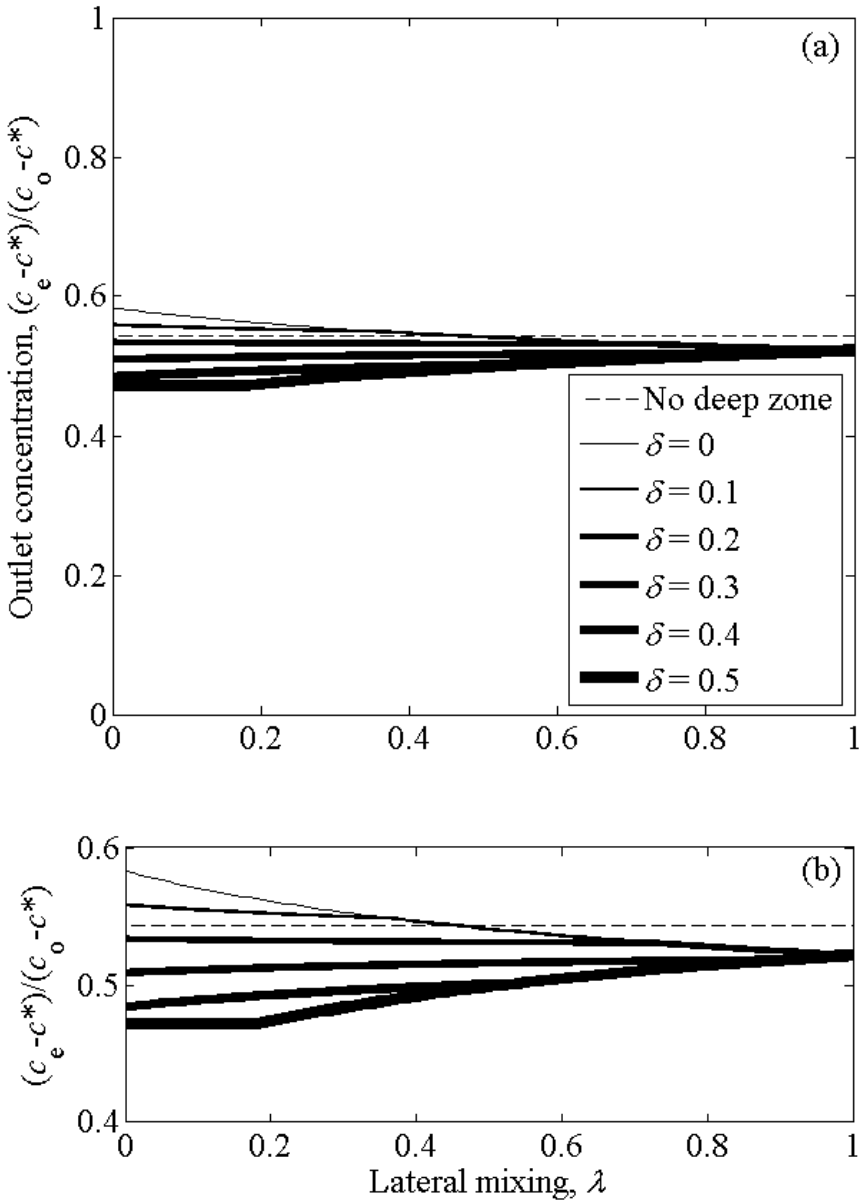

Figure 4-12: Analytic calculations of the effect of separation distance between upstream and downstream fast flowpaths near a single deep zone located in the middle of the wetland on the outlet concentration at the end of a downstream marsh section. Results are shown for different values of the lateral mixing λ within the deep zone. (a) All possible outlet concentrations. (b) Close-up of $0.4 \leq (c_e - c*)/(c_o - c*) \leq 0.6$. It is assumed that $Da = 1$ and $L_{dz}/L = 0.2$.

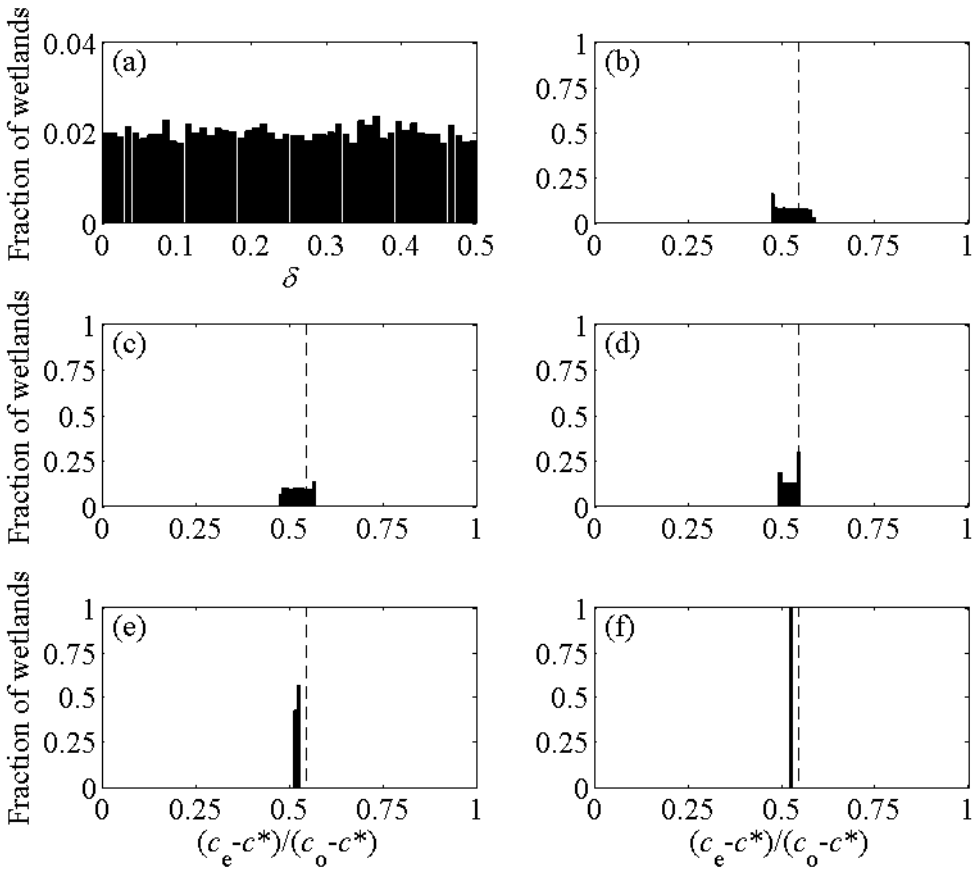

Figure 4-13: Monte Carlo simulations of outlet concentration from a wetland with a single deep zone with different amounts of lateral mixing λ. (a) Distribution of the distance between two short-circuiting flowpaths, $\delta = |y_1 - y_2|/B_f$, produced in 10,000 realizations in which y_1 and y_2 are selected randomly from uniform distributions. (b)–(f) Histograms of Monte Carlo simulations of outlet concentration from a marsh region following a single deep zone. Results are shown for different amounts of lateral mixing: (b) $\lambda = 0$, (c) $\lambda = 0.2$, (d) $\lambda = 0.5$, (e) $\lambda = 0.8$, (f) $\lambda = 1$. The vertical dashed line in each subplot indicates the performance of a wetland of the same length with no deep zone and one short-circuiting flowpath passing through the entire wetland. It is assumed that $Da = 1$ and $L_{dz}/L = 0.2$.

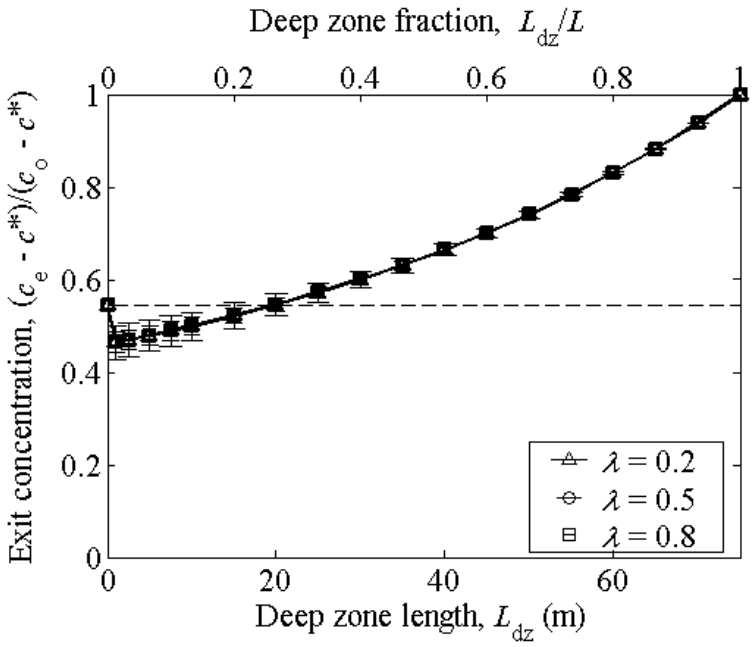

Figure 4-14: Mean exit concentrations from Monte Carlo simulations of flow through 10,000 75-m-long wetlands with a single deep zone of different lengths. Vertical bars indicate the standard deviation associated with each mean value. As shown in the legend, the length of the caps at the end of the bars indicates the associated value of λ. The dashed line is the removal expected in a short-circuiting marsh without a deep zone. $Da = 1$ in all simulations.

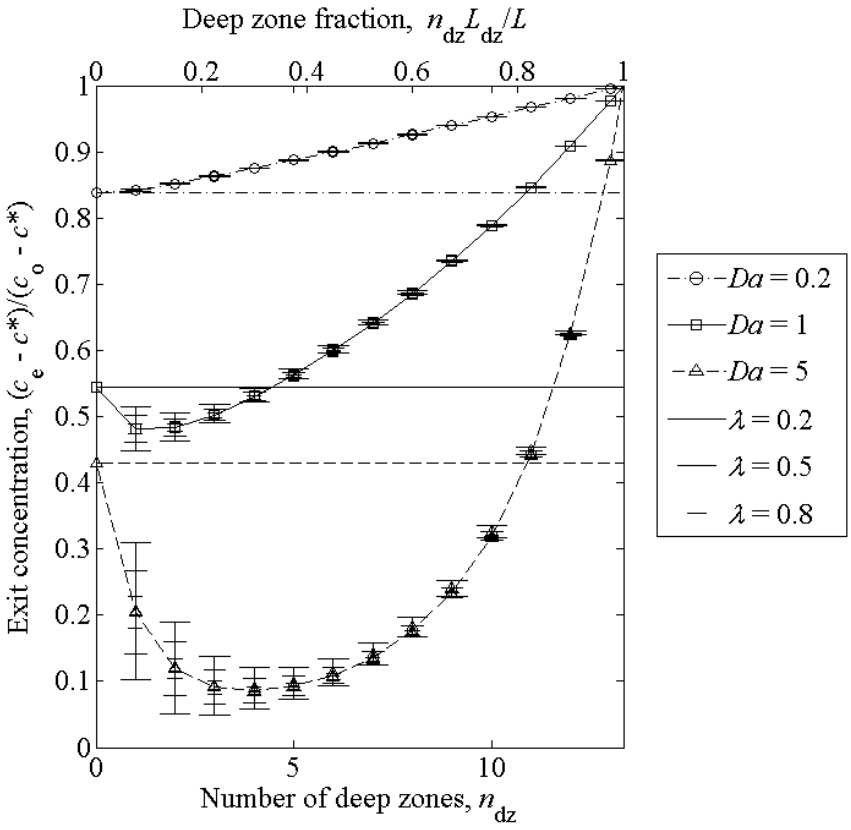

Figure 4-15: Mean exit concentrations from Monte Carlo simulations of flow through wetlands with different numbers of 15-m-long deep zones. For each number of deep zones, the marker shows the mean outlet concentration from simulations of 10,000 200-m-long wetlands in which the locations of short-circuiting flowpaths within each marsh region are chosen at random from a uniform distribution. Vertical bars indicate the standard deviation associated with each mean value. As shown in the legend, the length of the caps at the end of the bars indicates the associated value of λ. The horizontal lines are the removal expected in a short-circuiting marsh without a deep zone ($n_{dz} = 0$).

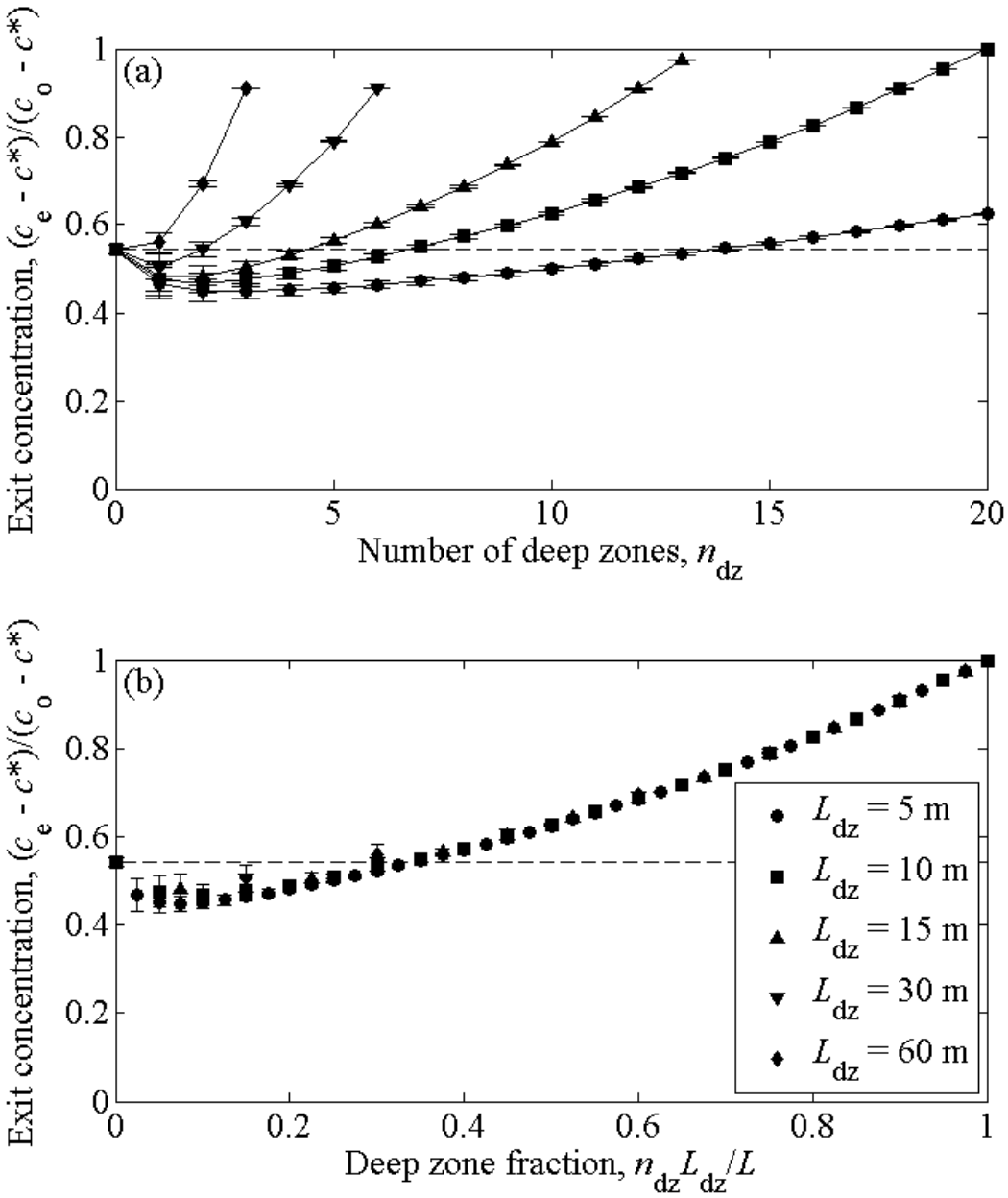

Figure 4-16: Mean exit concentrations from Monte Carlo simulations of flow through 10,000 200-m-long wetlands with different numbers of deep zones of different lengths. (a) Ensemble mean normalized exit concentration plotted as a function of the number of deep zones in each wetland. Vertical bars indicate the standard deviation associated with each mean value. (b) The same data plotted as a function of the fraction of wetland occupied by deep zones. The dashed line is the removal expected in a short-circuiting marsh without a deep zone. $Da = 1$ and $\lambda = 0.2$ in all simulations.

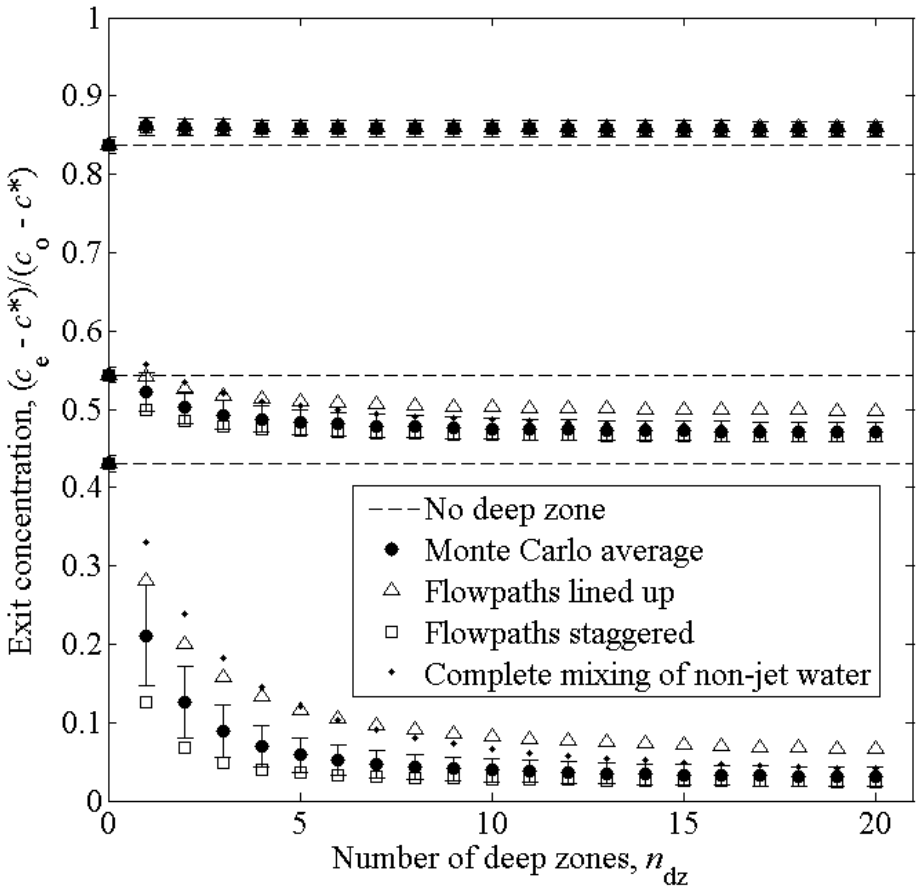

Figure 4-17: Mean exit concentrations from Monte Carlo simulations of flow through wetlands with different numbers of deep zones but the same fraction of deep zone area, $n_{dz}L_{dz}/L = 0.2$. Three different Damkohler numbers are shown: $Da = 0.2$ at the top, $Da = 1$ in the middle, and $Da = 5$ at the bottom. For each deep zone number, large filled circles indicate the mean outlet concentration from simulations of 10,000 wetlands in which the locations of short-circuiting flowpaths within each marsh region are chosen at random from a uniform distribution. Vertical bars indicate the standard deviation in the exit concentration. Also shown are the outlet concentrations for two specific flowpath configurations that serve as limiting cases: the "aligned" situation in which all fast flowpaths are located at the same transverse position, and the "staggered" situation in which flowpaths alternate at $y/B_f = 0$ and $y/B_f = 0.5$. These simulations all assume that non-jet water is not mixed; the small dots show the analytic result predicted when non-jet water is completely mixed. $\lambda = 0.5$ in all simulations.

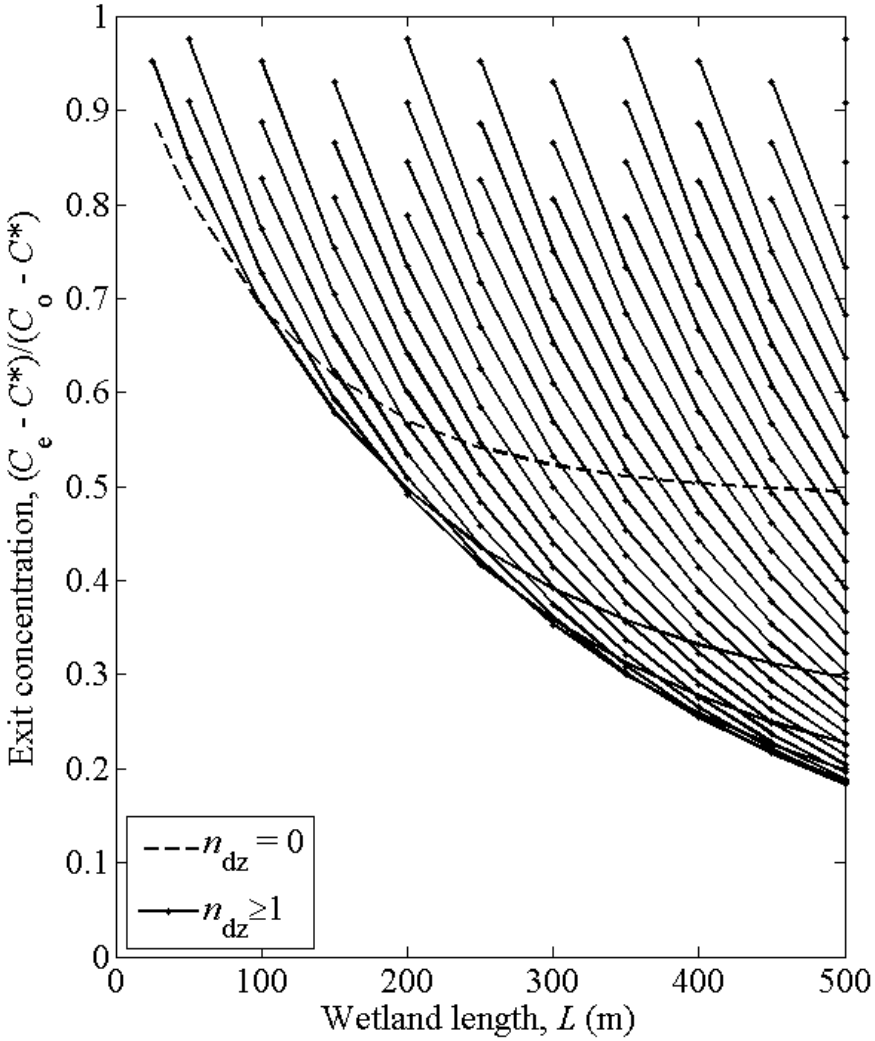

Figure 4-18: Mean exit concentration produced within wetlands of different lengths with different numbers of 15-m-long deep zones. For each combination of wetland length and number of deep zones, a dot indicates the mean exit concentration from a Monte Carlo simulation of 10,000 wetlands. The standard deviation associated with each point is not shown but is comparable to that shown in Fig. 4-15. Lines connect different points with the same number of deep zones; n_{dz} increases as the lines are added from left to right. It is assumed that $\lambda = 0.5$ and that $Da = 1$ when $L = 200$ m. The dashed line indicates the expected exit concentration when no deep zones are present.

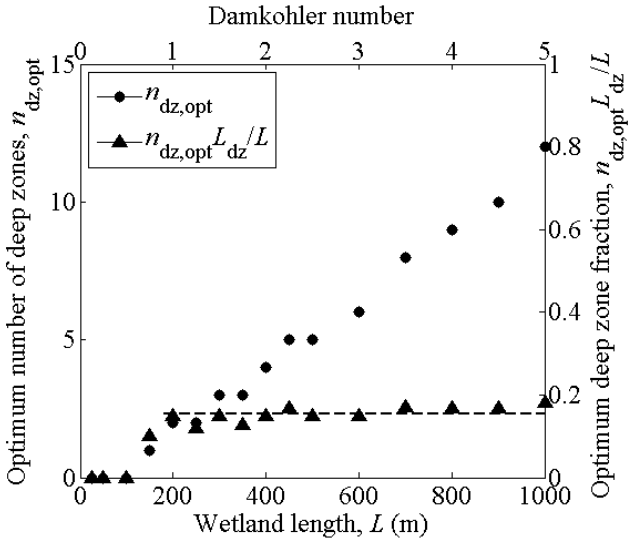

Figure 4-19: Optimum number of deep zones for wetlands of various lengths. For each wetland length shown in Fig. 4-18, the circle represents the number of deep zones that produces the lowest exit concentration. The corresponding deep zone length fraction $n_{dz,opt}\ L_{dz}/L$ is also shown for each wetland length. The dashed lined is located at $n_{dz,opt}L_{dz}/L = 0.15$. As in Fig. 4-18, it is assumed that $\lambda = 0.5$ and that $Da = 1$ when $L = 200$ m.

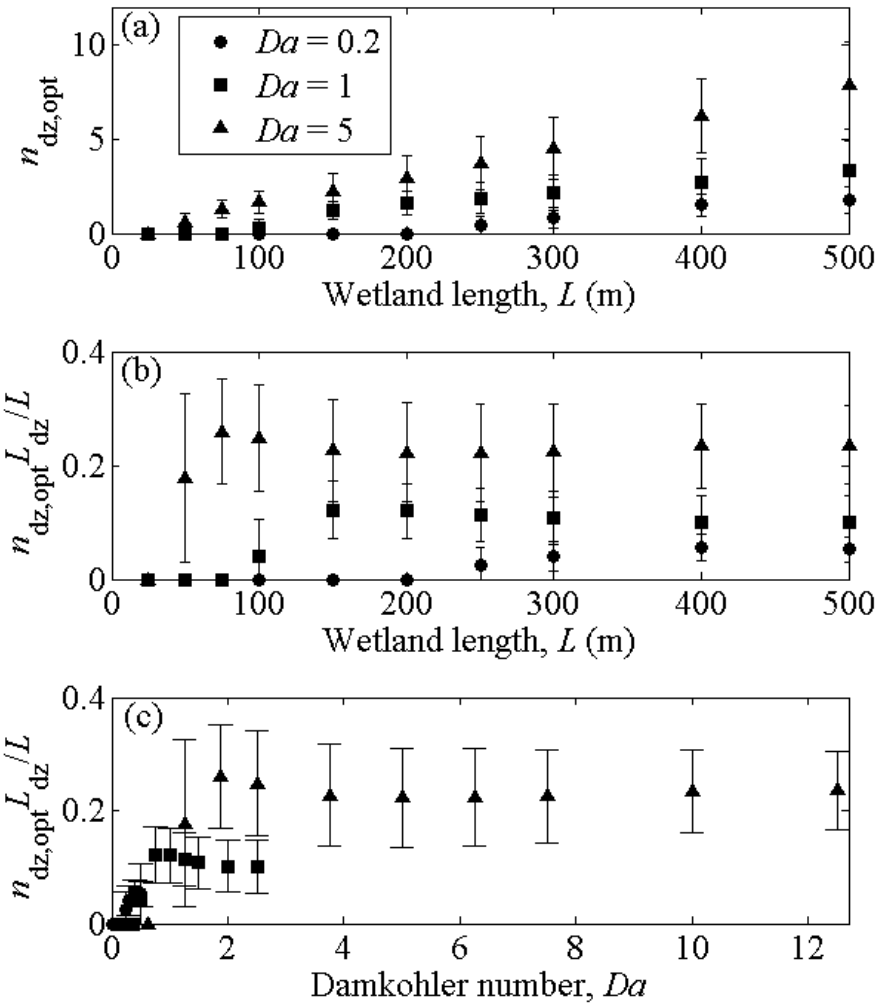

Figure 4-20: Optimal number of poorly mixed deep zones for wetlands of various lengths with different Damkohler numbers. (a) Number of deep zones that produces the minimum exit concentration, averaged over simulations of 10,000 different wetlands. Vertical bars indicate standard deviation in the value of $n_{dz,opt}$. (b) Same data, replotted to show the optimal deep zone fraction for wetlands of various lengths. (c) Same data, replotted as a function of the Damkohler number. Data are shown for three different Damkohler numbers measured for L = 200 m. In all simulations,$\lambda = 0.2$ and L_{dz} = 15 m.

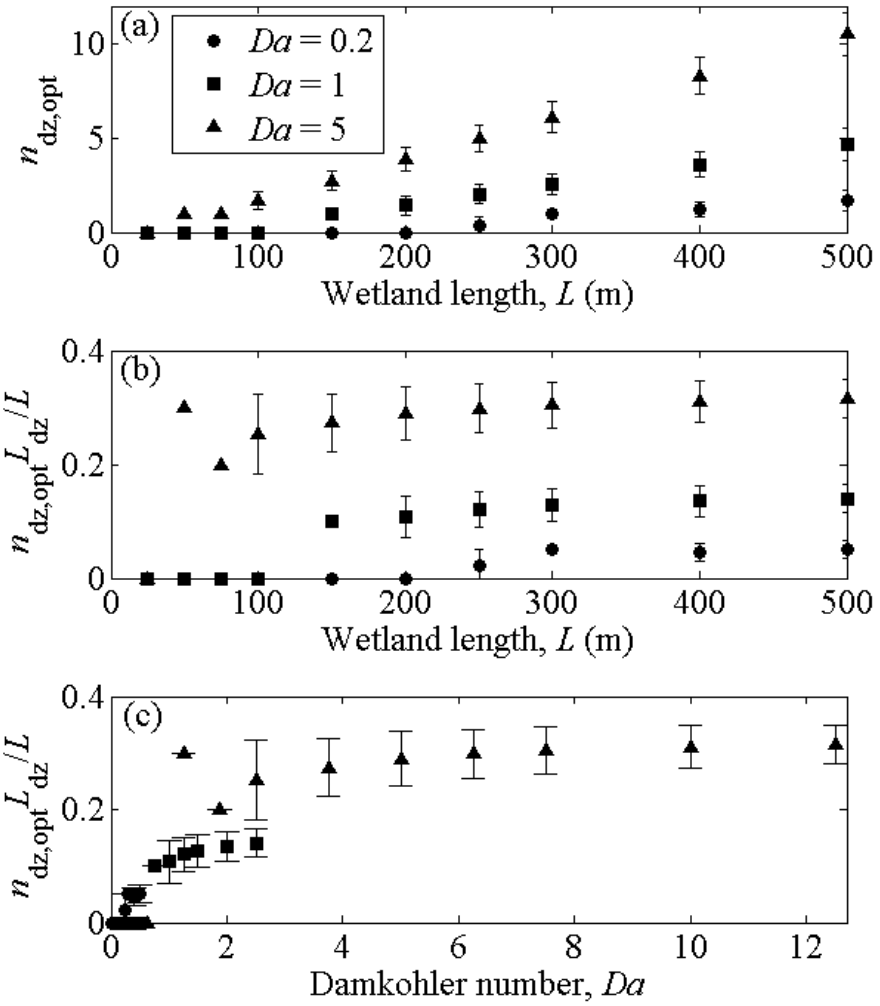

Figure 4-21: Optimal number of well-mixed deep zones for wetlands of various lengths with different Damkohler numbers. (a) Number of deep zones that produces the minimum exit concentration, averaged over simulations of 10,000 different wetlands. Vertical bars indicate standard deviation in the value of $n_{dz,opt}$. (b) Same data, replotted to show the optimal deep zone fraction for wetlands of various lengths. (c) Same data, replotted as a function of the Damkohler number. Data are shown for three different Damkohler numbers measured for $L = 200$ m. In all simulations,$\lambda = 0.8$ and $L_{dz} = 15$ m.

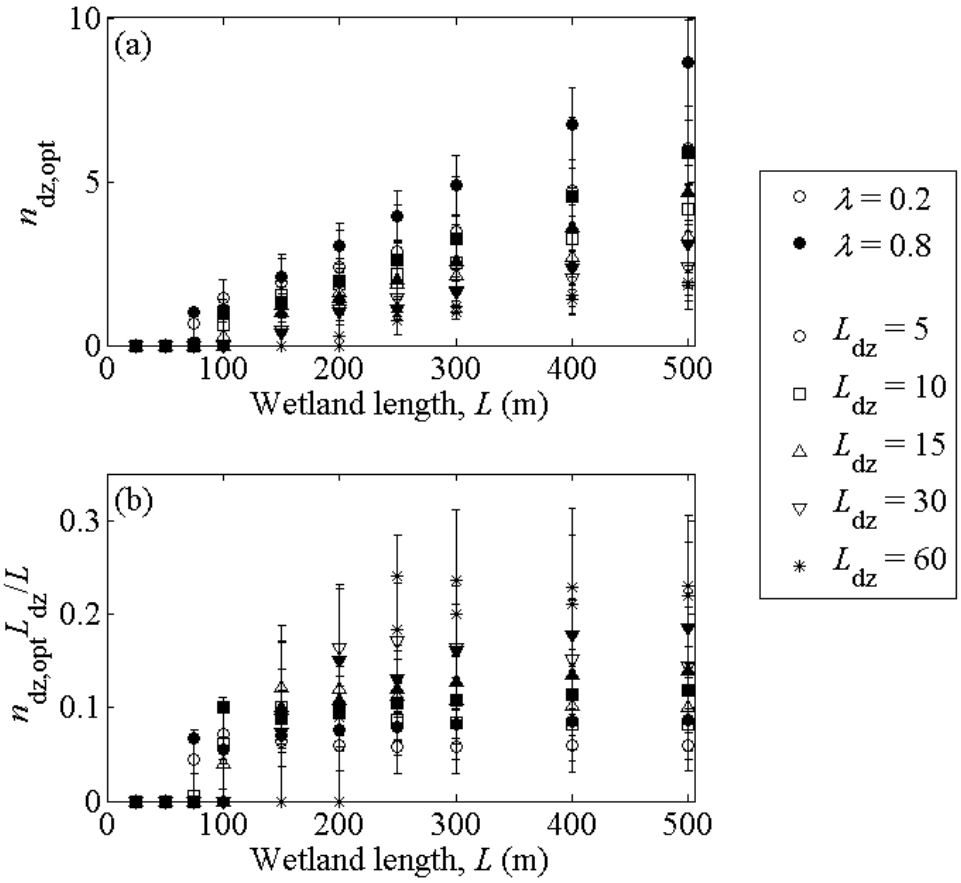

Figure 4-22: Optimal number of deep zones for wetlands of various lengths with different deep zone lengths. (a) Number of deep zones that produces the minimum exit concentration, averaged over simulations of 10,000 different wetlands. Vertical bars, which are horizontally offset to minimize overlap, indicate standard deviation in the value of $n_{dz,opt}$. (b) Same data, replotted to show the optimal deep zone fraction for wetlands of various lengths. Data are shown for five different deep zone lengths, which are assumed longer than the minimum length necessary for both momentum dissipation and construction. Also shown are two different levels of lateral mixing, $\lambda = 0.2$ and $\lambda = 0.8$. In all simulations, $Da = 1$ for $L = 200$ m.

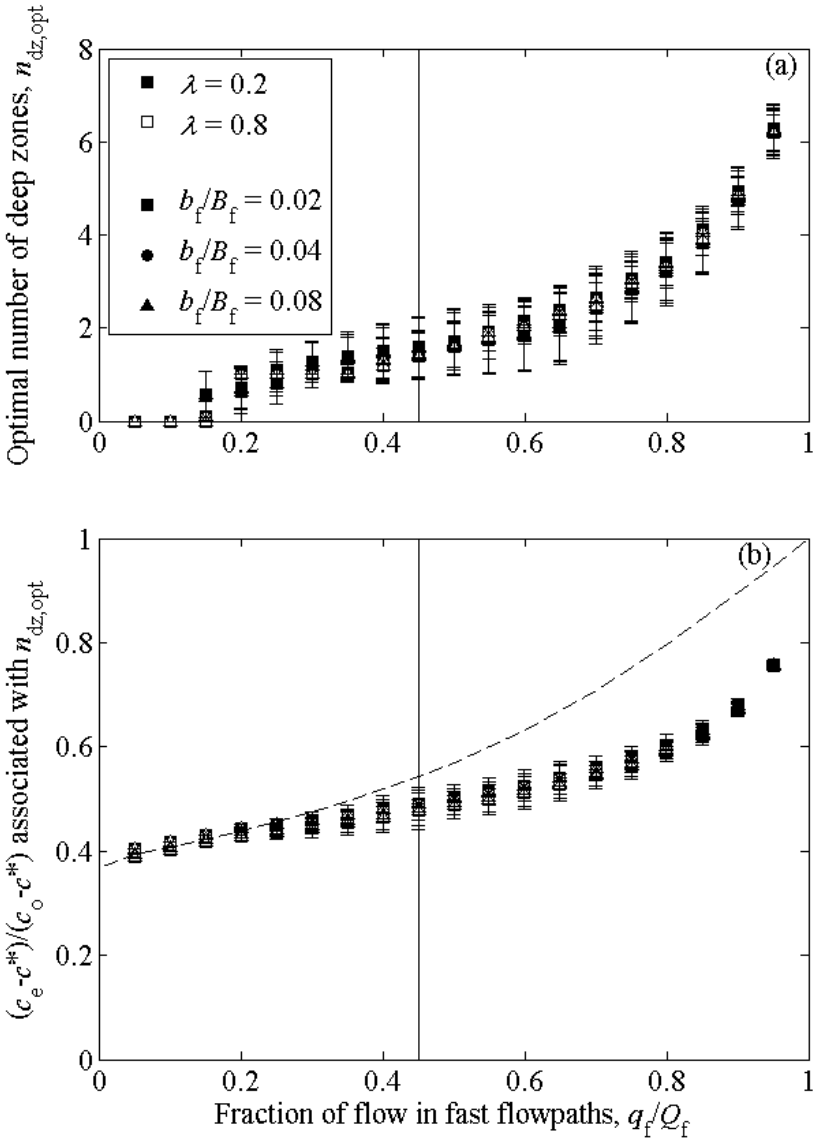

Figure 4-23: Optimal number of deep zones for wetlands with different amounts of short-circuiting flow. (a) For each flowpath fraction, the number of deep zones that produces the minimum exit concentration, averaged over simulations of 10,000 different wetlands. (b) The average exit concentration produced by the optimal number of deep zones for each configuration. The dashed line shows the expected outlet concentration when no deep zones are present. The vertical line shows $q_f/symQsingle = 0.45$, which is the value used in other figures. Vertical bars indicate standard deviation. Data are shown for three different flowpath widths, which result in velocity ratios $U_f/U_s = 1$–196, and two different levels of lateral mixing. In all simulations, $L = 200$ m, $L_{dz} = 15$ m, and $Da = 1$.

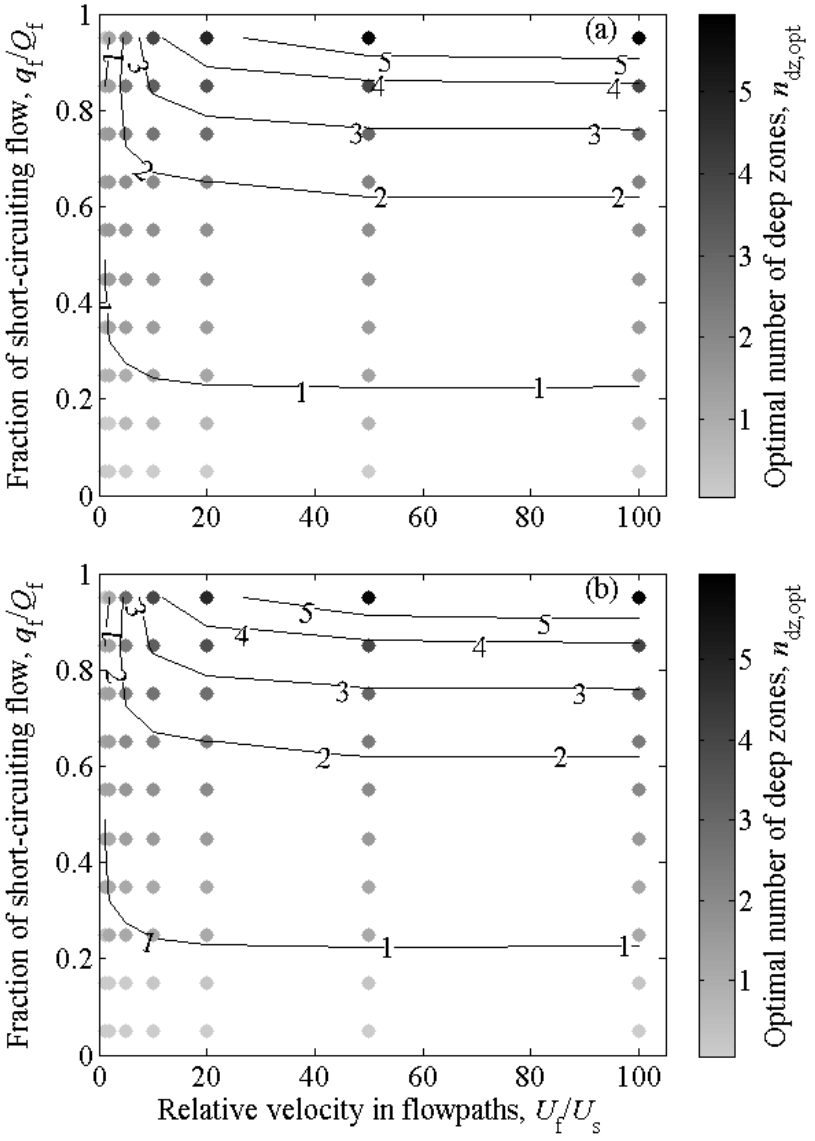

Figure 4-24: Optimal number of deep zones for wetlands with different velocities of short-circuiting flow. The color of the circles indicates the number of deep zones that produces the minimum exit concentration, averaged over simulations of 10,000 different wetlands, for each combination of fast and slow flow velocity ratio $1.1 \leq U_f/U_s \leq 100$ and fraction of short-circuiting flow $0.05 \leq q_f/Q_f \leq 0.95$. The contour lines show the interpolated positions of integer values of $n_{dz,opt}$. The width ratio for the velocity and flow fractions shown here varies over the range $0.0005 \leq b_f/B_f \leq 0.95$. Two different levels of lateral mixing are shown: (a) $\lambda = 0.2$ and (b) $\lambda = 0.8$. In all simulations, $L = 200$ m, $L_{dz} = 15$ m, and $Da = 1$.

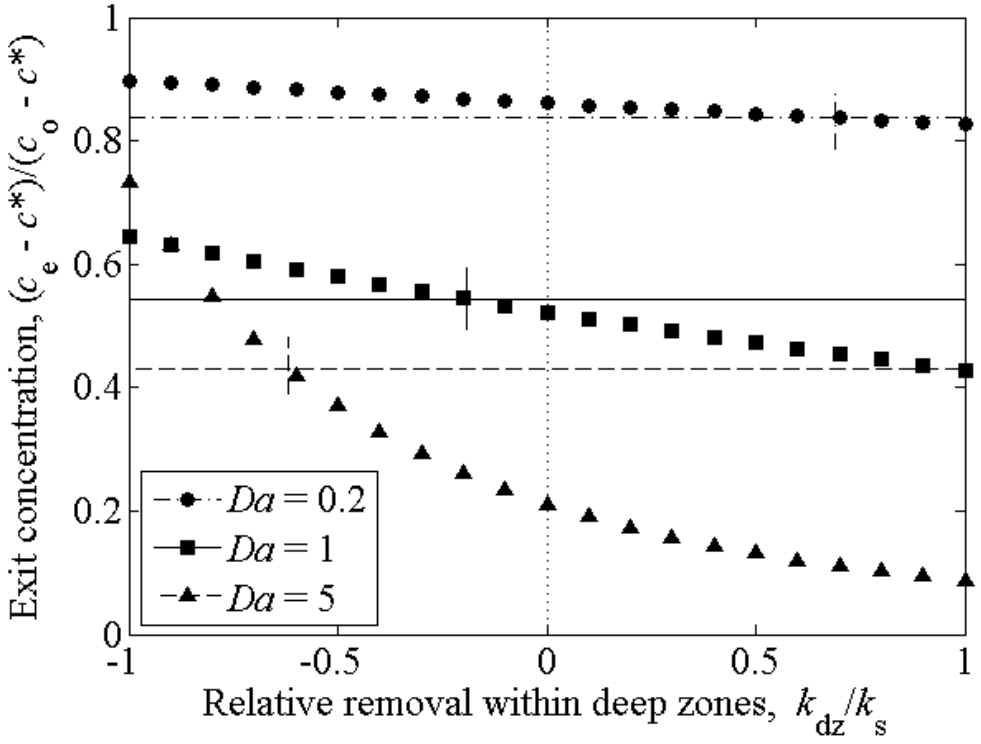

Figure 4-25: Mean exit concentration from a 75-m-long wetland with a single centrally located 15-m-long deep zone with different contaminant removal rates. The vertical dotted line indicates the exit concentration when no removal occurs within the deep zone ($k_{dz} = 0$). For each Damkohler number shown, the thin horizontal line represents the removal expected in a short-circuiting marsh without a deep zone, and the short vertical line indicates where the expected removal for wetlands with deep zones crosses the prediction without deep zones. Note that the relative removal rate is presented on an areal basis; in the Augusta wetland, $h_{dz}/h_m = 0.3$. Full lateral mixing ($\lambda = 1$) is assumed within the deep zone in all simulations.

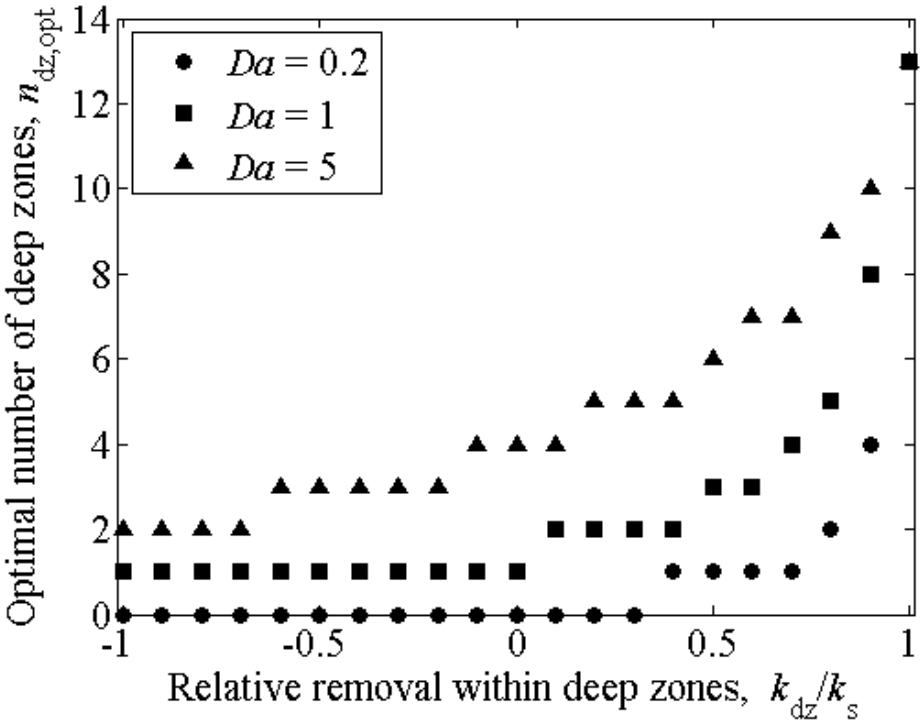

Figure 4-26: Optimal number of 15-m-long deep zones for 200-m-long wetlands with different contaminant removal rates and different Damkohler numbers. Full lateral mixing ($\lambda = 1$) is assumed within the deep zone in all simulations.

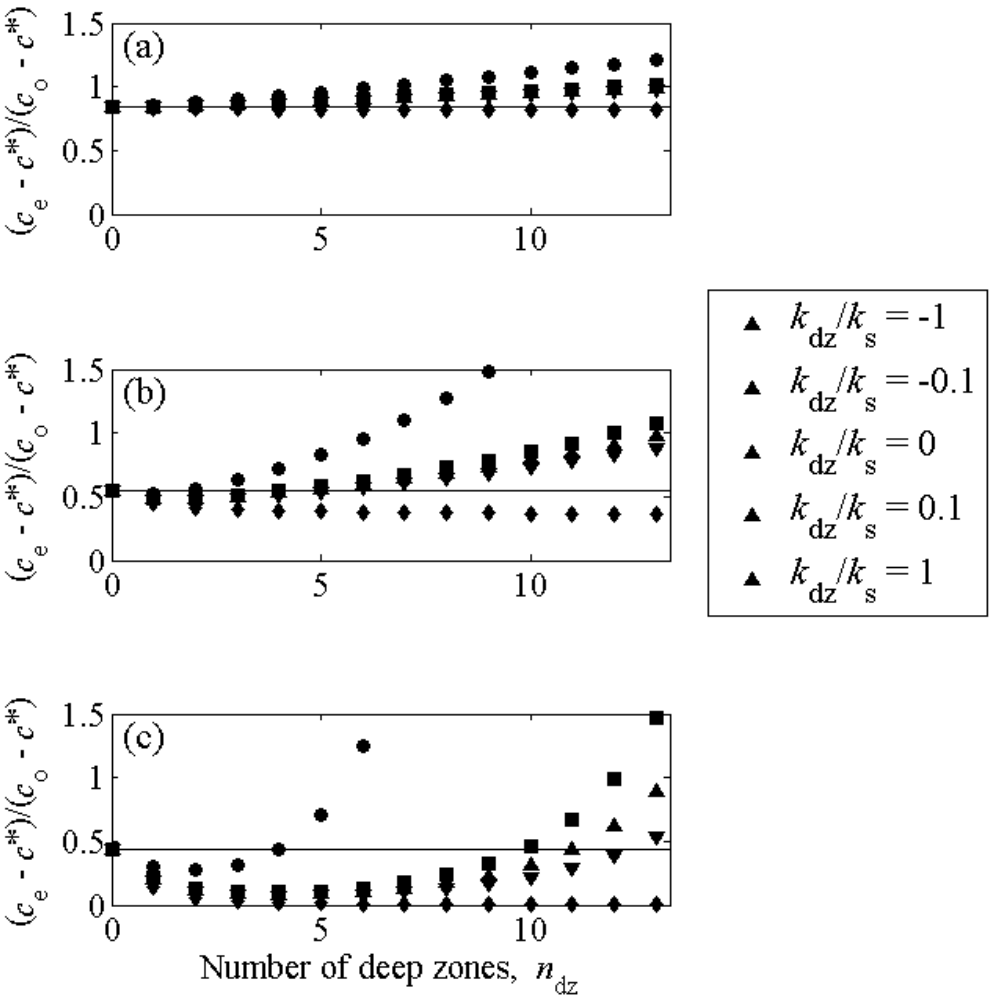

Figure 4-27: Mean exit concentrations from 200-m-long wetlands with various numbers of 15-m-long deep zones and different contaminant removal rates: (a) $Da = 0.2$, (b) $Da = 1$, and (c) $Da = 5$. The horizontal thin line in each subplot indicates the exit concentration when no deep zone is present ($n_{dz} = 0$). Full lateral mixing ($\lambda = 1$) is assumed within the deep zone in all simulations.

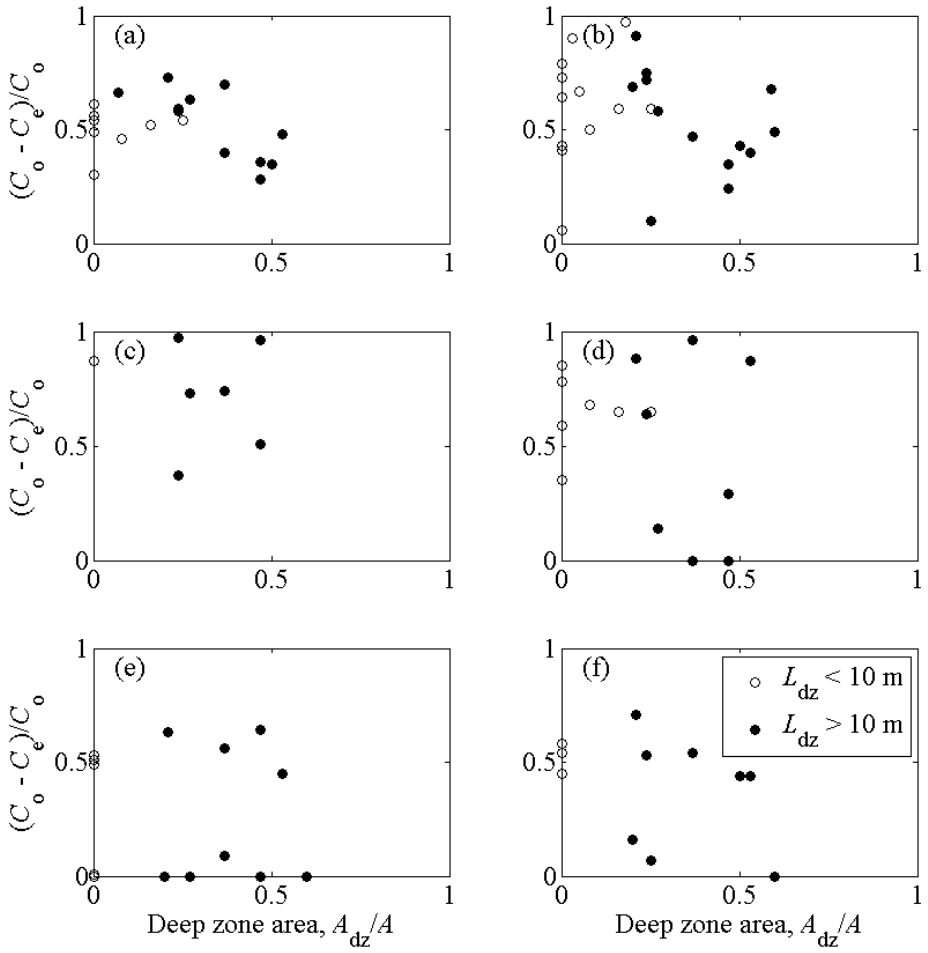

Figure 4-28: Nitrogen removal data for wetlands with interior deep zones presented in Table 1.3. Negative removals are plotted at zero. (a) Total nitrogen, (b) Ammonium nitrogen, (c) Nitrite nitrogen removal, (d) Nitrate nitrogen, (e) Organic nitrogen, (f) Total Kjeldhal nitrogen. All concentrations shown are reported as mg-N/L.

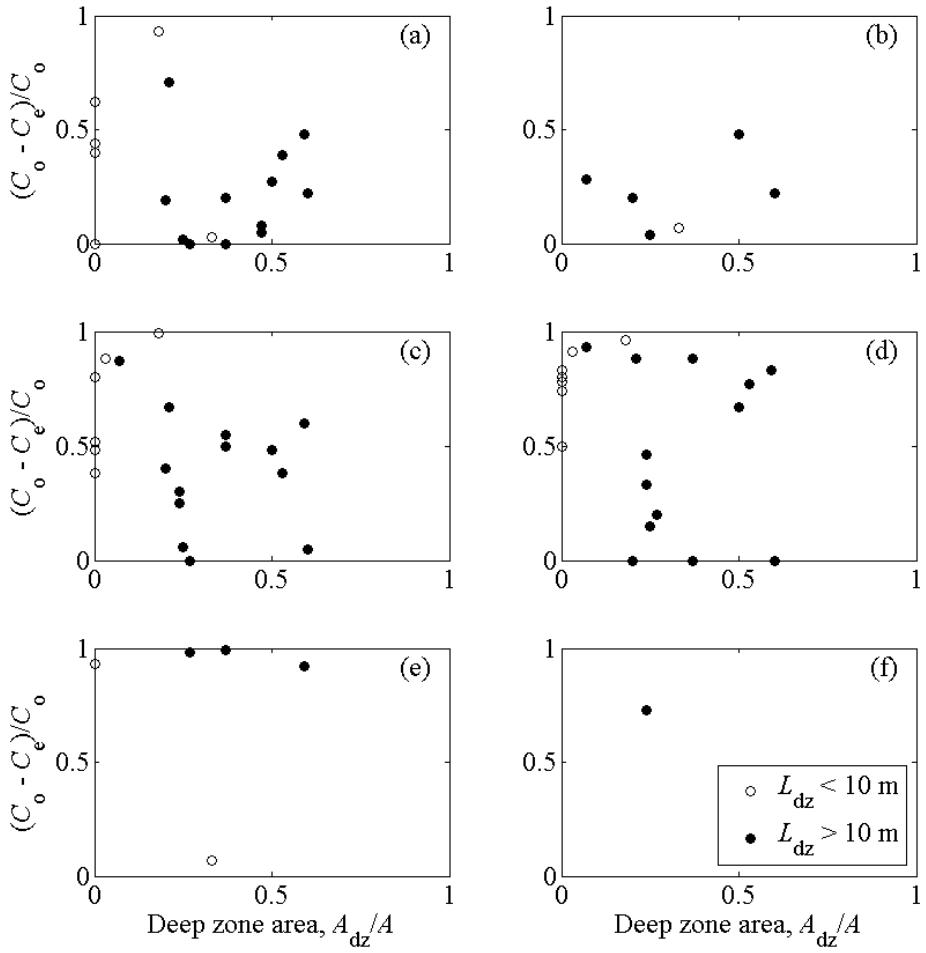

Figure 4-29: Removal data for wetlands with interior deep zones presented in Table 1.3. Negative removals are plotted at zero. (a) Total phosphorus (mg/L), (b) Organic phosphorus (mg-P/L), (c) 5-day Biological oxygen demand (mg/L), (d) Total suspended solids (mg/L), (e) Fecal coliforms (cfu/100 mL), (f) Volatile organic compounds (μg/mL).

Chapter 5

Design Recommendations and Areas for Further Research

The previous sections have shown that narrow, distinct fast flowpaths, surrounded by but not exchanging with slow flow, carry a large fraction of the water through marsh areas within the Augusta wetland. Moreover, when this fast-flowing water enters the deep zones, lateral mixing is correlated with the strength of wind directed transversely across the wetland. A laboratory scale model confirmed that the drag present within the system contributed to rapid momentum loss within the deep zone, and that jet entrainment was limited as a result. In addition, the rapid momentum decay separated the effect of downstream flow paths on transport within the deep zone. Finally, these results were combined in a conceptual mathematical model that examines the effect of wetland short-circuiting on performance. The numerical model shows that deep zones can improve wetland performance through two separate mechanisms. When lateral mixing is present within the deep zone, it dilutes the water that has traveled through the fast flowpath and reduces the fraction of water that short-circuits the entire wetland length. In addition, by dissipating the high velocity associated with the fast flowpaths, it is likely that deep zones reduce the probability that fast flowpaths will align throughout the entire wetland. Therefore, even when no lateral mixing is present within the deep zones, there is a much greater probability that all water will receive some treatment, again increasing performance. Design rec-

ommendations based on these findings are presented below, along with suggestions for further research.

5.1 Design recommendations

The above numerical modeling efforts, which are based on field and laboratory observations, suggest the following recommendations for future wetland design. The model is insufficient to provide exact predictions of how deep zones affect wetland performance because the position of fast flowpaths in a particular wetland cannot be predicted a priori. In addition, wetland performance will depend on many factors in addition to the inclusion of deep zones, and it is impossible to predict wetland removal without knowing those variables. Even so, preliminary recommendations are provided here to illuminate trends and relative tradeoffs between various design choices.

- **Design wetlands with short-circuiting in mind.** Due to the presence of short-circuiting, plug-flow approaches are inadequate to predict constructed treatment wetland removal. In the absence of canals, ditches, or other obvious features that affect local topography, the exact pattern of fast flowpaths is most likely beyond human control. Wetland designers should assume that short-circuiting will develop, however, and take measures such as including deep zones to prevent some water from completely bypassing the wetland designed to treat it.

- **Make deep zones as short as possible to provide momentum dissipation**. The minimum deep zone length $L_{dz,min}$ that can be constructed and that can provide complete momentum dissipation will depend on site-specific factors; in the Augusta wetland, it was found to be $L_{dz,min} = 15$ m. Under calm conditions, no hydraulic benefit is obtained from including deep zones longer than the minimum deep zone length, $L_{dz,min}$. Because the presence of deep zones eliminates area that could otherwise be used for productive marsh zones, longer deep zones may decrease removal.

- **Do not include interior deep zones in small wetlands.** If deep zones cannot

provide direct removal (e.g., if thick stands of periphyton are not present), do not include deep zones in short wetlands (wetland length $L < 50$ m for a deep zone length of $L_{dz} = 15$ m) or in wetlands that are undersized relative to the contaminant of interest (Damkohler number $Da < 1$). Within these wetlands, deep zones will occupy valuable area that could be planted with biologically active marsh areas.

- **Place deep zones in the middle of the wetland.** Space deep zones evenly within the wetland (e.g., a single interior deep zone should be located halfway down the wetland). When deep zones are included, they should stretch completely across the wetland (Fig. 1-1) to provide the maximum amount of lateral flow redistribution.

- **Commit 5–35% of the wetland area to deep zones.** The optimal fraction of wetland area is within the range 5–35%, depending on the Damkohler number, the amount of lateral mixing within the deep zone, the length of each deep zone, the fraction of flow in fast flowpaths, and the removal within the deep zone (see Figs. 4-20, 4-21, 4-22, 4-23, and 4-27). For a particular deep zone fraction, include the most deep zones possible (Fig. 4-17) while making each deep zone long enough to attain complete momentum dissipation ($L > L_{dz,min}$).

- **Foster periphyton and macrophyte growth within deep zones.** It is likely that periphyton, floating aquatic vegetation, and submerged aquatic vegetation within the deep zones may serve to dissipate momentum, creating a narrower minimum deep zone length. Although they may also inhibit wind mixing, this effect will not on average reduce wetland performance. In addition, plants within the deep zones may provide contaminant removal, which will increase wetland performance. Although the presence of vegetation within the deep zone may inhibit air-water exchange of oxygen and other gases, it may also aerate the water column through biological production during photosynthesis.

- **Size wetlands appropriately for the contaminant of interest.** Modeled results presented above confirm that the removal expected from a constructed wetland is sensitive to the Damkohler number, Da. Even a complicated design cannot compensate

for an under-sized wetland with too short a residence time. As a result, surface-flow treatment wetlands may not be appropriate for highly urbanized areas where land costs prohibit projects with large footprints.

- **Reduce the development of short-circuiting flowpaths.** Because short-circuiting is so damaging to wetland performance and the performance reduction increases in proportion to the volume of flow that short-circuits the wetlands, reduce the occurrence of fast flowpaths as much as possible. During wetland construction, ditches, canals, and stream beds directed longitudinally within the wetland should be filled (John et al., 2001), and microtopography should be graded as flat as possible. Wetlands used to treat storm water or other flashy flows should include an upstream retention basin or bypass to eliminate intense flooding events, which can damage wetland vegetation. Exclude nutria and muskrats, which can destroy large patches of vegetation. Different species of vegetation will respond to different water levels differently (Giovannini and da Motta Marques, 1999) and will exert different drag on the flow (Tsihrintzis and Madiedo, 2000; Jordanova et al., 2006), so when multiple species of macrophytes are included they should be planted in transverse bands across the wetland.

- **Pay attention to the dominant wind direction.** In a narrow wetland, the wetland should be oriented perpendicular to the direction of prevailing winds and located away from forests and buildings that can shelter it. In wetlands in which deep zones align, wind can provide lateral mixing within deep zones that will reduce the risk of short-circuiting water traversing the deep zone and entering another fast flowpath downstream. Note, however, that in a wide wetland the wind can create a large setup that could cause overtopping of berms (Eidson et al., 2005).

- **Consider local cost constraints during wetland design.** Installing multiple deep zones within a wetland is not necessarily more expensive than creating a uniform, flat wetland within the same footprint. Most successful constructed wetlands necessitate large amounts of grading whether or not deep zones are present, and the additional complicated bathymetry of a wetland with deep zones may increase

costs slightly but not substantially. In fact, in some wetlands deep zones represent a cost savings, by serving as borrow pits for fill used during berm construction and by reducing the need for vegetation and planting.

- **Oversize wetland deep zones to account for sediment deposition over time.** Over time, sediment deposition and macrophyte colonization will decrease the volume of deep zones. To ensure that the momentum dissipation length remains shorter than the deep zone length even as the wetland ages, deep zones must initially be oversized and built longer and deeper than necessary.

- **Provide appropriate maintenance.** Good flow patterns are promoted by clearing the outlet box, especially in systems without a final deep zone. Replant vegetation after storm events so that an incipient fast flowpath will not expand. Every decade, deep zones may need to be scraped to removed accumulated sediment.

5.2 Areas for further research

To increase confidence in these results and develop more specific recommendations, additional work should be performed in the following areas:

5.2.1 Model validation

- **Model assumptions**. A model is only as good as its assumptions. Here, there are numerous assumptions, which reduce the complexity of a wetland ecosystem to a deterministic series of equations. Model results have not yet been verified with detailed measurements of contaminant removal within the Augusta wetland or elsewhere. Verification is necessary because certain necessary simplifications may prove to remove a vital part of the system. For example, the Damkohler numbers and removal expectations discussed here are based on the average removal, which is based on the average loading. However, due to stochastic processes, monthly loadings can be as much as three times the monthly average (Kadlec and Knight, 1996; Kadlec, 1997, p. 608). In general, it is likely that these simplifications will be able to describe

flow in a relatively small wetland well, but assumptions of uniform marsh areas and normal flow will break down in a large wetland cell that is longer than approximately 1000 m.

- **Verification in additional wetlands**. Present understanding of fast flowpaths is based on detailed measurements of the short-circuiting flow rates within portions of a single wetland during a single month. Although results are consistent with prior measurements, similar measurements have not been performed at other wetlands, and these conclusions have not been verified elsewhere. For example, there are no data from other wetlands to test the assumption that flowpaths are coherent, or that two flowpath speeds are sufficient to represent all wetlands, or that the momentum dissipation length is much less than the deep zone length in all systems. Therefore, further investigations are necessary to confirm that these results are generalizable. In the Augusta wetland, although periphyton was present within the bench regions of the deep zones, most of the volume of the deep zones was open. In other wetlands, including sloughs, thick periphyton colonies, algal mats, or a large prevalence of floating aquatic vegetation may alter the effect of deep zones, by sheltering the area from lateral wind mixing.

- **Momentum dissipation length.** The momentum dissipation length is vital because it limits how short deep zones can be while still providing lateral transport. It is likely that the type, density, and location of species within the deep zone affects this length scale, and measurements should be performed in additional wetlands to explore these relationships and obtain a robust method of estimating the minimum necessary length.

- **Removal rates within short-circuiting vegetation.** Wetland hydraulics by themselves are not sufficient to predict contaminant removal in a constructed wetland. The removal process, and its associated rate constants, must also be estimated. Although existing experimental data can often be fit to a first-order removal model (e.g., Kadlec and Knight, 1996), the resulting estimate of the volumetric or areal removal rate constant averages over the heterogeneity present within that wetland

(Kadlec, 2000). Measurements of the spatially varying removal rate could be obtained in concert with detailed measurements of short-circuiting, for example, by using different tracers to mark fluid within different flowpaths and then comparing the effluent concentration of each different flow stream. It is also possible to use internal concentration measurements under steady flow conditions to compare removal within identified short-circuiting flowpaths and the surrounding marsh (Dierberg et al., 2005) and to obtain robust estimates of first-order removal by comparing the residence time distributions (RTDs) of simultaneous releases of a conservative tracer and a reactive substance (Keefe et al., 2004; Luo et al., 2006). In addition, for some contaminants, such as total suspended solids (TSS), different removal rates may govern different fractions of the contaminant, and the average removal rate for the wetland may depend on the flow rate and the degree of short-circuiting (Kadlec, 2003*b*).

- **Effect of deep zone vegetation and periphyton on wind mixing and removal.** Detailed studies have not yet been performed on how the presence of floating aquatic vegetation or surface piercing periphyton may impact wind mixing. In addition, vegetation and algae within the deep zone will likely impact the removal rate in this region, but detailed internal measurements must be taken to quantify the effect.

5.2.2 Model extensions

- **Stratification within the deep zone.** As Wong et al. (1999) point out, the presence of vertical stratification in a deep zone area would reduce the available storage volume within the wetland. In addition, it is assumed here that water completely expands to fill the water depth as it flows out into the deep zone. Since temperature effects were measured and found to be substantial within the Augusta wetland (Sec. 2.3.3), the presence of stratification and the possibility for different flow patterns at different times of day should be explored. It is possible that, if the deep zone is stratified and the outflowing fast water enters the top of the water column, it experiences reduced drag and may not experience complete momentum dissipation by the end of the deep zone. On the other hand, if the water entering the deep zone area has a lower

temperature that the water within it, it would tend to sink, which would possibly increase mixing in analogy to a density current traveling down the entrance slope.

- **Seasonal effects.** Predicting wetland removal is further complicated because the removal rate may vary over the course of a year in response to seasonal changes in temperature, dissolved oxygen levels, vegetation, and the microbial community. During the winter, first-order removal kinetics may not be appropriate to model contaminant removal, in part due to changes in wetland chemistry during those periods (Goulet et al., 2001). For example, Goulet et al. (2001) report that a small constructed wetland in Ontario is a net sink for iron and manganese in the spring when the wetland is oxic, but anoxic conditions during summer, fall, and winter result in release from the wetland. A variety of removal rates should therefore be used. In addition, vegetation dieback and the formation of ice during winter months may affect flow patterns within surface flow wetlands in northern latitudes, although Smith et al. (2005) found that the detention time in a wetland in Nova Scotia containing interior deep zones was not reduced and short-circuiting was not increased in winter. In cold climates in systems in which vegetation detritus is rapidly decomposed, the model presented here may only work during the summer and fall growing seasons, when vegetation is dense and contributes drag that dominates flow through the marsh areas.

- **Unsteady flow.** Steady conditions are never truly present within a wetland. Even wetlands with nominally constant wastewater influent will exhibit some periodic fluctuations on the period of days to months in flow rates and input loadings (Kadlec, 1997; Bays and Knight, 2002). If these fluctuations are not large enough to deflect vegetation, then the velocity ratio between fast and slow flowpaths within the vegetation will not change (cf. Sand-Jensen, 2003; Lightbody and Nepf, 2006*a*), and the fraction of flow that short circuits the wetland will remain the same under different flow rates. When the timescale associated with changes in flow rate is much longer than the hydraulic residence time (HRT) of the wetland, then flow can be considered quasi-steady, and model simulations performed above (Chap. 4) can be applied di-

rectly, using the Damkohler number present at each point in time. When the flow rate changes rapidly but the vegetation is not deflected, then the RTDs for a given wetland will be invariant when normalized by flow-weighted time(Werner and Kadlec, 2000; Holland et al., 2004), and an analytic extension to the model presented in Chap. 4 would be possible. If, however, the changes in flow rate are able to deflect or dislodge vegetation and wrack, then the relative drag and hence flow patterns within marsh areas will change (Andradóttir and Nepf, 2000; Holland et al., 2004; Lee et al., 2004). The inflow rate to a wetland treating storm water can vary by several orders of magnitude, and the influent concentration of nitrogen and phosphorus can also increase in response to such storm events (Raisin and Mitchell, 1995; Raisin et al., 1997), but the changes in loading to a wetland treating secondary wastewater are less drastic (Fig. 2-3). Therefore, it is likely that unsteady conditions will be important in storm water wetlands (Raisin and Mitchell, 1995; Walker, 1998; Rash and Liehr, 1999; Andradóttir and Nepf, 2000; Ishida et al., 2006) and less important in constructed wetlands designed to treat wastewater. Further work should consider the effect of unsteady hydraulic and contaminant loading to better account for real-world conditions in storm water wetlands.

- **Other design features.** Many other design considerations (Sec. 1.7) affect the success of a particular wetland. Important factors include the presence and type of pretreatment, the number and design of inlet and outlet structures, the initial planting and vegetation establishment, the inclusion of periodic transverse benches or flow-through berms, and wetland maintenance. The inclusion (or not) of deep zones is simply one factor among many that affect these complicated biological systems, and it cannot be made in isolation. Therefore, the effect of other design choices on wetland performance should be explored.

5.2.3 Flowpath measurement

- **Measurements of short-circuiting.** Detailed measurements of the size, flow, and distribution of fast flowpaths are necessary to properly represent the hydraulics of a

wetland system, but obtaining these measurements is difficult in a mature wetland. Flowpaths in the Augusta wetland could not be identified by eye, and a tracer study was found to be the only reliable method of identification. To assist with obtaining similar information at other wetlands, it would be helpful to develop less invasive measurement techniques to identify and quantify flow through short-circuiting flowpaths. Temperature measurements from the field (Sec. 2.3.3) suggest that remote sensing techniques may be able to help with flowpath identification. During daylight hours, a nearly 1°Celsius (C) difference in temperature was observed between fast-flowing and slow-flowing water. Because water traveled down fast flowpaths as a coherent stream and retained the thermal signature of an open water area upstream, its temperature was greater than water that traveled more slowly through dense vegetation. In fact, on some lateral traverses with the fluorometer and Conductivity, Temperature, and Depth (CTD) probe, elevated temperatures were present at the same lateral locations as short-circuiting was observed. Therefore, temperature could be used as a tracer of water velocity within this system. One possible but as yet unexplored technique would be to map the afternoon or evening thermal signature of water exiting marsh regions using an infrared thermal image of the wetland or a high-resolution fiber-optic cable, both of which are now able to detect temperature differences of 0.1°C at 1-m spatial resolution (Loheide II and Gorelick, 2006; Selker et al., 2006).

Note, however, that although temperature signatures may help identify the location and width of fast flowpaths, they could not directly quantify the flow rate of short-circuiting flowpaths. It may be possible to determine the rate at which warm short-circuiting water passing through dense vegetation loses heat, and then use an observed temperature decrease over a known distance to estimate the transit time. Another possibility would be to assume a fixed flow speed for all short-circuiting water. Additional detailed studies that quantify the amount of short-circuiting water in a variety of wetland types and locations are therefore necessary before temperature signatures can be used to identify and quantify the flow within short-circuiting regions.

- **Fast flowpath development.** Wetland designers need a better understanding of and control over flowpath formation. Little is known about the development and persistence of fast flowpaths within areas of dense vegetation. The high velocities present within freshwater and tidal streams erode the streambed and produce tidal creeks that are lower than the surrounding marsh platform (Fagherazzi and Sun, 2004; D'Alpaos et al., 2005). Periodic flood events within constructed wetlands may have a similar effect, leading to the development of a dominant, deeper, main channel. Once developed, flowpaths are likely to be sustained by positive feedback: fast flows increase shear stress on the few plants that remain or sprout within them, and the root systems of vegetation present within slow-flow zones stabilizes the soil surface against the formation of erosion channels (Brix, 1994; Fox et al., 2002; Schutten et al., 2004; Perucca et al., 2007). The result is likely to be that, whereas lateral mixing within a deep zone can vary over the course of a day as wind strength and direction shift, the locations of flowpaths likely persist within a single marsh region over a period of months if not years. It is also possible that an insufficiently long deep zone will tend to produce aligned flowpaths, which will decrease removal, because the water exiting a fast flowpath will not lose its excess momentum and so will create high stress at the vegetated region downstream. Operational methods may be able to reduce the formation of short-circuiting flowpaths.

- **Vegetated exchange.** Successful models of flow through wetlands must account for interactions between deep and shallow areas with different vegetation densities (Feng and Molz, 1997). However, flow interactions and exchange between deep zones and marsh areas are still not well understood. As noted above (Sec. 2.3.3), thermal exchange zones may be present and may comprise a large fraction of overall flux between a vegetated region and an open water zone (James and Barko, 1991). In addition, flow patterns within tidal marshes are complicated by asymmetrical flood and drainage patterns, which enhance dispersion on the marsh platform (Mazda et al., 1999; Lawrence et al., 2004).

5.3 Final thoughts

Constructed treatment wetlands hold much promise for low-cost, natural water treatment in an increasingly industrialized world. Additional information about past wetland installations and careful scientific examination of future wetland design elements hold promise for reducing the observed performance variability associated with these systems. Because of the importance of site-specific factors associated with each project, however, it will never be possible to predict and control the entire system in advance. The self-sustaining ecosystem within successful constructed treatment wetlands results in many of their most important benefits, including their ability to remove a wide range of contaminants, their low maintenance needs, and the habitat they provide for a diverse range of species. However, self-organization also leads to the development of short-circuiting, which poses one of the greatest challenges for wetland designers.

Bibliography

Abbas, H., R. Nasr, and H. Seif. 2006. Study of waste stabilization pond geometry for the wastewater treatment efficiency. *Ecological Engineering* 28: 25–34.

Abramovich, G. N. 1963. *The Theory of Turbulent Jets*. Cambridge, Massachusetts: The Massachusetts Institute of Technology Press, 671 pp.

Albertson, M. L., Y. B. Dai, R. A. Jensen, and H. Rouse. 1950. Diffusion of submerged jets. *Transactions of the American Society of Civil Engineers* 115: 639–697.

Alvord, H. H. and R. H. Kadlec. 1996. Atrazine fate and transport in the Des Plaines wetlands. *Ecological Modelling* 90: 97–107.

Andersen, D. C., J. J. Sartoris, J. S. Thullen, and P. G. Reusch. 2003. The effects of bird use on nutrient removal in a constructed wastewater-treatment wetland. *Wetlands* 23(2): 423–435.

Andradóttir, H. O. and H. M. Nepf. 2000. Thermal mediation in a natural littoral wetland: Measurements and modeling. *Water Resources Research* 36(10): 2937–2946.

Arega, F. and B. F. Sanders. 2004. Dispersion model for tidal wetlands. *Journal of Hydraulic Engineering* 130(8): 739–754.

Arzabe, M. 2000. *Evaluation of deep zone flow fields in constructed wetlands using a physical model*. MS thesis, Arizona State University, Tempe, Arizona. 78 pp.

Ates, N. and U. Ozesmi. 2002. A community grassroots project for domestic wastewater treatment through a created wetland. In: *Proceedings of the Eighth International Conference on Wetland Systems for Water Pollution Control*, Arusha, Tanzania: International Water Association, vol. 2, pp. 1049–1058.

Bachand, P. A. M. and A. J. Horne. 2006. Denitrification in constructed free-water surface wetlands: II. Effects of vegetation and temperature. *Ecological Engineering* 14: 17–32.

Bashir, J. and M. S. Uberoi. 1975. Experiments on turbulent structure and heat transfer in a two-dimensional jet. *Physics of Fluids* 18(4): 405–410.

Bays, J. S. and R. L. Knight. 2002. Fort Deposit constructed treatment wetlands system: 10-year review. In: J. Pries (ed.), *Treatment Wetlands for Water Quality Improvement: Quebec 2000 Conference Proceedings*. Waterloo, Ontario: CH2M HILL Canada Limited, Pandora Press, pp. 35–44.

Blahnik, T. and J. Day, Jr. 2000. The effects of varied hydraulic and nutrient loading rates on water quality and hydrologic distributions in a natural forested treatment wetland. *Wetlands* 20(1): 48–61.

Bolster, C. H. and J. E. Saiers. 2002. Development and evaluation of a mathematical model for surface-water flow within the Shark River Slough of the Florida Everglades. *Journal of Hydrology* 259: 221–235.

Bonomo, L., G. Pastorelli, and N. Zambon. 1997. Advantages and limitations of duckweed-based wastewater treatment systems. *Water Science and Technology* 35(5): 239–246.

Bracho, N., B. Lloyd, and G. Aldana. 2006. Optimisation of hydraulic performance to maximise faecal coliform removal in maturation ponds. *Water Research* 40: 1677–1685.

Bradbury, L. J. S. 1965. The structure of a self-preserving turbulent plane jet. *Journal of Fluid Mechanics* 23(1): 31–64.

Bradbury, L. J. S. and J. Riley. 1967. The spread of a turbulent plane jet issuing into a parallel moving airstream. *Journal of Fluid Mechanics* 27(2): 381–394.

Bragato, C., H. Brix, and M. Malagoli. 2006. Accumulation of nutrients and heavy metals in *Phragmites australis* (Cav.) Trin. ex Steudal and *Bolboschoenus maritimus* (L.) Palla in a constructed wetland of the Venice lagoon watershed. *Environmental Pollution* 144(3): 967–975.

Brix, H. 1994. Functions of macrophytes in constructed wetlands. *Water Science and Technology* 29(4): 71–78.

Brodie, G. A., D. A. Hammer, and D. A. Tomljanovich. 1989. Treatment of acid drainage with a constructed wetland at the Tennessee Valley Authority 950 coal mine. In: D. A. Hammer (ed.), *Constructed Wetlands for Wastewater Treatment*, Chelsea, Michigan: Lewis Publishers, pp. 201–209.

Broholm, M. M., K. Rügge, N. Tuxen, A. L. Højberg, H. Mosbæk, and P. L. Bjerg. 2001. Fate of herbicides in a shallow aerobic aquifer: A continuous field injection experiment (Vejen, Denmark). *Water Resources Research* 37(12): 3163–3176.

Brueske, C. C. and G. W. Barrett. 1994. Effects of vegetation and hydrologic load on sedimentation patterns in experimental wetland ecosystems. *Ecological Engineering* 3: 429–447.

Brunn, A. and W. Nitsche. 2003. Separation control by periodic excitation in a turbulent axisymmetric diffuser flow. *Journal of Turbulence* 4(1): Art. No. 009. doi:10.1088/1468-5248/4/1/009.

Buchberger, S. G. and G. B. Shaw. 1995. An approach toward rational design of constructed wetlands for wastewater treatment. *Ecological Engineering* 4: 249–275.

Campagna, A. R. and D. da Motta Marques. 2001. The effect of refinery effluent on the aquatic macrophytes *Scirpus californicus*, *Typha subulata*, and *Zizaniopsis bonariensis*. *Water Science and Technology* 44(11-12): 493–498.

Carapeto, C. and D. Purchase. 2002. Artificial wetlands and their importance for water quality. In: J. Pries (ed.), *Treatment Wetlands for Water Quality Improvement: Quebec 2000 Conference Proceedings*. Waterloo, Ontario: CH2M HILL Canada Limited, Pandora Press, pp. 45–52.

Carleton, J. N. 2002. Damköhler number distributions and constituent removal in treatment wetlands. *Ecological Engineering* 19: 233–248.

Carleton, J. N. and H. J. Montas. 2007. A modeling approach for mixing and reaction in wetlands with continuously varying flow. *Ecological Engineering* 29: 33–44.

CH2M Hill. 1993. West Jackson Co., MS: Constructed wetland treatment system case history. Office of Water, U. S. Environmental Protection Agency, Atlanta, Georgia, 9 pp.

Chen, C. J. and W. Rodi. 1980. *Vertical turbulent buoyant jets: a review of experimental data*. Elmsford, New York: Pergamon Press.

Chen, D. and G. H. Jirka. 1998. Linear stability analysis of turbulent mixing layers and jets in shallow water layers. *Journal of Hydraulic Research* 36(5): 815–830.

Chen, D. and G. H. Jirka. 1999. LIF study of plane jet bounded in shallow water layer. *Journal of Hydraulic Engineering* 125(8): 817–826.

Chen, S., G. T. Wang, and S. K. Xue. 1999. Modeling BOD removal in constructed wetlands with mixing cell method. *Journal of Environmental Engineering* 125(1): 64–71.

Chendorain, M., M. Yates, and F. Villegas. 1998. The fate and transport of viruses through surface water constructed wetlands. *Journal of Environmental Quality* 27: 1451–1458.

Chimney, M. J., L. Wenkert, and K. C. Pietro. 2006. Patterns of vertical stratification in a subtropical constructed wetland in south Florida (USA). *Ecological Engineering* 27: 322–330.

Chu, P. C. K., J. H. Lee, and V. H. Chu. 1999. Spreading of turbulent round jet in coflow. *Journal of Hydraulic Engineering* 125(2): 193–204.

Chu, V. H. and W. D. Baines. 1989. Entrainment by buoyant jet between confined walls. *Journal of Hydraulic Engineering* 115(4): 475–492.

Chu, V. H., J. H. Wu, and R. E. Khayat. 1991. Stability of transverse shear flows in shallow open channels. *Journal of Hydraulic Engineering* 117: 1370–1388.

City of Phoenix, W. S. D. 2001. Tres Rios Demonstration Constructed Wetlands Project: Water quality data analysis report. Phase 1, 1995 to 1998, U. S. Bureau of Reclamation, Denver, Colorado, 175 pp.

Conn, R. M. and F. R. Fiedler. 2003. Optimization of residence time in constructed free water surface wetlands through bathymetric design. In: *Getting it done: The role of TMDL implementation in watershed restoration: Conference Proceedings, October 29–30, 2003*. Stevenson, Washington: Cooperative State Research, Education, and Extension Service Pacific Northwest Regional Water Quality Program, 10 pp. `http://www.swwrc.wsu.edu/conference2003/index.html`.

Connor, M. A. and A. Luczak. 2002. Designing wetland treatment systems that contribute to wildlife conservation. In: *Proceedings of the Eighth International Conference on Wetland Systems for Water Pollution Control*, Arusha, Tanzania: International Water Association, vol. 2, pp. 1024–1037.

Cooper, A. B. 1994. Coupling wetland treatment to land treatment: An innovative method for nitrogen stripping? *Water Science and Technology* 29(4): 141–149.

Dal Cin, L. and J. Persson. 2000. The influence of vegetation on hydraulic performance in a surface flow wetland. In: K. R. Reddy and R. H. Kadlec (eds.), *Proceedings of the Seventh International Conference on Wetland Systems for Water Pollution Control*, Lake Buena Vista, Florida: International Water Association, vol. 2, pp. 539–546.

Dale, H. and T. Gillespie. 1976. The influence of floating vascular plants on the diurnal fluctuations of temperature near the water surface in early spring. *Hydrobiologia* 49: 245–256.

Dale, P., H. Chapman, and M. Greenway. 2002. Treatment constructed wetlands for sewage effluent treatment: Do they encourage mosquito breeding? In: J. Pries (ed.), *Treatment Wetlands for Water Quality Improvement: Quebec 2000 Conference Proceedings*. Waterloo, Ontario: Pandora Press, pp. 163–171.

D'Alpaos, A., S. Lanzoni, M. Marani, S. Fagherazzi, and A. Rinaldo. 2005. Tidal network ontogeny: channel initiation and early development. *Journal of Geophysical Research* 110: F02001. doi:10.1029/2004JF000182.

D'Alpaos, A., S. Lanzoni, S. M. Mudd, and S. Fagherazzi. 2006. Modeling the influence of hydroperiod and vegetation on the cross-sectional formation of tidal channels. *Estuarine Coastal and Shelf Science* 69(3-4): 311–324.

Danckwerts, P. V. 1953. Distribution of residence time. *Chemical Engineering Science* 2: 1–13.

Davidson, M. J. and H. J. Wang. 2002. Strongly advected jet in a coflow. *Journal of Hydraulic Engineering* 128(8): 742–752.

Davies, A. E., J. F. Ketter, and W. D. Baines. 1975. Spread of a heated plane turbulent jet. *Physics of Fluids* 18(7): 770–775.

DePaoli, L. L. 1999. *Numerical modeling of wetland hydrodynamics.* MS thesis, Massachusetts Institute of Technology, Cambridge, Massachusetts. 125 pp.

Dierberg, F. E., J. J. Juston, T. A. DeBusk, K. Pietro, and B. Gu. 2005. Relationship between hydraulic efficiency and phosphorus removal in a submerged aquatic vegetation-dominated treatment wetland. *Ecological Engineering* 25: 9–23.

Doody, D., R. Moles, H. Tunney, I. Kurz, D. Bourke, K. Daly, and B. O'Regan. 2006. Impact of flow path length and flow rate on phosphorus loss in simulated overland flow from a humic gleysol grassland soil. *Science of the Total Environment* 372: 247–255.

Dracos, T., M. Giger, and G. H. Jirka. 1992. Plane turbulent jets in a bounded fluid layer. *Journal of Fluid Mechanics* 241: 587–614.

Ead, S. A. and N. Rajaratnam. 2002. Plane turbulent wall jets in shallow tailwater. *Journal of Engineering Mechanics* 128(2): 143–155.

Economopoulou, M. A. and V. A. Tsihrintzis. 2004. Design methodology of free water surface constructed wetlands. *Water Resources Management* 18: 541–565.

Eger, P. 1994. Wetland treatment for trace metal removal from mine drainage: the importance of aerobic and anaerobic processes. *Water Science and Technology* 29(4): 249–256.

Eidson, G. W., O. Flite, and A. M. Garman. 2005. Constructed wetlands optimization study. Project No. 90155, Augusta-Richmond County, Southeastern Natural Sciences Academy, Augusta, Georgia, 105 pp.

Eidson, G. W. and O. P. Flite. 2005. Multi-year research on the use of constructed wetlands for advanced wastewater treatment. In: K. J. Hatcher (ed.), *Proceedings of the 2005 Georgia Water Resources Conference.* Athens, Georgia: Institute Ecology, The University of Georgia, 5 pp.

Eriksson, P. G. 2001. Interaction effects of flow velocity and oxygen metabolism on nitrification and denitrification in biofilms on submersed macrophytes. *Biogeochemistry* 55: 29–44.

Fagherazzi, S. and T. Sun. 2004. A stochastic model for the formation of channel networks in tidal marshes. *Geophysical Research Letters* 31: L21503. doi: 10.1029/2004GL020965.

Fang, X. and H. G. Stefan. 1991. Integral jet model for flow from an open channel into a shallow lake or reservoir. Project Report No. 315, St. Anthony Falls Hydraulic Laboratory, University of Minnesota, Minneapolis, Minnesota, 226 pp.

Fang, X. and H. G. Stefan. 2000. Dependence of dilution of a plunging discharge over a sloping bottom on inflow conditions and bottom friction. *Journal of Hydraulic Research* 38(1): 15–25.

Feng, K. and F. J. Molz. 1997. A 2-D, diffusion-based, wetland flow model. *Journal of Hydrology* 196: 230–250.

Fink, D. F. and W. J. Mitsch. 2007. Hydrology and nutrient biogeochemistry in a created river diversion oxbow wetland. *Ecological Engineering* 30: 93–102.

Fischer, H. B., E. J. List, R. C. Y. Koh, J. Imberger, and N. H. Brooks. 1979. *Mixing in Inland and Coastal Waters*. San Diego: Academic Press, 483 pp.

Flite, III, O. P., J. W. Moak, B. S. Metts, and G. W. Eidson. 2006. Constructed wetlands tracer study, Final Report. Project No. 90155, Augusta-Richmond County, Southeastern Natural Sciences Academy, Augusta, Georgia, 51 pp.

Flokstra, C. 1977. The closure problem for depth-averaged two-dimensional flow. Report. No. 190, Delft Hydraulics Laboratory, Delft, The Netherlands, 12 pp.

Fox, A. M. and W. T. Haller. 2000. Production and survivorship of the functional stolons of giant cutgrass, *Zizaniopsis miliacea* (poaceae). *American Journal of Botany* 87: 811–818.

Fox, P., H. J. S. Fernando, R. V. Rodriguez, T. Serra, and M. Arzabe. 2002. Evaluation of flow fields in wetlands using physical models. Program Report No. 49, Bureau of Reclamation, U.S. Department of the Interior, Agreement Number 98-FC-81-0051, Desalination Research and Development, 45 pp.

Frossard, W., D. Andrews, L. E. Mokry, A. H. Plummer, Jr, and J. L. Mancini. 1996. Use of constructed wetlands for protection of water quality in water supply reservoirs. Tech. Report. 807, American Water Works Association Research Foundation, Denver, Colorado, 152 pp.

Gaskin, S. and T. R. Wood. 2001. The axisymmetric and the plane jet in a coflow. *Journal of Hydraulic Research* 39(5): 451–458.

Gaskin, S. J., M. McKernan, and F. Xue. 2004. The effect of background turbulence on jet entrainment: an experimental study of a plane jet in a shallow coflow. *Journal of Hydraulic Research* 42(5): 531–540.

Gearheart, R. A., F. Klopp, and G. Allen. 1989. Constructed free surface wetlands to treat and receive wastewater: pilot project to full scale. In: D. A. Hammer (ed.), *Constructed Wetlands for Wastewater Treatment*, Chelsea, Michigan: Lewis Publishers, pp. 121–138.

George, D. G. 1981. Wind-induced water movements in the South Basin of Windermere. *Freshwater Biology* 11: 37–60.

Gerke, S., L. A. Baker, and Y. Xu. 2001. Nitrogen transformations in a wetland receiving lagoon effluent: Sequential model and implications for water reuse. *Water Research* 35(16): 3857–3866.

Giger, M., T. Dracos, and G. H. Jirka. 1991. Entrainment and mixing in plane turbulent jets in shallow water. *Journal of Hydraulic Research* 29(5): 615–641.

Giovannini, S. G. T. and D. M. L. da Motta Marques. 1999. Establishment of three emergent macrophytes under different water regimes. *Water Science and Technology* 40(3): 233–240.

Goulet, R. R., F. R. Pick, and R. L. Droste. 2001. Test of the first-order removal model for metal retention in a young constructed wetland. *Ecological Engineering* 17: 357–371.

Granger, R. A. 1985. *Fluid Mechanics*. New York: Holt, Rinehart and Winston, 884 pp.

Guardo, M. and R. S. Tomasello. 1995. Hydrodynamic simulations of a constructed wetland in South Florida. *Water Resources Bulletin* 31(4): 687–701.

Hammer, D. A. and D. L. Burckhard. 2000. Designs for nitrogen removal—Minot's constructed wetland—10 years later. In: K. R. Reddy and R. H. Kadlec (eds.), *Proceedings of the Seventh International Conference on Wetland Systems for Water Pollution Control*, Lake Buena Vista, Florida: International Water Association, vol. 1, pp. 247–252.

Hammer, D. A. and R. L. Knight. 1994. Designing constructed wetlands for nitrogen removal. *Water Science and Technology* 29(4): 15–27.

Hammer, D. A., B. P. Pullin, R. A. McCaskey, J. Eason, and V. W. E. Payne. 1993. Treating livestock wastewaters with constructed wetlands. In: G. A. Moshiri (ed.), *Constructed Wetlands for water quality improvement*, Boca Raton, Florida: Lewis Publishers, pp. 343–347.

Hammer, D. E. and R. H. Kadlec. 1986. A model for wetland surface water dynamics. *Water Resources Research* 22(13): 1951–1958.

Hart, D. R., P. J. Mulholland, E. R. Marzolf, D. L. DeAngelis, and S. P. Hendricks. 1999. Relationships between hydraulic parameters in a small stream under varying flow and seasonal conditions. *Hydrological Processes* 13: 1497–1510.

Harvey, J. W., J. E. Saiers, and J. T. Newlin. 2005. Solute transport and storage mechanisms in wetlands of the Everglades, south Florida. *Water Resources Research* 41: W05009. doi:10.1029/2004WR003507.

Hauenstein, W. and T. H. Dracos. 1984. Investigation of plunging density currents generated by inflows in lakes. *Journal of Hydraulic Research* 22(3): 157–179.

Henderson, F. M. 1966. *Open Channel Flow.* New York: The Macmillan Company, 522 pp.

Hey, D. L., J. A. Kostel, A. P. Hurter, and R. H. Kadlec. 2005. Nutrient farming and traditional removal: an economic comparison. 03-WSM-6CO, Water Environment Research Foundation, Alexandria, Virginia, 58 pp.

Hinze, J. O. 1975. *Turbulence.* New York: McGraw-Hill Book Company, Inc., 2nd ed., 790 pp.

Hodges, C., P. Dipas, and T. Younos. 1997. Resistance to flow through riparian wetlands. In: S. S. Y. Wang and T. Carstens (eds.), *Environmental and Coastal Hydraulics: Protecting the Aquatic Habitat, Proceedings of Theme B: Water for a Changing Global Community,* The 27th Congress of the International Association for Hydraulic Research, San Francisco, California, August 10-15, 1997, New York: American Socity of Civil Engineers, vol. 2, pp. 913–918.

Holland, J. F., J. F. Martin, T. Granata, V. Bouchard, M. Quigley, and L. Brown. 2004. Effects of wetland depth and flow rate on residence time distribution characteristics. *Ecological Engineering* 23: 189–203.

Ishida, C. K., J. J. Kelly, and K. A. Gray. 2006. Effects of variable hydroperiods and water level fluctuations on denitrification capacity, nitrate removal, and benthic-microbial community structure in constructed wetlands. *Ecological Engineering* 28: 363–373.

Isichenko, M. B. 1992. Percolation, statistical topography, and transport in random media. *Reviews of Modern Physics* 64(4): 961–1043.

Jadhav, R. S. and S. G. Buchberger. 1995. Effects of vegetation on flow through free water surface wetlands. *Ecological Engineering* 5: 481–496.

James, W. F. and J. W. Barko. 1991. Estimation of phosphorus exchange between littoral and pelagic zones during nighttime convective circulation. *Limnology and Oceanography* 36(1): 179–187.

Järvelä, J. 2002. Flow resistance of flexible and stiff vegetation: a flume study with natural plants. *Journal of Hydrology* 269: 44–54.

Jenkins, G. A. and M. Greenway. 2005. The hydraulic efficiency of fringing versus banded vegetation in constructed wetlands. *Ecological Engineering* 25: 61–72.

Jin, C.-X. and M. J. M. Römkens. 2001. Experimental studies of factors in determining sediment trapping in vegetative filter strips. *Transactions of the American Society of Agricultural Engineers* 44(2): 277–288.

Jirka, G. H. 1994. Shallow jets. In: P. A. Davies and M. J. Valente Neves (eds.), *Recent Research Advances in the Fluid Mechanics of Turbulent Jets and Plumes*. The Netherlands: Kluwer Academic Publishers, pp. 155–175.

Jirka, G. H. 2004. Integral model for turbulent buoyant jets in unbounded stratified flows, Part I: Single round jet. *Environmental Fluid Mechanics* 4: 1–56.

Jirka, G. H. 2006. Integral model for turbulent buoyant jets in unbounded stratified flows, part ii: Plane jet dynamics resulting from multiport diffuser jets. *Environmental Fluid Mechanics* 6: 43–100.

John, C. V., S. J. Miller, and F. W. Morris. 2001. Numerical simulation of the effect of canal plugs on the modification of Saint Johns Marsh Conservation Area hydraulics in the Upper St. Johns River Basin, Florida. In: D. F. Hayes (ed.), *Proceedings of the 2001 Wetlands Engineering & River Restoration Conference, Reno, NV, August 27-31*. American Society of Civil Engineers, CD-ROM.

Johnson, T. R. and H. G. Stefan. 1988. Experimental study of density induced plunging flow into reservoirs and coastal regions. Project Report No. 245, St. Anthony Falls Hydraulic Laboratory, University of Minnesota, Minneapolis, Minnesota, 162 pp.

Jordanova, A. A. and C. S. James. 2003. Experimental study of bed load transport through emergent vegetation. *Journal of Hydraulic Engineering* 129(6): 474–478.

Jordanova, A. A., C. S. James, and A. L. Birkhead. 2006. Practical estimation of flow resistance through emergent vegetation. *Water Management* 159(WM3): 173–181.

Kadlec, R. H. 1979. Wetlands for tertiary treatment. In: P. E. Greeson, J. R. Clark, and J. E. Clark (eds.), *Wetland Functions and Values: The State of Our Understanding*. Minneapolis, Minnesota: American Water Resources Association, pp. 490–504.

Kadlec, R. H. 1987. Northern natural wetland water treatment systems. In: K. R. Reddy and W. H. Smith (eds.), *Aquatic Plants for Water Treatment and Resource Recovery*, Magnolia Publishing, Inc., pp. 83–98.

Kadlec, R. H. 1994. Detention and mixing in free water wetlands. *Ecological Engineering* 3: 345–380.

Kadlec, R. H. 1997. Deterministic and stochastic aspects of constructed wetland performance and design. *Water Science and Technology* 35(5): 149–156.

Kadlec, R. H. 2000. The inadequacy of first-order treatment wetland models. *Ecological Engineering* 15: 105–119.

Kadlec, R. H. 2003*a*. Integrated natural systems for landfill leachate treatment. In: J. Vymazal (ed.), *Wetlands-nutriends, metals, and mass cycling*, Leiden, The Netherlands: Backhuws Publisers, pp. 1–34.

Kadlec, R. H. 2003*b*. Pond and wetland treatment. *Water Science and Technology* 48(5): 1–8.

Kadlec, R. H. 2005*a*. The effects of deep zones on wetland nitrogen processing. , Wetland Management Services, Chelsea, MI, 35 pp.

Kadlec, R. H. 2005*b*. Wetland to pond treatment gradients. *Water Science and Technology* 51(9): 291–298.

Kadlec, R. H. 2006. Water temperature and evapotranspiration in surface flow wetlands in hot arid climate. *Ecological Engineering* 26: 328–340.

Kadlec, R. H., W. Bastiaens, and D. T. Urban. 1993. Hydrological design of free water surface treatment wetlands. In: G. A. Moshiri (ed.), *Constructed Wetlands for water quality improvement*, Boca Raton, Florida: Lewis Publishers, pp. 77–86.

Kadlec, R. H., P. S. Burgoon, and M. E. Henderson. 1997. Integrated natural systems for treating potato processing wastewater. *Water Science and Technology* 35(5): 263–270.

Kadlec, R. H. and R. L. Knight. 1996. *Treatment Wetlands*. Boca Raton, Florida: CRC Press LLC, 893 pp.

Kadlec, R. H., R. L. Knight, J. Vymazal, H. Brix, P. Cooper, and R. Haberl. 2000. Constructed wetlands for pollution control. , International Water Association Specialist Group on Use of Macrophytes in Water Pollution Control, London, 156 pp.

Kadlec, R. H., J. Pries, and H. Mustard. 2007. Muskrats (*Ondatra zibethicus*) in treatment wetlands. *Ecological Engineering* 29: 143–153.

Kassem, A., J. Imran, and J. A. Khan. 2003. Three-dimensional modeling of negatively buoyant flow in diverging channels. *Journal of Hydraulic Engineering* 129(12): 936–947.

Keefe, S. H., L. B. Barber, R. L. Runkel, J. N. Ryan, D. M. McKnight, and R. D. Wass. 2004. Conservative and reactive solute transport in constructed wetlands. *Water Resources Research* 40: W01201. doi:10.1029/2003WR002130.

Keller, C. H. and J. S. Bays. 2002. Tracer studies for treatment wetlands. In: J. Pries (ed.), *Treatment Wetlands for Water Quality Improvement: Quebec 2000 Conference Proceedings*. Waterloo, Ontario: CH2M HILL Canada Limited, Pandora Press, pp. 173–181.

Kjellin, J., A. Wörman, H. Johansson, and A. Lindahl. 2007. Controlling factors for water residence time and flow patterns in ekeby treatment wetland, sweden. *Advances in Water Resources* 30: 838–850.

Knight, R. L. 1987. Effluent distribution and basin design for enhanced pollutant assimilation by freshwater wetlands. In: K. R. Reddy and W. H. Smith (eds.), *Aquatic Plants for Water Treatment and Resource Recovery*, Magnolia Publishing, Inc., pp. 913–921.

Knight, R. L., R. A. Clarke, Jr., and R. K. Bastian. 2000*a*. Treatment wetlands as habitat for wildlife and humans. In: K. R. Reddy and R. H. Kadlec (eds.), *Proceedings of the Seventh International Conference on Wetland Systems for Water Pollution Control*, Lake Buena Vista, Florida: International Water Association, vol. 2, pp. 37–52.

Knight, R. L., J. Hilleke, and S. Grayson. 1994. Design and performance of the champion pilot-constructed wetland treatment system. *Tappi Journal* 77(5): 240–245.

Knight, R. L. and M. E. Iverson. 1990. Design of the Fort Deposit, Alabama, constructed wetlands treatment system. In: P. F. Cooper and B. C. Findlater (eds.), *Constructed wetlands in water pollution control*, New York, NY: Pergamon Press, pp. 521–524.

Knight, R. L., W. E. Walton, G. O'Meara, W. K. Reisen, and R. Wass. 2000*b*. Design strategies for effective mosquito control in constructed treatment wetlands. In: K. R. Reddy and R. H. Kadlec (eds.), *Proceedings of the Seventh International Conference on Wetland Systems for Water Pollution Control*, Lake Buena Vista, Florida: International Water Association, vol. 2, pp. 425–440.

Koch, D. L. and A. J. C. Ladd. 1997. Moderate Reynolds number flows through periodic and random arrays of aligned cylinders. *Journal of Fluid Mechanics* 349: 31–66.

Korkusuz, E. A. and C. Yurteri. 2000. Feasibility of constructed wetlands designed for the Mogan-Eymir basin. In: K. R. Reddy and R. H. Kadlec (eds.), *Proceedings of the Seventh International Conference on Wetland Systems for Water Pollution Control*, Lake Buena Vista, Florida: International Water Association, vol. 2, pp. 859–867.

Koskiaho, J. 2003. Flow velocity retardation and sediment retention in two constructed wetland-ponds. *Ecological Engineering* 19: 325–337.

Kruka, V. and S. Eskinazi. 1964. The wall-jet in a moving stream. *Journal of Fluid Mechanics* 20(4): 555–579.

Kundu, P. K. and I. M. Cohen. 2002. *Fluid Mechanics*. San Diego: Academic Press, 2nd ed., 730 pp.

Lawrence, D. S. L., J. R. L. Allen, and G. M. Havelock. 2004. Salt marsh morphodynamics: an investigation of tidal fflows and marsh channel equilibrium. *Journal of Coastal Research* 20(1): 301–316.

Lawrence, G. A., K. I. Ashley, N. Yonemitsu, and J. R. Ellis. 1995. Natural dispersion in a small lake. *Limnology and Oceanography* 40(8): 1519–1526.

Lee, J. H. and G. H. Jirka. 1980. Multiport diffuser as line source of momentum in shallow water. *Water Resources Research* 16(4): 695–708.

Lee, J. H., G. H. Jirka, and D. R. F. Harleman. 1977. Modelling of unidirectional thermal diffusers in shallow water. Ralph M. Parsons Laboratory for Water Resources and Hydrodynamics Report. 228, Massachusetts Institute of Technology, Cambridge, Massachusetts, 304 pp.

Lee, J. H. W. and V. H. Chu. 2003. *Turbulent jets and plumes: a Lagrangian approach.* Boston: Kluwer Academic Publishers, 390 pp.

Lee, J. K., L. C. Roig, H. L. Jenter, and H. M. Visser. 2004. Drag coefficients for modeling flow through emergent vegetation in the Florida Everglades. *Ecological Engineering* 22: 237–248.

Leonard, L. A. and M. E. Luther. 1995. Flow hydrodynamics in tidal marsh canopies. *Limnology and Oceanography* 40(8): 1474–1484.

Li, X., D. Xiao, R. H. Jongman, W. B. Harms, and A. K. Bregt. 2003. Spatial modeling on the nutrient retention of an estuary wetland. *Ecological Modelling* 167(1-2): 33–46.

Lightbody, A. F., M. E. Avener, and H. M. Nepf. Submitted. Observations of short-circuiting flow paths within a free-surface wetland in Augusta, Georgia, USA. Submitted to *Limnology and Oceanography* .

Lightbody, A. F. and H. M. Nepf. 2006*a*. Prediction of near-field shear dispersion in an emergent canopy with heterogeneous morphology. *Environmental Fluid Mechanics* 6(5): 477–488. doi:10.1007/s10652-006-9002-7.

Lightbody, A. F. and H. M. Nepf. 2006*b*. Prediction of velocity profiles and longitudinal dispersion in emergent salt marsh vegetation. *Limnology and Oceanography* 51: 218–228.

Lightbody, A. F., H. M. Nepf, and J. S. Bays. 2007. Mixing in deep zones within constructed treatment wetlands. *Ecological Engineering* 29: 209–220.

Lin, A. Y.-C., J.-F. Debroux, J. A. Cunningham, and M. Reinhard. 2003. Comparison of rhodamine WT and bromide in the determination of hydraulic characteristics of constructed wetlands. *Ecological Engineering* 20(1): 75–88. doi:10.1016/S0925-8574(03)00005-3.

Linde, L. W. and R. Alsbro. 2000. Ekeby wetland—the largest construced SF wetland in Sweden. In: K. R. Reddy and R. H. Kadlec (eds.), *Proceedings of the Seventh International Conference on Wetland Systems for Water Pollution Control*, Lake Buena Vista, Florida: International Water Association, vol. 2, pp. 1101–1109.

List, E. J. 1982. Turbulent jets and plumes. *Annual Review of Fluid Mechanics* 14: 189–212.

List, E. J. and R. Dugan. 1994. Transition from jet plume dilution to ambient turbulent mixing. In: P. A. Davies and M. J. Valente Neves (eds.), *Recent Research Advances in the Fluid Mechanics of Turbulent Jets and Plumes*, Netherlands: Kluwer Academic Publishers, pp. 1–11.

Loheide II, S. P. and S. M. Gorelick. 2006. Quantifying stream-aquifer interactions through the analysis of remotely sensed thermographic profiles and in situ temperature histories. *Environmental Science and Technology* 40(10): 3336–3341.

López, F. and M. H. García. 2001. Mean flow and turbulence structure of open-channel flow through non-emergent vegetation. *Journal of Hydraulic Engineering* 127(5): 392–402.

Lund, M. A., P. S. Lavery, and R. F. Froend. 2001. Removing filterable reactive P from highly coloured stormwater using constructed wetlands. *Water Science and Technology* 44(11-12): 85–92.

Luo, J., O. A. Cirpka, M. N. Fienen, W. Wu, T. L. Mehlhorn, J. Carley, P. M. Jardine, C. S. Criddle, and P. K. Kitanidis. 2006. A parametric transfer function methodology for analyzing reactive transport in nonuniform flow. *Journal of Contaminant Hydrology* 83: 27–41.

Maine, M. A., N. S. ne, H. Hadad, G. Sánchez, and C. Bonetto. 2006. Nutrient and metal removal in a constructed wetland for wastewater treatment from a metallurgic industry. *Ecological Engineering* 26: 341–347.

Marani, M., S. Silvestri, E. Belluco, N. Ursino, A. Comerlati, O. Tosatto, and M. Putti. 2006. Spatial organization and ecohydrological interactions in oxygen-limited vegetation ecosystems. *Water Resources Research* 42: W06D06. doi: 10.1029/2005WR004582.

Martinez, C. J. and W. R. Wise. 2003*a*. Analysis of constructed treatment wetland hydraulics with the transient storage model OTIS. *Ecological Engineering* 20: 211–222.

Martinez, C. J. and W. R. Wise. 2003*b*. Hydraulic analysis of Orlando Easterly Wetland. *Journal of Environmental Engineering* 129(6): 553–560.

Matthews, R. R., W. E. Watt, J. Marsalek, A. A. Crowder, and B. C. Anderson. 1997. Extending retention times in a stormwater pond with retrofitted baffles. *Water Quality Research Journal of Canada* 32(1): 73–87.

Mazda, Y., N. Kanazawa, and T. Kurokawa. 1999. Dependence of dispersion on vegetation density in a tidal creek-mangrove swamp system. *Mangroves and Salt Marshes* 3: 59–66.

McCormick, P. V., R. B. E. Shuford III, and M. J. Chimney. 2006. Periphyton as a potential phosphorus sink in the Everglades Nutrient Removal Project. *Ecological Engineering* 27: 279–289.

Mitsch, W. J. and J. G. Gosselink. 2000. *Wetlands*. New York: John Wiley & Sons, Inc., 3rd ed., 920 pp.

Mitsch, W. J. and S. E. Jorgensen. 2004. *Ecological Engineering and Ecosystem Restoration*. Hoboken, NY: John Wiley & Sons, Inc., 411 pp.

Moreno, L., J. Crawford, and I. Neretnieks. 2006. Modelling radionuclide transport for time varying flow in a channel network. *Journal of Contaminant Hydrology* 86: 215–238.

Morton, B. R., G. Taylor, and J. S. Turner. 1956. Turbulent gravitational convection from maintained and instantaneous sources. *Proceedings of the Royal Society of London, Series A* 234: 1–23.

Mott, R. L. 2000. *Applied Fluid Mechanics*. Upper Saddle River, New Jersey: Prentice Hall, 5th ed., 597 pp.

Negretti, M. E., S. A. Socolofsky, A. C. Rummel, and G. H. Jirka. 2005. Stabilization of cylinder wakes in shallow water flows by means of roughness elements: an experimental study. *Experiments in Fluids* 38(4): 403–414.

Nepf, H., M. Ghisalberti, B. White, and E. Murphy. 2007. Retention time and dispersion associated with submerged aquatic canopies. *Water Resources Research* 43: W04422. doi:10.1029/2006WR005362.

Nepf, H. M. 1999. Drag, turbulence, and diffusion in flow through emergent vegetation. *Water Resources Research* 35(2): 479–489.

Nepf, H. M., J. A. Sullivan, and R. A. Zavistoski. 1997. A model for diffusion within emergent vegetation. *Limnology and Oceanography* 42(8): 1735–1745.

Nungesser, M. K. and M. J. Chimney. 2006. A hydrologic assessment of the everglades nutrient removal project, a subtropical constructed wetland in South Florida (USA). *Ecological Engineering* 27: 331–344.

O'Brien, W. J. 1976. Algae removal by rock filtration. In: E. F. Gloyna, J. F. Malina, Jr., and E. M. Davis (eds.), *Ponds as a wastewater alternative*, Austin, Texas: Center for Research in Water Resources, University of Texas, pp. 351–366.

Okabe, T., T. Yuuki, and M. Kojima. 1997. Bed-load rate on movable beds covered by vegetation. In: S. S. Y. Wang and T. Carstens (eds.), *Environmental and Coastal Hydraulics: Protecting the Aquatic Habitat, Proceedings of Theme B: Water for a Changing Global Community,* The 27th Congress of the International Association for Hydraulic Research, San Francisco, California, August 10-15, 1997. New York: American Socity of Civil Engineers, vol. 2, pp. 1396–1401.

Oldham, C. E. and J. J. Sturman. 2001. The effect of emergent vegetation on convective flushing in shallow wetlans: Scaling and experiments. *Limnology and Oceanography* 46(6): 1486–1493.

Parr, T. W. 1990. Factors affecting reed (*Phragmites australis*) growth in u.k. reed bed treatment systems. In: P. F. Cooper and B. C. Findlater (eds.), *Constructed Wetlands in Water Pollution Control*, New York: Pergamon Press, Inc., pp. 67–76.

Pasche, E. and G. Rouvé. 1985. Overbank flow with vegetatively roughened flood plains. *Journal of Hydraulic Engineering* 111(9): 1262–1278.

Patel, R. P. 1971. Turbulent jets and wall jets in uniform streaming flow. *The Aeronautical Quarterly* 22: 311–326.

Persson, J. 2005. The use of design elements in wetlands. *Nordic Hydrology* 36(2): 113–120.

Persson, J., N. L. G. Somes, and T. H. F. Wong. 1998. Hydraulic efficiency of constructed wetlands and ponds. In: *Proceedings of the Sixth International Conference on Wetland Systems for Water Pollution Control*, Aguas de Sao Pedro, Brazil: International Water Association, pp. 317–328.

Persson, J., N. L. G. Somes, and T. H. F. Wong. 1999. Hydraulics efficiency of constructed wetlands and ponds. *Water Science and Technology* 40(3): 291–300.

Persson, J. and H. B. Wittgren. 2003. How hydrological and hydraulic conditions affect performance of ponds. *Ecological Engineering* 21: 259–269.

Perucca, E., C. Camporeale, and L. Ridolfi. 2007. Significance of the riparian vegetation dynamics on meandering river morphodynamics. *Water Resources Research* 43: W03430. doi:10.1029/2006WR005234.

Peterson, C. H., R. A. Luettich, Jr, F. Micheli, and G. A. Skilleter. 2004. Attenuation of water flow inside seagrass canopies of differing structure. *Marine Ecology Progress Series* 268: 81–92.

Pietro, K. C., M. J. Chimney, and A. D. Steinman. 2006. Phosphorus removal by the *Ceratophyllum*/periphyton complex in a south Florida (USA) freshwater marsh. *Ecological Engineering* 27: 290–300.

Pilkey, O. H. and L. Pilkey-Jarvis. 2007. *Useless Arithmetic: Why Environmental Scientists Can't Predict the Future*. New York: Columbia University Press, 230 pp.

Pinney, M. L., P. K. Westerhoff, and L. Baker. 2000. Transformations in dissolved organic carbon through constructed wetlands. *Water Research* 34(6): 1897–1911.

Raisin, G. W. and D. S. Mitchell. 1995. The use of wetlands for the control of non-point source pollution. *Water Science and Technology* 32(3): 177–186.

Raisin, G. W., D. S. Mitchell, and R. L. Croome. 1997. The effectiveness of a small constructed wetland in ameliorating diffuse nutrient loadings from an australian rural catchment. *Ecological Engineering* 9: 19–35.

Rajaratnam, N. 1976. *Turbulent Jets*. New York, New York: Elsevier Scientific Publishing Company, 304 pp.

Rajaratnam, N. 1984. Non-buoyant and buoyant circular surface jets in coflowing streams. *Journal of Hydraulic Research* 22(2): 117–140.

Rash, J. K. and S. K. Liehr. 1999. Flow pattern analysis of constructed wetlands treating landfill leachate. *Water Science and Technology* 40(3): 309–315.

Reddy, G. B., P. G. Hunt, R. Phillips, K. Stone, and A. Grubbs. 2001. Treatment of swine wastewater in marsh-pond-marsh constructed wetlands. *Water Science and Technology* 44(11-12): 545–550.

Reed, S. C., R. W. Crites, and E. J. Middlebrooks. 1995. *Natural systems for waste management and treatment*. New York: McGraw-Hill, Inc., 2nd ed., 433 pp.

Reilly, J. F., A. J. Horne, and C. D. Miller. 2000. Nitrate removal from a drinking water supply with lare free-surface constructed wetlands prior to groundwater recharge. *Ecological Engineering* 14: 33–47.

Reitberger, J. H., L. E. Mokry, and R. L. Knight. 2000. Achieving multiple benefis from a constructed wetland. In: K. R. Reddy and R. H. Kadlec (eds.), *Proceedings of the Seventh International Conference on Wetland Systems for Water Pollution Control*, Lake Buena Vista, Florida: International Water Association, vol. 2, pp. 749–758.

Romero, J. A., F. A. Comín, and C. García. 2000. Experimental evidence on the spatial heterogeneity of nutrient removal in wetlands used for agricultural wastewater treatment. In: K. R. Reddy and R. H. Kadlec (eds.), *Proceedings of the Seventh International Conference on Wetland Systems for Water Pollution Control*, Lake Buena Vista, Florida: International Water Association, vol. 2, pp. 1445–1452.

Rubin, Y. 1995. Flow and transport in bimodal heterogeneous formations. *Water Resources Research* 31(10): 2461–2468.

Runkel, R. L. 1998. One dimensional transport with inflow and storage (OTIS): A solute transport model for streams and rivers. Water-Resources Investigation Report 98-4018, U.S. Geological Survey, Denver, Colorado, 73 pp.

Sand-Jensen, K. 2003. Drag and reconfiguration of freshwater macrophytes. *Freshwater Biology* 48: 271–283.

Sartoris, J. J., J. S. Thullen, and L. B. Barber. 2000*a*. Effect of hemi-marsh reconfiguration on nitrogen transformations in a sourthern California treatment wetland. In: K. R. Reddy and R. H. Kadlec (eds.), *Proceedings of the Seventh International*

Conference on Wetland Systems for Water Pollution Control, Lake Buena Vista, Florida: International Water Association, vol. 2, pp. 359–364.

Sartoris, J. J., J. S. Thullen, L. B. Barber, and D. E. Salas. 2000*b*. Investigation of nitrogen transformations in a southern california constructed wastewater treatment wetland. *Ecological Engineering* 14: 49–65.

Schaffranek, R. W. and H. L. Jenter. 2001. Observations of daily temperature patterns in the southern Florida Everglades. In: D. F. Hayes (ed.), *Proceedings of the 2001 Wetlands Engineering & River Restoration Conference, Reno, NV, August 27-31.* American Society of Civil Engineers, CD-ROM.

Schueler, T. R. 1992. Design of stormwater wetland systems: guidelines for creating diverse and effective stormwater wetlands in the mid-Atlantic Region. Anacostia Restoration Team, Department of Environmental Programs, Metropolitan Council of Governments, Washington, D.C., 133 pp.

Schueler, T. R. 2000. The pond premium. In: T. R. Schueler and H. K. Holland (eds.), *The Practice of Watershed Protection*, Ellicott City, MD: Center for Watershed Protection, pp. 461–462.

Schutten, J., J. Dainty, and A. J. Davy. 2004. Wave-induced hydraulic forces on submerged aquatic plants in shallow lakes. *Annals of Botany* 93: 333–341.

Schwarz, W. H. and W. P. Cosart. 1961. The two-dimensional turbulent wall-jet. *Journal of Fluid Mechanics* 10: 481–495.

Selker, J. S., L. Thévenaz, H. Huwald, A. Mallet, W. Luxemburg, N. van de Giesen, M. Stejskal, J. Zeman, M. Westhoff, and M. B. Parlange. 2006. Distributed fiber-optic temperature sensing for hydrologic systems. *Water Resources Research* 42: W12202. doi:10.1029/2006WR005326.

Sharp, J. J. 1981. *Hydraulic Modelling*. London: Butterworths, 242 pp.

Shi, Z., J. S. Pethick, F. Burd, and B. Murphy. 1996. Velocity profiles in a salt marsh canopy. *Geo-Marine Letters* 16: 319–323.

Simi, A. 2000. Water quality assessment of a surface flow constructed wetland treating oil refinery wastewater. In: K. R. Reddy and R. H. Kadlec (eds.), *Proceedings of the Seventh International Conference on Wetland Systems for Water Pollution Control*, Lake Buena Vista, Florida: International Water Association, vol. 2, pp. 1295–1304.

Simi, A. L. and C. A. Mitchell. 1999. Design and hydraulic performance of a constructed wetland treating oil refinery wastewater. *Water Science and Technology* 40(3): 301–307.

Sirivedhin, T. and K. A. Gray. 2006. Factors affecting denitrification rates in experimental wetlands: Field and laboratory studies. *Ecological Engineering* 26(2): 167–181.

Smith, E., R. Gordon, A. Madani, and G. Stratton. 2005. Cold climate hydrological flow characteristics of constructed wetlands. *Canadian Biosystems Engineering* 47: 1.1–1.7.

Smith, E., R. Gordon, A. Madani, and G. Stratton. 2006. Year-round treatment of dairy wastewater by constructed wetlands in Atlantic Canada. *Wetlands* 26(2): 349–357.

Somes, N. L. G., W. A. Bishop, and T. H. F. Wong. 1999. Numerical simulation of wetland hydrodynamics. *Environmental International* 25(6/7): 773–779.

Somes, N. L. G., J. Person, and T. J. F. Wong. 1998. Influence of wetland design parameters on the hydrodynamics of stormwater wetlands. In: D. J. Walker and T. M. Daniell (eds.), *Hydrastorm '98. Proceedings of the 3rd International Symposium on Stormwater Management and 6th International Conference on Hydraulics in Civil Engineering*, Adelaide, Australia: The Institution of Engineers, pp. 123–128.

Spieles, D. J. and W. J. Mitsch. 2000. The effects of season and hydrologic and chemical loading on nitrate retention in constructed wetlands: a comparison of low- and high-nutrient riverine systems. *Ecological Engineering* 14(1-2): 77–91.

Stern, D. A., R. Khanbilvardi, J. C. Alair, and W. Richardson. 2001. Description of flow through a natural wetland using dye tracer tests. *Ecological Engineering* 18: 173–184.

Stolzenbach, K. D. and D. R. F. Harleman. 1971. An analytical and experimental investigation of surface discharges of heated water. Ralph M. Parsons Laboratory for Water Resources and Hydrodynamics Report 135, Ralph M. Parsons Laboratory, Massachusetts Institute of Technology, Cambridge, Massachusetts, 212 pp.

Stone, B. M. and H. T. Shen. 2002. Hydraulic resistance of flow in channels with cylindrical roughness. *Journal of Hydraulic Engineering* 128(5): 500–506.

Stone, K. C., M. E. Poach, P. G. Hunt, and G. B. Reddy. 2004. Marsh-pond-marsh constructe wetland design analysis for swine lagoon wastewater treatment. *Ecological Engineering* 23: 127–133.

Struve, J., R. A. Falconer, and Y. Wu. 2003. Influence of model mangrove trees on the hydrodynamics in a flume. *Estuarine Coastal and Shelf Science* 58: 163–171.

Su, X. and C. W. Li. 2002. Large eddy simulation of free surface turbulent flow in partly vegetated open channels. *International Journal for Numerical Methods in Fluids* 39: 919–937. doi:10.1002/fld.352.

Sundaravadivel, M. and S. Vigneswaran. 2001. Constructed wetlands for wastewater treatment. *Critical Reviews in Environmental Science and Technology* 31(4): 351–409.

Swain, E. D., M. A. Wolfert, J. D. Bales, and C. R. Goodwin. 2004. Two-dimensional hydrodynamic simulation of surface-water flow and transport to Florida Bay through the southern inland and coastal systems (SICS). Water-Resources Investigations Report 03-4287, U. S. Geological Survey, 55 pp.

Tanino, Y., H. M. Nepf, and P. S. Kulis. 2005. Gravity currents in aquatic canopies. *Water Resources Research* 41: W12402. doi:10.1029/2005WR004216.

Tanner, C. C. 1996. Plants for constructed wetland treatment systems—a comparison of the growth and nutrient uptake of eight emergent species. *Ecological Engineering* 7: 59–83.

Tanner, C. C., J. S. Clayton, and M. P. Upsdell. 1995. Effect of loading rate and planting on treatment of dairy farm wastewaters in constructed wetlands – II. Removal of nitrogen and phosphorus. *Water Research* 29(1): 27–34.

Tarutis, Jr., W. J., L. R. Stark, and F. M. Williams. 1999. Sizing and performance estimation of coal mine drainage wetlands. *Ecological Engineering* 12: 353–372.

Thackston, E. L., F. D. Shields, Jr, and P. R. Schroeder. 1987. Residence time distributions of shallow basins. *Journal of Environmental Engineering* 113(6): 1319–1332.

Thompson, J. R., J. R. Sørenson, H. Gavin, and A. Refsgaard. 2004. Application of the coupled MIKE SHE/MIKE 11 modelling system to a lowland wet grassland in southest England. *Journal of Hydrology* 293: 151–179.

Thullen, J. S., J. J. Sartoris, and S. M. Nelson. 2005. Managing veetation in surface-flow wastewater-treatment wetlands for optimal treatment performance. *Ecological Engineering* 25: 583–593.

Thullen, J. S., J. J. Sartoris, and W. E. Walton. 2002. Effects of vegetation management in constructed wetland treatment cells on water quality and mosquito production. *Ecological Engineering* 18: 441–457.

Thurman, H. V. 1997. *Introduction to Oceanography.* Upper Saddle River, New Jersey: Prentice Hall, 8th ed., 544 pp.

Tilley, D. R. and M. T. Brown. 1998. Wetland networks for stormwater management in subtropical urban watersheds. *Ecological Engineering* 10: 131–158.

Tomenko, V., S. Ahmed, and V. Popov. 2007. Modelling constructed wetland treatment system performance. *Ecological Modelling* 205: 355–364.

Tsihrintzis, V. A. and E. E. Madiedo. 2000. Hydraulic resistance determination in marsh wetlands. *Water Resources Management* 14: 285–309.

U. S. Department of Agriculture. 2006. Agricultural statistics 2006. ISBN 0-16-036158-3, National Agricultural Statistics Service, Washington, DC, 532 pp.

U. S. Environmental Protection Agency. 2000. Constructed wetlands treatment of municipal wastewaters. 625-R-99-010, Office of Research and Development, Cincinatti, Ohio, 165 pp.

Ultsch, G. 1973. The effect of water hyacinth (*Eichhornia crassipes*) on the microenvironment of aquatic communities. *Archiv. Hydrobiologia* 72: 460–473.

Walker, D. J. 1998. Modelling residence time in stormwater ponds. *Ecological Engineering* 10: 247–262.

Walker, Jr., W. W. 1995. Design basis for Everglades Stormwater Treatment Areas. *Water Resources Bulletin* 31(4): 671–685.

Walton, W. 2002. Multipurpose constructed treatment wetlands in the arid southwest United States: Are the benefits worth the risks? In: J. Pries (ed.), *Treatment Wetlands for Water Quality Improvement: Quebec 2000 Conference Proceedings.* Waterloo, Ontario: Pandora Press, pp. 115–123.

Wang, H. and J. W. Jawitz. 2006. Hydraulic analysis of cell-network treatment wetlands. *Journal of Hydrology* 330: 721–734.

Wang, H., J. W. Jawitz, J. R. White, C. J. Martinez, and M. D. Sees. 2006. Rejuvenating the largest municipal treatment wetland in Florida. *Ecological Engineering* 26(2): 132–146. doi:10.1016/j.ecoleng.2005.07.016.

Wang, H. J. and M. J. Davidson. 1997. Merging of weakly advected coflowing jets. In: S. S. Y. Wang and T. Carstens (eds.), *Environmental and Coastal Hydraulics: Protecting the Aquatic Habitat, Proceedings of Theme B: Water for a Changing Global Community,* The 27th Congress of the International Association for Hydraulic Research, San Francisco, California, August 10-15, 1997. New York: American Socity of Civil Engineers, vol. 1, pp. 85–125.

Werner, T. M. and R. H. Kadlec. 2000. Wetland residence time distribution modeling. *Ecological Engineering* 15(1-2): 77–90.

Wetzel, R. G. 1975. *Limnology.* Philadelphia: W. B. Saunders, 743 pp.

White, B. L. 2006. *Momentum and mass transport by coherent structures in a shallow vegetated shear flow.* Ph.D. thesis, Massachusetts Institute of Technology, Cambridge, Massachusetts. 231 pp.

White, B. L. and H. M. Nepf. 2003. Scalar transport in random cylinder arrays at moderate Reynolds number. *Journal of Fluid Mechanics* 487: 43–79.

White, F. M. 1991. *Viscous Fluid Flow.* New York: McGraw-Hill, 2nd ed., 614 pp.

Whittle, J. and M. Philcox. 1996. Constructed wetlands for water quality control for the Lower Murray reclaimed swamps. Primary Industries South Australia, Lower Murray Irrigation Action Group, 63 pp.

Wong, T. H. F., P. F. Breen, S. Lloyd, T. Walker, B. Dahnke, and R. Wootton. 2000. Suspended solids removal in stormwater wetlands: quantifying the role of aquatic macrophytes. In: K. R. Reddy and R. H. Kadlec (eds.), *Proceedings of the Seventh International Conference on Wetland Systems for Water Pollution Control*, Lake Buena Vista, Florida: International Water Association, vol. 2, pp. 1545–1552.

Wong, T. H. F., P. F. Breen, and N. L. G. Somes. 1999. Ponds vs wetlands – performance considerations in stormwater quality management. In: *1st South Pacific Conference on Comprehensive Stormwater and Aquatic Ecosystem Management*. Auckland, New Zealand, vol. 2, pp. 223–231.

Wong, T. H. F., T. D. Fletcher, H. P. Duncan, and G. A. Jenkins. 2006. Modelling urban stormwater treatment—A unified approach. *Ecological Engineering* 27: 58–70.

Wörman, A. and V. Kronnäs. 2005. Effect of pond shape and vegetation heterogeneity on flow and treatment performance of constructed wetlands. *Journal of Hydrology* 301: 123–128.

Wright, S. J. 1994. The effect of ambient turbulence on jet mixing. In: P. A. Davies and M. J. Valente Neves (eds.), *Recent Research Advances in the Fluid Mechanics of Turbulent Jets and Plumes*, Netherlands: Kluwer Academic Publishers, pp. 13–27.

Yalin, M. S. 1971. *Theory of hydraulic models*. London: Macmillan, 266 pp.

Zhang, J.-B. and V. H. Chu. 2003. Shallow turbulent flows by video imaging method. *Journal of Engineering Mechanics* 129(10): 1164–1172.

Zijnen, B. G. and B. G. Van der Hegge. 1958. Measurements of the velocity distribution in a turbulent plane jet of aiar. *Appled Scientific Research Section A* 7: 256–276.

Zinn, B. and C. F. Harvey. 2003. When good statistical models of aquifer heterogeneity go bad: a comparison of flow, dispersion, and mass transfer in connected and multivariate Gaussian hydraulic conductivity fields. *Water Resources Research* 39(3): 1051. doi:10.1029/2001WR001146.

Appendix A

Governing equations

A.1 Flow through free-surface wetlands

A Reynolds decomposition can be used to write the governing equations for the longitudinal velocity $u(x, y, z, t)$, lateral velocity $v(x, y, z, t)$, vertical velocity $w(x, y, z, t)$, scalar concentration $c(x, y, z, t)$, and fluid pressure $P(x, y, z, t)$ within a wetland in terms of a temporal average plus a temporally varying component. Here x is used to denote the longitudinal coordinate, y the lateral coordinate, z vertical distance below the surface, and t time. The velocities are those within the fluid volume, e.g., the depth-averaged velocity $\langle \bar{u} \rangle = Q/Bh(1-\phi)$, where Q is the volume flow rate through the wetland, B is the wetland width, h is the water depth, and ϕ is the volume fraction of the vegetation. The time-averaged values, denoted by an overbar, are as follows:

$$\bar{u} = \frac{1}{\hat{T}} \int_0^{\hat{T}} u \mathrm{d}t \tag{A.1}$$

$$\bar{v} = \frac{1}{\hat{T}} \int_0^{\hat{T}} v \mathrm{d}t \tag{A.2}$$

$$\bar{w} = \frac{1}{\hat{T}} \int_0^{\hat{T}} w \mathrm{d}t \tag{A.3}$$

$$\bar{c} = \frac{1}{\hat{T}} \int_0^{\hat{T}} c \mathrm{d}t \tag{A.4}$$

$$\bar{P} = \frac{1}{\hat{T}} \int_0^{\hat{T}} P \mathrm{d}t \tag{A.5}$$

where the averaging time scale $\hat{T}$ is longer than turbulent time scale, but less than the timescale of variations in the mean flow due to outside forcing, such as tidal or storm flows. The velocity at each point in time and space can then be written in terms of the temporal average plus a deviation from it:

$$u(x,y,z,t) = \bar{u}(x,y,z) + u'(x,y,z,t) \tag{A.6}$$

$$v(x,y,z,t) = \bar{v}(x,y,z) + v'(x,y,z,t) \tag{A.7}$$

$$w(x,y,z,t) = \bar{w}(x,y,z) + w'(x,y,z,t) \tag{A.8}$$

$$c(x,y,z,t) = \bar{c}(x,y,z) + c'(x,y,z,t) \tag{A.9}$$

$$P(x,y,z,t) = \bar{P}(x,y,z) + P'(x,y,z,t) \tag{A.10}$$

where a single prime indicates deviation from the time-averaged quantity. The result of this Reynolds-averaging process can be substituted into the governing equations for fluid flow, which are the continuity equation, which represents conservation of fluid mass in an incompressible fluid:

$$\frac{\partial \bar{u}}{\partial x} + \frac{\partial \bar{v}}{\partial y} + \frac{\partial \bar{w}}{\partial z} = 0 \tag{A.11}$$

the equations for the conservation of fluid linear momentum:

$$\begin{aligned} \frac{\partial \bar{u}}{\partial t} + \bar{u}\frac{\partial \bar{u}}{\partial x} + \bar{v}\frac{\partial \bar{u}}{\partial y} + \bar{w}\frac{\partial \bar{u}}{\partial z} &= -\frac{1}{\rho_w}\frac{\partial \bar{P}}{\partial x} + \nu\left(\frac{\partial^2 \bar{u}}{\partial x^2} + \frac{\partial^2 \bar{u}}{\partial y^2} + \frac{\partial^2 \bar{u}}{\partial z^2}\right) \\ &\quad - \left(\frac{\partial \overline{u'^2}}{\partial x} + \frac{\partial \overline{u'v'}}{\partial y} + \frac{\partial \overline{u'w'}}{\partial z}\right) - \frac{1}{\rho_w}F_{d,x} \end{aligned} \tag{A.12}$$

$$\begin{aligned} \frac{\partial \bar{v}}{\partial t} + \bar{u}\frac{\partial \bar{v}}{\partial x} + \bar{v}\frac{\partial \bar{v}}{\partial y} + \bar{w}\frac{\partial \bar{v}}{\partial z} &= -\frac{1}{\rho_w}\frac{\partial \bar{P}}{\partial y} + \nu\left(\frac{\partial^2 \bar{v}}{\partial x^2} + \frac{\partial^2 \bar{v}}{\partial y^2} + \frac{\partial^2 \bar{v}}{\partial z^2}\right) \\ &\quad - \left(\frac{\partial \overline{u'v'}}{\partial x} + \frac{\partial \overline{v'^2}}{\partial y} + \frac{\partial \overline{v'w'}}{\partial z}\right) - \frac{1}{\rho_w}F_{d,y} \end{aligned} \tag{A.13}$$

$$\frac{\partial \bar{w}}{\partial t} + \bar{u}\frac{\partial \bar{w}}{\partial x} + \bar{v}\frac{\partial \bar{w}}{\partial y} + \bar{w}\frac{\partial \bar{w}}{\partial z} = -\frac{1}{\rho_w}\frac{\partial \bar{P}}{\partial z} + \rho_w g + \nu\left(\frac{\partial^2 \bar{w}}{\partial x^2} + \frac{\partial^2 \bar{w}}{\partial y^2} + \frac{\partial^2 \bar{w}}{\partial z^2}\right)$$

$$- \left(\frac{\partial \overline{u'w'}}{\partial x} + \frac{\partial \overline{v'w'}}{\partial y} + \frac{\partial \overline{w'^2}}{\partial z} \right) - \frac{1}{\rho_w} F_{d,z} \quad \text{(A.14)}$$

and the transport equation, which represents the conservation of tracer mass:

$$\frac{\partial \bar{c}}{\partial t} + \bar{u}\frac{\partial \bar{c}}{\partial x} + \bar{v}\frac{\partial \bar{c}}{\partial y} + \bar{w}\frac{\partial \bar{c}}{\partial z} = D_m \left(\frac{\partial^2 \bar{c}}{\partial x^2} + \frac{\partial^2 \bar{c}}{\partial y^2} + \frac{\partial^2 \bar{c}}{\partial z^2} \right) - \left(\frac{\partial \overline{u'c'}}{\partial x} + \frac{\partial \overline{v'c'}}{\partial y} + \frac{\partial \overline{w'c'}}{\partial z} \right) \pm \dot{r} \quad \text{(A.15)}$$

where ρ_w is the density of the fluid, ν is the molecular kinematic viscosity of the fluid, g is the gravitational acceleration constant, D_m is the molecular diffusivity of the scalar, $\dot{r}$ is the rate of contaminant gain or loss within the fluid volume, and $F_{d,x}$, $F_{d,y}$, $F_{d,z}$ is a distributed drag force, as would be produced by vegetation or other obstructions within the flow volume. Because nearly all constructed wetlands have a length $L < 10$ km, the Coriolis force is not included. Note that the turbulent stresses, e.g., $\frac{\partial \overline{u'v'}}{\partial x}$, represent transport due to correlated turbulent fluctuations and are typically larger than the viscous stresses, e.g., $\nu \frac{\partial^2 u}{\partial y^2}$. It is here assumed that no density differences or net precipitation, infiltration, or evapotranspiration are present within the wetland. Note that this process averages over instantaneous temporal and spatial fluctuations, which can be significant during the initial region of jet development (List and Dugan, 1994). Under these conditions, the vertical boundary conditions for flow within a free-surface wetland are as follows:

$$\bar{u} = 0 \quad \text{at} \quad z = h \quad \text{(A.16)}$$

$$u' = 0 \quad \text{at} \quad z = h \quad \text{(A.17)}$$

$$\nu \frac{\partial \bar{u}}{\partial x} = \tau_{b,x} \quad \text{at} \quad z = h \quad \text{(A.18)}$$

$$\nu \frac{\partial \bar{u}}{\partial x} = \tau_{b,y} \quad \text{at} \quad z = h \quad \text{(A.19)}$$

$$\bar{v} = 0 \quad \text{at} \quad z = h \quad \text{(A.20)}$$

$$v' = 0 \quad \text{at} \quad z = h \quad \text{(A.21)}$$

$$\nu \frac{\partial \bar{v}}{\partial x} = \tau_{s,x} \quad \text{at} \quad z = 0 \quad \text{(A.22)}$$

$$\nu \frac{\partial \bar{v}}{\partial x} = \tau_{s,y} \quad \text{at} \quad z = 0 \quad \text{(A.23)}$$

$$\bar{w} = \bar{w}_s \quad \text{at} \quad z = 0 \tag{A.24}$$

$$w' = 0 \quad \text{at} \quad z = 0 \tag{A.25}$$

$$\bar{w} = \bar{w}_b \quad \text{at} \quad z = h \tag{A.26}$$

$$w' = 0 \quad \text{at} \quad z = h \tag{A.27}$$

$$c' = 0 \quad \text{at} \quad z = 0 \tag{A.28}$$

$$c' = 0 \quad \text{at} \quad z = h \tag{A.29}$$

$$\frac{\partial \bar{c}}{\partial x} = \dot{r}_s \quad \text{at} \quad z = 0 \tag{A.30}$$

$$\frac{\partial \bar{c}}{\partial x} = \dot{r}_b \quad \text{at} \quad z = h \tag{A.31}$$

where τ_b is the surface shear stress, τ_s is the bed shear stress, $\bar{w}_s$ is net precipitation (e.g., precipitation minus evapotranspiration), $\bar{w}_b$ is net infiltration, $\dot{r}_s$ is the net exchange of contaminant with the atmosphere, and $\dot{r}_b$ is the net exchange of contaminant with the bed.

Within a shallow system within which $h \ll B$ and $h \ll L$, it is convenient to consider two-dimensional (2-D) flow in the x-y plane. In analogy to using a Reynolds decomposition to take a temporal average of the momentum equation, the depth-averaged values are introduced, indicated by angle brackets:

$$\langle \bar{u} \rangle = \frac{1}{h} \int_0^h \bar{u} \mathrm{d}z \tag{A.32}$$

$$\langle \bar{v} \rangle = \frac{1}{h} \int_0^h \bar{v} \mathrm{d}z \tag{A.33}$$

$$\langle \bar{c} \rangle = \frac{1}{h} \int_0^h \bar{c} \mathrm{d}z \tag{A.34}$$

It is assumed that water depth variations arise from variations in the bed elevation that are steady over time in addition to possible time-varying fluctuations in the position of the free surface. The local velocity can then be written in terms of the depth average plus a deviation from it:

$$\bar{u}(x, y, z) = \langle \bar{u} \rangle (x, y) + \bar{u}''(x, y, z) \tag{A.35}$$

$$\bar{v}(x,y,z) = \langle\bar{v}\rangle(x,y) + \bar{v}''(x,y,z) \tag{A.36}$$

$$\bar{c}(x,y,z) = \langle\bar{c}\rangle(x,y) + \bar{c}''(x,y,z) \tag{A.37}$$

where a double prime indicates deviation from the depth average. These terms can be substituted into the governing momentum and transport equations (Eqs. A.11, A.12, A.13, A.14, and A.15). Multiplying by the total water depth h and integrating over depth, Flokstra (1977) is followed to produce the two-dimensional equations of motion:

$$\frac{\partial h}{\partial t} + \frac{\partial\left[h\langle\bar{u}\rangle\right]}{\partial x} + \frac{\partial\left[h\langle\bar{v}\rangle\right]}{\partial y} = 0 \tag{A.38}$$

$$\begin{aligned}\frac{\partial\left[h\langle\bar{u}\rangle\right]}{\partial t} + \langle\bar{u}\rangle\frac{\partial\left[h\langle\bar{u}\rangle\right]}{\partial x} + \langle\bar{v}\rangle\frac{\partial\left[h\langle\bar{u}\rangle\right]}{\partial y} &= -\frac{1}{\rho_w}\frac{\partial\left[\bar{P}h\right]}{\partial x} + \nu\left(\frac{\partial^2\left[h\langle\bar{u}\rangle\right]}{\partial x^2} + \frac{\partial^2\left[h\langle\bar{u}\rangle\right]}{\partial y^2}\right) \\ &\quad - \left(\frac{\partial\left[h\langle\overline{u'^2}\rangle\right]}{\partial x} + \frac{\partial\left[h\langle\overline{u'v'}\rangle\right]}{\partial y}\right) \\ &\quad - \left(\frac{\partial\left[h\langle\bar{u}''^2\rangle\right]}{\partial x} + \frac{\partial\left[h\langle\bar{u}''\bar{v}''\rangle\right]}{\partial y}\right) \\ &\quad - \frac{h}{\rho_w}\langle F_{d,x}\rangle\end{aligned} \tag{A.39}$$

$$\begin{aligned}\frac{\partial\left[h\langle\bar{v}\rangle\right]}{\partial t} + \langle\bar{u}\rangle\frac{\partial\left[h\langle\bar{v}\rangle\right]}{\partial x} + \langle\bar{v}\rangle\frac{\partial\left[h\langle\bar{v}\rangle\right]}{\partial y} &= -\frac{1}{\rho_w}\frac{\partial\left[\bar{P}h\right]}{\partial y} + \nu\left(\frac{\partial^2\left[h\langle\bar{v}\rangle\right]}{\partial x^2} + \frac{\partial^2\left[h\langle\bar{v}\rangle\right]}{\partial y^2}\right) \\ &\quad - \left(\frac{\partial\left[h\langle\overline{u'v'}\rangle\right]}{\partial x} + \frac{\partial\left[h\langle\overline{v'^2}\rangle\right]}{\partial y}\right) \\ &\quad - \left(\frac{\partial\left[h\langle\bar{u}''\bar{v}''\rangle\right]}{\partial x} + \frac{\partial\left[h\langle\bar{v}''^2\rangle\right]}{\partial y}\right) \\ &\quad - \frac{h}{\rho_w}\langle F_{d,y}\rangle\end{aligned} \tag{A.40}$$

$$0 = -\frac{\partial\left[\bar{P}h\right]}{\partial z} + \rho_w g \tag{A.41}$$

$$\begin{aligned}\frac{\partial\left[h\langle\bar{c}\rangle\right]}{\partial t} + \langle\bar{u}\rangle\frac{\partial\left[h\langle\bar{c}\rangle\right]}{\partial x} + \langle\bar{v}\rangle\frac{\partial\left[h\langle\bar{c}\rangle\right]}{\partial y} &= D_m\left(\frac{\partial^2\left[h\langle\bar{c}\rangle\right]}{\partial x^2} + \frac{\partial^2\left[h\langle\bar{c}\rangle\right]}{\partial y^2}\right) \\ &\quad - \left(\frac{\partial\left[h\langle\overline{u'c'}\rangle\right]}{\partial x} + \frac{\partial\left[h\langle\overline{v'c'}\rangle\right]}{\partial y}\right) \\ &\quad - \left(\frac{\partial\left[h\langle\bar{u}''\bar{c}''\rangle\right]}{\partial x} + \frac{\partial\left[h\langle\bar{v}''\bar{c}''\rangle\right]}{\partial y}\right) \pm \langle\dot{r}\rangle\end{aligned} \tag{A.42}$$

The depth-averaged drag terms $\langle F_{d,x} \rangle$ and $\langle F_{d,y} \rangle$ may include a contribution from bed and surface drag in addition to a distributed drag component, and the depth-averaged reaction rate $\langle \dot{r} \rangle$ includes exchanges with the sediment and the atmosphere. Note that the z-momentum equation (Eq. A.41) simply states hydrostatic equilibrium. Integrating this equation over z:

$$\bar{P}h = \rho_w g z \tag{A.43}$$

Therefore, within the x- and y-momentum equations,

$$\frac{1}{\rho_w}\frac{\partial \left[\bar{P}h\right]}{\partial x} = gh\frac{\partial h}{\partial x} \tag{A.44}$$

$$\frac{1}{\rho_w}\frac{\partial \left[\bar{P}h\right]}{\partial y} = gh\frac{\partial h}{\partial y} \tag{A.45}$$

A.2 Flow through continuous vegetation

Within marsh vegetation, deviations in velocity over depth are larger than turbulent fluctuations (Leonard and Luther, 1995; López and García, 2001), so the spatial covariant stresses are expected to dominate both the turbulent and the molecular stresses. To attain closure of the stress terms, a gradient transport relationship between spatial covariant stresses and velocity gradients is assumed within the mean flow. The coefficient of this relationship is the eddy viscosity ν_t, which is assumed to be anisotropic but homogeneous. The vertical variations in velocity also create enhanced depth-averaged dispersion (Lightbody and Nepf, 2006*a*,*b*), so dispersive stresses will be dominated the contributions of correlations in the velocity and concentration deviations from the depth-averaged mean, which will be represented by the longitudinal and lateral Fickian dispersion coefficients K_x and K_y, respectively. With these substitutions, and under conditions of steady flow ($\frac{\partial}{\partial t} = 0$), the depth-averaged governing equations become:

$$\frac{\partial[h\langle\bar{u}\rangle]}{\partial x} + \frac{\partial[h\langle\bar{v}\rangle]}{\partial y} = 0 \tag{A.46}$$

$$\langle\bar{u}\rangle\frac{\partial[h\langle\bar{u}\rangle]}{\partial x}+\langle\bar{v}\rangle\frac{\partial[h\langle\bar{u}\rangle]}{\partial y} = -gh\frac{\partial h}{\partial x}-\left(\nu_{t,xx}\frac{\partial^2[h\langle\bar{u}\rangle]}{\partial x^2}+\nu_{t,xy}\frac{\partial^2[h\langle\bar{u}\rangle]}{\partial y^2}\right) -\frac{1}{\rho_w}\langle F_{d,x}\rangle \quad \text{(A.47)}$$

$$\langle\bar{u}\rangle\frac{\partial[h\langle\bar{v}\rangle]}{\partial x}+\langle\bar{v}\rangle\frac{\partial[h\langle\bar{v}\rangle]}{\partial y} = -\left(\nu_{t,yx}\frac{\partial^2[h\langle\bar{v}\rangle]}{\partial x^2}+\nu_{t,yy}\frac{\partial^2[h\langle\bar{v}\rangle]}{\partial y^2}\right)-\frac{1}{\rho_w}\langle F_{d,y}\rangle$$

$$\langle\bar{u}\rangle\frac{\partial[h\langle\bar{c}\rangle]}{\partial x}+\langle\bar{v}\rangle\frac{\partial[h\langle\bar{c}\rangle]}{\partial y} = K_x\frac{\partial^2[h\langle\bar{c}\rangle]}{\partial x^2}+K_y\frac{\partial^2[h\langle\bar{c}\rangle]}{\partial y^2}\pm k_v h\left(\langle\bar{c}\rangle-c*\right) \quad \text{(A.48)}$$

where a first-order removal process has been assumed with k_v the volumetric removal rate and $c*$ the background concentration.

In open channel flow, the drag force is related to the slope of the energy grade line, S_E:

$$\langle F_{d,x}\rangle=\rho_w g R S_E \quad \text{(A.49)}$$

where R is the hydraulic radius of the cross section, which can be approximated by h in a wide wetland with $B\gg h$. When flow is fully rough turbulent and drag is due entirely to bed shear stress, Manning's equation can be used to characterize the drag. In metric units, Manning's equation is:

$$\langle\bar{u}\rangle=\frac{1}{n_M}R^{2/3}S_E^{1/2} \quad \text{(A.50)}$$

where n_M is the dimensionless Manning resistance coefficient. Manning's equation can be solved for S_E and substituted into the resistance equation, resulting in the following expressions for the depth-averaged drag force:

$$\langle F_{d,x}\rangle=\rho_w g n_M^2\frac{\langle\bar{u}\rangle\sqrt{\langle\bar{u}\rangle^2+\langle\bar{v}\rangle^2}}{h^{1/3}} \quad \text{(A.51)}$$

$$\langle F_{d,y}\rangle=\rho_w g n_M^2\frac{\langle\bar{v}\rangle\sqrt{\langle\bar{u}\rangle^2+\langle\bar{v}\rangle^2}}{h^{1/3}} \quad \text{(A.52)}$$

Note that Manning's equation was derived under assumptions of drag due to bed friction under fully rough turbulent flow, although most wetland situations have transitional or even laminar flow. In these cases, Manning's equation is valid only if n_M is a function of Reynolds number (Tsihrintzis and Madiedo, 2000). In addition, high

flows through a wetland may deflect vegetation, increasing the sensitivity of the drag force to the Reynolds number (Järvelä, 2002). Manning's equation also assumes all drag results from bed friction, but flow in wetland marsh regions is controlled by the vegetation drag, which is distributed (often unequally) throughout the water column (Tsihrintzis and Madiedo, 2000; Lightbody and Nepf, 2006*b*). Manning's equation is therefore not directly applicable to wetland situations, although previous modeling attempts have shown that it can represent observed flow patterns if the coefficient n_M is selected to represent an equivalent roughness that incorporates drag due to vegetation (Jenkins and Greenway, 2005; D'Alpaos et al., 2006).

Another method of parameterizing the drag force is to introduce a quadratic drag law related to the velocity field through a nondimensional friction coefficient C_f (e.g., Lee and Jirka, 1980; Jirka, 1994).

$$\frac{1}{\rho_w}\langle F_{d,x}\rangle = C_f\langle\bar{u}\rangle\left(\langle\bar{u}\rangle^2+\langle\bar{v}\rangle^2\right)^{1/2} \tag{A.53}$$

$$\frac{1}{\rho_w}\langle F_{d,y}\rangle = C_f\langle\bar{v}\rangle\left(\langle\bar{u}\rangle^2+\langle\bar{v}\rangle^2\right)^{1/2} \tag{A.54}$$

where C_f is a function of Reynolds number and is directly proportion to the frontal area of stems within the flow (Peterson et al., 2004; Lightbody and Nepf, 2006*b*) . If friction is due to bed drag only, then the friction coefficient C_f is related to the Darcy-Weisbach friction coefficient f_o by $C_f = f_o/8$, to the Chèzy resistance factor C_z by $C_f = g/C_z^2$, and to the Manning coefficient by $C_f = h^{2/3}n_M^2$ (cf. Henderson, 1966, pp. 90ff).

A.3 Flow created when a short-circuiting flowpath enters a deep zone

Consider steady flow ($\frac{\partial}{\partial t} = 0$) created when a fast flowpath of width b_f and velocity U_f traveling through a marsh region of depth h_m, width B_f, and velocity U_s enters a quiescent deep zone that reaches a depth h_{dz}. It is assumed that the water depth

only varies in the longitudinal direction, $h = h(x)$ and that the Reynolds number $Re = U_f b_f/\nu > 2000$, so that the flow exiting the flowpath creates a turbulent jet within the deep zone (Lee and Chu, 2003, p. 21). First, scaling arguments will be used to show that the boundary layer approximation applies to flow through a turbulent jet for $x \gg b_{u,o}$. For $Re > 2000$, the jet is narrow, and the half-width of the jet $b_u(x)$ is much less than the distance it has traveled downstream, x (e.g., Giger et al., 1991). That is, at a distance $\hat{X}$ from the inlet, at which the jet has characteristic width $\hat{B} \ll \hat{X}$, $\frac{\partial}{\partial x} \sim \frac{1}{\hat{X}}$ and $\frac{\partial}{\partial y} \sim \frac{1}{\hat{B}}$, so $\frac{\partial}{\partial x} \ll \frac{\partial}{\partial y}$. Similarly, $\frac{\partial^2}{\partial x^2} \sim \frac{1}{\hat{L}^2}$ and $\frac{\partial^2}{\partial y^2} \sim \frac{1}{\hat{B}^2}$. Therefore, within the velocity stress terms and the concentration correlation terms, the longitudinal gradients ($\frac{\partial}{\partial x}$ and $\frac{\partial^2}{\partial x^2}$) can be neglected.

Next, consider the $O(1)$ scaled variables $y \sim \hat{B}$, $x \sim \hat{X}$, $\langle \bar{u} \rangle \sim \hat{U}$, and $h \sim h_{dz}$, where $\hat{U}$ is a characteristic velocity scale of the flow. When these quantities are substituted into the continuity equation (Eq. A.38), the result is $\langle \bar{v} \rangle \sim \hat{B}\hat{U}/\hat{X}$. Substituting these scaling relationships into either momentum equation (Eq. A.39 and A.40), it becomes clear that both inertial terms scale as, e.g., $\langle \bar{u} \rangle \frac{\partial [h\langle \bar{u} \rangle]}{\partial x} \sim \frac{\hat{U}^2 h}{\hat{X}}$ and the viscous terms scale as, e.g., $\nu \frac{\partial^2 [h\langle \bar{u} \rangle]}{\partial y^2} \sim \frac{\nu h \hat{U}}{\hat{B}^2}$. The ratio of the two is $\frac{\hat{U}\hat{X}}{\nu} \frac{\hat{B}^2}{\hat{X}^2} = Re \frac{\hat{B}^2}{\hat{X}^2}$. Therefore, when $\hat{B} \ll \hat{X}$ and $Re > 2000$, the inertial terms dominate the viscous terms. This scaling is not surprising, because in most turbulent flows the contribution of viscosity is much less than the turbulent shear stresses. For example, the contribution of molecular viscosity within a free jet have been found to constitute only 4% of the contribution of turbulent shear stress (Lee and Chu, 2003, p. 30). The viscous stress terms and the molecular diffusion terms are therefore neglected within the momentum equations.

Finally, note that $\frac{1}{\rho_w} \frac{\partial \bar{P}}{\partial y} = gh \frac{\partial h}{\partial y} \sim 1$ but that the inertial terms both scale as $\langle \bar{u} \rangle \frac{\partial \langle \bar{v} \rangle}{\partial x} \sim v \frac{\partial \langle \bar{v} \rangle}{\partial y} \sim \frac{1}{Re}$, so the inertial terms can be neglected. With these considerations, the y-momentum equation (Eq. A.40) reduces to:

$$0 = -gh\frac{\partial h}{\partial y} - \frac{\partial \left[h\overline{v'^2}\right]}{\partial y} - \frac{\partial \left[h\langle \bar{v}''^2 \rangle\right]}{\partial y} - C_f \langle \bar{v} \rangle \left(\langle \bar{u} \rangle^2 + \langle \bar{v} \rangle^2\right)^{1/2} \tag{A.55}$$

Integrating Eq. A.55, with the boundary conditions that $\bar{P} = P_\infty$ and $\langle \bar{v} \rangle \to 0$ at

$y = \pm\infty$, produces:

$$gh^2 = ghh_\infty - h\overline{v'^2} - h\langle\bar{v}''^2\rangle \tag{A.56}$$

Differentiating according to x:

$$gh\frac{\mathrm{d}h}{\mathrm{d}x} = gh\frac{\mathrm{d}h_\infty}{\mathrm{d}x} - \frac{\partial\left[h\overline{v'^2}\right]}{\partial x} - \frac{\partial\left[h\langle\bar{v}''^2\rangle\right]}{\partial x} \tag{A.57}$$

Another common simplifying assumption is that the pressure gradient in the outer fluid $\frac{1}{\rho_w}\frac{\mathrm{d}P_\infty}{\mathrm{d}x}$ is negligible. Lee and Jirka (1980) let the pressure deviation scale on the lateral turbulent entrainment, $\frac{\mathrm{d}\bar{P}}{\mathrm{d}x} \sim (\alpha_e\langle\bar{u}\rangle)^2/2g$, which, because the entrainment coefficient $\alpha_e = O(1/10)$, means that the scaled pressure can be dropped. Giger et al. (1991) confirmed this assertion by measuring the pressure variation under the midline and boundary of a shallow turbulent jet with $h_m/b_f = 8$ and found that the pressure under both the axis and boundaries was not significantly different from the pressure as $y \to \infty$ and that the small observed pressure difference was too small to explain the observed change in momentum flux.

Under these conditions, the governing equations (Eqs. A.39, A.40, A.41, and A.42) become:

$$\frac{\partial\left[h\langle\bar{u}\rangle\right]}{\partial x} + \frac{\partial\left[h\langle\bar{v}\rangle\right]}{\partial y} = 0 \tag{A.58}$$

$$\begin{aligned}\langle\bar{u}\rangle\frac{\partial\left[h\langle\bar{u}\rangle\right]}{\partial x} + \langle\bar{v}\rangle\frac{\partial\left[h\langle\bar{u}\rangle\right]}{\partial y} &= -\frac{\partial\left[h\langle\overline{u'v'}\rangle\right]}{\partial y} - \frac{\partial}{\partial x}\left(\left[h\langle\overline{u'^2}\rangle\right] - \left[h\overline{v'^2}\right]\right) \\ &\quad -\frac{\partial\left[h\langle\bar{u}''\bar{v}''\rangle\right]}{\partial y} - \frac{\partial}{\partial x}\left(\left[h\langle\bar{u}''^2\rangle\right] - \left[h\langle\bar{v}''^2\rangle\right]\right) \\ &\quad -C_f\langle\bar{u}\rangle^2\end{aligned} \tag{A.59}$$

$$\begin{aligned}\langle\bar{u}\rangle\frac{\partial\left[h\langle\bar{c}\rangle\right]}{\partial x} + \langle\bar{v}\rangle\frac{\partial\left[h\langle\bar{c}\rangle\right]}{\partial y} &= -\left(\frac{\partial\left[h\langle\overline{u'c'}\rangle\right]}{\partial x} + \frac{\partial\left[h\langle\overline{v'c'}\rangle\right]}{\partial y}\right) \\ &\quad -\left(\frac{\partial\left[h\langle\bar{u}''\bar{c}''\rangle\right]}{\partial x} + \frac{\partial\left[h\langle\bar{v}''\bar{c}''\rangle\right]}{\partial y}\right)\end{aligned} \tag{A.60}$$

The cross-correlation stress terms are typically larger than the normal stress terms, i.e. $\tau_{xy} \gg \tau_{xx}, \tau_{yy}$ and $\frac{\partial\langle\overline{u'c'}\rangle}{\partial x} \ll \frac{\partial\langle\overline{v'c'}\rangle}{\partial y}$ (Rajaratnam, 1976, p. 4). For a plane turbulent free jet (i.e., no losses to friction, $C_f = 0$, and a constant velocity profile over depth,

$\langle \bar{u}''\bar{v}'' \rangle = 0$), with h constant, these equations reduce to the well-known equations of motion for a planar turbulent free jet (e.g., Rajaratnam, 1976, p. 5; Lee and Chu, 2003, pp. 28-29):

$$\frac{\partial \langle \bar{u} \rangle}{\partial x} + \frac{\partial \langle \bar{v} \rangle}{\partial y} = 0 \tag{A.61}$$

$$\langle \bar{u} \rangle \frac{\partial \langle \bar{u} \rangle}{\partial x} + \langle \bar{v} \rangle \frac{\partial \langle \bar{u} \rangle}{\partial y} = -\frac{\partial \langle \overline{u'c'} \rangle}{\partial y} \tag{A.62}$$

$$\langle \bar{u} \rangle \frac{\partial \langle \bar{c} \rangle}{\partial x} + \langle \bar{v} \rangle \frac{\partial \langle \bar{c} \rangle}{\partial y} = -\frac{\partial \langle \overline{v'c'} \rangle}{\partial y} \tag{A.63}$$

Before continuing, note that the chain rule provides that:

$$\begin{aligned} \langle \bar{u} \rangle \frac{\partial \left[h \langle \bar{u} \rangle \right]}{\partial x} + \langle \bar{v} \rangle \frac{\partial \left[h \langle \bar{u} \rangle \right]}{\partial y} &= \left(\frac{\partial \left[h \langle \bar{u} \rangle^2 \right]}{\partial x} - \langle \bar{u} \rangle \frac{\partial \left[h \langle \bar{u} \rangle \right]}{\partial x} \right) + \left(\frac{\left[h \partial \langle \bar{u} \rangle \langle \bar{v} \rangle \right]}{\partial y} - \langle \bar{u} \rangle \frac{\partial \left[h \langle \bar{v} \rangle \right]}{\partial y} \right) \\ &= \frac{\partial \left[h \langle \bar{u} \rangle^2 \right]}{\partial x} + \frac{\partial \left[h \langle \bar{u} \rangle \langle \bar{v} \rangle \right]}{\partial y} - \langle \bar{u} \rangle \left(\frac{\partial \left[h \langle \bar{u} \rangle \right]}{\partial x} + \frac{\partial \left[h \langle \bar{v} \rangle \right]}{\partial y} \right) \\ &= \frac{\partial \left[h \langle \bar{u} \rangle^2 \right]}{\partial x} + \frac{\partial \left[h \langle \bar{u} \rangle \langle \bar{v} \rangle \right]}{\partial y} \end{aligned} \tag{A.64}$$

where continuity (Eq. A.58) is used to eliminate the last term in Eq. A.64. Therefore, Eq. A.59 can be rewritten as:

$$\begin{aligned} \frac{\partial \left[h \langle \bar{u} \rangle^2 \right]}{\partial x} &+ \frac{\partial \left[h \langle \bar{u} \rangle \langle \bar{v} \rangle \right]}{\partial y} + \frac{\partial}{\partial x} \left(\left[h \langle \overline{u'^2} \rangle \right] - \left[h \langle \overline{v'^2} \rangle \right] \right) + \frac{\partial}{\partial x} \left(\left[h \langle \bar{u}''^2 \rangle \right] - \left[h \langle \bar{v}''^2 \rangle \right] \right) \\ &= -\frac{\partial \left[h \langle \overline{u'v'} \rangle \right]}{\partial y} - \frac{\partial \left[h \langle \bar{u}'' \bar{v}'' \rangle \right]}{\partial y} - C_f \langle \bar{u} \rangle^2 \end{aligned} \tag{A.65}$$

Similarly,

$$\begin{aligned} \langle \bar{u} \rangle \frac{\partial \left[h \langle \bar{c} \rangle \right]}{\partial x} + \langle \bar{v} \rangle \frac{\partial \left[h \langle \bar{c} \rangle \right]}{\partial y} &= \left(\frac{\partial \left[h \langle \bar{c} \rangle \langle \bar{u} \rangle \right]}{\partial x} - \langle \bar{c} \rangle \frac{\partial \left[h \langle \bar{u} \rangle \right]}{\partial x} \right) + \left(\frac{\partial \left[h \langle \bar{c} \rangle \langle \bar{v} \rangle \right]}{\partial y} - \langle \bar{c} \rangle \frac{\partial \left[h \langle \bar{v} \rangle \right]}{\partial y} \right) \\ &= \frac{\partial \left[h \langle \bar{c} \rangle \langle \bar{u} \rangle \right]}{\partial x} + \frac{\partial \left[h \langle \bar{c} \rangle \langle \bar{v} \rangle \right]}{\partial y} \langle \bar{c} \rangle \left(\frac{\partial \left[h \langle \bar{u} \rangle \right]}{\partial x} + \frac{\partial \left[h \langle \bar{v} \rangle \right]}{\partial y} \right) \\ &= \frac{\partial \left[h \langle \bar{c} \rangle \langle \bar{u} \rangle \right]}{\partial x} + \frac{\partial \left[h \langle \bar{c} \rangle \langle \bar{v} \rangle \right]}{\partial y} \end{aligned} \tag{A.66}$$

Therefore, Eq. A.63 can be rewritten as:

$$\frac{\partial\left[h\langle\bar{c}\rangle\langle\bar{u}\rangle\right]}{\partial x}+\frac{\partial\left[h\langle\bar{c}\rangle\langle\bar{v}\rangle\right]}{\partial y}=-\frac{\partial\left[h\langle\overline{u'c'}\rangle\right]}{\partial x}-\frac{\partial\left[h\langle\overline{v'c'}\rangle\right]}{\partial y}-\frac{\partial\left[h\langle\bar{u}''\bar{v}''\rangle\right]}{\partial x}-\frac{\partial\left[h\langle\bar{v}''\bar{c}''\rangle\right]}{\partial y} \tag{A.67}$$

One way to achieve turbulence and spatial closure and simplify the analysis of jet dynamics is to integrate all variables across the jet (e.g., in the y and z coordinates) to reduce the problem to one dimension in x. These depth-averaged equations will be integrated over the full jet width from $y = 0$ to a location outside the jet, denoted by b_j, where the local velocity equals the co-flow velocity u_c and the local concentration equals the co-flow concentration c_s.

First, the continuity equation (Eq. A.58) is integrated across the jet width (cf. Lee et al., 1977, pp. 92-93):

$$\int_0^{b_j}\frac{\partial\left[h\langle\bar{u}\rangle\right]}{\partial x}\mathrm{d}y=-\int_0^{b_j}\frac{\partial\left[h\langle\bar{v}\rangle\right]}{\partial y}\mathrm{d}y=h\left(u_c\frac{\mathrm{d}b_u}{\mathrm{d}x}-v_e\right) \tag{A.68}$$

where v_e is the entrainment velocity and assuming that the water depth is a function of x only. Invoking the Leibniz rule to bring the integral inside of the differential, this equation can be rewritten as a function of the jet volume flux $q_j(x)$.

$$\frac{\mathrm{d}q_j}{\mathrm{d}x}=\frac{\mathrm{d}}{\mathrm{d}x}\left(h\int_0^{b_j}\langle\bar{u}\rangle\mathrm{d}y\right)=h\left(u_c\frac{\mathrm{d}b_u}{\mathrm{d}x}-v_e\right) \tag{A.69}$$

The rate of change in the jet flow rate, $\frac{1}{h}\frac{\mathrm{d}q_j}{\mathrm{d}x}$, is called the entrainment velocity v_e. Morton et al. (1956) advanced the entrainment hypothesis, which holds that the rate of entrainment at the edge of the plume is proportional to the jet characteristic velocity, here taken to be the difference between the centerline velocity u_m and the co-flow velocity u_c, such that:

$$v_e=\alpha_e(u_m-u_c) \tag{A.70}$$

where the entrainment coefficient α_e does not depend on x. Therefore, the continuity

equation becomes:

$$\frac{\mathrm{d}}{\mathrm{d}x}\int_0^{b_j} h\langle\bar{u}\rangle \mathrm{d}y = \alpha_e h(u_m - u_c) \tag{A.71}$$

The jet is expected to entrain fluid as long as its velocity is elevated over that of the background co-flow velocity. Experiments have shown that, if $q_f = b_f h_m U_f$ is the initial jet flow rate, then $q_j/q_f > 1$ at all points downstream (Rajaratnam, 1976).

Next integrate the depth-averaged x-momentum equation (Eq. A.65) from $y = 0$ to $y = b_j$:

$$\begin{aligned}\int_0^{b_j} \left\{ \frac{\partial\left[h\langle\bar{u}\rangle^2\right]}{\partial x} \right. &+ \left. \frac{\partial\left[h\langle\bar{u}\rangle\langle\bar{v}\rangle\right]}{\partial y} + \frac{\partial}{\partial x}\left(\left[h\overline{u'^2}\right] - \left[h\overline{v'^2}\right]\right) + \frac{\partial}{\partial x}\left(\left[h\langle\bar{u}''^2\rangle\right] - \left[h\langle\bar{v}''^2\rangle\ \right]\right) \right\} \mathrm{d}y \\ &= \int_0^{b_j} \left\{ -\frac{\partial\left[h\overline{u'v'}\right]}{\partial y} - \frac{\partial\left[h\langle\bar{u}''\bar{v}''\rangle\right]}{\partial y} - C_f\langle\bar{u}\rangle^2 \right\} \mathrm{d}y \end{aligned} \tag{A.72}$$

Following Rajaratnam (1976, pp. 5–6), using the Leibniz rule the first term in Eq. A.72 can be rewritten as:

$$\int_0^{b_j} \frac{\partial\left[h\langle\bar{u}\rangle^2\right]}{\partial x}\mathrm{d}y = \frac{\mathrm{d}}{\mathrm{d}x}\int_0^{b_j} h\langle\bar{u}\rangle^2 \mathrm{d}y \tag{A.73}$$

Again invoking the Leibniz rule, the third and fourth terms in Eq. A.72 become:

$$\int_0^{b_j} \frac{\partial}{\partial x}\left(\left[h\langle\overline{u'^2}\rangle\right] - \left[h\langle\overline{v'^2}\rangle\right]\right)\mathrm{d}y = \frac{\mathrm{d}}{\mathrm{d}x}\int_0^{b_j}\left(\left[h\langle\overline{u'^2}\rangle\right] - \left[h\langle\overline{v'^2}\rangle\right]\right)\mathrm{d}y \tag{A.74}$$

$$\int_0^{b_j} \frac{\partial}{\partial x}\left(\left[h\langle\bar{u}''^2\rangle\right] - \left[h\langle\bar{v}''^2\rangle\right]\right)\mathrm{d}y = \frac{\mathrm{d}}{\mathrm{d}x}\int_0^{b_j}\left(\left[h\langle\bar{u}''^2\rangle\right] - \left[h\langle\bar{v}''^2\rangle\right]\right)\mathrm{d}y \tag{A.75}$$

Meanwhile, the second, fifth, and sixth terms in Eq. A.72 reduce to 0:

$$\int_0^{b_j} \frac{\partial\left[h\langle\bar{u}\rangle\langle\bar{v}\rangle\right]}{\partial y}\mathrm{d}y = h\langle\bar{u}\rangle\langle\bar{v}\rangle\Big|_0^{b_j} = 0 \tag{A.76}$$

$$\int_0^{b_j} \frac{\partial\left[h\langle\overline{u'v'}\rangle\right]}{\partial y}\mathrm{d}y = h\langle\overline{u'v'}\rangle\Big|_0^{b_j} = 0 \tag{A.77}$$

$$\int_0^{b_j} \frac{\partial\left[h\langle\bar{u}''\bar{v}''\rangle\right]}{\partial y}\mathrm{d}y = h\langle\bar{u}''\bar{v}''\rangle\Big|_0^{b_j} = 0 \tag{A.78}$$

due to the boundary conditions, for which $\langle\bar{u}\rangle \to 0$ as $y \to \pm\infty$, and $\frac{\partial\langle\bar{u}\rangle}{\partial y} \to 0$ and $\langle\overline{u'v'}\rangle \to 0$ as $y \to \pm\infty$. The integral x-momentum equation therefore reduces to:

$$\frac{\mathrm{d}}{\mathrm{d}x}\int_0^{b_j} h\left[\langle\bar{u}\rangle^2 + (\langle\overline{u'^2}\rangle - \langle\overline{v'^2}\rangle)\right]\mathrm{d}y = -\int_0^{b_j} C_f\langle\bar{u}\rangle^2\mathrm{d}y \tag{A.79}$$

Eq. A.79 describes the rate in change of the jet momentum as it travels downstream. Experimental observations suggest that in a turbulent jet the turbulent flux terms are less than 10% of the magnitude of the other term on the left-hand side of Eq. A.79 (Lee and Chu, 2003; Gaskin et al., 2004), so they are often neglected. However, Lee and Chu (2003, pp. 186-187) suggest that an additional term should be added to the left-hand-side of Eq. A.79 to account for the longitudinal advection of momentum into the expanding jet; that term will be included here by considering the rate of change in jet excess momentum m. Multiplying by the fluid density ρ_w, the jet excess momentum m in a planar jet will evolve within the deep zone such that:

$$\frac{\mathrm{d}m}{\mathrm{d}x} = \frac{\mathrm{d}}{\mathrm{d}x}\int_0^{b_j} \rho_w h\langle\bar{u}\rangle(\langle\bar{u}\rangle - u_c)\mathrm{d}y = -\int_0^{b_j} \rho_w C_f\langle\bar{u}\rangle\left(\langle\bar{u}\rangle - u_c\right)\mathrm{d}y \tag{A.80}$$

The initial momentum flux m_o is an important physical quantity controlling the behavior of a plane jet. It effectively replaces individual values of b_f and U_f. That is, for a given value of m_o, the same normalized velocity profile within the jet will be obtained for different combinations of b_f and U_f (Rajaratnam, 1976).

Similarly, the expression for conservation of scalar mass (Eq. A.67) can be integrated over jet width:

$$\int_0^{b_j}\left(\frac{\partial\left[h\langle\bar{c}\rangle\langle\bar{u}\rangle\right]}{\partial x} + \frac{\partial\left[h\langle\bar{c}\rangle\langle\bar{v}\rangle\right]}{\partial y}\right)\mathrm{d}y = \int_0^{b_j}\left(-\frac{\partial\left[h\langle\overline{u'c'}\rangle\right]}{\partial x} - \frac{\partial\left[h\langle\overline{v'c'}\rangle\right]}{\partial y} - \frac{\partial\left[h\langle\bar{u}''\bar{c}''\rangle\right]}{\partial x} - \frac{\partial\left[h\langle\bar{v}''\bar{c}''\rangle\right]}{\partial y}\right)\mathrm{d}y \tag{A.81}$$

Invoking the Leibniz rule, the first, third, and fifth terms in Eq. A.81 can be rewritten

as:

$$\int_0^{b_j} \frac{\partial \left[h\langle\bar{c}\rangle\langle\bar{u}\rangle\right]}{\partial x}\mathrm{d}y = \frac{\mathrm{d}}{\mathrm{d}x}h\int_0^{b_j}\langle\bar{c}\rangle\langle\bar{u}\rangle\mathrm{d}y \tag{A.82}$$

$$\int_0^{b_j}\left(\frac{\partial\left[h\langle\overline{u'c'}\rangle\right]}{\partial x}\right)\mathrm{d}y = \frac{\mathrm{d}}{\mathrm{d}x}h\int_0^{b_j}\langle\overline{u'c'}\rangle\mathrm{d}y \tag{A.83}$$

$$\int_0^{b_j}\left(\frac{\partial\left[h\langle\bar{u}''\bar{c}''\rangle\right]}{\partial x}\right)\mathrm{d}y = \frac{\mathrm{d}}{\mathrm{d}x}h\int_0^{b_j}\langle\bar{u}''\bar{c}''\rangle\mathrm{d}y \tag{A.84}$$

The second, fourth, and sixth terms in Eq. A.81 evaluate to zero:

$$\int_0^{b_j} \frac{\partial \left[h\langle\bar{c}\rangle\langle\bar{v}\rangle\right]}{\partial y}\mathrm{d}y = \langle\bar{c}\rangle\langle\bar{v}\rangle\big|_0^{b_j} = 0 \tag{A.85}$$

$$\int_0^{b_j}\left(\frac{\partial\left[h\langle\overline{v'c'}\rangle\right]}{\partial y}\right)\mathrm{d}y = \langle\overline{v'c'}\rangle\big|_0^{b_j} = 0 \tag{A.86}$$

$$\int_0^{b_j}\left(\frac{\partial\left[h\langle\bar{v}''\bar{c}''\rangle\right]}{\partial y}\right)\mathrm{d}y = \langle\bar{v}''\bar{c}''\rangle\big|_0^{b_j} = 0 \tag{A.87}$$

if the co-flow concentration $c_s = 0$, so $\langle\bar{c}\rangle \to 0$ and $c' \to 0$ as $y \to \pm b_j$. In addition, at the edge of the jet the lateral velocity $\langle\bar{v}\rangle \to v_e$. Making these substitutions, Eq. A.81 can be rewritten as:

$$\frac{\mathrm{d}}{\mathrm{d}x}h\int_0^{b_j}\left(\langle\bar{c}\rangle\langle\bar{u}\rangle + \langle\overline{u'c'}\rangle\right)\mathrm{d}y = 0 \tag{A.88}$$

Eq. A.88 implies that the jet mass flux J is conserved. If the turbulent flux is negligible ($\langle\bar{c}\rangle\langle\bar{u}\rangle \gg \langle\overline{u'c'}\rangle$ and $\langle\bar{c}\rangle\langle\bar{u}\rangle \gg \langle\bar{u}''\bar{c}''\rangle$), then the governing equation for mass flux becomes:

$$\frac{\mathrm{d}J}{\mathrm{d}x} = \frac{\mathrm{d}}{\mathrm{d}x}\int_0^{b_j} h\langle\bar{c}\rangle\langle\bar{u}\rangle\mathrm{d}y = 0 \tag{A.89}$$

Eqs. A.71, A.80, and A.89 are the governing equations for the development of a planar jet developing within a fluid region of varying depth with drag.